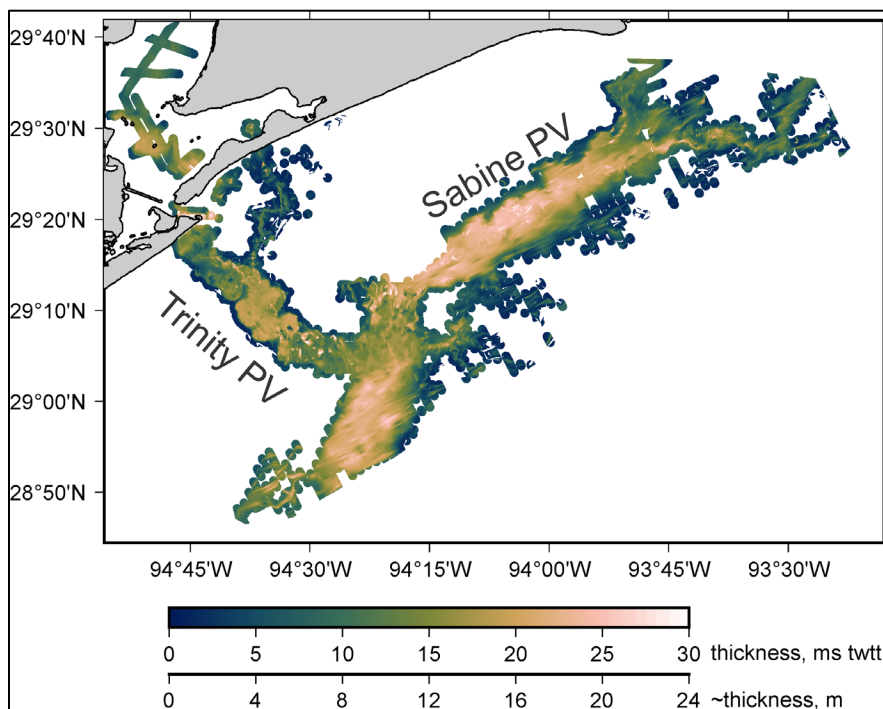


# Texas Offshore Sediment Resources Inventory: Development and Application of Geophysical Processing Workflows for Sand Resource Evaluation



US Department of the Interior  
Bureau of Ocean Energy Management  
Marine Minerals Program  
New Orleans Office



# **Texas Offshore Sediment Resources Inventory: Development and Application of Geophysical Processing Workflows for Sand Resource Evaluation**

June 2022

Authors:

John A. Goff  
Sean S.P.S. Gulick  
Chris M. Lowery  
Gail L. Christeson

Prepared under Cooperative Agreement M16AC00020

by

Institute for Geophysics  
University of Texas at Austin  
JJ Pickle Research Campus, Bldg. 196 (ROC)  
10100 Burnet Rd. (R2200)  
Austin, TX 78758-4445

## **DISCLAIMER**

Study collaboration and funding were provided by the US Department of the Interior, Bureau of Ocean Energy Management (BOEM), Marine Minerals Program, Gulf of Mexico Regional Office, New Orleans, Louisiana, under Agreement Number M16AC00020. This report has been technically reviewed by BOEM, and it has been approved for publication. The views and conclusions contained in this document are those of the authors and should not be interpreted as representing the opinions or policies of the US Government, nor does mention of trade names or commercial products constitute endorsement or recommendation for use.

## **REPORT AVAILABILITY**

To download a PDF file of this report, go to the US Department of the Interior, Bureau of Ocean Energy Management, Marine Minerals Program, Marine Minerals Resource Evaluation Research webpage (<https://www.boem.gov/marine-minerals/marine-mineral-research-studies/marine-mineral-resource-evaluation-research>) and use the Browse Library tools to search report title, report number, region (state), or year.

## **CITATION**

Goff JA, Gulick SPS, Lowery CM, Christeson GL (University of Texas Institute for Geophysics, Austin, Texas). 2022. Texas offshore sediment resources inventory: development and application of geophysical processing workflows for sand resource evaluation. New Orleans (LA): US Department of the Interior, Bureau of Ocean Energy Management. 140 p. Cooperative Agreement No.: M16AC00020. Report No.: 2022-035.

## **ABOUT THE COVER**

Sediment thickness map of the fill units of the Trinity and Sabine River paleovalleys (PV), on the continental shelf of East Texas. Data are based on interpretation of chirp subbottom data from several sources.

## **ACKNOWLEDGMENTS**

The authors gratefully acknowledge the participation of current and former BOEM colleagues in the work supported by this cooperative agreement, including Mike Miner, Jessica Mallindine, Tershara Matthews, Jennifer Steele, and Nicholas Ferina. The authors also express their great appreciation for the University of Texas Institute for Geophysics (UTIG) technical support staff for their efforts at sea and in the lab, including Marcy Davis, Dan Duncan, and Steffen Sastrup.

# Contents

List of Figures.....	vii
List of Tables.....	ix
List of Abbreviations and Acronyms.....	x
1 Introduction .....	13
1.1 Study Area.....	14
2 Expedited Chirp Data Workflow.....	17
2.1 Bottom Picking .....	17
2.2 Static Corrections.....	19
2.2.1 Recording Delay Correction.....	19
2.2.2 Towfish Depth .....	19
2.2.3 Heave Compensation.....	19
2.2.4 Tide Corrections .....	20
2.3 Signal Processing .....	20
2.3.1 Frequency Filtering .....	20
2.3.2 Deconvolution.....	20
2.3.3 Gain Correction .....	20
2.3.4 Water Column Muting .....	22
2.4 Layback Corrections .....	22
3 Data Archiving.....	23
3.1 Seismic Data .....	23
3.2 Core Data.....	25
3.3 Literature Synthesis .....	26
4 New Data Collection for TRiPP.....	27
4.1 2017 MGG Field Course .....	27
4.2 2018 MGG Field Course .....	28
4.3 2018 R/V <i>Trident</i> Survey.....	28
4.4 2019 R/V <i>Manta</i> Coring Cruise .....	29
5 Core Analysis.....	30
5.1 Introduction.....	30
5.2 Region Setting and/or Background .....	32
5.3 Methods.....	35

5.3.1	Seismic Data .....	35
5.3.2	Piston and gravity coring .....	36
5.3.3	Foraminiferal analysis .....	36
5.3.4	Radiocarbon dating .....	38
5.3.5	Age models .....	38
5.4	Results .....	38
5.4.1	Piston core 2 .....	39
5.4.2	Piston core 4 .....	41
5.4.3	Gravity core 6 .....	41
5.4.4	Gravity cores 4 and 5 .....	43
5.4.5	Gravity core 1 .....	46
5.4.6	Gravity core 2 .....	48
5.5	Discussion .....	48
5.5.1	Stable paleoestuary .....	54
5.5.2	Paleoshoreline changes .....	54
5.5.3	Timeline of sea-level rise .....	56
5.5.4	Minimal modern seafloor sedimentation .....	56
5.6	Conclusions .....	57
6	Deltaic Stratigraphy .....	59
6.1	Introduction .....	59
6.2	Study Area .....	60
6.3	Methods .....	63
6.4	Results and Interpretation .....	66
6.5	Discussion .....	72
6.6	Conclusions .....	76
7	Estuarine and Tidal Stratigraphy .....	77
7.1	Introduction .....	77
7.2	Study Area .....	79
7.3	Methods .....	81
7.3.1	Chirp and 3D Seismic Data .....	81
7.3.2	Core Data .....	82
7.4	Results and Interpretation .....	82
7.4.1	Seismic Facies .....	83
7.4.2	Seismic Horizons .....	85
7.4.3	Seismic Units .....	95

7.5	Discussion .....	103
7.5.1	Preservation of Estuarine Deposits.....	103
7.5.2	Estuarine Interaction with Underlying Geology.....	104
7.5.3	Paleo-barrier Island Evolution.....	107
7.6	Conclusions.....	110
8	Reconnaissance Surveys of Trinity-Sabine Paleovalley System .....	111
8.1	Chirp Analysis: Heald and Sabine Banks .....	112
8.1.1	Heald Bank Unit .....	112
8.1.2	Sabine Bank Unit.....	115
8.1.3	Discussion .....	119
8.2	Chirp Analysis: Trinity and Sabine River Paleovalley System .....	121
8.3	Sparker Data .....	123
8.4	Core Analyses .....	126
	References.....	128

## List of Figures

Figure 1.1. Study area location .....	13
Figure 1.2. The east Texas inner continental shelf and Trinity incised valley .....	14
Figure 1.3. Holocene and last ~150 ka sea level curves .....	15
Figure 1.4. Transgressive depositional sequences of the Trinity valley .....	16
Figure 2.1. Example of before-and-after processing of full waveform and envelope chirp records .....	18
Figure 2.2. Bottom Picking .....	19
Figure 3.1. Track lines for data archived to the Academic Seismic Portal .....	24
Figure 3.2. Map of the core geodatabase .....	25
Figure 3.3. Example of digitized core description in the geodatabase .....	26
Figure 4.1. 2017 Field course track lines .....	27
Figure 4.2. 2018 Field course track lines and core locations.....	28
Figure 4.3. 2018 R/V <i>Trident</i> track lines .....	29
Figure 5.1. Study area offshore Galveston Bay, Texas.....	32
Figure 5.2. Holocene sea level curve.....	33
Figure 5.3. Trinity River transgressive systems tract.....	33
Figure 5.4. Cross section of the Trinity River Paleovalley in modern Galveston Bay, Texas.....	34
Figure 5.5. Foraminiferal predominance facies of Galveston Bay, Texas .....	37
Figure 5.6. Stratigraphic columns and select core images from this study .....	39
Figure 5.7. Piston Core 2 (PC-2) .....	40
Figure 5.8. Piston Core 4 (PC-4) .....	42
Figure 5.9. Gravity Core 6 (GC-6).....	43
Figure 5.10. Comparison of GC-6 upper sample (7–8.5 cm) to modern foram assemblages.....	44
Figure 5.11. Gravity Core 4 (GC-4).....	45
Figure 5.12. Gravity Core 5 (GC-5).....	46
Figure 5.13. Gravity core 1 (GC-1) .....	47
Figure 5.14. Gravity core 2 (GC-2) .....	49
Figure 5.15. Fence diagram of prominent environmental changes within cores within study area .....	50
Figure 5.16. Timeline of environmental change and sea-level rise in Galveston paleoestuary .....	51
Figure 5.17. Paleoenvironmental change of Holocene estuary offshore Galveston Bay, Texas .....	53
Figure 6.1. The east Texas inner continental shelf and Trinity incised valley .....	60
Figure 6.2. Holocene and last ~150 ka sea level curves .....	61
Figure 6.3. Transgressive depositional sequences of the Trinity valley .....	62
Figure 6.4. Data coverage of the Trinity incised valley .....	64
Figure 6.5. Comparison of seismic data types and resolutions .....	64
Figure 6.6. 3D seismic crossline of the Trinity incised valley.....	65
Figure 6.7. 3D attribute extract of valley surface horizon .....	66

Figure 6.8. Chirp strike line across the valley close at upper extent of study area.....	67
Figure 6.9. Example of full waveform chirp imaging of valley stratigraphy from Figure 6.8 .....	68
Figure 6.10. Chirp strike line across the valley close at lower extent of study area .....	68
Figure 6.11. Example of full waveform chirp imaging of valley stratigraphy from Figure 6.10 .....	69
Figure 6.12. Chirp dip line down center of the valley .....	70
Figure 6.13. Example of full waveform chirp imaging of valley stratigraphy from Figure 6.12 .....	71
Figure 6.14. Core penetrating top of fluvial terrace and correlation to full waveform chirp .....	72
Figure 6.15. Paleo-environments of valley fill stratigraphy based on core-full waveform chirp correlation	73
Figure 6.16. Time structure maps of key horizons and example full waveform chirp line .....	74
Figure 6.17 Thickness maps (ms) of Trinity valley stratigraphy.....	75
Figure 6.18. Chirp lines crossing paleo-Trinity channel.....	76
Figure 7.1. Map of the east Texas inner shelf.....	78
Figure 7.2. Proposed shoreline history of the Texas inner shelf.....	80
Figure 7.3. Chirp geophysical tracklines .....	81
Figure 7.4. Seismic facies diagram.....	83
Figure 7.5. TRiPP Line 38 envelope record.....	84
Figure 7.6. TRiPP Line 38 full waveform record west.....	85
Figure 7.7. TRiPP Line 38 full waveform record central .....	86
Figure 7.8. TRiPP Line 38 full waveform record east .....	87
Figure 7.9. 2018 CH Line 3 envelope record .....	88
Figure 7.10. 2018 CH Line 3 full waveform record central .....	89
Figure 7.11. 2018 CH Line 3 full waveform record central .....	90
Figure 7.12. Boring 4 and Gravity Core 6 .....	91
Figure 7.13. Gravity Cores 4 and 5.....	92
Figure 7.14. Piston Cores 2 and 4 .....	93
Figure 7.15. Gravity Core 2.....	94
Figure 7.16. TRiPP Line 43 envelope record.....	96
Figure 7.17. TRiPP Line 43 full waveform record .....	97
Figure 7.18 Time-structure maps .....	99
Figure 7.19. Time-thickness maps .....	101
Figure 7.20. Paleovalley morphology.....	106
Figure 7.21. Model for paleovalley evolution .....	108
Figure 8.1. Chirp track locations .....	111
Figure 8.2. East Texas shelf .....	113
Figure 8.3. Chirp line OCS53.....	114
Figure 8.4. Chirp Line OCS53 enlargement.....	114
Figure 8.5. Archival core logs of Heald Bank Unit .....	115
Figure 8.6. Isopach map of the Heald/Shepard Bank Unit .....	116

Figure 8.7. Chirp line OCS46 .....	117
Figure 8.8. Chirp line OCS36 .....	117
Figure 8.9. Chirp line OCS216 .....	118
Figure 8.10. Chirp Line OCS53 enlargement.....	118
Figure 8.11. Isopach map of the Sabine Bank Unit .....	119
Figure 8.12. Chirp line TS308b .....	120
Figure 8.13. Illustration of proximal washover stratigraphy .....	120
Figure 8.14. Chirp line OCS100 .....	122
Figure 8.15. Chirp line OCS14 .....	122
Figure 8.16. Isopach map of the valley fill unit.....	123
Figure 8.17. Sparker track locations .....	124
Figure 8.18. Example before and after processing shot gathers for sparker data.....	125
Figure 8.19. Example of imaging using the Edgetech 216 and the Dura-Spark.....	126

## List of Tables

Table 3.1. SCS data archived to Academic Seismic Portal .....	23
Table 3.2. Chirp data archived to Academic Seismic Portal.....	24
Table 3.3. Number of manuscripts added to the TRiPP literature database .....	26
Table 5.1. Core locations and depositional environments .....	58
Table 5.2. List of radiocarbon dating samples and their calibrated ages .....	58
Table 8.1 List of acquired sparker lines during 2021 R/V Tommy Munro acquisition .....	127

## List of Abbreviations and Acronyms

Short form	Long form
AGC	automatic gain control
BOEM	Bureau of Ocean Energy Management
bp	before present
DOI	US Department of the Interior OR Document Object Identifier
GC	gravity core
GLO	Texas' General Land Office
GPS	global positioning system
Hz	Hertz (measure of frequency)
.jsf	file extension of data format utilized by Edgetech
ka	kilo-anums (1000 years)
kyr	thousand years
LIS	Laurentide Ice Sheet
mbsl	meters below sea level
MGG	Marine Geology and Geophysics
MIS	Marine Isotope Stage
ms	milliseconds
NOAA	National Oceanic and Atmospheric Administration
NOSAMS	National Ocean Sciences Accelerator Mass Spectrometry
PC	piston core
RSLR	relative sea-level rise
SEGY	standard seismic data storage format (Society of Exploration Geophysicists – Y)
TMB	Texas Mud Blanket
TRiPP	Trinity River Paleovalley Project
twt or twtt	two-way travel time
USBL	ultra-short base line
USGS	United States Geologic Survey
UTIG	University of Texas Institute for Geophysics
VE	vertical exaggeration

## Summary

The primary motivation for establishing this Texas Cooperative Agreement was to catalog sand resources on the Texas shelf in Federal waters. More fundamentally, we sought to understand these deposits from a systems approach; that is, to understand the fluvial, estuarine, and marine processes by which these sediments were transported, deposited, modified, and ultimately preserved. We have made numerous accomplishments in support of these complimentary goals. These range from improvements to chirp data processing, which enhance our ability to map subsurface deposits, to rescue and archive of existing data, which improves capability to conduct desktop surveys, to collection and interpretation of newly collected data to discover and research new potential resource locations. These efforts were also integrated into the University of Texas Marine Geology and Geophysics field course to provide a strong educational component to these efforts.

The chirp workflow has been fully tested and is operational using scripts that use Paradigm's ECHOS seismic processing package. During two field classes, we successfully trained students to operate the processing scheme, and they were able to run the processing in near real time in the field. A "best practices" white paper has been prepared, which was reviewed, revised, and accepted by BOEM. The white paper is available on EarthArXiv and has been downloaded over 540 times, as of this published report.

We have archived 22 chirp and/or seismic cruises in the Academic Seismic Portal. We have completed the digitization, georeferencing, and creation of a geodatabase containing 642 cores and platform borings across the western and central Gulf of Mexico. These represent samples compiled from available academic literature and technical reports, as well as digitization of previously unpublished holdings from Rice University.

We focused our new data collection efforts on the Trinity River Paleovalley, offshore of Galveston, Texas. This structure was chosen both for the potential of sandy deposits, such as fluvial, deltaic, or overwash, and for demonstrating the efficacy of chirp subbottom data in surveying such deposits. We collected chirp and coring data on five separate occasions, including two field course cruises that provided reconnaissance lines and cores, one dedicated chirp cruise that collected a dense grid of data, and one coring cruise. One of these multidisciplinary cruises focused on the linkages between the Trinity River and Sabine River paleovalleys, and also included sparker seismic data that imaged the base of the fluvial, likely sand rich facies lying at the base of these incised valleys.

Our doctoral student, John Swartz, successfully defended his dissertation in November of 2019, completing his research project on interpreting the fluvial section of the Trinity River Paleovalley and writing up his work as a chapter of his dissertation. In his interpretation, the chirp data show the transition of individual fluvial channels from sand rich, laterally migrating systems to muddy channels that show high rates of vertical aggradation and little lateral movement. We observe interaction of these channels with the paleo-floodplain and show that aggradation and infilling of the incised valley is dominated by fluvial processes before a transition to bay and estuarine conditions. This work illustrates that traditional models of incised valley filling and fluvial response to transgression fail to fully capture the morphodynamics of coastal river systems.

The uppermost estuarine unit characterized by high-amplitude, laminated reflectors, has been mapped now throughout the study region by our Master's degree student, Jake Burstein. Based on foraminiferal assemblages in cores, this unit is identified as an outer bay facies, and is composed of alternating sand and mud layers. The sand-rich intervals are interpreted as likely barrier island washover deposits. Work has also begun on interpreting a complex set of channelized ravinements located at the distal third of our

survey area. We interpret these as components of a tidal ravinement filled in part by flood tide delta deposits, which includes lenses of dipping reflectors possibly consisting of alternating sand and mud deposits.

Grain size analysis completed before COVID-19-related lab closures provided quantitative grain size data from PC-4, located on a Pleistocene terrace deposit, revealing up to 80% sand in the base of the valley. Micropaleontological analysis of cores has been completed by our undergraduate student Patricia Standing. Assemblages of benthic foraminifera have revealed paleoenvironments ranging from middle bay to outer bay to back barrier lagoons. Carbon dating of micro and macrofossil carbonate and plant organic matter has constrained the age of the paleoestuary from ~9,300 to ~ 4,300 Cal yr bp.

A final round of data collection occurred in April 2021. This effort consisted of a reconnaissance effort to investigate the offshore continuance of the Trinity paleovalley to its confluence with the Sabine paleovalley, the landward extension of Sabine from the confluence, as well as Heald and Sabine banks. We were able to combine our data collection with a survey of the banks by APTIM, collected under funding by BOEM through the Texas General Land Office under Coastal Erosion Planning and Response Act (CEPRA) project 1706. This provided us with wide regional coverage of this extensive paleovalley system.

# 1 Introduction

This report summarizes accomplishments made over the five-year span of this cooperative agreement, which has several parallel overarching goals, and which encompass the specific objectives and tasks and delineated in the Cooperative Agreement:

- (1) Develop our long-used, in-house chirp processing workflow into a product that can be robustly and easily used by BOEM and other, non-seismic processing expert users, and disseminate our own understanding of best practices for chirp data collection and processing in a white paper (complete);
- (2) Collect chirp and coring data, construct a data base of existing data, and perform a literature review and synthesis for a study area of mutual interest to the University of Texas Institute for Geophysics (UTIG) and Bureau of Ocean Energy Management (BOEM). Particular emphasis was placed on sand resource investigations, gathering and synthesizing existing data and literature within this region, and linking these efforts with the educational component provided by UTIG's marine geology and geophysics class; and
- (3) "Rescue" seismic and core data holdings for the broader study area of the Texas shelf, digitize and format to BOEM specifications, and upload them to accessible digital archives, particularly those collected over the years by the just-retired John Anderson and his students at Rice University.

The study area, chosen in Year 1, focused on the Trinity River Paleovalley (**Figure 1.1**), both for its potential to harbor significant sand resources, and for the challenges it poses to geophysical and geological investigation. New plans were later formed for extending reconnaissance coverage seaward to the Trinity-Sabine confluence, and then landward along the Sabine paleovalley and including Heald and Sabine Banks. This includes additional data collected by APTIM.

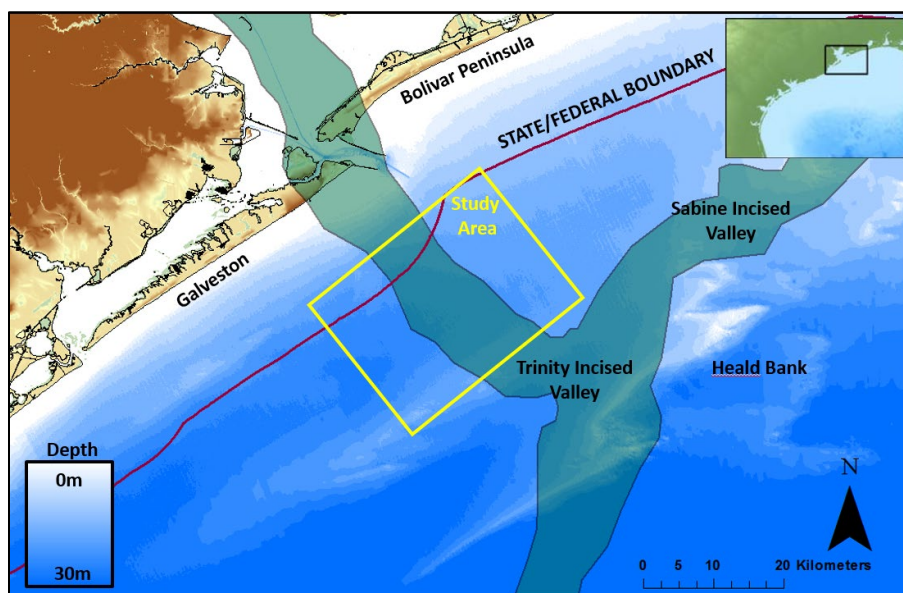


**Figure 1.1. Study area location**

Map showing the East Texas shelf, with the TRiPP (Trinity River Paleovalley Project) study area in yellow.

## Study Area

The Trinity incised valley has been the focus of significant research over the past several decades, and, as a result, detailed maps and models of the valley sedimentary architecture and patterns and timing of shifts in depositional environment have been created primarily using geotechnical borings, sediment cores, and seismic datasets of varied frequency (e.g., Thomas and Anderson, 1994; Rodriguez et al., 2005; Anderson et al., 2008; **Figure 1.2**). The majority of this work has focused on understanding the overall evolution of the Trinity valley and surrounding east Texas continental shelf from previous sea-level highstands to the present (Anderson et al., 2016). The Trinity incised valley began forming during sea-level fall from marine isotope stage (MIS) 5-3 and extended from the modern-day Trinity Bay across the continental shelf (Thomas and Anderson, 1994; **Figure 1.3B**). It reached its maximum shelf edge location during the last lowstand (MIS 2) at 22-17 ka bp and the associated erosion produced a significant, regionally correlatable erosional surface (Simms et al., 2007). Total relief of the valley surface has been measured at 30–40 m across the shelf, although due to subsequent infilling it exists offshore only as a stratigraphic feature entirely buried beneath the modern seafloor (Thomas and Anderson, 1994).

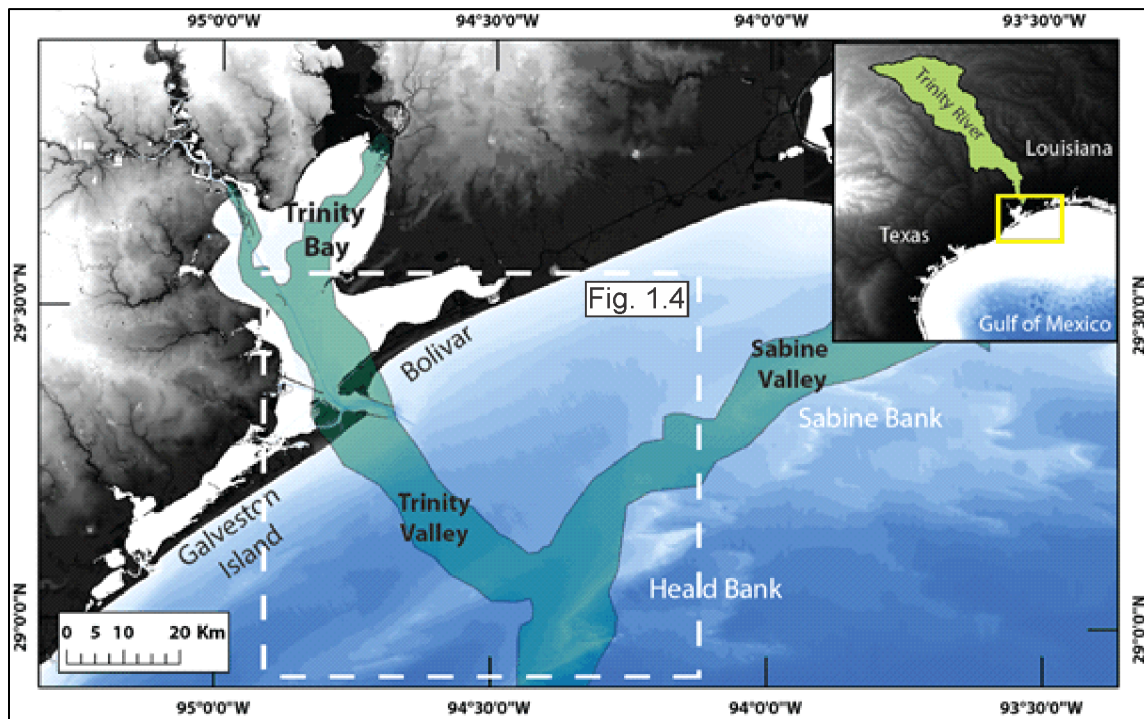


**Figure 1.2. The east Texas inner continental shelf and Trinity incised valley**

Map of the study area. The shaded valley represents the previously determined extent of the Trinity and Sabine incised valley systems during MIS2. Inset panel shows location of study area within the northern Gulf of Mexico and the outline of the modern Trinity River drainage basin.

Sea-level rise following the MIS2 lowstand-triggered aggradation and valley filling across the continental shelf for the Trinity and other Gulf of Mexico fluvial systems (Anderson et al., 2016). Despite the rapid rates of sea-level rise between ~17 ka and ~10 ka the Trinity system maintained a shelf-edge delta until at least ~14 ka before beginning to transgress towards its modern position (Wellner et al., 2004). The record of Holocene sea-level rise in the Gulf of Mexico is relatively well constrained and captures the transition

from relatively rapid rates of 4.2 mm/yr from 12 ka to 1.4 mm/yr at 7.9 ka (Milliken et al., 2008; **Figure 1.3A**). From ~10 ka onward The Trinity valley was filled by a series of landward stepping transgressive depositional packages interpreted as successions of fluvial, deltaic, bay, and tidal deposits (Rodriguez et al., 2005; Thomas and Anderson, 1994; **Figure 1.4**). The relatively rapid transition from fluvial deposition to deltaic and estuarine as well as the back-stepping nature of the deposits towards the modern Trinity bayhead delta has been interpreted as due to the episodic nature of early Holocene sea-level rise, or alternatively due to differential flooding of antecedent topography (Anderson et al., 2008; Rodriguez et al., 2005; Simms and Rodriguez, 2014; Thomas and Anderson, 1994; **Figure 1.3A**). Additionally, the pattern of back-stepping as well as the presence of the modern Galveston Bay throughout the Holocene implies that sediment supply of the Holocene Trinity River was unable to keep up with rates of base-level rise, in contrast to several other Gulf of Mexico-area rivers (Simms et al., 2006; Anderson et al., 2016).

The stratigraphic architecture of the Trinity valley has been previously interpreted on a broad scale through a combination of cores and geophysical data (**Figure 1.4B**; Anderson et al., 2016; Rodriguez et al., 2005; Thomas and Anderson, 1994). The following framework is that build by Thomas (1991). The broad erosional valley base in the study area is located ~30 m below the modern seafloor and is immediately overlain by a 10–15 m thick package of gravels, sands, interbedded silts and clays as well as dense peats and vegetation lenses. This basal unit has been interpreted to represent an amalgamated package of fluvial sands and floodplain sediments deposited during the early Holocene transgression, with some radiocarbon dating indicating the upper portions were deposited as recently as 10.3 ka bp. Thomas (1991) also noted that the top of this unit is commonly associated with seismic blanking and little acoustic penetration, which is a potential signature of either coarse grained material or shallow biogenic gas accumulation along lithologic contacts. Above this unit is a 5–15 m section of interbedded sand, mud, and silt that micropaleontological analysis indicates is made up of floodplain, deltaic and upper bay sediments, with deposition occurring between 8–0 ka bp. The final unit sees a transition to more open bay or estuarine conditions, and in portions of the study area significant scours associated with flood-tide delta deposits (Anderson et al., 2016; Thomas, 1991). Thomas and Anderson (1994) proposed this succession of units as representative of the overall transgressive sequence, with relatively constant fluvial conditions and backstepping driven by relative sea-level rise rather than aggradation or changes in fluvial dynamics or sediment flux (**Figure 1.4A**).

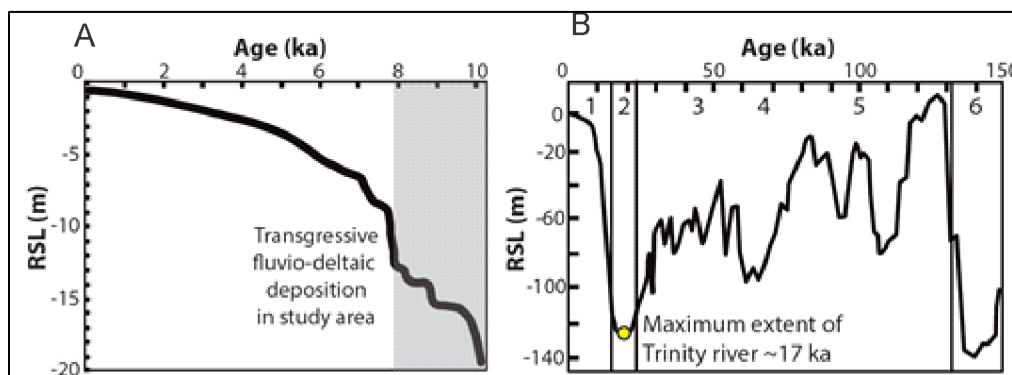


**Figure 1.3. Holocene and last ~150 ka sea level curves**

A) Composite sea level curve for the study area (modified from Milliken et al., 2008). The grey area represents the previously determined period of fluvial/deltaic sedimentation prior to transgression and onset of estuarine conditions (Anderson et al., 2016). B) Eustatic sea-level curve modified from Shackleton (2000). Marine Isotope Stages (MIS) 1–6 are labeled. The yellow dot indicates when the paleo-Trinity River reached its maximum shelf-edge location at ~17 ka (Thomas and Anderson, 1994).

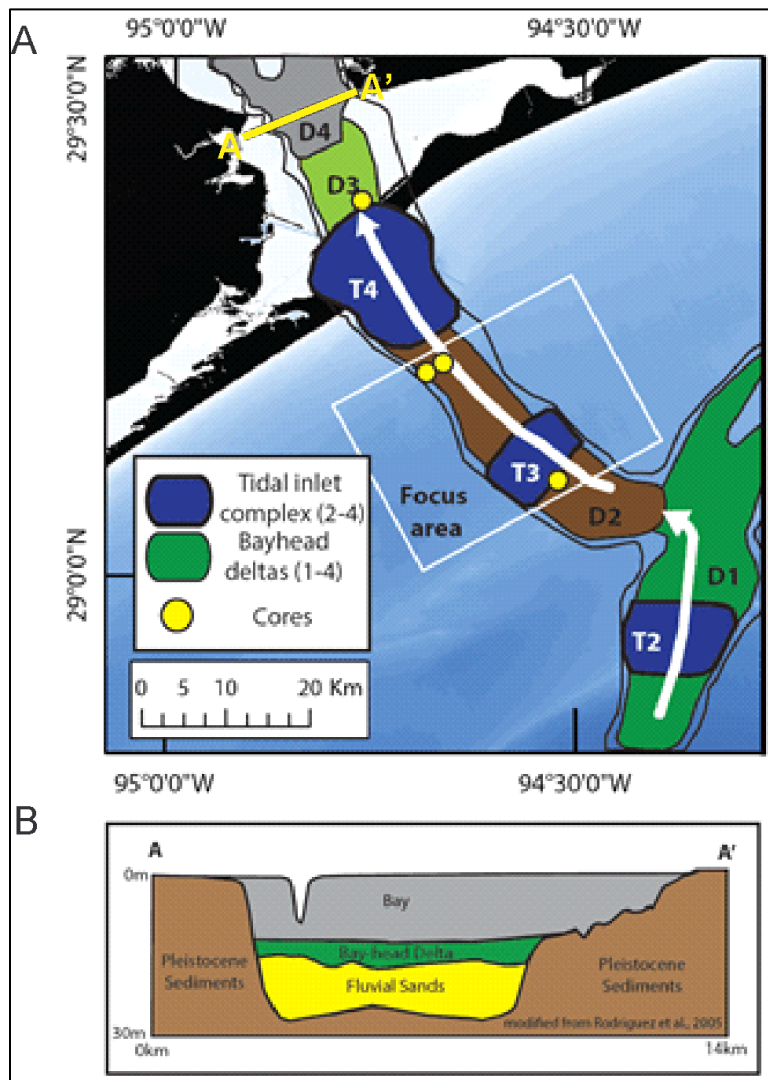


**Figure 1.4. Transgressive depositional sequences of the Trinity valley**

A) Map of backstepping bayhead deltas and associated tidal inlets infilling the Trinity incised valley during the Holocene transgression (modified from Anderson et al., 2016). The study area covers the interpreted delta 2 and tidal inlet complex 3, formed ~7–8 ka. B) Representative cross section of Trinity incised valley stratigraphy. The valley base is formed by a broad erosional unconformity covered with a transgressive sequence of fluvial sands, bay-head delta deposits, and finally bay sedimentation (modified from Rodriguez et al., 2005). Location in **Figure 1.2**.

## 2 Expedited Chirp Data Workflow

We have found that even a quick and automated level of processing of chirp data can render the envelope data much more interpretable, and the underutilized, higher-resolution full waveform data more accessible. We have developed a proposed chirp processing flow to perform these tasks. At its core this processing flow is an iterative high-resolution seafloor picking and smoothing scheme designed to be as robust, accurate, and automated as possible. Selected digital signal processing is also performed on the full waveform data.

Edgetech chirp data are typically recorded as “.jsf”-formatted files, a native Edgetech format that includes four different data channels: “real,” “imaginary,” “envelope,” and “spectrum.” The two channels of interest to the following processing scheme are “real”, which are the full waveform record, and “envelope”, which are the envelope-processed data more commonly seen (**Figure 2.1**). Following data archiving (primary recording to top-side main drive and backup to secondary external drive), and prior to processing, these records must be converted to SEGY format files, which can be done with a number of available utilities. If a single survey line consists of multiple individual files, we find it useful to first convert and then concatenate these records into a single SEGY file for processing. The Edgetech acquisition software also provides an option to record directly to SEGY format. However, this format only includes envelope records; full waveform is only retained in the .jsf files. As noted above, we highly recommend acquiring field data in .jsf or an analogous format, such as .keb files for Knudsen systems, that retains both data types.

Our chirp processing scheme involves three primary data streams. The first of these streams includes the critical step of picking the seafloor (to within a fraction of a wavelength at ~5000 Hz, or about 0.1 ms), which provides the basis for the other two data streams: real and envelope processing. Processing of real and envelope data in turn involves three steps: static corrections (heave compensation, towfish depth and tides), signal processing to improved image clarity, and layback correction for navigation.

### 2.1 Bottom Picking

The key step to being able to remove heave artifacts from chirp data, as well as for some signal processing, is to generate a precise pick of the seafloor reflection. A fully-automated bottom picker is desirable for ease-of-use but, in our experience, can fail regularly in the presence of high noise, low seafloor signal, or amplitude variability. Our own bottom-picking algorithm involves an iterative process, beginning with a coarse pick using a simple threshold algorithm, and successively refining using both automated methods (**Figure 2.2A**) and, optionally, user interaction in more difficult cases. The details of this algorithm are complex and beyond the scope of this document. Once completed, the bottom pick enables the user’s ability to move individual records up or down (i.e., apply a “static”) in relation to the seafloor arrival. Heave filtering, described below, is one such application. It is also possible to flatten the record to the seafloor (**Figure 2.2B**), which is useful for quality control; i.e., enhance both the user’s ability to visually identify bad bottom picks and the algorithm’s ability to iteratively refine the picks. Flattening is also a prerequisite for some of the processing steps described below. The seafloor flattening step is reversed later in the processing stream to preserve true topographic features at the seafloor.

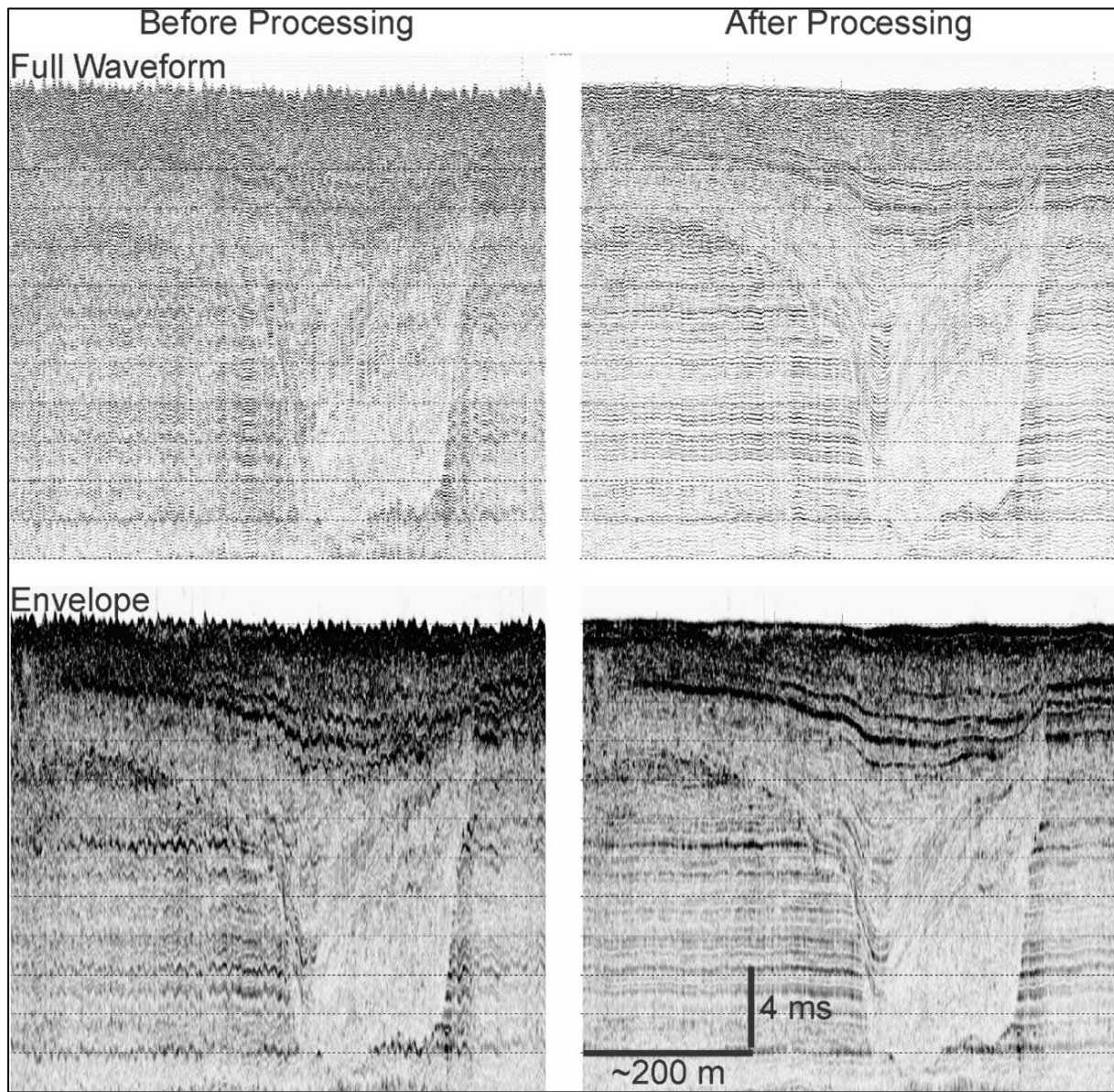


**Figure 2.1. Example of before-and-after processing of full waveform and envelope chirp records**  
 Example exhibits highly detailed stratigraphic structure, to demonstrate the level of improvement in stratigraphic imaging that can be attained with chirp processing. Data were collected offshore of Freeport, Texas using an Edgetech 512i towfish with a 20 ms 0.7–12 kHz pulse.

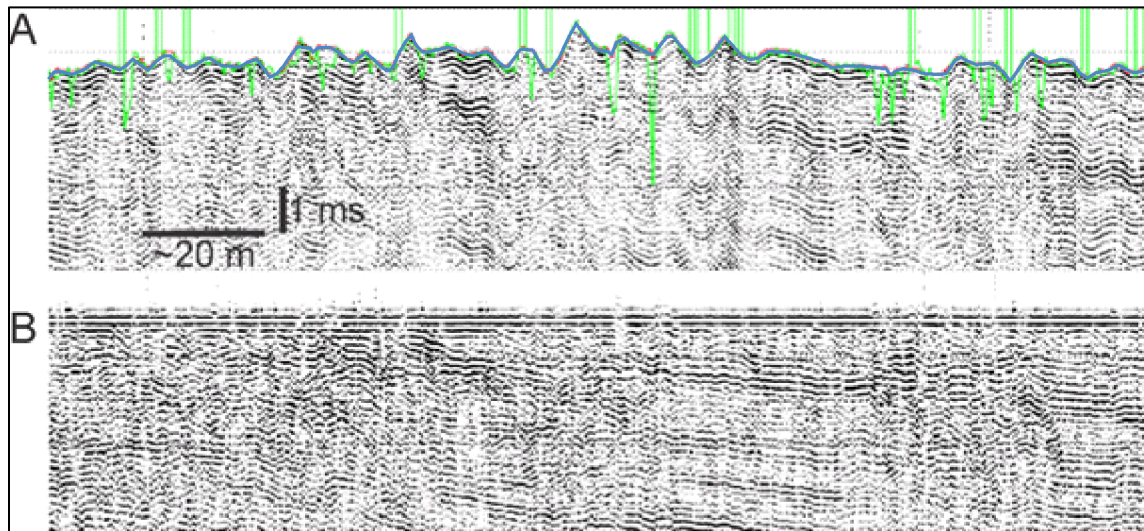


**Figure 2.2. Bottom Picking**

(A) Highly enlarged section of a chirp full-waveform record showing an initial bottom pick (bright green), which has many spurious picks, and an iteratively refined bottom pick (blue). (B) Same record shown in (A) flattened to the seafloor defined by the refined bottom pick. These data are a subsection of data shown in **Figure 2.1**.

## 2.2 Static Corrections

### 2.2.1 Recording Delay Correction

The data are corrected for any recording delay (nonzero start recording time, also called deepwater delay) that may have been used in the field. This is often the case when operating in deep water; a delayed start of the recording time (a simple option in Edgetech systems, for example) can be used skip over large quantities of potentially useless water column returns and thereby keep record lengths and file sizes to manageable values.

### 2.2.2 Towfish Depth

A time series for towfish depth is recorded in the field and used to correct to a sea-surface datum. This depth can be estimated using a variety of methods, including cable length and/or angle, a pressure sensor mounted on or integrated into the towfish, or ascertained with a USBL system. For best results, this step should be performed before the seafloor picking. We use a simple time interpolation between observed or recorded points.

### 2.2.3 Heave Compensation

The seafloor picks are smoothed using a user-defined (nominally 35–75 pings) low-pass filter that is large enough to average out heave artifacts. The difference between the filtered and unfiltered seafloor picks forms a static correction to correspondingly shift the traces up or down to compensate for heave (Figure 7A, B). Care must be taken during this step to not over-smooth the seafloor and remove true topography (although this is not always possible if seafloor features are of similar wavelength to heave artifacts). Heave correction values as calculated on the full waveform data are stored in a database and applied identically to both envelope and full waveform data. An important best practice for processed data is to incorporate values for final picked seafloor time, smoothed seafloor time, and seafloor static into the trace

header. This enables heave compensation filtering to be “undone” so that other correction algorithms can be applied (e.g., fitting the picked seafloor to a known bathymetric surface).

## 2.2.4 Tide Corrections

A tide time series, either observed or predicted, is used to correct to Mean Low Tide or any other local datum. This time series should be smoothed as necessary beforehand to avoid artifact. Tide corrections are needed to ensure that reflectors on crossing lines will have the same twtt.

## 2.3 Signal Processing

Signal processing (frequency filtering, deconvolution, gain correction, and water column muting) is performed after the data have been temporarily flattened at the seafloor (**Figure 2.2B**) for best results. Some signal processing methods, such as frequency filtering and deconvolution, can be applied only to the real, full waveform data traces.

### 2.3.1 Frequency Filtering

Full waveform data are bandpass-filtered using a filter comparable to the source wavelet band (e.g. 700–12000 Hz Butterworth Filter, with a filter length of 91 samples). This step primarily removes low-frequency towing noise.

### 2.3.2 Deconvolution

Full waveform data are deconvolved (multi-ping predictive deconvolution) to account for slight inconsistencies in the match-filtering process (likely owing to differences between modeled and actual outgoing pulse waveforms) and to attenuate very-short-period interbed multiples. This procedure is applied to flattened records (**Figure 2.2A**), which is reversed after the deconvolution is performed. The net visual result is to give the data a less “ringy” quality (**Figure 2.3C**). In practice for our data, we use a deconvolution operator calculated from the chirp data (e.g., a 31-trace predictive deconvolution with a filter length of 15 samples and a prediction distance of 4 samples); this is not to collapse the original outgoing pulse but rather the remnant of the outgoing pulse not removed by the match filtering in the towfish. Doing this step on temporarily seafloor-flattened data allows for the use of a constant design window of 10ms starting at the seafloor which saves having to define a design window that moves up and down with the seafloor. Additional details regarding predictive deconvolution of chirp data can be found in Baradello (2014).

### 2.3.3 Gain Correction

Amplitudes are corrected to account for lateral variation spatially (due largely to towfish pitch), and temporally to account for transmission loss and spherical divergence. This step is done using a water-velocity spherical divergence correction followed by a windowed lateral trace balance. This gain preserves the true amplitudes of the data and your final data product can be saved with this type of gain correction applied. An additional automatic gain control (AGC, 30 ms length is common) scaling is optional and produces improved displays (**Figure 2.3D**), but this gain will mask true amplitude variations. Therefore, an AGC is advised for display purposes only but not for data processing and archiving.

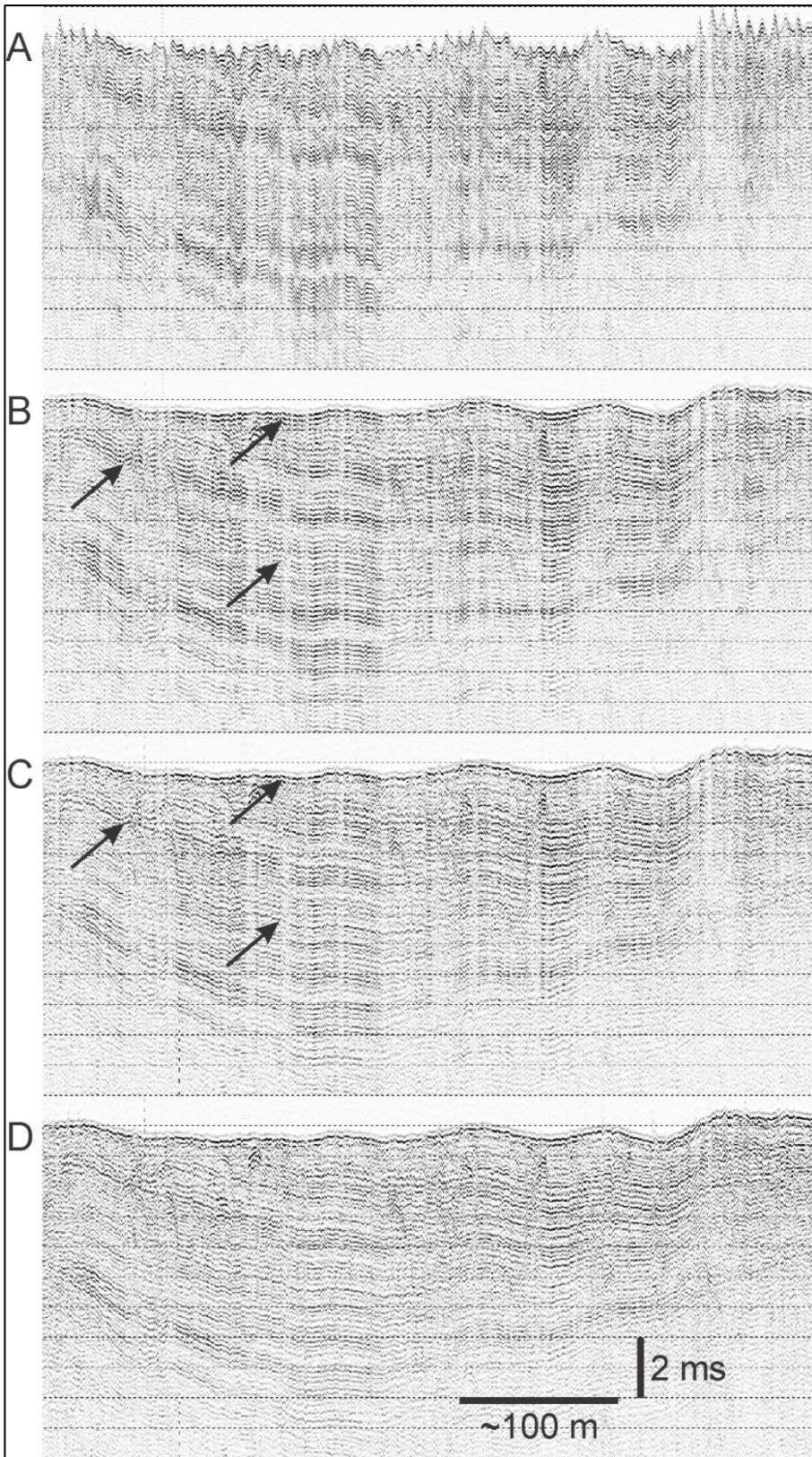


**Figure 2.3.**  
**Illustration of key chirp processing steps**

(A) Raw full-waveform record collected on the Rio Grande delta. (B) After bottom picking and heave filtering. (C) After secondary deconvolution. Arrows in (B) and (C) identify several examples of ringy reflectors (including seafloor) that have been sharpened by the secondary deconvolution. (D) After gain correction, which reduces vertical banding.

### **2.3.4 Water Column Muting**

Data may be muted above the picked seafloor arrival time to remove any water column noise. This is done primarily for generating a cleaner display for publication. This step should not be performed, however, if there are features of interest in the water column (e.g., active gas seeps).

## **2.4 Layback Corrections**

X and Y layback corrections, either estimated from tow observations, or determined acoustically with ultra-short baseline (USBL) location instruments, are applied to the original GPS navigation recorded in the SEG-Y trace headers. These new values are then inserted into the trace headers, replacing the original positions. Original SEG-Y files are retained to preserve original navigation recordings, but the layback corrected files are used for stratigraphic interpretation.

Chirp data are generally recorded with GPS data in the trace headers and thus are in geographic coordinates (latitude and longitude). However, for use in interpretation software, it can be useful (or for some software required) to convert geographic position output (commonly listed as arc-seconds in the trace header where longitude is the X value and latitude the Y value) to Universal Transverse Mercator (or other projections) where the X and Y values are generally meters or feet. This conversion assists in distance, area, and volume calculations done during interpretation. No map projection can simultaneously preserve area, distance, shape, and angle so selecting a project for the final data use is advised.

### 3 Data Archiving

We have recovered and archived seismic and core/boring data from the decades of Rice University led studies on the Gulf of Mexico continental shelves. The lead investigator Professor John Anderson has retired; he and his students have been extremely forthcoming with data including electronic seismic data (SEG-Y and Elics format), paper records, and a series of files related to core and borings. We detail our accomplishments with each below.

#### 3.1 Seismic Data

We have digitized navigation for 5 single-channel seismic (SCS) and 14 chirp datasets and archived them in the Academic Seismic Portal (**Tables 3.1 and 3.2; Figure 3.1**), including 3 chirp datasets from DAT tapes provided by Jim Flocks (USGS). We have now archived all of the SEG-Y data that we can associate with navigation from DVDs and tapes in the collection of boxes obtained from John Anderson and from personal communication with his former students. We have a number of Elics-formatted seismic data files, but it is unclear whether these files have navigation in their headers. So far, our attempts to obtain a system to read this format have failed. **Figure 3.1** summarizes the location of all data from this project that have been archived in the Academic Seismic Portal of the Marine Geoscience Data System<sup>1</sup>. We have also completed an inventory of all paper records obtained from John Anderson's group at Rice University.

**Table 3.1. SCS data archived to Academic Seismic Portal**

Dataset	References	#SEG-Y Files	Volume (GB)	DOI
LS9001	Abdulah (1995); Anderson et al. (1996); Abdulah et al. (2004)	5	3.4	10.1594/IEDA/500171
LS9101	Abdulah (1995); Anderson et al. (1996); Abdulah et al. (2004)	16	1.9	10.1594/IEDA/500172
LS9201	Abdulah (1995); Anderson et al. (1996); Abdulah et al. (2004)	19	1.3	10.1594/IEDA/500184
LS9301	Abdulah (1995); Anderson et al. (1996); Abdulah et al. (2004)	4	0.2	10.1594/IEDA/500185
LS9509	Banfield (1998); Anderson et al. (2004); Banfield and Anderson (2004)	77	1.7	10.1594/IEDA/500167 10.1594/IEDA/500168

---

<sup>1</sup> See <https://www.marine-geo.org/collections/#!/collection/Seismic#summary>

**Table 3.2. Chirp data archived to Academic Seismic Portal**

Dataset	References	#SEG-Y Files	Volume (GB)	DOI
LS9601	Rodriguez (1999); Rodriguez et al. (1999)	14	1.9	10.1594/IEDA/500170
LS9606G B	Rodriguez (1999); Rodriguez et al. (1999)	14	1.9	<a href="https://doi.org/10.1594/IEDA/500186">10.1594/IEDA/500186</a>
LS9606TS	Rodriguez (1999); Rodriguez et al. (1999)	33	3.6	10.1594/IEDA/500183
LS9607	Rodriguez (1999); Rodriguez et al. (1999)	26	3.4	<a href="https://doi.org/10.1594/IEDA/500188">10.1594/IEDA/500188</a>
LS9705	Rodriguez (1999); Rodriguez et al. (1999)	17	2.6	<a href="https://doi.org/10.1594/IEDA/500182">10.1594/IEDA/500182</a>
LS9807M B	Rodriguez (1999); Rodriguez et al. (1999); Rodriguez et al. (2008)	12	1.4	<a href="https://doi.org/10.1594/IEDA/500187">10.1594/IEDA/500187</a>
LS99WB	Rodriguez, 1999; Rodriguez et al. (1999); Anderson et al. (2008)	12	0.9	<a href="https://doi.org/10.1594/IEDA/500189">10.1594/IEDA/500189</a>
JN0201	Rodriguez et al. (2008)	19	0.6	<a href="https://doi.org/10.1594/IEDA/500207">10.1594/IEDA/500207</a>
JN0205	Lambert et al. (2003); Lambert et al. (2008)	13	0.3	<a href="https://doi.org/10.1594/IEDA/500220">10.1594/IEDA/500220</a>
JN0206	Green (2006); Green et al. (2007); Rodriguez et al. (2008)	12	0.4	<a href="https://doi.org/10.1594/IEDA/500195">10.1594/IEDA/500195</a>
JN0208	Rodriguez et al. (2008)	6	0.2	<a href="https://doi.org/10.1594/IEDA/500208">10.1594/IEDA/500208</a>
JN0306	Green (2006); Green et al. (2007); Rodriguez et al. (2008)	66	2.1	<a href="https://doi.org/10.1594/IEDA/500196">10.1594/IEDA/500196</a>
JN0405	Rodriguez et al. (2008)	9	0.3	<a href="https://doi.org/10.1594/IEDA/500235">10.1594/IEDA/500235</a>
JN0406	Green (2006); Green et al. (2007); Rodriguez et al. (2008)	12	0.4	<a href="https://doi.org/10.1594/IEDA/500197">10.1594/IEDA/500197</a>

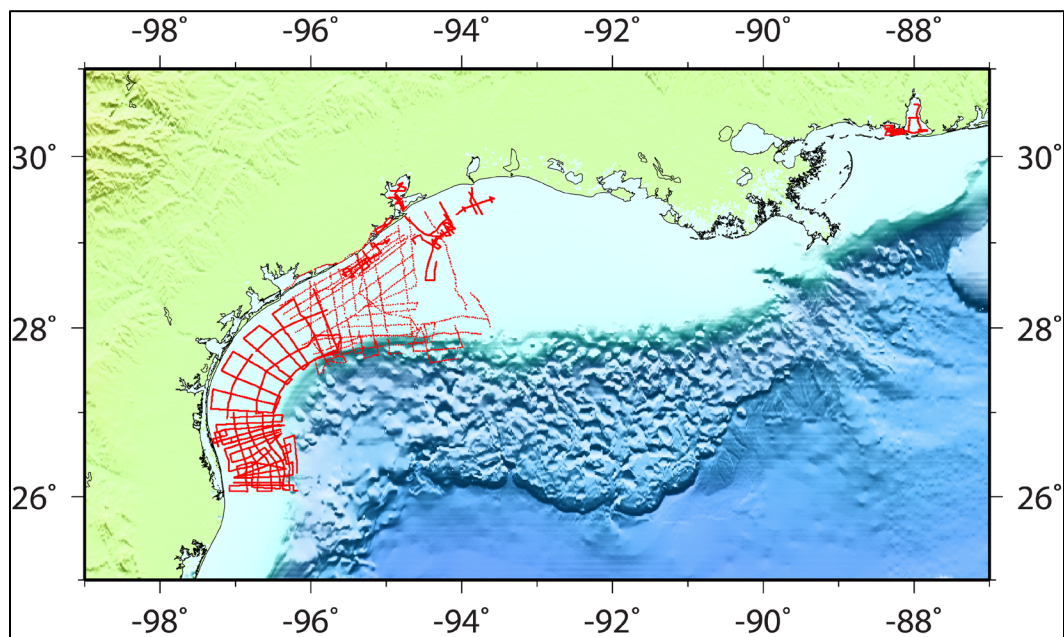


**Figure 3.1. Track lines for data archived to the Academic Seismic Portal**

### 3.2 Core Data

The Texas continental shelf within the study area has been the focus of numerous academic, government, and industrial studies for myriad purposes. As a result, hundreds of sediment samples, cores, platform borings, and other types of geologic data have been collected and published in the form of academic papers, technical reports, and online databases. In tandem with our data recovery efforts focused on digitizing geophysical data collected by Rice University, we successfully digitized, georeferenced, and archived numerous core and platform boring descriptions located in Rice University holdings. Combined with the literature review and geotechnical reports, these have allowed for the creation of a geological database that contains 642 cores and platform borings, 489 of which have associated pdf files containing the original core descriptions and other information. These samples span the western and central Gulf of Mexico (**Figure 3.2**) and represent a significant advancement over currently available sample databases in both the breadth and types of data now available for analysis and integration with ongoing studies.

The geological database was formatted according to the provided BOEM spatial data template, and all ArcGIS™ files and corresponding core pdf images are contained within a single geodatabase. The database can be queried by year of acquisition, depth of penetration, author, data type, and numerous other categories and the original scanned core descriptions brought up within ArcGIS on the fly (**Figure 3.3**). This database will provide crucial geologic ground truth to our ongoing geophysical interpretations of the Trinity incised valley system and surrounding continental shelf.

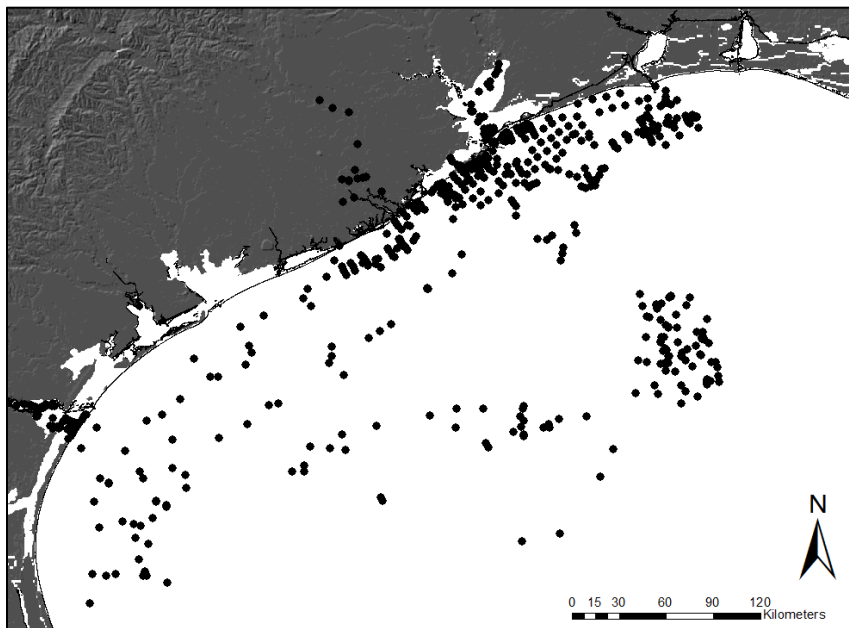


**Figure 3.2. Map of the core geodatabase**

Image displays all archived cores and platform borings across the western and central Gulf of Mexico.

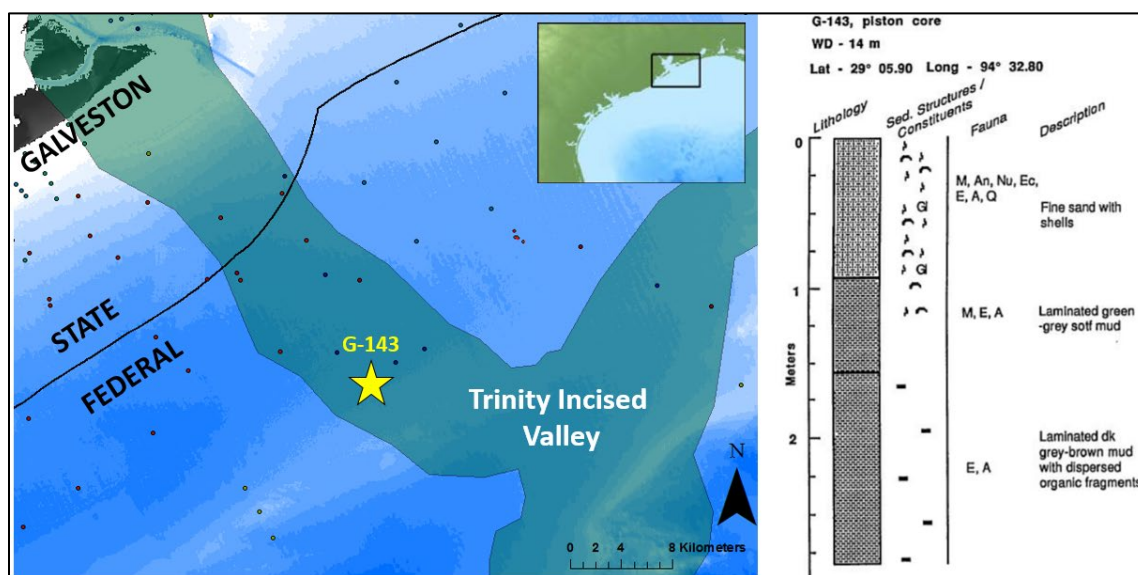


**Figure 3.3. Example of digitized core description in the geodatabase**

Core G-143, digitized from a Rice University PhD dissertation, samples the upper valley fill of the Trinity Incised Valley.

### 3.3 Literature Synthesis

The literature database for the TRiPP project is organized into five main categories that relate to the cooperative agreement: 1) Regional Texas sedimentology and stratigraphy, 2) Incised valley and paleo-channel system examples from global passive margins, 3) Controls on fluvial stratigraphic creation and preservation, 4) Transgressive/modern coastal system evolution and 5) Technical reports. This database is continually added to as new papers are published or older relevant works discovered, but it is substantially complete at this stage. Regional papers from the Texas shelf that included geologic data were digitized and incorporated into the TRiPP ArcGIS database. **Table 3.3** summarizes the literature synthesis holding to date.

**Table 3.3. Number of manuscripts added to the TRiPP literature database**

	Regional Stratigraphy	Incised Valley Systems	Fluvial Morphodynamics and Stratigraphy	Coastal System Evolution	Technical Reports, Theses, Grey Literature
Count	33	58	40	22	15

## 4 New Data Collection for TRiPP

New data were collected during four separate field campaigns in support of the TRiPP project: (1) the 2017 University of Texas' Marine Geology and Geophysics (MGG) field course, (2) the 2018 MGG field course, (3) a dedicated chirp survey aboard the R/V *Trident* in 2018, and (4) a coring effort aboard the R/V *Manta* in 2019.

### 4.1 2017 MGG Field Course

The MGG field course was held May 17–June 5, 2017, with field work conducted May 22–26. For offshore chirp data collection, we used the R/V *Manta* out of Galveston, Texas. We planned to collect chirp data May 22–25, and attempt piston coring on the 26th. Work on May 22nd was curtailed due to severe thunderstorms (including a tornado warning), and operations were limited to inshore. Data were collected May 23–25, although operations were again cut short on the 25th due both to worsening weather and equipment issues. Weather was again inclement on the 26th, preventing offshore operations for piston coring. Despite weather setbacks, we ultimately collected ~150 line-km of chirp data (**Figure 4.1**), including three complete strike (along-shore) crossings of the paleovalley at a range of depths, and one long dip (across-shore) line down-axis of the paleovalley.

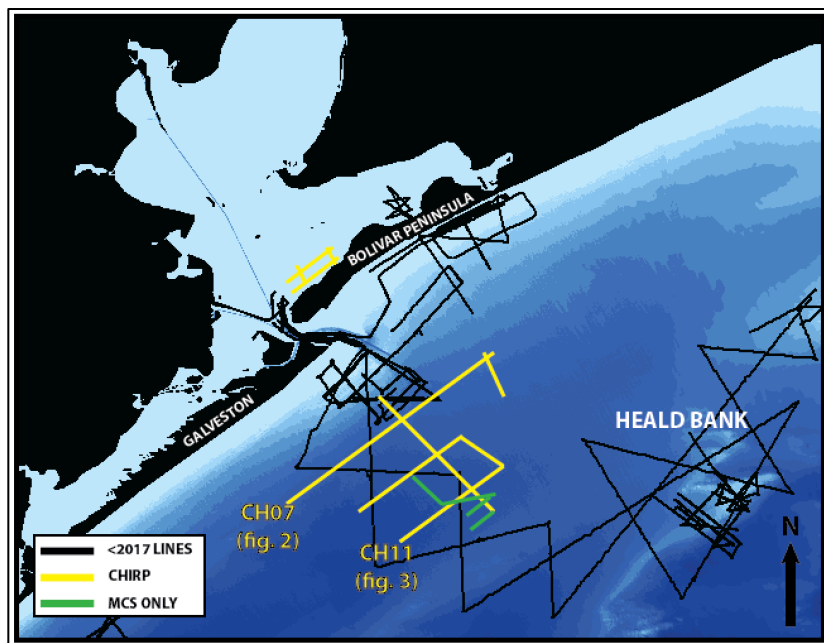


**Figure 4.1. 2017 Field course track lines**

Geophysical tracklines are shown, with yellow and green highlighting the new datasets collected as part of the 2017 UTIG Field Course. Background image show bathymetry of the East Texas inner shelf.

These data vastly improved our constraints of the bounds and pathway of the paleovalley and provided very high-quality images of the complex stratigraphy of the channel fill sediments. These were the primary goals of this reconnaissance and provided a strong basis for planning more detailed survey work during our follow-up cruise (May and August 2018) to the same area. We infer and/or hypothesize that the paleovalley is floored by abundant fluvial sands, primarily point-bar deposits associated with

extensive river channel meander and migration; the top of this unit is well imaged in the data, although the bottom is not due to loss of acoustic energy.

## 4.2 2018 MGG Field Course

The May 2018 field course (see below) was successfully and safely accomplished using the R/V *Scott Petty* for inshore work (bathymetry, sidescan and grab sampling), and the R/V *Brooks McCall* for offshore work (chirp, airgun/streamer seismic data, and piston coring). Over 275 km of chirp and 191 km of seismic lines were collected across key regions of the Trinity incised valley, expanding on the data acquired in the 2017 field course (**Figure 4.2**). These new lines allow for better delineation of the incised valley geometry of the TRiPP field area and have been instrumental in observing the significant stratigraphic heterogeneities within the valley. Five cores were successfully collected, ranging in length from 6–10 m. The coring capabilities of the R/V *Brooks McCall* represent a significant improvement over previous platforms used, and the 10 m piston core penetrated through the upper valley stratigraphy to sample fluvial sands present in the lower valley fill. These cores are the first successful ground-truthing of an interval previously interpreted on the chirp geophysics as a likely sand-rich body and confirms our hypothesis of significant fluvial sands located at the valley base. This year also marked the involvement of a biostratigrapher colleague at UTIG who recruited an undergraduate student to perform a detailed paleo-environmental analysis of the collected cores. This provided a new dimension to our understanding of the depositional environments of the entire Trinity incised valley fill succession and allowed for increased confidence in tying of identified seismic facies to distinct sedimentary systems, lithologies, and environments.

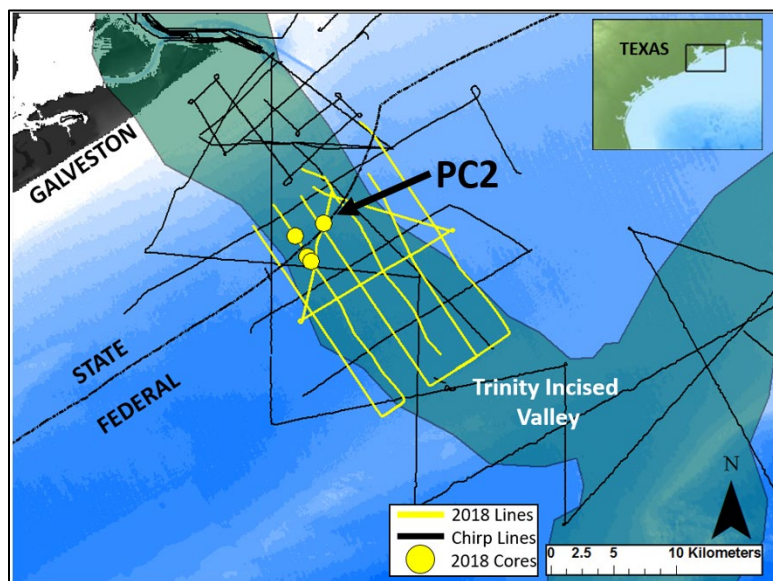


**Figure 4.2. 2018 Field course track lines and core locations**

Yellow lines are the 2018 field course data, while yellow circles are the field course cores. These data bracket the valley and provide greatly increased imaging of incised valley structures and stratigraphy. PC = piston core.

## 4.3 2018 R/V *Trident* Survey

During August 3 through 8, 2018, the Texas Coop team from UTIG chartered the R/V *Trident* operated by Texas A&M Galveston. The goal of this short cruise was to collect a grid of chirp lines over the TRiPP

study area to fill in between the more regional lines collected in the 2017 and 2018 UT Marine Geology and Geophysics Field Camps (**Figure 4.1**). The cruise participants were Sean Gulick (chief scientist), Steffen Saustrup (marine technician), Patricia Standing (undergraduate student) and Eric Hiatt (undergraduate student). August 3 was a mobilization day to install the UTIG Edgetech 512i chirp, topside, and computing lab onto the R/V *Trident*. We sailed early on August 4 and acquired 8 chirp lines during worsening weather. When the seas reached beyond the operational limits of the vessel, we set into port and spent the night waiting on weather. Before first light, we returned to the study area and from August 5 through midday on August 8 were able to do 24 operations acquiring chirp data. In total, we acquired 44 chirp lines totaling over 700 km of data. The R/V *Trident* proved to have an operational limit of ~0.9 m when surveying at 4.5 knots with seas to the beam. However, a near complete imaging at 250 m line spacing was accomplished despite this challenge. For the survey, the chirp towfish was kept at 5 m depth to minimize the noise during acquisition. Final lines acquired are shown in **Figure 4.3** and the cruise proved to be an excellent educational opportunity for students and military veterans Standing and Hiatt, who ensured that quality data was acquired even under challenging sea states. Both these students subsequently signed on to continue working with the UTIG team at the Texas Coop into the Fall and Spring semesters, 2018–2019, and went on to pursue their PhDs at UT Austin.

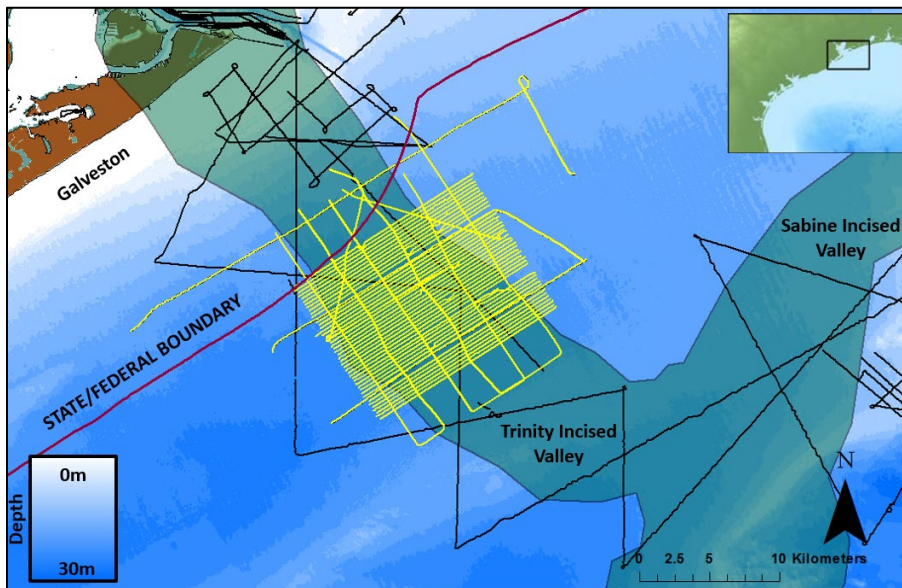


**Figure 4.3. 2018 R/V *Trident* track lines**

Black lines are older chirp datasets, while yellow lines are data collected during the *Trident* cruise and the 2017 and 2018 field courses.

#### 4.4 2019 R/V *Manta* Coring Cruise

A two-day cruise aboard the R/V *Manta* was planned for June 30–July 1, 2019, for the purpose of collecting additional piston cores, and to test a mid-frequency sparker system with a colleague at Texas A&M. We successfully collected six cores on the first day, but the remainder of the cruise was cut short by an engine fire that forced us to return to port. The cores we were able to collect sampled outer- to middle-bay estuarine muds, sandy overwash deposits, and sandy ebb tide delta deposits.

## 5 Core Analysis

This chapter is excerpted from Standing et al. (2021).

### 5.1 Introduction

As global sea levels continue to rise, constraining how coastlines respond is increasingly important for coastal planning. High estimates of sea-level rise exceed 2 m above current mean levels by 2100 for +5°C of warming, in which CO<sub>2</sub> emissions are not curbed; lower estimates for +2°C of warming, which falls in line with plans that cut CO<sub>2</sub> emissions globally, put sea-level rise at 0.26–0.81 m by 2100 (Bamber et al., 2019). Although the most recent Intergovernmental Panel on Climate Change Assessment Report indicates low confidence for higher end estimates of sea-level rise by 2100, these estimates “cannot be ruled out due to the deep uncertainty in ice processes” (IPCC, 2021). Even this lower range of sea-level rise presents a significant threat to coastal communities (Bamber et al., 2019; Bernstein et al., 2019) which represent ~10% of the world’s population (FitzGerald et al., 2008). A 1.8 m rise in sea level would inundate six million coastal homes in the US and risk one trillion dollars in damage to coastal residential real estate (Bernstein et al., 2019). Global mean sea-level rise does not impact areas equally and some areas will experience significantly higher flooding rates over the next century (Vitousek et al., 2017); thus, it is important to understand regional and local coastal response to rising seas.

Low-gradient, low-elevation coastlines around the Gulf of Mexico are especially vulnerable to the destruction caused by large storms and hurricanes, requiring significant periods of time for barrier island systems to adjust and recover (Bernstein et al., 2019; FitzGerald et al., 2008; Goff et al., 2010; Palermo et al., 2021; Shawler et al., 2021). Industrial development, dredging for navigation purposes in the back-barrier, reduction of natural wetlands, and increased subsidence due to onshore extraction of hydrocarbons and groundwater contribute to the Gulf Coast’s vulnerability to sea-level rise and coastal inundation, particularly in areas like Galveston Bay (Anderson et al., 2008; Kirwan and Megonigal, 2013; Paine, 1993; Shawler et al., 2021; White et al., 2002). Despite recent local regulations concerning groundwater extractions, compaction and subsidence from twentieth-century pumping is estimated to continue over several hundred years (Miller and Shirzaei, 2021). As the busiest shipping center in the US (Port of Houston, 2021), Galveston Bay represents a particular vulnerability of US supply chains and infrastructure due to sea level inundation. As a result of heavy development, the western boundary of Galveston Bay no longer consists of protective wetlands (Anderson et al., 2008) and overall wetland loss in the Trinity River delta area exists due to subsidence and relative sea-level rise (White et al., 2002). Barrier islands, like those that enclose Galveston Bay, evolve due to sea-level rise on centennial to millennial timescales, and sediment transport along the shoreline, with local-scale conditions altering the timing of barrier erosion and progradation processes (Fruergaard et al., 2015; Lentz et al., 2013; Raff et al., 2018; Shawler et al., 2021). These processes are also highly influenced by antecedent topography and slope, and sediment supply within the substrate, where muddier substrates result in barriers that are prone to collapse and drowning, and shallower slopes will experience more rapid drowning and disintegration of barrier systems than steeper slopes under the same rate of sea-level rise (Brenner et al., 2015; Lorenzo-Trueba and Ashton, 2014; Moore et al., 2010; Raff et al., 2018; Shawler et al., 2021). In general, shallower back-barrier environments experience more rapid landward migration of barrier islands (Lorenzo-Trueba and Ashton, 2014; Moore et al., 2010; Shawler et al., 2021). As back-barrier marshes and coastal wetlands are inundated and converted to intertidal and subtidal environments, the tidal prism of the bay is enlarged, which increases the volume of sand contributed to ebb- and flood-tidal deltas (Al Mukaimi et al., 2018; FitzGerald et al., 2008). This process leads to the denudation of barrier systems, furthering the erosion of coastal environments (FitzGerald et al., 2008).

Understanding how specific areas of the Gulf Coast have responded to relative sea-level rise in the past provides predictions for future coastal vulnerabilities, especially in populated areas that are undergoing rapid coastal land loss, like Galveston Bay, Texas (Anderson et al., 2016, 2008; Phillips et al., 2004; White et al., 2002). Flood hazard assessments predict over 76 km<sup>2</sup> along the Texas coast will subside below sea level by 2100, which alone increases the area of inundation due to sea-level rise by 39% (Miller and Shirzaei, 2021). Subsidence within Galveston Bay is lowest near the mouth of the San Jacinto River and the Houston Ship Channel, and although sedimentation rates are higher in this area than the rest of Galveston Bay, they are almost 50% lower than rates of sea-level rise generating an accretionary deficit (Al Mukaimi et al., 2018).

Instrumental records help identify trends in sea level changes along the coasts, while highlighting specific coastal regions at increased risk of land loss. Monthly mean sea level measurements at Galveston Bay Pier 21 establish relative sea-level rise trends with a 95% confidence level of  $+6.59 \pm 0.22$  mm/yr over the time period from 1904 to 2020, and at  $+6.62 \pm 0.69$  mm/yr from 1957 to 2011 for Galveston Pleasure Pier (NOAA, 2021). This rate is significantly higher than all other stations along the Texas Coast, and even double in some cases. For example, Padre Island data show a sea-level rising trend of  $+3.48 \pm 0.75$  mm/yr from 1958 to 2006, and  $+3.54 \pm 0.70$  mm/yr at Port Mansfield, Texas, from 1963 to 2020 (NOAA, 2021). Nearby Sabine Pass, Texas, shows a similar, but lower, trend of  $+6.16 \pm 0.74$  mm/yr from 1958–2020 (NOAA, 2021). Observations of coastal erosion by the Texas Bureau of Economic Geology show a net retreat of 1.24 m/yr for the entire Texas coast, and a rate of 0.4 m/yr for Galveston County on the western side of Galveston Bay, and 1.63 m/yr for Chambers County on the eastern side of Galveston Bay (Paine et al., 2011). The report specifically highlighted the area of sandy beach west of the seawall on Galveston Island as undergoing significant shoreline retreat, whereas longshore current causes net shoreline advance on Bolivar Peninsula east of the Bolivar Roads tidal inlet, which is likely due to the construction of jetties on either side of the inlet (Paine et al., 2011).

Unfortunately, instrumental data are limited by the short timescales they cover, on the Gulf Coast only going as far back as the early 1900s (and more commonly several decades later). These instrument records often start after accelerated sea-level rise has been initiated, introducing a potential bias in future rising sea level predictions and modeling (Horton et al., 2019). Therefore, it is necessary to use the geologic record to augment the instrumental data and determine how past coastal changes have been influenced by accelerated sea-level rise (Horton et al., 2019).

Looking further back in time provides insight into the impact of rapid sea-level rise on coastlines (Dutton et al., 2015; Horton et al., 2019). As part of a BOEM-funded effort to identify subsurface sand resources along the Gulf shelf for coastal resilience and nourishment projects, the Trinity River Incised Paleo-Valley Project has conducted multiple seismic surveys and sediment coring to map the Trinity River-incised valley offshore modern Galveston Bay and chart its transformation from a Pleistocene fluvial to Holocene estuarine to modern open marine environment. Here, we use high-resolution seismic data in combination with micropaleontological analysis, sedimentology, carbon dating, and age modeling from sediment cores to develop a comprehensive history of Holocene paleoenvironmental and coastal change in the Trinity paleo-valley over the last 10 thousand years (kyr), during which time sea-level rise slowed from 5 mm/yr to 3 mm/yr (Milliken et al., 2008). We identify periods of estuary stability through barrier island development and subsequent shoreline retreat.

## 5.2 Region Setting and/or Background

Modern Galveston Bay is located on the northeast Texas coast in the Gulf of Mexico and consists of multiple bays that comprise the Estuary Complex (**Figure 5.1**). The microtidal, wave-dominated regime in the Gulf of Mexico allows for long, narrow, relatively straight barrier island system protecting the estuary, consisting of Bolivar Peninsula on the eastern side of the bay and Galveston Island on the western side (Anderson et al., 2016, 2014; Davis and Hayes, 1984; FitzGerald et al., 2008; Rodriguez et al., 2004). The shape of Galveston Bay developed when existing fluvial topography was inundated as the bay mouth was restricted to a tidal inlet ~2.5 ka (Anderson et al., 2016, 2008; Rodriguez et al., 2004). Construction of jetties has restricted sediment flow through Bolivar Roads, the primary inlet into the estuary (Anderson et al., 2008; Siringan and Anderson, 1993).

John Anderson and his research group at Rice University established a firm foundation of research on modern Galveston Bay and its transformation throughout the Holocene (Anderson et al., 2016, 2014, 2008; Milliken et al., 2008; Rodriguez et al., 2005, 2004; Simms et al., 2007; Siringan and Anderson, 1993). During Marine Isotope Stages (MIS) 5–3, the region experienced episodic sea-level fall, which led to the creation of Trinity and San Jacinto incised river valley (**Figures 5.2, 5.3**) (Anderson et al., 2016, 2014; Swartz et al., 2022; Chapter 6). Stepped downcutting resulted in terraced morphology (Anderson et al., 2016, 2008; Rodriguez et al., 2005). The upper, wider portions of the incised valley are not visible in the sediment record because they have been removed by shoreface erosion to the transgressive ravinement during Holocene sea-level rise, identified at -8 to -10 m depth along the Texas coast as the onlapping of marine muds onto a “decapitated shoreface” (Anderson et al., 2016; Rodriguez et al., 2004).

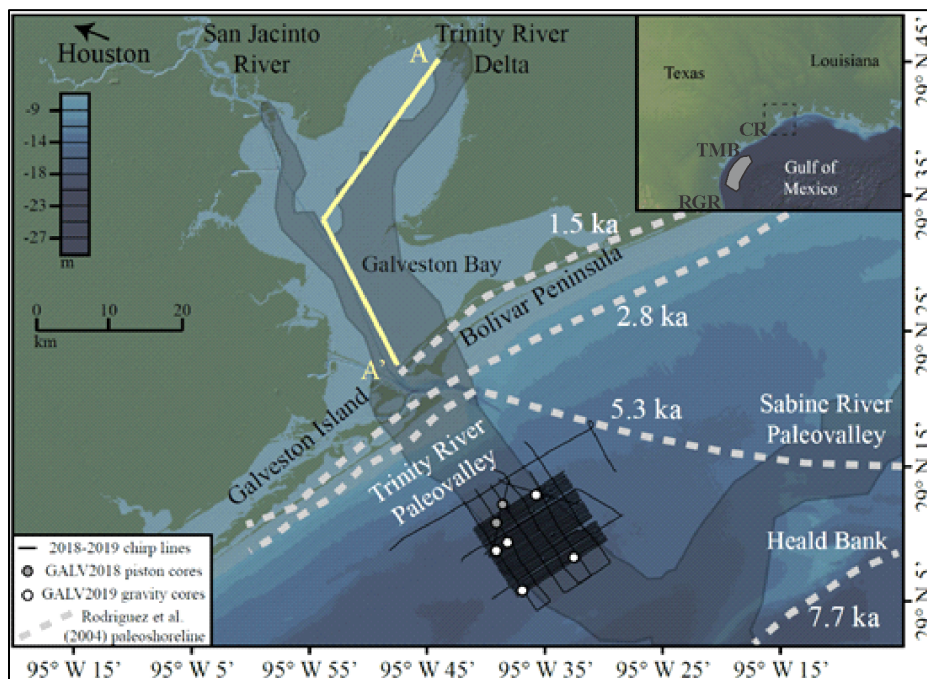


**Figure 5.1. Study area offshore Galveston Bay, Texas**

Map shows Trinity River incised valley (gray outline), A-A' profile of cross-section shown in **Figure 5.4** from Anderson et al. (2008), high-resolution seismic lines (black lines), 2018 piston cores (gray circles), 2019 gravity cores (white circles), and paleoshorelines (grey dashed) based on interpretation from Rodriguez et al. (2004). Figure made with GeoMapApp ([www.geomapapp.org](http://www.geomapapp.org)) and Global Multi-Resolution Topography Data Synthesis (Ryan et al., 2009). TMB and grey polygon: Texas Mud Blanket. RGR: outlet of Rio Grande River. CR: outlet of Colorado River. Topographic data from Global Multi-Resolution Topography Data Synthesis (Ryan et al., 2009).

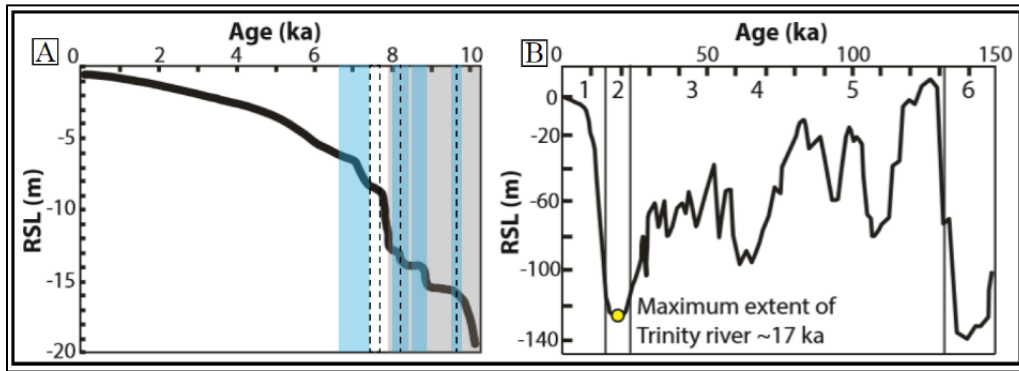


**Figure 5.2. Holocene sea level curve**

A) Sea-level rise over the last 10 kyr with periods of rapid sea-level rise identified by Milliken et al. (2008) (boxed in blue) and rapid sea-level rise in Galveston Bay, Texas, identified by Anderson et al. (2008) (dashed lines). B) Holocene sea level curve over last 150 kyr showing Marine Isotope Stages 1–6 and maximum lowstand for the Trinity River occurring approximately 17 ka (modified from Swartz et al., 2022).

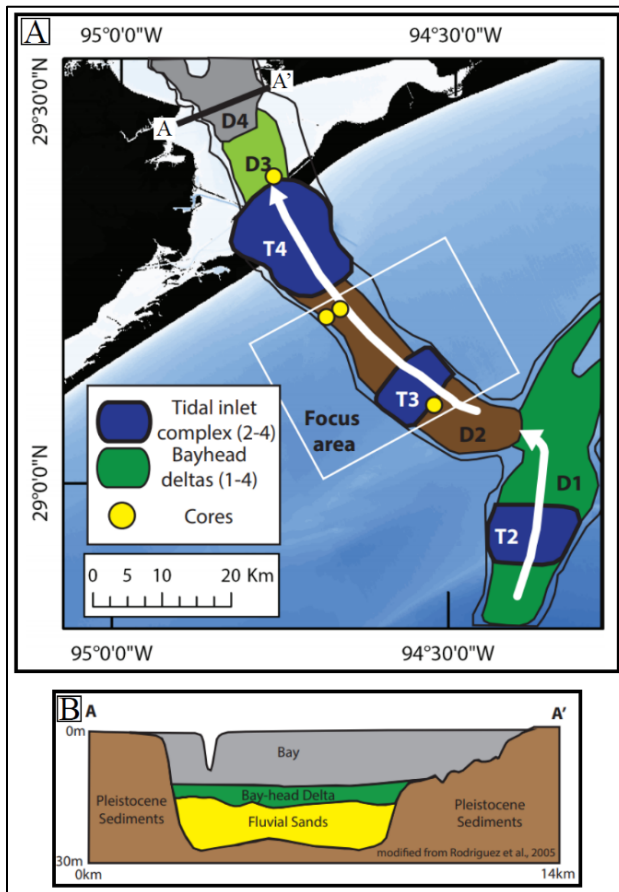


**Figure 5.3. Trinity River transgressive systems tract**

A) Landward changes of depositional facies due to Holocene sea-level rise and study area offshore Galveston Bay, Texas. B) Cross-section of Trinity River Paleovalley within modern Galveston Bay, with generalized valley fill transitioning from fluvial sands to bay-head delta and bay fill deposits (modified from Swartz et al., 2022).

Global sea-level rise between ~11.4 and 8.2 ka is estimated at ~15 m/kyr followed by a reduced rate of sea-level rise 8.2–6.7 ka, coinciding with the final deglaciation of North America (Lambeck et al., 2014). Along the Gulf Coast, sea level began to rise episodically between ~10 and 7 ka, after which it slowed to steady present day levels (**Figure 5.2**) (Anderson et al., 2016, 2014; Milliken et al., 2008; Swartz et al., 2022). The Anderson group identified multiple flooding surfaces within the Trinity incised valley that occur either contemporaneously with other areas along the Gulf coast and are attributed to rapid sea-level rise, or exist locally, suggesting forcing mechanisms such as changing sediment supply and/or antecedent topography (Anderson et al., 2016; Rodriguez et al., 2005). Radiocarbon dating in sediment cores from modern Galveston Bay constrain rapid sea-level rise events to 9.6 ka, 8.2 ka, and between 7.7 and 7.4 ka, in which each inundation was complete after only a few centuries (**Figure 5.4**) (Anderson et al., 2008). Milliken et al., (2008) identified flooding events consistent with radiocarbon dates and relative sea level changes within the Gulf of Mexico at 9.5–9.8 ka, 8.5–8.9 ka, 8.0–8.4 ka, and 6.8–7.4 ka (**Figure 5.2**).

Estimates of Antarctic ice-sheet fluctuations since the Last Glacial Maximum vary widely, so most Holocene sea-level rise is attributed to the better constrained demise of the Laurentide Ice Sheet (LIS), with some evidence for Antarctic melting after ~6 ka (Lambeck et al., 2014). Higher resolution analysis of LIS deglaciation reveals multiple meltwater pulses at 9.1 ka, 8.7 ka, 8.6 ka, and 8.2 ka, and 7.4 ka (Jennings et al., 2015). After 8.15 ka, Laurentide Ice Sheet (LIS) retreat accelerated with remnant ice domes melting by ~6.7 ka (Lambeck et al., 2014; Ullman et al., 2016). Remaining global sea-level rise is attributed to the loss of ice volume from the West Antarctic ice-sheet during the late Holocene (Ullman et al., 2016).

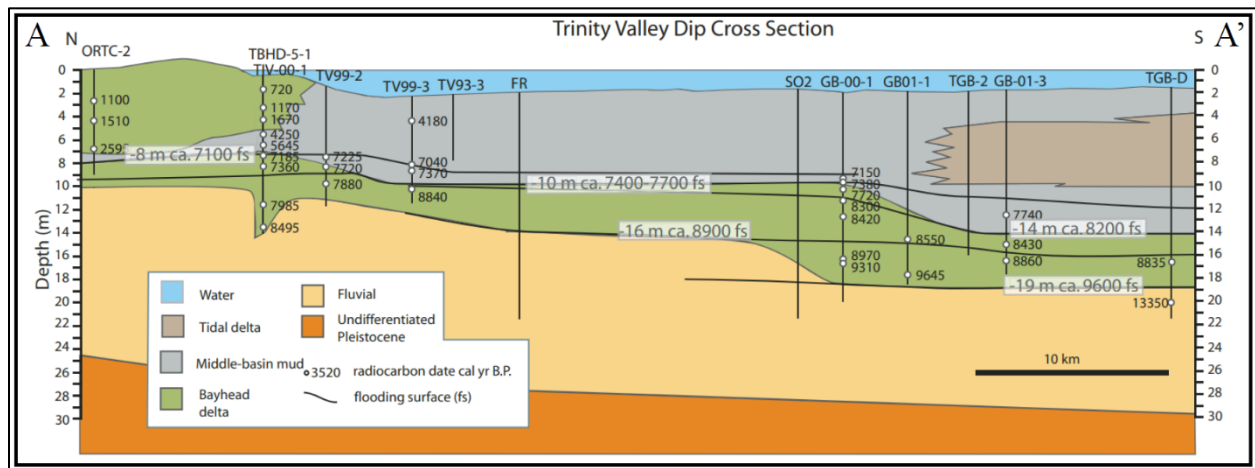


**Figure 5.4. Cross section of the Trinity River Paleovalley in modern Galveston Bay, Texas**  
Image compiled from seismic and core data analyzed by Anderson group displaying prominent sedimentary facies and flooding surfaces with radiocarbon ages (modified from Anderson et al., 2008). Location in **Figure 5.1**.

Approximately 9.6 ka, the initial inundation of modern Galveston Bay shifted the upper bay ~30 km up the incised valley, coincident with LIS retreat and Hudson Strait freshwater drainage (Anderson et al., 2008; Jennings et al., 2015; Lambeck et al., 2014; Thomas and Anderson, 1994). The early opening of the Tyrell Sea ~8.6 ka and the catastrophic release of freshwater from North American glacial lakes occurred at 8.15 ka (Jennings et al., 2015). At the same time the bayhead delta shifted ~10 km up the valley, partially attributed to a “dramatic decrease in sedimentation rates” from 4.6 mm/yr to 1.3 mm/yr and the coincident elevation of a Pleistocene-age terrace (**Figure 5.4**) (Anderson et al., 2008). Higher temperatures in the Atlantic Meridional Overturning Circulation, likely due to Antarctic ice sheet loss, and strengthening of the North Atlantic Deep Water led to a warming period 7.9 ka (Cronin et al., 2007)

in which remnant ice domes of the LIS were significantly melted (Ullman et al., 2016). Between 7.7 and 7.4 ka the upper bay shifted a further ~25 km up the valley at a rate of 8 km century<sup>-1</sup> but maintained its existing shoreline ~50 km seaward of the modern coastline, which produced a ~100-km-long paleoestuary (Anderson et al., 2008; Rodriguez et al., 2005). This flooding event occurred despite the decreasing rate of sea-level rise between 7.5 and 7.0 ka, with coincident events in Matagorda Bay and Sabine Lake, and is attributed to a Gulf Coast climate transition from cool and moist to warm and dry, reducing sediment supply (Anderson et al., 2008).

Radiocarbon dating of sandy sediments from Heald Bank suggest that the paleoshoreline was in that location by as late as 7.7 ka, while ages obtained from the oldest beach ridges on Galveston Island constrain its development to 5.5 ka (**Figure 5.1**) (Anderson et al., 2014, 2008; Rodriguez et al., 2005, 2004). Conflicting interpretations of Heald Bank sands call into question the 7.7-ka-shoreline, and suggest the bank may be marine in origin, like Thomas and Shepard Banks, and developed after the shoreline had already shifted up-valley (Thomas and Anderson, 1994). Bolivar Peninsula began to develop as a spit ~2.5 ka and as it prograded westward, the tidal inlet narrowed to a fraction of its original size to form Bolivar Roads tidal inlet allowing flooding along the bay boundaries, establishing the modern shape of Galveston Bay (Anderson et al., 2016, 2014, 2008; Rodriguez et al., 2005, 2004).

Although previous sedimentological and seismic research conducted by the Anderson group is thorough, it has thus far lacked sufficient paleoenvironmental evidence and the spatial coverage necessary to establish the evolution of the paleo-estuary (Anderson et al., 2008; Rodriguez et al., 2004). Additional higher resolution seismic data combined with radiocarbon dating of sediment cores and micropaleontological interpretations of facies changes will characterize coastal change by temporally and spatially constraining a large and long-term stable estuarine environment and the transformation of the coastline throughout the Holocene. Foraminifera are powerful proxies for paleoenvironmental and relative sea level change because of their sensitivity to temperature, salinity, and nutrient availability (Culver, 1988; Gehrels, 2013; Olson and Leckie, 2003; Phleger, 1951; Poag, 1981). Modern assemblages represent a specific “physicochemical environment” within ecological niches or biozones that can be translated to fossil assemblages in sediment cores to identify paleoenvironmental changes as a result of relative sea level fluctuations forming a link between instrumental and fossil records (Culver, 1988; Phleger, 1960; Gehrels, 2013; Olson and Leckie, 2003; Phleger, 1965; Poag, 1981). This link allows us to differentiate upper, middle, and outer bay environments within otherwise unremarkable successions of estuarine mud and separate sandy ebb- and flood-tidal delta deposits from back-barrier washover fans. Benthic foraminiferal assemblages provide paleoenvironmental context to seismic data and allow for the clarification of the timing of the inundation of the Trinity River Paleovalley and the interpretation of barrier island stability and rollover rate amid rising sea levels at a higher resolution than has previously been possible.

## 5.3 Methods

### 5.3.1 Seismic Data

Approximately 1,000 km of high-resolution seismic data were obtained during two field courses and two cruises funded by BOEM for the purpose of researching sand deposits. These surveys were conducted with an EdgeTech 512i sub-bottom profiler with 0.7 to 12 kHz frequency sweep, 20 ms pulses by the University of Texas Institute for Geophysics (UTIG) (**Figure 5.1**). These data were incorporated with 690 line-km of high-resolution chirp seismic surveys conducted by Texas A&M Galveston and USGS in 2009 using EdgeTech Geo-Star FSSB system and SB-0512i towfish with 20 ms pulse length and 0.7–12 kHz sweep frequency aboard the R/V *Manta* (Dellapenna et al., 2009). Processing of UTIG chirp data and

interpretation of seismic horizons were conducted by Swartz et al. (2022) and Burstein et al. (2021). UTIG data include full-waveform processing providing a higher resolution of the subsurface stratigraphy (Goff et al., 2015). Seismic lines corresponding to sediment cores were converted from two-way travel time in milliseconds to meters with an approximate seismic wave velocity of  $1525 \text{ m s}^{-1}$  (Abdulah et al., 2004).

### 5.3.2 Piston and gravity coring

Piston core (PC) sites (**Figure 5.1; Table 5.1**) were chosen based on sedimentary structures observed in seismic data to pinpoint key transitions in the sedimentary record and evaluate paleoenvironmental evolution from fluvial to estuarine to modern-day marine. Piston cores were collected during a cruise of the R/V *Brooks McCall* as part of UTIG's 2018 Marine Geology and Geophysics (MGG) Field Course. Gravity core (GC) locations (**Figure 5.1; Table 5.1**) were selected during processing to clarify additional points of interest, particularly along the valley edges, and were collected during a BOEM-UTIG cruise of the R/V *Manta* in 2019.

Piston and gravity cores were split onshore after both cruises were completed. The archive halves were stored at UTIG's refrigerated core storage facility, and the working halves were described for appearance, visual grain size, bioturbation, and presence of marine fauna (e.g., shell fragments and shell hash), and terrestrial organic material (e.g., plant debris). Sediment samples for microfossil analysis were selected at regular intervals from piston and gravity cores, and at specific points where a paleoenvironmental transition may have occurred based on changes observed in the core, avoiding sandier sediments. Piston core 2 (PC-2) was the longest core collected and was sampled at 10-cm intervals to serve as a reference section. Subsequent sampling in piston core 4 (PC-4) and all gravity cores (GC-1 thru GC-6) was done at 50-cm intervals with additional samples selected to more precisely identify paleoenvironmental transitions. Samples were soaked for at least 24 hours in a mixture of borax and hydrogen peroxide to break down clay floccules, washed over a 63- $\mu\text{m}$  sieve, and dried in an oven.

### 5.3.3 Foraminiferal analysis

Core samples were split to provide a reasonable amount of material and foraminifera were picked using a binocular microscope and placed on a slide. Population sizes of at least 100 foraminifera tests were picked where possible (some samples were barren or did not yield 100 individuals) and identified at the genus level. Foraminifera that were not identifiable at the genus level were classified as "benthic spp." Confidence interval calculations show that these population sizes are sufficient to track changes in predominance facies (i.e., *Ammonia* compared to *Elphidium*) within the estuary. Confidence intervals were based on the binomial method provided in Buzas (1990). Modern grab samples from Bolivar Roads tidal inlet obtained during the MGG 2018 Field Course were analyzed and used as a comparison for flood- and ebb-tidal delta sediments in the cores. Samples were soaked overnight in a 1% solution of Rose Bengal and water immediately after collection to stain specimens that were living or recently living. Samples were then sieved and dried in an oven. Populations of at least 300 individuals were picked and identified at the genus level; the larger numbers help ensure robust statistical determinations given the higher species diversity in these samples (Buzas, 1990).

Predominance facies are defined by genus of foraminifera (Culver, 1988; Poag, 1981). Poag (1981) synthesized analysis of modern benthic foraminiferal assemblages in the Gulf of Mexico (**Figure 5.5**) and outlined predominance facies for Galveston Estuary Complex based on the previous work conducted by Wantland (1969) within the Trinity Bay and written communication from W.V. Sliter of the USGS. Wantland (1969) collected 87 samples from stations within the subaerial Trinity River delta and Trinity Bay and used Rose Bengal solution to determine live taxa at time of collection. Live samples were picked

from 62- $\mu\text{m}$  sieved wet sediments and populations were based on at least 300 individual tests where possible (Wantland, 1969). Poag (1981) identified the following modern predominance facies for Galveston Bay: dominance of *Ammotium* represented upper bay or river delta facies, dominance of *Ammonia* indicated central bay facies, and dominance of *Elphidium* was determined to be outer bay facies (Figure 5.5). Culver (1988) also outlined a priori groups of prominent foraminifera genera by depth and environmental preference, which match well with Poag's predominance facies. Culver (1988) specified genera of foraminifera that can be considered diagnostic of certain environments: *Ammotium* for marshes, *Ammobaculites* and *Elphidium* for bays/estuaries, and *Bolivina* spp., *Bulimina* spp., and *Elphidium* spp. for inner shelf environments (Figure 5.5).

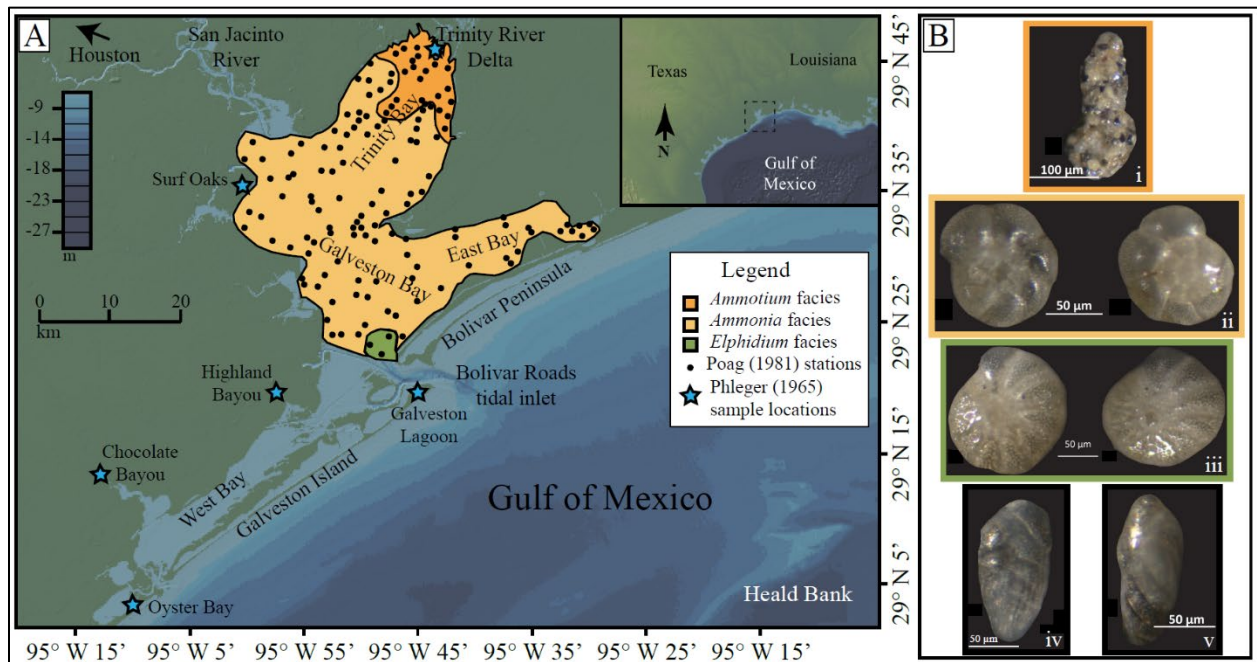


**Figure 5.5. Foraminiferal predominance facies of Galveston Bay, Texas**

Data are based on Poag (1981). A) Map of Galveston Bay, Texas, showing areas within the modern estuary that are dominated by specific genera of foraminifera, and locations of marshes (blue stars) studied by Phleger (1965). B) Images of dominant genera of foraminifera: i) *Ammotium salsum* (orange; upper bay facies), ii) *Ammonia* spp. (yellow-orange; central bay facies), iii) *Elphidium* spp. (green; outer bay facies), iv and v) *Bolivina* spp. and *Bulimina* spp., respectively, which are diagnostic genera for inner shelf facies (Culver, 1988) (modified from Poag, 1981, and Phleger, 1965).

Paleoenvironmental interpretations of the Holocene estuary system are based on assemblage percentages of three primary genera outlined by Poag (1981). Samples with  $>50\%$  *Ammonia* are interpreted as central bay facies, samples with  $\sim 50\%$  *Ammonia/Elphidium* are transitional to outer bay, and samples with  $>50\%$  *Elphidium* are outer bay facies. *Ammotium*, indicative of Poag's bayhead delta facies, was typically not identifiable at the genus or species level due to test fragmentation. Agglutinated taxa are generally uncommon and are poorly preserved in our cores, so they were categorized as agglutinated spp. We interpret increases in the presence of agglutinated spp. to indicate proximity to bay margin environments that are more likely to be dominated by agglutinated taxa. An overall increase in diversity including common inner shelf taxa (e.g., *Bulimina*, *Bolivina*, miliolids, etc.) coupled with a resurgence of *Ammonia* spp. likely indicates a transition to modern marine or open shelf facies (Culver, 1988; Olson and Leckie, 2003; Poag, 1981). Facies lacking in foraminifera were deemed barren and, given their stratigraphic position, interpreted to reflect the transition to terrestrial (e.g., fluvial) environments.

Estuaries are dynamic environments and reworking of material is likely common. To identify areas of potential reworking, foraminiferal test fragments (interpreted to be broken during redeposition) within each sample were counted in addition to individual identifiable tests for population totals. Total fragments were normalized to total foraminifera to provide a percent fragmentation for each sample. Peaks in fragmentation are interpreted as potential periods of increased energy or sediment reworking, and in some cases coincided with decreased foram populations.

#### 5.3.4 Radiocarbon dating

Sediment cores were sampled for radiocarbon dating to provide age constraints on paleoenvironmental transitions and develop age models for each core. A total of 28 samples were sent to the National Ocean Sciences Accelerator Mass Spectrometry (NOSAMS) at Woods Hole Oceanographic Institute for radiocarbon dating using the Libby half-life of 5,568 yr and corrected for carbon isotopic fractionation. Of these samples, 23 were mollusk shells, 2 were comprised of foraminiferal tests, and 3 contained organic material/plant debris (**Table 5.2**). Mollusk and foraminiferal samples containing at least 4 mg of material underwent hydrolysis where carbon in the samples were converted to CO<sub>2</sub> using a strong acid H<sub>2</sub>PO<sub>3</sub>. Mollusk samples were powdered to allow NOSAMS staff to subsample material >9 mg. Radiocarbon dates from organic material were calibrated with IntCal20 (Reimer et al., 2020) and mollusk and foraminifera ages were corrected for reservoir variations using a correction specific to the Gulf of Mexico offshore Galveston Bay (Wagner et al., 2009) and then calibrated using Marine20 (Heaton et al., 2020). The IntCal20 calibrations were done using OxCal 4.4 (Ramsey, 2009) and the Marine20 calibrations were applied through Bchron (Haslett and Parnell, 2008). Errors in ages were calculated by NOSAMS where the error is determined by the larger of two estimates, the internal statistical error calculated using the total number of <sup>14</sup>C counts (error = 1/√n) and the external error determined by the ratio of <sup>14</sup>C and <sup>12</sup>C of a sample calculated 10 separate times while the sample was being run.

#### 5.3.5 Age models

Age models were developed using the code rbacon (Blaauw and Christen, 2011), which calculates sediment accumulation rates based on a gamma autoregressive semiparametric model using a Markhov chain Monte Carlo algorithm. The model provides a predictive window with 95% confidence of the age of sediments given depth and radiocarbon age constraints and the assumption of consistent deposition unless hiatuses are applied. Although we suspect a significant amount of erosion may have occurred during transgression, the lack of upper core carbon dates limits the application of hiatus depths in the model and interpolated ages for the upper core are likely incorrect. Interpolated ages from the models for each core (except for GC-1) were used to identify environmental transitions between radiocarbon ages, and in a few instances, extrapolations were used to identify transitions outside the range of carbon dates.

### 5.4 Results

Sediment cores range from <1 m to ~ 5.6 m in depth and primarily contain medium-gray mud varying from clay to silty-clay with sandy intervals that occasionally coincide with shell hash layers or abundant shell fragments (**Figure 5.6**). GC-4 contains significantly more organic material and less shell material than all the other cores. GC-1 and PC-4 contain sharp and gradual contacts, respectively, between stiff, light-gray Pleistocene clay terraces and Holocene sediments (**Figures 5.6B,H**). PC-2 and PC-4 did not contain any analyzable upper seafloor sediments due to coring disturbance caused by over-penetration of the piston corer and the soupy nature of the uppermost sediments. Here, we summarize the key observations for each core, proceeding from the most proximal to most distal core.

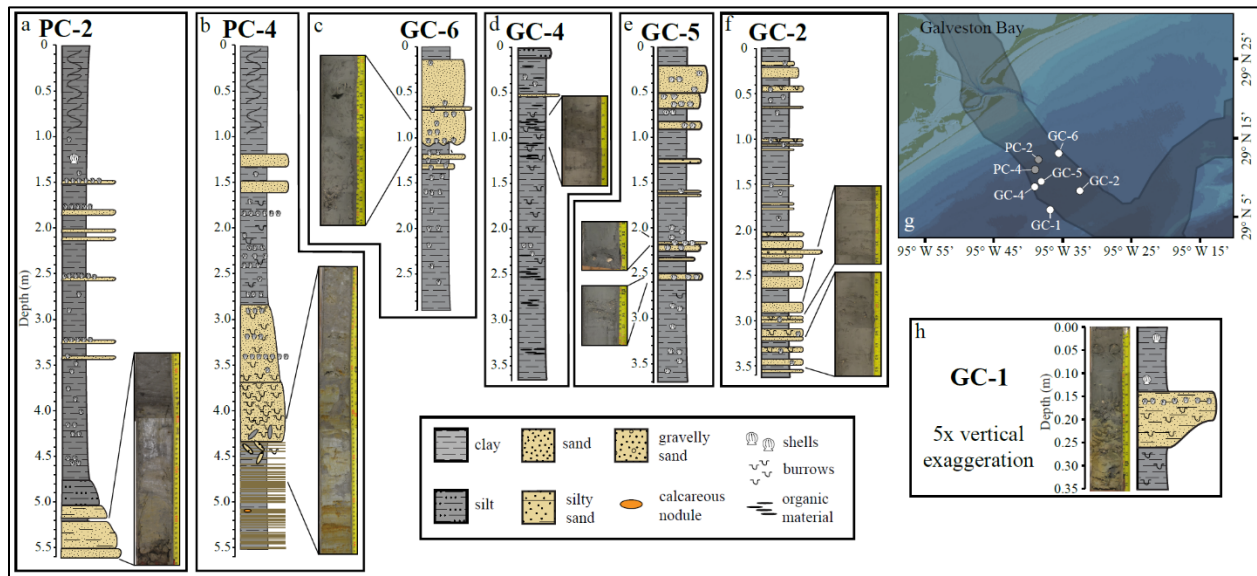


**Figure 5.6. Stratigraphic columns and select core images from this study**

A) PC-2 column with image of fluvial and upper bay sands (~5.2–5.6 m); B) PC-4 column with image of the Pleistocene terrace with oxidized sand in clay to upper bay heavily burrowed sands (~4.1–4.8 m); C) GC-6 column with image of outer bay shelly sands (0.8–1.1 m); D) GC-4 column with image of organic material (0.7–1.1 m); E) GC-5 column with images of large shells (2.1–2.2 m) and shell hash (2.5–2.6 m) in sandy sections; F) GC-2 column with images of sandy intervals containing shell fragments (2.8–2.9 m and 3.2–3.5 m); G) map of core locations offshore Galveston Bay; and H) GC-1 column and image of entire core (not at same scale as other cores).

#### 5.4.1 Piston core 2

PC-2 was selected for identification of a fluvial terrace toward the western edge of the incised valley (**Figure 5.7A**). It consists primarily of massive medium-gray clay with sporadic sandy layers that coincide with increased shell fragments and in some cases shell hash layers (**Figure 5.7**). The core catcher contains silty medium sand which is overlain by silt and clay (**Figure 5.6A**). As the reference section representing the complete transition from fluvial to outer bay deposition, this core was sampled at the highest resolution at least every 10 cm. The base of the core is barren of foraminifera and is interpreted as fluvial deposits, which are capped by upper bay and/or deltaic deposits dominated by agglutinated benthics and dated to  $9,794 \pm 215$  Cal yrs bp from a mollusk shell at 5.10 m depth (**Figure 5.7B**). The increase in percentage of fragmented foraminifera tests represents a higher energy environment with potentially more reworked material (**Figure 5.7B**). Upper bay deposits transition at ~9.5 ka upward into ~2.8 m of central bay sediments that are generally dominated by *Ammonia* with some increases in presence of *Elphidium*. The age model of this core (**Figure 5.7B**) indicates that this central estuary assemblage existed from at least 9.5 to 8.0 ka, indicating a long period of stability in the estuary system during this time. By  $7,800 \pm 134$  Cal yrs bp (mollusk shell at 1.82 m), the environment had transitioned to outer bay, with a foraminiferal assemblage dominated by *Elphidium*. The uppermost meter of the core was not analyzed due to coring disturbance.



#### 5.4.2 Piston core 4

PC-4 was obtained at the location of another fluvial terrace originally interpreted seismically to be a point bar (**Figure 5.8A**), but which was instead revealed to be a Pleistocene flood plain deposit comprised of light-gray, stiff Beaumont Clay, into which the MIS5-3 river valley was incised. The terrace is heavily laminated with oxidized sand layers and contains a calcareous nodule, which are relatively common in the Beaumont (Rehkemper, 1969). The terrace gradually transitions upward into heavily burrowed sand (**Figure 5.6B**), and both the terrace and the overlying sandy section are barren of microfossils and interpreted as fluvial/terrestrial sediments. At approximately 3.5 m depth, foraminiferal assemblages appear in the sandy sediments and indicate a transition to an upper bay environment, dated to  $9,131 \pm 158$  Cal yrs bp (mollusk shell at 3.44 m) (**Figure 5.8B**). These sediments also contain visible burrows and a higher percentage of fragmented foraminifera tests. PC-4 contains less central bay sediments compared to PC-2, likely due to the elevation of the Pleistocene terrace. The seismic data show draping of sediments above and over the terrace (**Figure 5.8A**). Central bay sediments were dominated by *Ammonia* and dated to  $8,815 \pm 175$  Cal yrs bp by a mollusk shell at 2.66 m depth. At approximately 2 m depth, *Elphidium* becomes more dominant and the environment transitions to outer bay sediments. According to the age model for this core (**Figure 5.8B**), the central bay to outer bay transition occurred  $\sim 8.0$  ka, coinciding with the same transition in PC-2. The increase in diversity of foraminifera at  $\sim 1.30$  m depth (e.g., increase in common inner shelf genera, like *Bulimina* and *Bolivina*, and agglutinated taxa) indicate the beginning of a transition to open marine/inner shelf sediments. This section contains two carbon dates at approximately the same depth (1.59 m) from mollusk shells, one of which likely contains reworked material because it records an unreasonable age for sediments filling a Holocene estuary ( $41,030 \pm 1,703$  Cal yrs bp). The other date provides an age of  $7,787 \pm 136$  Cal yrs bp for the outer bay sediments. The upper 1 m section of PC-4 also consisted of material not suitable for sampling likely containing unconsolidated, unstratified inner shelf deposits that became mixed during retrieval. While fragmentation of tests appears low throughout the core, there is a slight increase in the number of fragments in the outer bay section of the core, indicating a higher energy environment.

#### 5.4.3 Gravity core 6

Along the eastern edge of the paleovalley, GC-6 penetrated bright seismic reflectors that are represented in the core as a  $\sim 0.8$  m sandy package of sediments atop medium-gray estuarine sediments (**Figure 5.9A**). Starting at the base of GC-6, clay sediments are dominated by *Ammonia*, indicating a central bay environment dated to  $8,367 \pm 181$  Cal yrs bp (mollusk at  $\sim 2.1$  m depth). These central bay sediments transition to outer bay, as indicated by an increase in *Elphidium* at  $\sim 1.7$  m depth, with an approximate age of 8.2 ka based on the age model (**Figure 5.9B**). Smaller sandy intervals at the top of the outer bay sediments provide mollusk carbon dates of  $7,709 \pm 147$  Cal yrs bp and  $7,760 \pm 142$  Cal yrs bp preceding an irregular contact with the sandy package of sediments (**Figure 5.9B**). Shell fragments decrease in abundance going up the core, while foraminifera test fragmentation increases going up the core, potentially indicating that the sandy package contains reworked material. A mollusk shell within the sandy package was dated to  $4,319 \pm 165$  Cal yrs bp and foraminifera within the sandy package indicate a transition from outer bay to inner shelf was taking place until the uppermost sample (GC-6 7–8.5). This sample contained a foram assemblage that did not match any other assemblages in the study area. It was compared to modern foraminifera assemblages obtained by Phleger (1965) from Galveston Lagoon on Galveston Island, and two grab samples taken from within the flood- and ebb-tidal areas of Bolivar Roads tidal inlet by the MGG 2018 Field Course (**Figure 5.10, Table 5.2**). A similar method of foram assemblage comparison was used by Hawkes and Horton (2012) to identify inner shelf-sourced washover sediments from Hurricane Ike on Galveston and San Luis Islands. Our GC-6 comparison revealed that the uppermost sample most closely resembles Phleger's Station 11 sample from Galveston Lagoon (**Figure 5.10**). However, the sample does not contain a higher amount of plant debris as would be expected in a

back-barrier marsh environment. As a result, the lower portion of the sandy package is interpreted as transgressive lag capped by probable washover deposits, rather than a relict drowned barrier island.

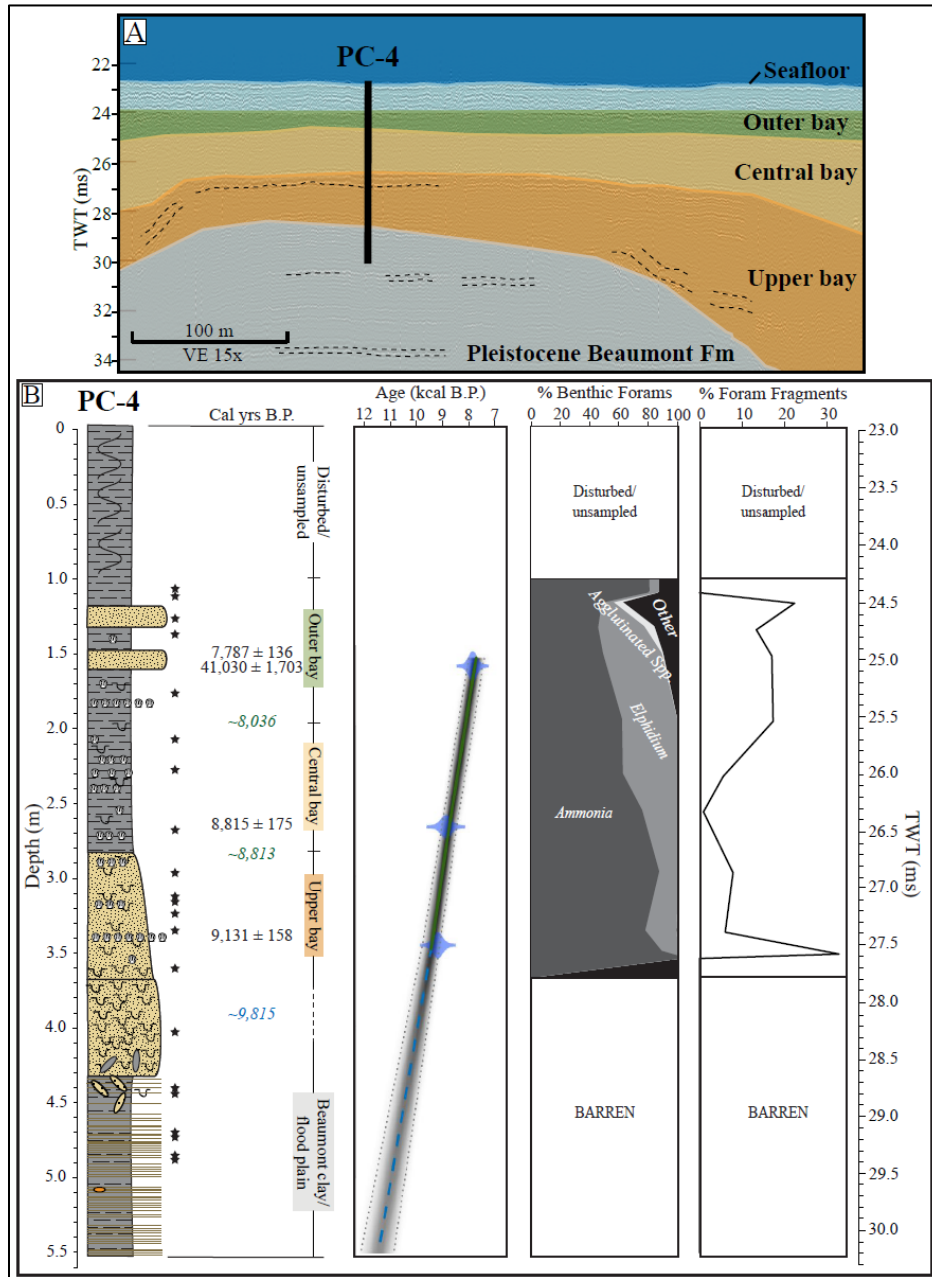


**Figure 5.8. Piston Core 4 (PC-4)**

A) Interpreted seismic data with approximated depth for PC-4 into a Pleistocene terrace (location in **Figure 5.6**). Seismic interpretation from Burstein et al. (2021) (VE = vertical exaggeration). B) Stratigraphic column with sample locations (black stars), carbon dates (black text), and interpolated (green) and extrapolated (blue) ages from age model. Age model based off of radiocarbon ages (blue ovals tapering to error range), with mean age depicted by dark green solid line for interpolated ages, light green dashed line for extrapolated ages, and gray scale out to 95% confidence interval predicted by the model. Interpreted depositional facies based off of foraminiferal assemblage abundances and percent foram fragments. Two-way travel time scale for stratigraphic column in ms calculated from approximate seismic velocity of 1,525 m/s starting at time of seafloor.

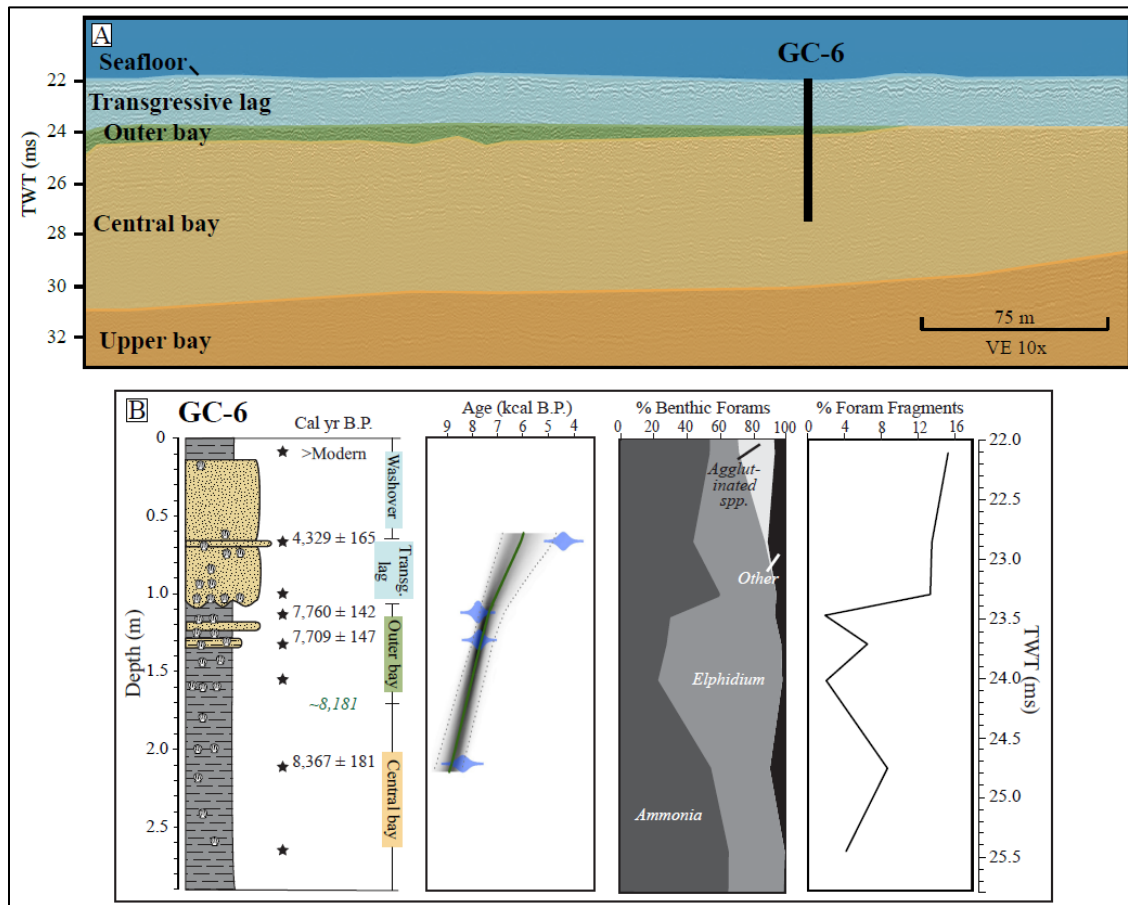


**Figure 5.9. Gravity Core 6 (GC-6)**

A) Interpreted seismic data with approximate depth of penetration for GC-6 (location in **Figure 5.6**). Seismic interpretation from Burstein et al. (2021) (VE = vertical exaggeration). B) Stratigraphic column with sample locations (black stars), radiocarbon dates (black text), interpolated ages (italicized in green) based off of age model. Age model based off of radiocarbon ages (blue ovals tapering to error range), with mean age depicted by solid green line and gray scale out to 95% confidence interval predicted by the model. Interpreted depositional facies based off of foraminiferal assemblage abundances and percent foram fragments. Two-way travel time scale for stratigraphic column in ms calculated from approximate seismic velocity of 1,525 m/s starting at time of seafloor.

#### 5.4.4 Gravity cores 4 and 5

GC-4 and GC-5 represent a composite section sampling two different seismic facies along the same seismic line, both of which contain central bay sediments (**Figures 5.11, 5.12**). GC-4, which penetrates the older seismic facies, is unique in that it contains the lowest populations of foraminifera of all the cores. All samples obtained from GC-4 contain less than 100 individuals, and sections of the core are barren of foraminifera (**Figure 5.11B**). Situated on the western edge of the paleovalley (**Figure 5.11A**), GC-4 primarily consists of medium-gray clay with a relatively higher amount of organic material (**Figure 5.6D**), lower amount of shell fragments, and more visible burrowing. The base of the core contains a barren section, which is interpreted as bay margin deposits, and organic material at 3.35 m depth was dated to  $8,470 \pm 144$  Cal yrs bp. These deposits transition to central bay sediments dominated by *Ammonia* and *Elphidium* with decreased organic material and increased burrowing and shell fragments (**Figure 5.11B**). The age model for this core (**Figure 5.11B**) indicates the transition took place  $\sim 8.3$  ka. Above the central bay sediments, the core transitions back to barren deposits characterized by burrows and organic

material at 0.82 m depth dated to  $7,977 \pm 221$  Cal yrs bp and the age model dates the transition at  $\sim 1.4$  m depth to  $\sim 8.1$  ka. The upper section of the core contains a thin sand interval with organic material at 0.56 m dated to  $7,913 \pm 255$  Cal yrs bp and is capped by a section of silty sediments. The foraminiferal assemblage in this section is dominated by *Ammonia* and *Elphidium* with a slight increase in agglutinated and common inner shelf taxa indicating a transition to outer bay and then inner shelf deposits.

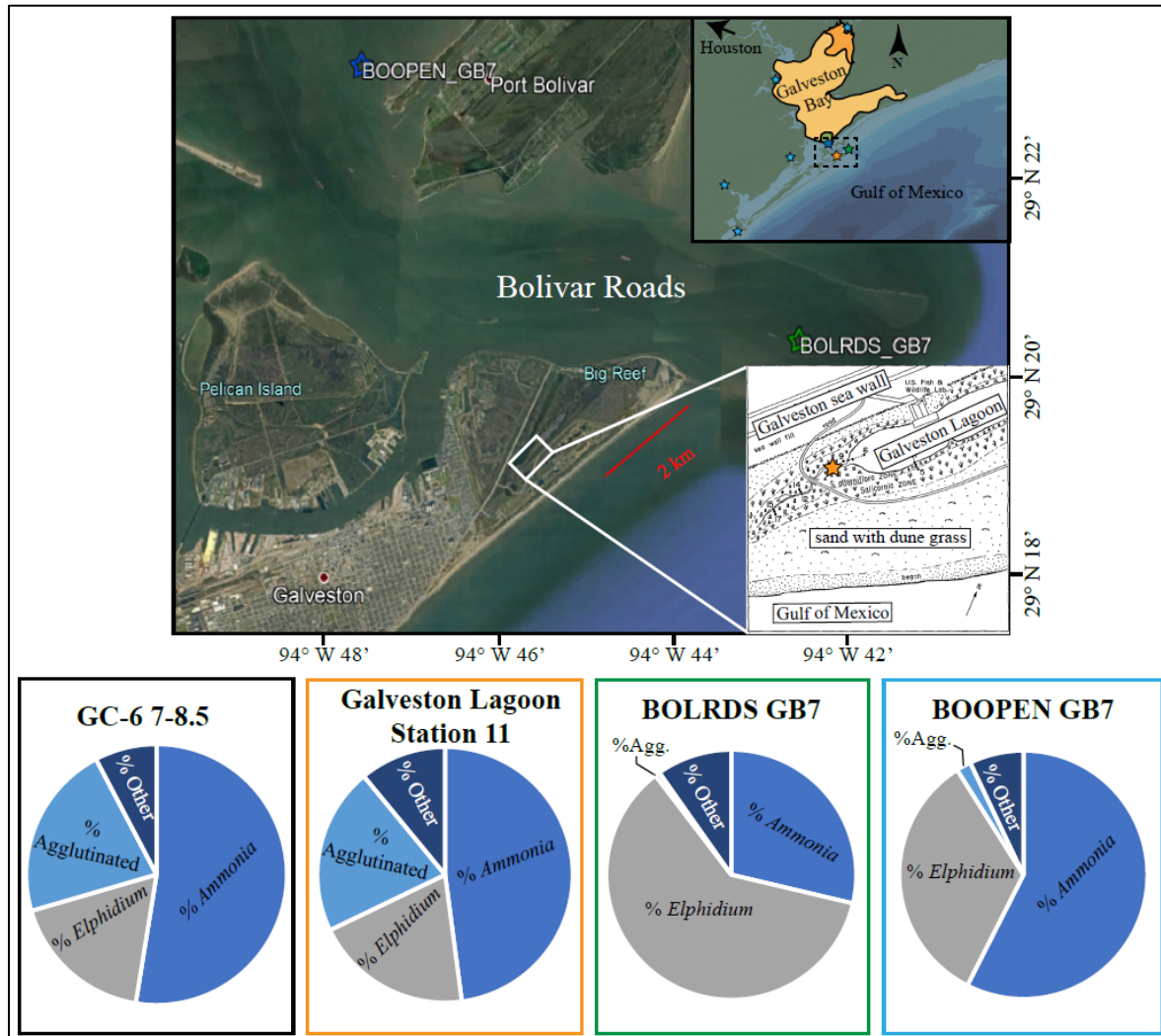


**Figure 5.10. Comparison of GC-6 upper sample (7–8.5 cm) to modern foram assemblages**

Galveston Lagoon sample from Station 11 analyzed by Phleger (1965) (orange), BOLRDS GB7 grab sample taken from the outer edge of the tidal inlet (green), and BOOPEN GB7 grab sample taken from the inner edge of the tidal inlet (blue). The Station 11 sample is closest approximation to the GC-6 sample. Image source Google Earth (2021).

GC-5, which penetrated the younger seismic facies in this two-core composite section, contains central bay sediments capped by outer bay deposits (Figure 5.12). The base of GC-5 contains medium-gray clay with shell fragments, and a single burrow (Figure 5.6E). Shell material in this section (2.92 m depth) was dated to  $8,467 \pm 130$  Cal yrs bp and foraminifera are dominated by *Ammonia*. The age model (Figure 5.12B) indicates the central bay to outer bay transition occurred  $\sim 8.4$  ka. The outer bay sediments are composed of medium-gray clay containing sporadic 2–4 cm-scale sandy layers that thicken toward the top of the core to decimeter scale layers with more shell fragments. The upper portion of the core also

contains a peak in foram fragmentation and is dominated by *Elphidium*. Increasing diversity and presence of agglutinated forams from 1.0 m depth to the top of the core indicate an outer bay depositional environment transitioning to modern day marine inner shelf. The peak in fragmentation at approximately 1.0 m depth coincides with a peak in dominance of *Ammonia* and suggests that the increase in *Ammonia* likely represents reworked material. The outer bay section was dated to  $8,445 \pm 135$  Cal yrs bp at 2.50 m depth and  $6,661 \pm 169$  Cal yrs bp near the top at 0.73 m depth.

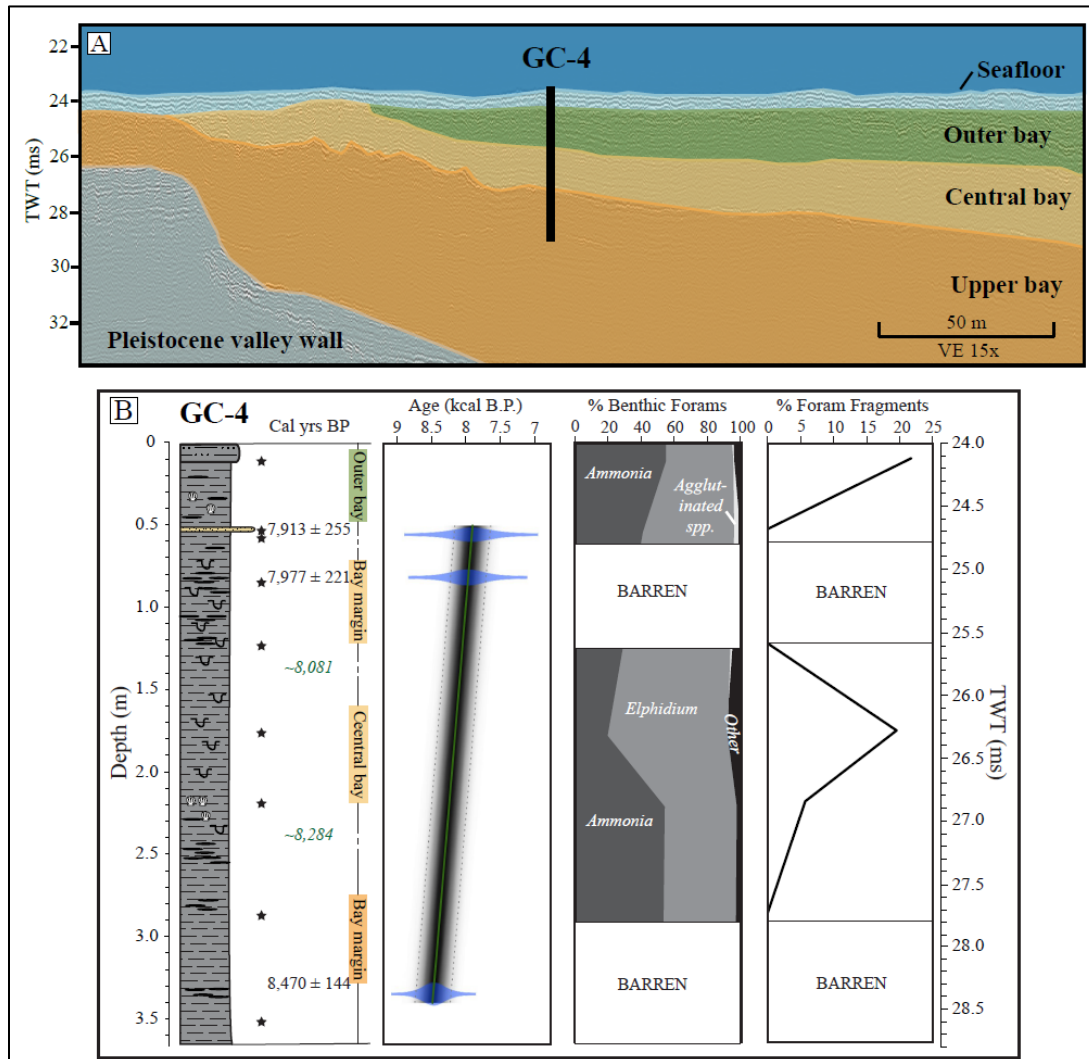


**Figure 5.11. Gravity Core 4 (GC-4)**

A) Interpreted seismic data with approximate depth of penetration for GC-4 (location in **Figure 5.6**). Seismic interpretation from Burstein et al. (2021) (VE = vertical exaggeration). B) Stratigraphic column of GC-4 showing samples (black stars) with radiocarbon ages (black text), interpolated ages (italicized in green) from age model. Age model based off of radiocarbon ages (blue ovals tapering to error range), with mean age depicted by solid green line and gray scale out to 95% confidence interval predicted by the model. Interpreted depositional facies based off of foraminiferal assemblage abundances and percent foram fragments. Two-way travel time scale for stratigraphic column in ms calculated from approximate seismic velocity of 1,525 m/s starting at time of seafloor.

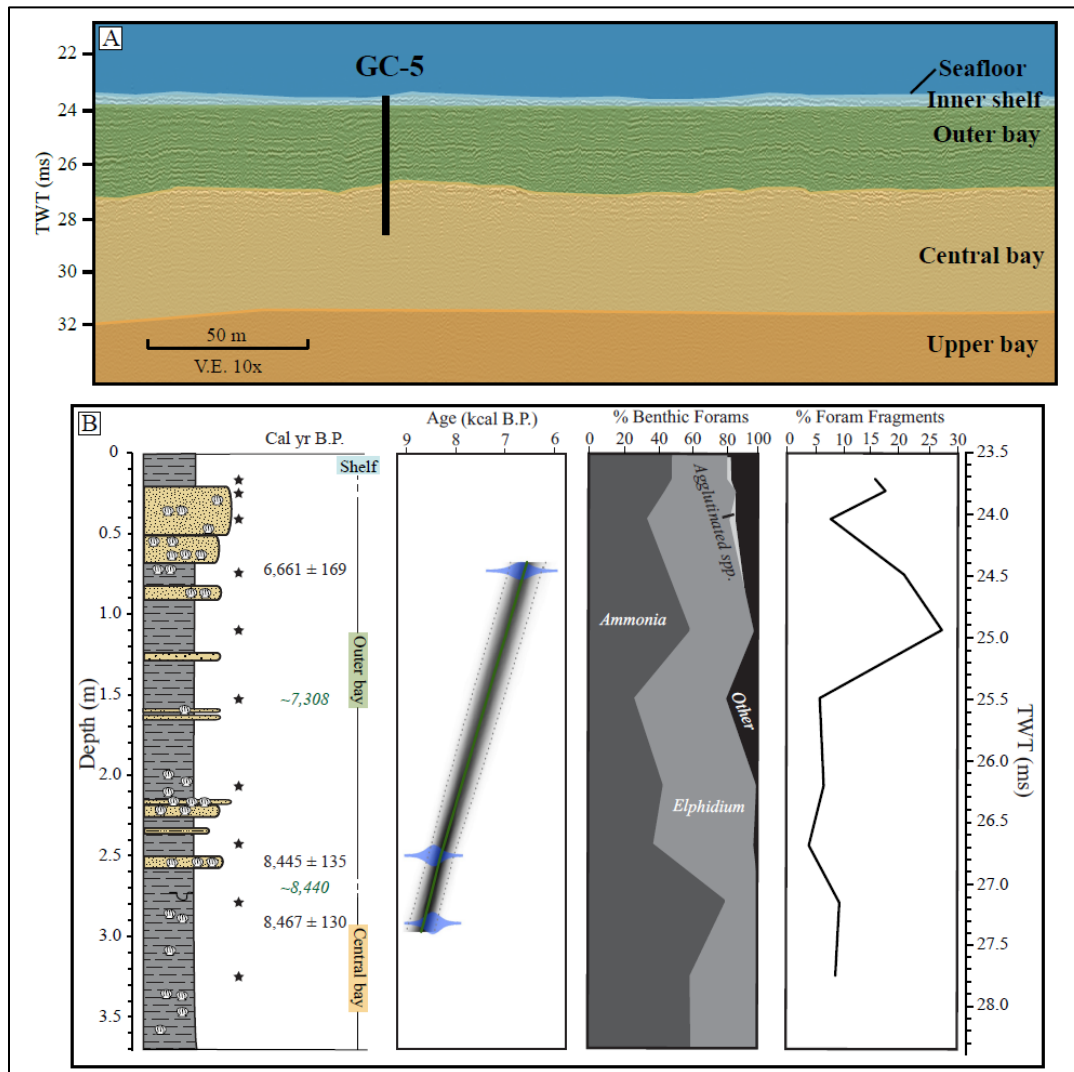


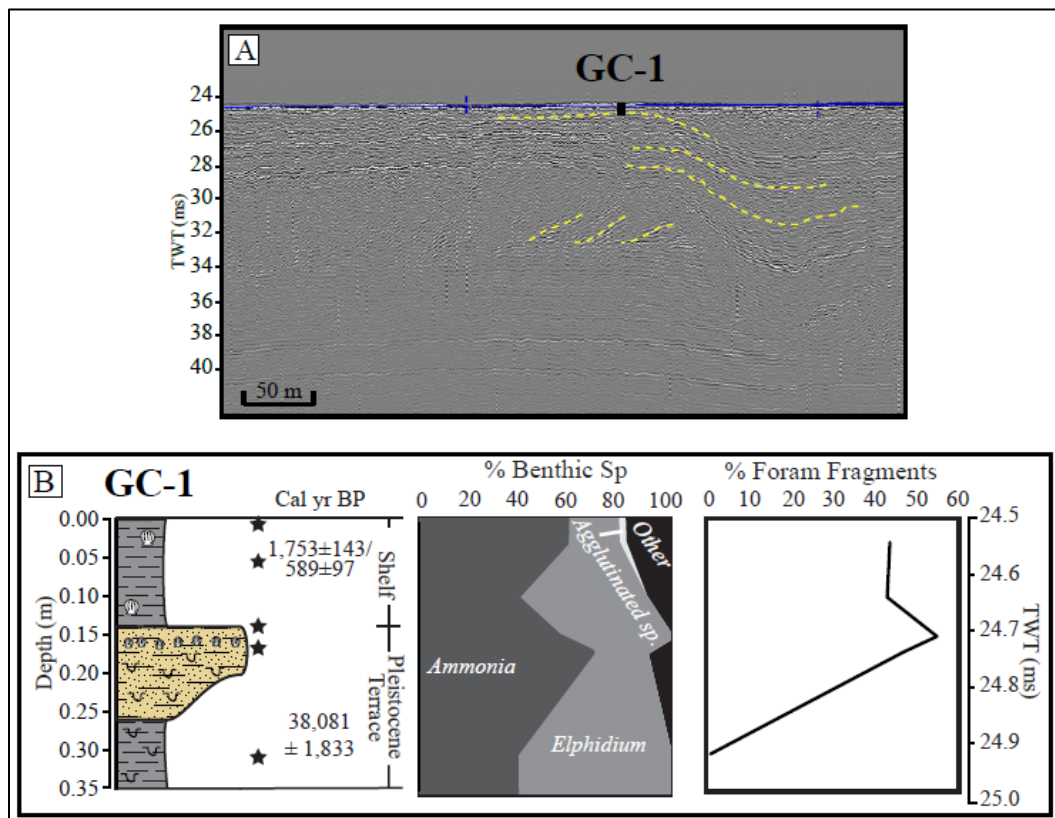
**Figure 5.12. Gravity Core 5 (GC-5)**

A) Interpreted seismic data with approximate depth of penetration for GC-5 (location in **Figure 5.6**). Seismic interpretation from Burstein et al. (2021) (VE = vertical exaggeration). B) Stratigraphic column of GC-5 showing samples (black stars) with radiocarbon ages (black text), interpolated ages (italicized in green) from age model. Age model based off of radiocarbon ages (blue ovals tapering to error range), with mean age depicted by solid green line and gray scale out to 95% confidence interval predicted by the model. Interpreted depositional facies based off of foraminiferal assemblage abundances and percent foram fragments. Two-way travel time scale for stratigraphic column in ms calculated from approximate seismic velocity of 1,525 m/s starting at time of seafloor.

### 5.4.5 Gravity core 1

GC-1 is an extremely short (0.35 m) core (**Figure 5.6H**). Its location was selected to investigate dipping reflectors seen in seismic data hypothesized to be a Holocene-aged point bar deposit from a tributary at the edge of the Trinity Paleovalley (**Figure 5.13**). Instead, the core penetrated a Pleistocene-age terrace containing sticky, dense, burrowed Beaumont Clay. This clay is capped by burrowed sand and thick shell hash and has a sharp contact with modern inner shelf deposits at approximately 0.14 m depth (**Figure 5.13B**). Foraminiferal analysis revealed a large population of foraminifera, dominated by *Elphidium*, within one of the burrows of the terrace. Carbon dating of these foraminifera tests revealed an age of

38,081 ± 1,833 Cal yrs bp almost certainly owing to the inclusion of older material, potentially in the form of dissolved inorganic carbon from the Beaumont Formation. Samples at the terrace contact contained lower populations of foraminifera dominated by *Ammonia*. Sediments above the terrace were dominated by both *Elphidium* and *Ammonia* with a slight increase in agglutinated forams and a more significant increase in inner shelf genera, indicating a transition to a modern marine environment. Two radiocarbon ages were obtained from approximately the same interval in the core (0.05 m depth) as a method of comparing ages from foraminifera tests and mollusk shells. The foraminifera provided an older age of 1,753 ± 143 Cal yrs bp than the mollusk shell, which was dated to 589 ± 97 Cal yrs bp. The difference in the ages may indicate an amalgamation of material in a condensed section on the sediment-starved modern shelf, the presence of sediments containing detrital carbonate within the foram tests resulting in an older age, or perhaps diagenetic alteration of the foram tests, with recrystallization of pore water carbonate incorporating older material on the foraminifer tests, which have a higher surface to mass ratio than the mollusk shells. Regardless, both ages indicate a much younger age for the 14 cm thick open shelf deposit (**Figure 5.13B**) than any of the estuary sediments in the river valley. A spike in fragmentation of foram tests coincides with the contact between the terrace and modern deposition, indicating a more significant amount of reworking at the contact. Seismic data at this location show prominent draping of sediments along the edges of the terrace (**Figure 5.13A**).



#### 5.4.6 Gravity core 2

GC-2's location was chosen to identify a set of dipping reflectors believed to be part of a paleo-tidal-delta (**Figure 5.14A**). The core consists primarily of medium-gray clay with numerous layers of silty sand (**Figure 5.6F**). The lower part of the core contains foraminifera approximating 50-50 *Ammonia* and *Elphidium*. This assemblage combined with the increased sand content and the relatively higher percent of foram test fragmentation indicate this section likely contains tidal delta deposits. Because it is capped by a less-sandy section dominated by *Elphidium* indicating an outer bay environment, the base of the core is interpreted as a flood-tidal delta. Carbon dates obtained near the transition from tidal delta to outer bay provide ages of  $8,445 \pm 135$  Cal yrs bp from a mollusk shell at 2.07 m depth and  $8,546 \pm 173$  Cal yrs bp also from a mollusk shell at 2.19 m depth. The top of the core contains a spike in *Ammonia* coupled with an increase in fragmentation. Similar to GC-5, coincident increase in fragmentation with a spike in *Ammonia* likely represent a reworking of central bay material in the outer bay environment. The top of the core contains a transition to modern inner shelf deposition at  $\sim 7.0$  ka, represented by the increase in diversity and presence of agglutinated foraminifera at  $\sim 0.5$  m depth.

### 5.5 Discussion

The coring locations in this study were chosen to sample specific seismic facies and were not intended to provide a cross section down the Holocene estuary. However, the data can provide several short cross sections along strike in the proximal, middle, and distal parts of our study area. Together, these cross sections provide a composite picture of the nature and timing of environmental change across this part of the estuary from its initial flooding  $\sim 10$  ka to its continued evolution by  $\sim 6$  ka. A cross section analysis of the cores across the incised valley combined with interpolated ages from the age models shows consistent paleoenvironmental changes across multiple cores (**Figure 5.15**). PC-2 and PC-4 do not transition from upper bay to central bay environments at the same time, likely due to the elevation of the Pleistocene terrace at PC-4's location. However, PC-2, PC-4, and GC-6 all transition from central bay to outer bay environments at approximately the same time—8.2-8.0 ka. Shortly after this change, GC-4 transitions to an outer bay environment at  $\sim 7.9$  ka, and outer bay sediments thicken in the cores moving seaward from PC-2. Similarly, GC-2 and GC-5 show a coincident transition to outer bay environment at  $\sim 8.4$  ka (**Figure 5.15**).

Additionally, all cores in the study area, except for GC-6, appear to transition to an inner shelf environment by  $\sim 6.0$  ka, although this interval is difficult to date because of the likely erosion of material during transgression and the limited upper seafloor sediments observed in all cores (**Figure 5.16**). This coincident timing suggests that the paleoestuary was stable and changes in shoreline position and/or lateral shifts in the position of the tidal inlet led to the observed environmental transitions. Overall, the lateral differences in sediments within the cores reflect contemporaneous estuarine environmental variability.

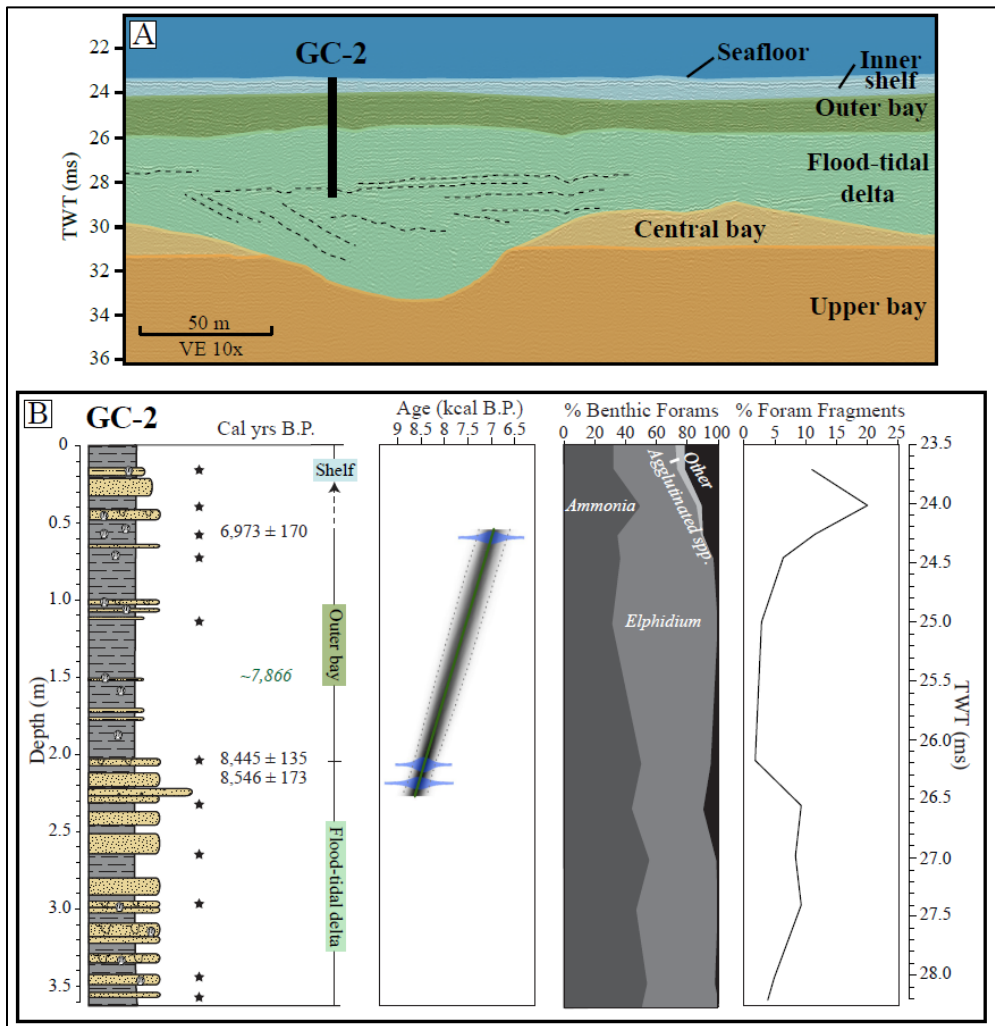


**Figure 5.14. Gravity core 2 (GC-2)**

A) Interpreted seismic data with approximate depth of penetration for GC-2 (location in **Figure 5.6**). Seismic interpretation from Burstein et al. (2021) (VE = vertical exaggeration). B) Stratigraphic column with sample locations (black stars), radiocarbon dates (black text), interpolated ages (italicized in green) from age model. Age model based off of radiocarbon ages (blue ovals tapering to error range), with mean age depicted by solid green line and gray scale out to 95% confidence interval predicted by the model. Interpreted depositional facies based off of foraminiferal assemblage abundances and percent foram fragments. Two-way travel time scale for stratigraphic column in ms calculated from approximate seismic velocity of 1,525 m/s starting at time of seafloor.

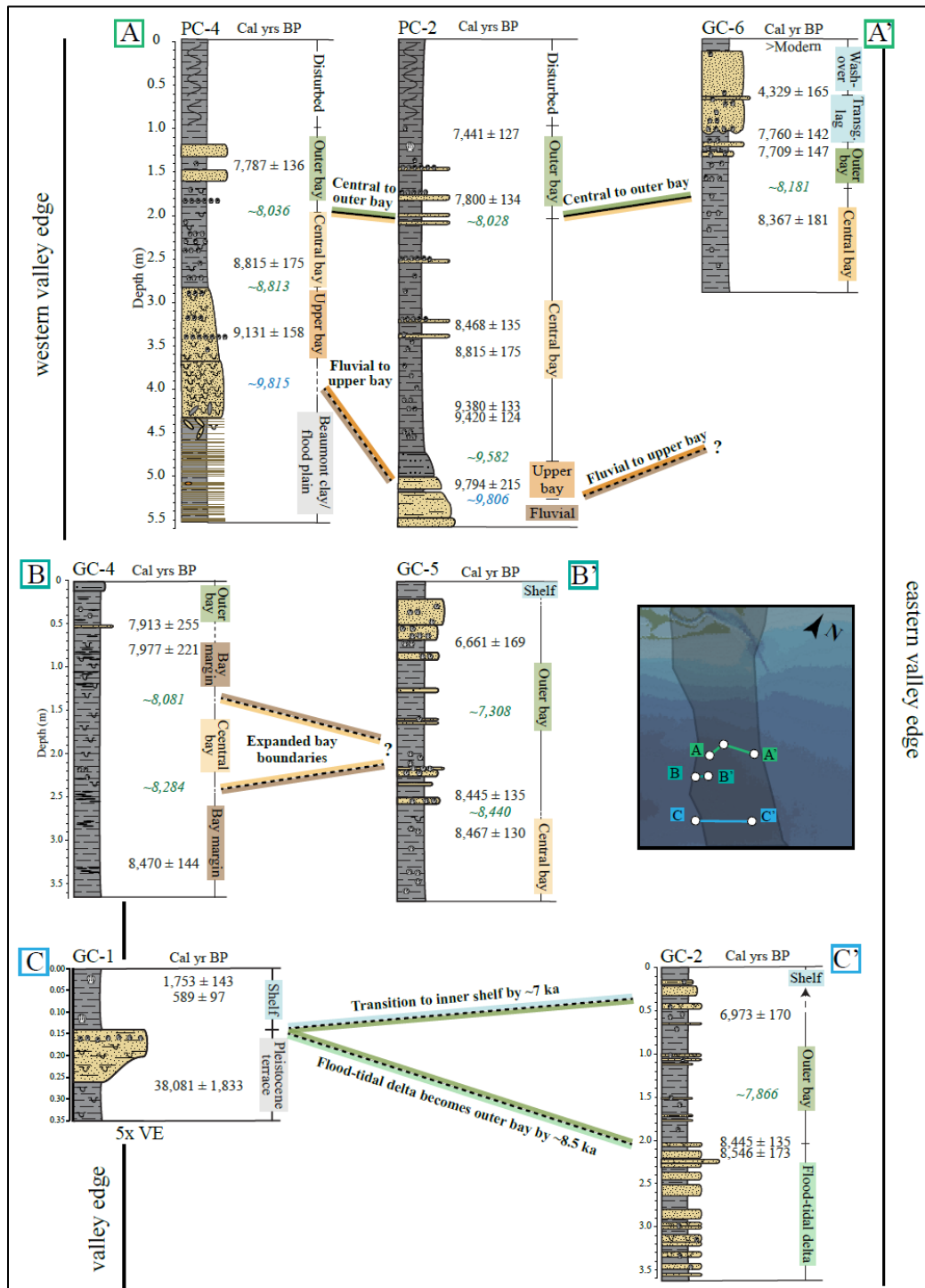


**Figure 5.15. Fence diagram of prominent environmental changes within cores within study area** Radiocarbon ages are in black text and interpolated and extrapolated ages from age model are italicized in green. Colored lines show connections between ages within cores along the profile.

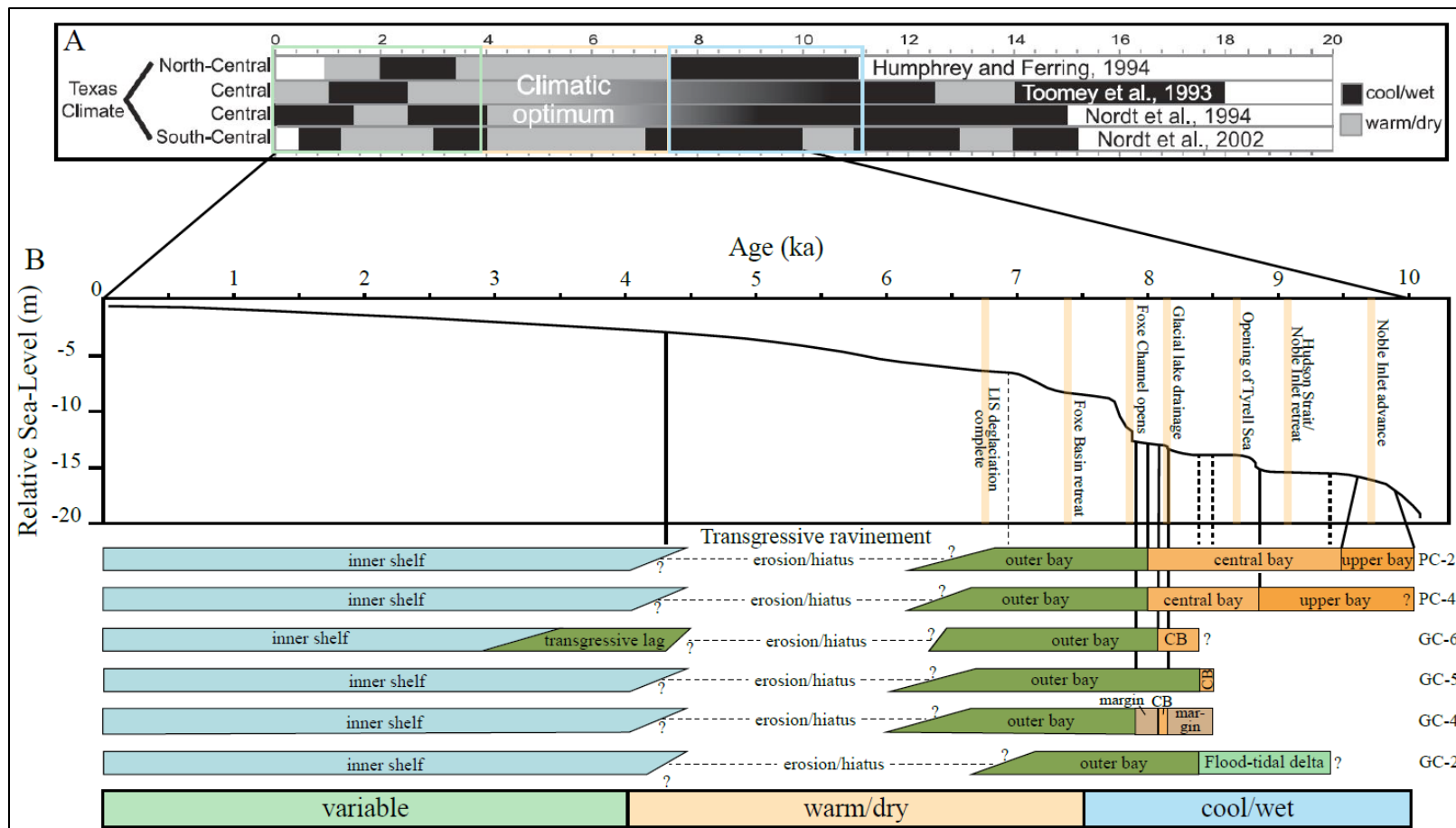


**Figure 5.16. Timeline of environmental change and sea-level rise in Galveston paleoestuary**

A) Compilation of Gulf Coast climate for the Holocene (modified from Weight et al., 2011). B) Gulf Coast Holocene sea level curve containing prominent North American glacial events (beige lines) identified in Jennings et al. (2015) (modified from Swartz et al., 2022) and a compilation of environmental change within Trinity River paleovalley cores and approximated period of transgressive erosion. A majority of environmental transitions take place during a cool/wet climate when sea-level rise was more rapid, while significant transgressive erosion took place during a warm/dry period when sea-level rise slowed significantly.

Micropaleontologic evidence from these cores confirm the existence of a long-term stable estuarine environment; however, the seaward boundary of this estuary differs from previous studies (**Figure 5.17**). Approximately 9.8–9.6 ka, a large estuary stretched from the modern shoreline of Galveston Bay to seaward of Heald Bank. The flood-tidal delta at the base of GC-2 combined with the 8.7 ka age of the transgressive ravinement identified by Thomas and Anderson (1994) indicates the shoreline shifted landward of Heald Bank by at least 8.8 ka. This finding is inconsistent with the interpretation by Rodriguez et al. (2004) that the paleoestuary extended to seaward of Heald Bank until 7.7 ka. Our data indicate the paleoestuary was stable landward of Heald Bank for ~2 kyr with some tidal inlet changes that altered the environment within the estuary without transgressing the shoreline (**Figure 5.17**). A subsequent landward shift took place ~6.9 ka when the barrier system transgressed to a location between GC-2 and GC-5. By ~6.0 ka the locations of almost all cores in the study area transitioned to inner shelf environments. Washover deposits in GC-6 combined with inner shelf environment of the cores, indicate the shoreline was landward of the study area, but did not reach its modern location until ~2.5 ka when Bolivar Peninsula began to prograde calling into question the interpretation of Galveston Island forming as early as 5.3 ka (Rodriguez et al., 2004).

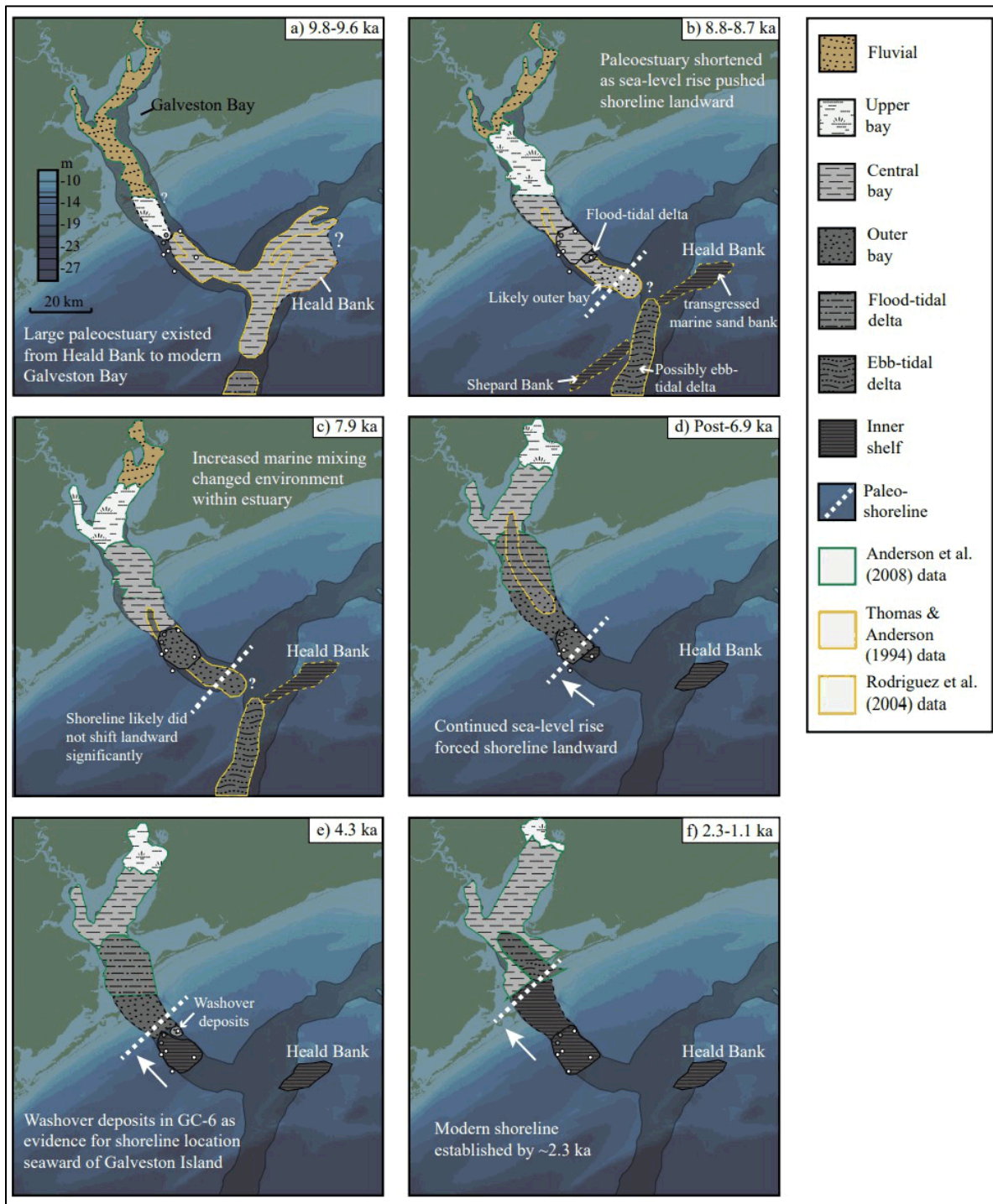


**Figure 5.17. Paleoenvironmental change of Holocene estuary offshore Galveston Bay, Texas**

Environmental facies at specific periods of time are based on micropaleontological analysis of cores in study areas and combined with previous research (outlined in green, yellow, and orange), and inferences were made between these study areas (dashed outlines). Facies are mapped within the bounds of the incised valley, but likely extended beyond those boundaries; however, the outer boundaries are difficult to determine due to probable removal of sediments during marine transgression. Paleoshorelines are estimated based on proximity to tidal delta and outer bay environments, and identification of washover sediments in cores.

### 5.5.1 Stable paleoestuary

Research conducted by the Anderson group argues for the existence of >75 km long paleoestuary from Heald Bank ~50 km offshore Galveston Bay to the modern bay between ~8.2–7.8 ka (**Figure 5.1**) (Anderson et al., 2008; Rodriguez et al., 2004). This evidence includes seismic data and carbon dating of sediment cores from within modern Galveston Bay and Heald Bank (Anderson et al., 2008; Rodriguez et al., 2004).

Our data support the long-term stability of the estuary system during this interval, but not the extension of the estuary all the way to Heald Bank. Foraminiferal analysis from PC-2 and PC-4 indicates that both sites were located in the central bay from at least 8.8 ka to 8.0 ka, although PC-2 transitioned to a central bay environment by ~9.6 ka, confirming the existence of a long-term stable estuary (**Figures 5.7, 5.8**). Foraminiferal assemblages in PC-2 and PC-4 during this time period were dominated by *Ammonia* with a secondary presence of *Elphidium*, corresponding to a central bay depositional environment. Assemblages in PC-4 moving up through the core show a decreasing abundance of *Ammonia* and an increase in *Elphidium* over time indicating a gradual environmental transition from upper bay to central bay and to outer bay. However, higher resolution analysis of PC-2 shows fluctuations in *Ammonia* and *Elphidium* abundances throughout the entire central bay interval, which may correspond to salinity fluctuations within the Holocene estuary as tidal inlets changed shape and/or location, or perhaps as precipitation in the catchment varied. Additionally, many of the peaks in *Ammonia* correspond to small increases in foram fragmentation, which may indicate reworking of central bay material during that interval. The PC-2 analysis indicates that portions of the estuary experienced marine mixing ~8.4 ka coinciding with a transition of seaward core locations to outer bay environments. Increased marine influence on the estuary may provide an explanation for the small variations in foraminiferal assemblages observed in the middle estuary.

GC-4 is located at the western edge of the paleovalley and contains sediment and foraminiferal assemblages that record lateral variation in the boundary of the estuary between ~8.2 ka and ~8.1 ka (**Figures 5.11, 5.15**). Though it is difficult to pinpoint the exact forcing mechanism for this expansion with existing evidence, the coincident timing of this flooding of boundaries and the environmental transition in GC-6 show that the outer western boundary of the paleoestuary flooded due to sea-level rise prior to probable partial barrier collapse and the transition to an outer bay seen first in GC-6 and subsequently in PC-2 and PC-4 (**Figure 5.15**). Although this flooding may have impacted the stability of the barrier system, it is unlikely that the shoreline changed significantly because GC-2 maintained an outer bay environment during this time (**Figure 5.14**), as well as the existence of tidal delta deposits identified by Thomas and Anderson (1994) (**Figure 5.17**). However, this hypothesis would require further analysis of high-resolution seismic data as well as additional coring and carbon dating to constrain the extent of the paleoestuary flooding.

### 5.5.2 Paleoshoreline changes

Rodriguez et al. (2004) describe estuarine muds in Heald Bank cores that were dated to  $8,015 \pm 50$  and  $7,770 \pm 65$  Cal yrs bp and suggested that the outer boundary of the paleoestuary was seaward of Heald Bank until ~7.77 ka. Due to the lack of preservation of barrier islands offshore in the sediment record, we must infer original island locations or areas of development based on the data that are preserved. Tidal inlet and tidal delta deposits are considered evidence for the presence of barrier systems that are not preserved (Anderson et al., 2016). Analysis of GC-2 reveals the existence of flood tide delta deposits dated to before ~8.5 ka, indicating that the inlet (and thus the barrier island system) was nearby and well landward of Heald Bank (**Figure 5.14**). Likewise, the presence of washover deposits in GC-5 at ~6.7 ka and GC-6 at ~4.3 ka demonstrates the landward migration of the paleoshoreline as sea level continued to

rise throughout the Holocene (**Figure 5.17**). Both GC-2 and GC-5 transition to outer bay environments by ~8.4 ka (**Figures 5.12, 5.14**), indicating that the outer boundary of the estuary shifted prior to the transition to what Rodriguez et al. (2004) describe as shoreface deposits in Heald Bank cores.

An earlier interpretation by Thomas and Anderson (1994) inferred Heald Bank and other sandy deposits on the Texas shelf to be marine sand banks. Despite their morphological similarities to barrier islands, many modern marine sand banks are not the result of “in-place drowning of barriers” (Snedden and Dalrymple, 1999); rather, they are actively modified marine deposits overlying a transgressive ravinement that likely formed from remnant ebb-tidal delta deposits as the shoreline shifted landward (**Figure 5.17**) (Dyer and Huntley, 1999; Penland et al., 1988). Based on the seismic interpretation of Thomas and Anderson (1994), Heald Bank formed from re-worked marine sands above a transgressive ravinement formed by erosion of estuarine deposits. The locations of Thomas, Shepard, and Heald Banks coincide with seismic facies interpreted as flood-tidal delta deposits (Thomas and Anderson, 1994), but were more likely to be ebb-tidal delta sediments (**Figure 5.17**). These sand banks likely formed as sand ridges off of seafloor irregularities at an angle from the ebb-tidal deltas and were later detached as the ebb-tidal delta was transgressed, providing source material for the sand banks (e.g., Type 2 sand ridges, Dyer and Huntley, 1999). Afterwards, these deposits were continually reworked by coastal currents as modern marine sand banks.

Sandy deposits in the outer bay sequence of GC-5 are likely washover sediments from a proximal barrier island. The absence of these sands in the bay margin intervals of GC-4 indicate that these washovers are not from the edge of the bay, westward of GC-5’s location (**Figure 5.12**). We hypothesize that a barrier system developed near GC-5’s position ~20 km seaward of the modern shoreline ~6.7 ka (**Figure 5.17**). Sandy intervals in the outer bay section of GC-2, located seaward of GC-5, dated to  $6,973 \pm 170$  Cal yrs bp also suggest that a barrier had developed nearby in the distal direction, and these sandy intervals could represent paleo-storm washover deposits from that barrier system.

In addition to the data provided in GC-2 and GC-5, washover deposits in GC-6 (**Figure 5.9**) indicate that there was a barrier system proximal to GC-6’s location between ~7.4 and 4.3 ka (**Figure 5.17**). The upper sample obtained from GC-6 closely resembles a modern marsh assemblage from Galveston Island (see 5.4.3), indicating that these washovers could be spilled over from either a back-barrier marsh or a marsh located on the edge of the paleoestuary, and are not a remnant ebb-tidal delta deposit (**Figure 5.10**).

Analysis of Galveston Island core data by Rodriguez et al. (2004) coupled with previous research on the island by Berrard et al. (1970) indicate that Galveston Island began prograding ~5.3 ka giving the paleoshoreline an irregular shape and showing rapid, rather than gradual, coastline changes in the past (**Figure 5.1**). Although Rodriguez et al. (2004) obtained their own radiocarbon ages, they indicated there was a significant amount of uncertainty in the methods used by Berrard et al. (1970). Excluding the work done by Berrard et al. (1970) leaves a single carbon date obtained by Rodriguez et al. (2004) from older beach ridges on Galveston Island providing an age of ~5.3 ka; this age could come from reworked material. The irregular shape of these paleoshorelines (**Figure 5.1**) is likely not representative of coastal changes which would have adjusted to sea-level rise “dynamically while maintaining a characteristic geometry that is unique to a particular coast” (FitzGerald et al., 2008). Based on probable washover sediments reported here, this paleoshoreline likely stepped landward multiple times until reaching its modern-day location by ~2.5 ka and the ~5.3 ka age thus represents reworked sediments. However, the lack of data between our study area and the modern shoreline makes it difficult to constrain this migration beyond its proximity to GC-6 at ~4.3 ka.

### 5.5.3 Timeline of sea-level rise

A comparison of environmental changes in the paleoestuary and the record of Gulf of Mexico sea-level rise indicates that most of these transitions coincide with or occurred after periods of rapid increases in sea level (**Figure 5.16**). A majority of these changes took place when global sea-level rise was greater than twice the modern rate (~15 mm/yr), although some environmental shifts transpired after global sea-level rise slowed significantly, indicating other regional and local changes, such as climate, may have contributed to these transitions (**Figure 5.16**).

Following the retreat of ice from Noble Inlet and Hudson Strait ~9.1 ka (Jennings et al., 2015), PC-4 transitioned to a central bay environment. The early opening of the Tyrell Sea in North America (now called Hudson Bay) ~8.7 ka (Jennings et al., 2015) preceded the transitions in GC-2 and GC-5 from central to outer bay as well as a brief increase in diversity in PC-2 that may represent increased marine mixing. The rapid discharge of freshwater from North American glacial lakes, dubbed the “8.2 ka event” that resulted in short-term climate cooling (Cronin et al., 2007; Jennings et al., 2015; Törnqvist et al., 2004; Ullman et al., 2016) coincided with the flooding of the paleoestuary that expanded at least the western boundary visible in GC-4, and the environmental change in GC-6 from central bay to outer bay ~8.2 ka. Following the 8.2 ka event, there was a reduced rate of global sea-level rise (Lambeck et al., 2014). GC-4 resumed a bay margin environment shortly afterwards, around the same time that PC-2 and PC-4 transitioned to outer bay (~8.1 ka). Glacial ice retreat in the Foxe Basin west of Baffin Island ~7.4 ka (Jennings et al., 2015) preceded a brief increase in diversity that we observe in GC-5, possibly associated with increased marine mixing due to an unstable barrier system ~7.3 ka. This change also coincides with a regional climate transition from cool/wet to warm/dry (**Figure 5.16**) (Weight et al., 2011), which may have contributed to environmental change through decreased precipitation and thus decreased sediment supply to the paleoestuary. GC-2 transitioned from outer bay to inner shelf ~6.9 ka approximately at the same time as the final deglaciation of the LIS ~6.7 ka (Jennings et al., 2015; Ullman et al., 2016). From 6.7 ka until the onset of recent accelerated sea-level rise (~100–150 yr ago), there was a progressive decrease in the rate of global sea-level rise (Lambeck et al., 2014). During this period, our study area transitioned to an inner shelf environment as the previously stable estuary system rapidly shifted landward (**Figure 5.16**), suggesting that climate-driven sediment supply played a significant role in maintaining the stability of the early-middle Holocene estuary and its protective barrier system and a reduction in this sediment supply precipitated retreat. The timing of the middle Holocene inner shelf transition is difficult to identify due to the removal of material above the transgressive ravinement with the exception of a single carbon date of a transgressive shell lag in GC-6 constraining probable washover deposits to younger than 4.3 ka.

### 5.5.4 Minimal modern seafloor sedimentation

The transition to a modern inner shelf environment is difficult to determine due to the limited amount of modern seafloor material and likely erosion and reworking of upper sediments from the transgressive ravinement. Although it appears to have happened slightly earlier in GC-2, it is probable that the study area was an inner shelf environment by ~6.0 ka and the transgression occurred over the period between 7.0 and 6.0 ka. The limited shelf material in the upper areas of each core represent deposition of ~0.01 cm per year, so it is more likely that material is being removed from the upper seafloor regularly.

The Texas Mud Blanket (TMB; **Figure 5.1**) is a large (~300 km<sup>3</sup>) depositional area on the western Gulf Coast between a bathymetric embayment of the ancient Rio Grande and Colorado River deltas containing ~5x10<sup>11</sup> tonnes of sediment (Weight et al., 2011). Weight et al. (2011) approximated mass accumulation rates in the TMB for the Holocene, with highest accumulation occurring from ~9 ka to ~5.5 ka and ~3.5 ka to present. The primary sediment source for the 9-5.5 ka period corresponds to the erosion of nearby

Brazos and Colorado deltas, and accumulation decreased as these sediment sources were depleted (Weight et al., 2011). The period of ~3.5 ka to present accounts for 57% of total volume accumulation in the TMB, which is attributed to increased efficiency of marine longshore current, specifically the Louisiana-Texas Coastal Current, bringing sediments from as far as the Mississippi River delta (Weight et al., 2011). It is likely that the same mechanism has depleted inner shelf sediments offshore Galveston Bay resulting in minimal modern seafloor sediments in our cores with sediment delivered to regions farther west along the Texas Coast including the TMB.

## 5.6 Conclusions

We revise the established Holocene coastal change model for the Trinity River incised valley based on new radiocarbon dates and micropaleontological analysis of sediment cores from offshore Galveston Bay, Texas. This study provides environmental context to previous research that primarily utilized seismic and sedimentological analyses revealing consistent environmental changes across multiple cores due to external sea-level rise and climate forcing. As a result of this analysis, we reached the following conclusions:

- -The barrier system was inshore of the modern position of Heald Bank before 8.5 ka with landward migration occurring in steps of barrier collapse and stabilization resulting in limited disruption during estuarine environmental transitions. It is unlikely that the shoreline migrated asymmetrically as previously hypothesized, but rather stepped landward in a pattern that approximates the geometry of the modern shoreline.
- -Heald Bank, along with other sand banks along the Texas coast, is likely a marine sand bank developed above the transgressive ravinement from re-worked material after the shoreline shifted before 8.5 ka. The development of this marine sand body possibly began in connection with ebb-tidal delta deposits and is not a remnant or drowned barrier island.
- -The Holocene estuary was stable for approximately 2 kyr (~6.9–8.8 ka), during which time the environment experienced minor, but noticeable, perturbations likely due to lateral variations in tidal inlets or partial collapse of barrier systems.
- -Probable washover sediments in multiple cores approximate the location of barrier islands as they migrated landward at ~7–6.7 ka and after ~4.3 ka. The lack of data between our study area and the modern shoreline precludes our ability to map the migration of the barrier system beyond these approximations.
- -Environmental changes within the Holocene estuary coincide with or follow glacial meltwater events from the LIS, with a majority of changes in the estuary occurring during the phase of more accelerated sea-level rise in the early Holocene. As the rate sea-level rise began to slow due to the final deglaciation of the LIS, additional probable regional hydroclimate forcing affecting the sediment supply resulted in continued environmental change shifting the estuary landward to its modern location.
- -All cores in the study area contain minimal modern seafloor sediments likely due to erosion from the transgressive ravinement and re-working of sediment from ocean currents contributing to the Texas Mud Blanket.

**Table 5.1. Core locations and depositional environments**

Core	Latitude	Longitude	Depositional Environments
PC-2	29.2092	94.6371	Shelf; outer, central and upper bay; fluvial
PC-4	29.1854	94.6503	Shelf; outer, central and upper bay; Beaumont
GC-1	29.099	-94.610	Shelf; Pleistocene terrace
GC-2	29.140	-94.534	Shelf; outer bay; flood-tide delta
GC-4	29.150	-94.649	Shelf; outer, central and upper bay
GC-5	29.161	-94.637	Shelf; outer, and central bay
GC-6	29.220	-94.588	Shelf; outer, and central bay

**Table 5.2. List of radiocarbon dating samples and their calibrated ages**

No.	NOSAMS OS No.	Sample	Type	Process	Calibrated Age (yr)	Error ( $\pm$ yr)
1	155814	PC-2-S3-7-8.5	Mollusc	Hydrolysis	7,441	127
2	152146	PC-2-S3-82-83.5	Mollusc	Hydrolysis	7,800	134
3	152138	PC-2-S2-69.5-71	Mollusc	Hydrolysis	8,468	135
4	152145	PC-2-S2-100.5-102	Mollusc	Hydrolysis	8,815	175
5	155815	PC-2-S1-14-16	Mollusc	Hydrolysis	9380	133
6	155816	PC-2-S1-23-25	Mollusc	Hydrolysis	9,420	124
7	155817	PC-2-S1-102-104	Mollusc	Hydrolysis	9,794	215
8	155818	PC-4-S3-58.5-60	Mollusc	Hydrolysis	7,787	136
9	152148	PC-4-S3-59	Mollusc	Hydrolysis	41,030	1,703
10	155819	PC-4-S2-15-16.5	Mollusc	Hydrolysis	8,815	175
11	152147	PC-4-S2-94-96	Mollusc	Hydrolysis	9,131	158
12	155820	GC-1-S1-4-6	Foraminifera	Hydrolysis	1,753	143
13	152314	GC-1-S1-5-6	Mollusc	Hydrolysis	589	97
14	152315	GC-1-S1-28.5-30	Foraminifera	Hydrolysis	38,081	1,833
15	155821	GC-2-S1-A-59-61	Mollusc	Hydrolysis	6,973	170
16	152310	GC-2-S2-144-145	Mollusc	Hydrolysis	8,445	135
17	152316	GC-2-S3-6-10	Mollusc	Hydrolysis	8,546	173
18	155902	GC-4-S1-55.5-56.5	Charcoal	Combustion	7,913	255
19	152149	GC-4-S2-13-13.5	Charcoal	Combustion	7,977	221
20	155903	GC-4-S3-120-122	Charcoal	Combustion	8,470	144
21	155822	GC-5-S2-3-5	Mollusc	Hydrolysis	6,661	169
22	155823	GC-5-S3-32-37.5	Mollusc	Hydrolysis	8,445	135
23	155824	GC-5-S3-74-76	Mollusc	Hydrolysis	8,467	130
24	155825	GC-6-S1-11-14	Mollusc	Hydrolysis	>Modern	
25	155826	GC-6-S1-64.5-66	Mollusc	Hydrolysis	4,329	165
26	157505	GC-6-S1-111.5-113	Mollusc	Hydrolysis	7,760	142
27	157506	GC-6-S1-130-131.5	Mollusc	Hydrolysis	7,709	147
28	157511	GC-6-S2-71-72.5	Mollusc	Hydrolysis	8,367	181

## 6 Deltaic Stratigraphy

This chapter is excerpted from Swartz et al. (2022).

### 6.1 Introduction

Alluvial rivers are dynamic sedimentary systems that adjust to external forcings and internal processes in ways that are not completely understood. In particular, how fluvial morphodynamics and sedimentation respond to base-level rise is an important topic for both predicting evolution of coastal systems under rising seas as well as interpreting the rock record (e.g., Blum and Tornqvist, 2000; Cattaneo and Steel, 2002; Jerolmack, 2009; Miall 2014). Some of the most complete records of fluvial and coastal evolution during periods of sea-level fall and rise are found in incised valleys: stratigraphic features generated by fluvial incision and commonly filled by transgressive fluvio-deltaic and coastal deposition (e.g., Anderson et al., 2014; Reijnen et al., 2011; Nordfjord et al., 2005; Zaitlin et al., 1994). Study of the Holocene fluvial record has helped develop commonly-applied models of river and delta transgression and back-stepping, in part due to the comparatively well-constrained rates of relative sea-level rise in this period (Anderson et al., 2016; Milliken et al., 2008; Moran et al., 2017). Additionally, sedimentary deposits of these Holocene rivers have recently come under increasing focus as potential sources of large quantities of sand and other sediments useful to coastal nourishment and resiliency projects as traditional sources disappear (e.g., Sutherland et al., 2017; Torres et al., 2017). The study of these Holocene systems therefore can help address both coastal evolution and fluvial dynamics in the face of increasing rates of sea-level rise while also unlocking the potential of their stratigraphy to aid in coastal restoration.

Lowland rivers experience a transition from uniform to varying flow conditions, or a backwater, as they approach the coast (e.g., Chatanantavet et al., 2012; Hoyal and Sheets, 2009; Lamb et al., 2012). On the modern Trinity River this interval is correlated with significant changes in geomorphology and sediment transport, including decreased lateral migration rates, downstream sediment fining, and a reduction in point bar area (Smith and Mohrig, 2017; Mason and Mohrig, 2018). Similar behavior is observed in a number of other alluvial rivers, including the Mississippi (Hudson and Kesel, 2000; Nittrouer et al., 2012). The onset of backwater hydraulics has also been proposed as a primary control on the location of distributary channel avulsions and thus predict overall patterns of fluvial-deltaic deposition (e.g., Ganti et al., 2014; Jerolmack and Swenson, 2007; Moodie et al., 2019; Zheng et al., 2019). Though many studies have shown the link between in-channel fluvial aggradation and base-level rise, the details of how the overall fluvial system adjusts are less clear (e.g., Mackin, 1948; Leopold and Bull, 1979). Due to the link between fluvial morphodynamics and the backwater zone, which is, in turn, a function of distance to the river mouth, an expectation emerges that fluvial systems should not simply aggrade, back-step and transgress, while maintaining constant morphology and dynamics. Rather these systems undergo a change in sediment transport and resulting geomorphology that leads to different depositional architecture (e.g., Fernandes et al., 2016; Moran et al., 2017; Trower et al., 2018).

To provide a more detailed characterization of the morphologic changes associated with the fluvial to deltaic transition, we focus on the Trinity incised valley offshore east Texas in the Gulf of Mexico (**Figure 6.1**; Anderson et al., 2016). This system has a well-developed stratigraphic framework that provides detailed characterization of lithology, age, and depositional paleoenvironments. However, earlier geophysical methodologies lacked the necessary resolution to accurately characterize the fine-scale stratigraphic architecture of the observed transitions and fully capture the adjustment and evolution of the fluvial system during relative sea-level rise (Thomas and Anderson, 2004). Here we revisit the Trinity incised valley and use a dense survey grid of high-resolution chirp reflection data, 3D seismic imaging, cores and digitized archival lithologic records. Using these data, we investigate the shallow stratigraphy

corresponding with the Holocene transgression and delineate several seismic units corresponding with periods of dominantly fluvial, deltaic, and estuarine deposition. We also detail the potential paleogeomorphology of the Trinity valley using 3D seismic surface extractions. This work demonstrates the evolution of the paleo-Trinity River from a laterally migrating meandering system that formed the incised valley to a system dominated by vertical aggradation and floodplain building as the system transitioned from terrestrial to more estuary-like conditions in the face of environmental change. Finally, we examine these transitions in the context of the geomorphic adjustment of fluvial systems to base-level. Additional papers from this project explore the estuarine section's stratigraphic (Burstein et al., 2021) and paleoenvironmental (Standing et al., 2021) evolution in detail.

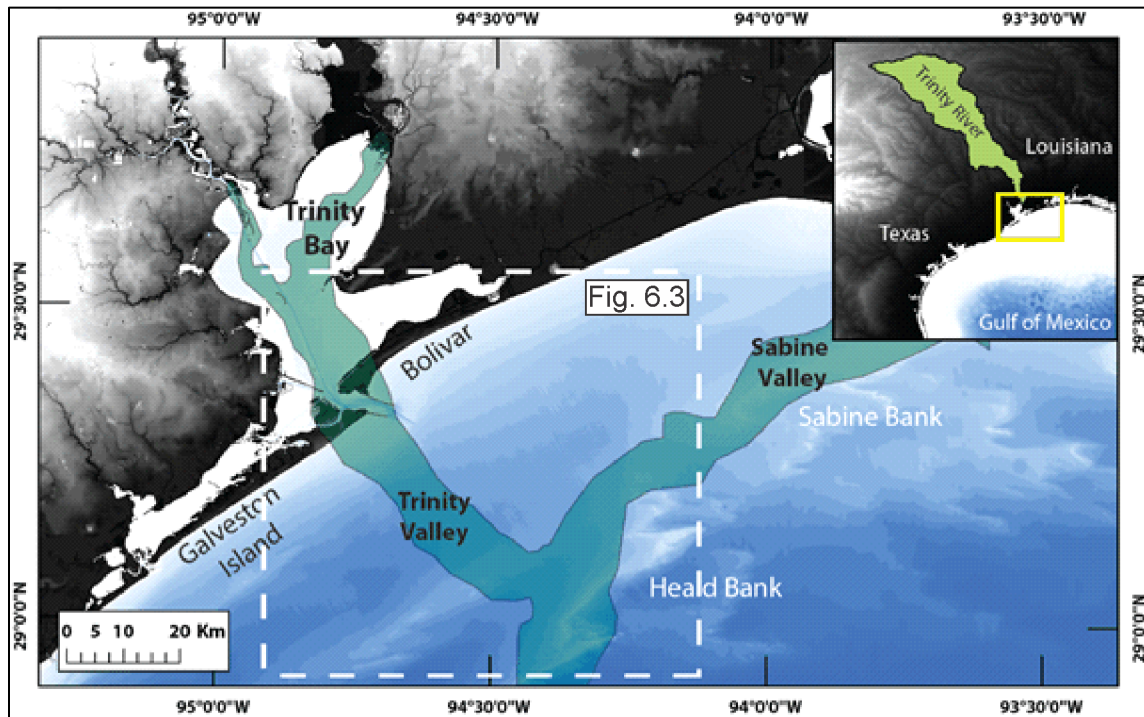


**Figure 6.1. The east Texas inner continental shelf and Trinity incised valley**

Map of the study area. The shaded valley represents the previously determined extent of the Trinity and Sabine incised valley systems during MIS2. Inset panel shows location of study area within the northern Gulf of Mexico and the outline of the modern Trinity River drainage basin. MIS2: Marine Isotope Stage 2.

## 6.2 Study Area

The Trinity incised valley has been the focus of significant research over the past several decades, and as a result detailed maps and models of the valley sedimentary architecture and patterns and timing of shifts in depositional environment have been created primarily using geotechnical borings, sediment cores, and seismic datasets of varied frequency and resolution (e.g., Thomas and Anderson, 1994; Rodriguez et al., 2005; Anderson et al., 2008; **Figure 6.1**). The majority of this work has focused on understanding the overall evolution of the Trinity valley and surrounding east Texas continental shelf from previous sea-level highstands to the present (Anderson et al., 2016). The Trinity incised valley began forming during sea-level fall from marine isotope stage (MIS) 5–3 wherein it extended from the modern-day Galveston Bay across the continental shelf (Thomas and Anderson, 1994; **Figure 6.2**). It reached its maximum shelf edge location during the last lowstand (MIS 2) at 22–17 ka bp and the associated erosion produced a

significant, regionally correlatable erosional surface (Simms et al., 2007). Total relief of the valley surface has been measured at 30–40 m across the shelf, although due to subsequent infilling it only exists offshore as a stratigraphic feature entirely buried beneath the modern seafloor (Thomas and Anderson, 1994).

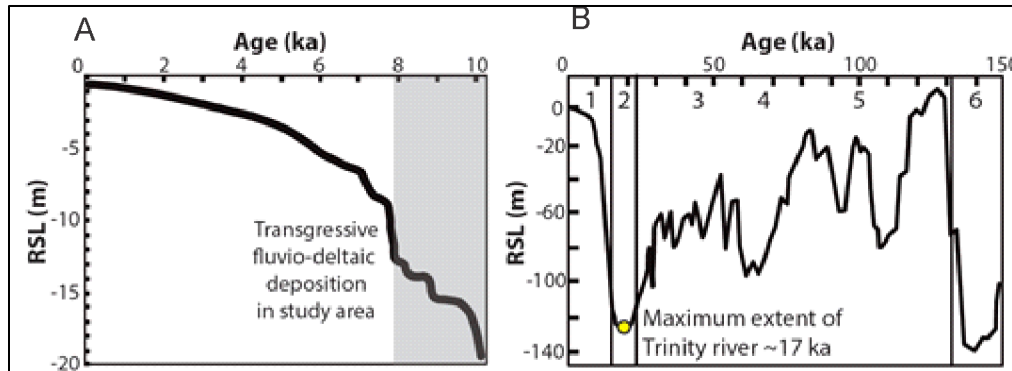


**Figure 6.2. Holocene and last ~150 ka sea level curves**

A) Composite sea level curve for the study area (modified from Milliken et al., 2008). The grey area represents the previously determined period of fluvial/deltaic sedimentation prior to transgression and onset of estuarine conditions (Anderson et al., 2016). B) Eustatic sea-level curve modified from Shackleton (2000). Marine Isotope Stages (MIS) 1–6 are labeled. The yellow dot indicates when the paleo-Trinity river reached its maximum shelf-edge location at ~17 ka (Thomas and Anderson, 1994).

Sea-level rise following the MIS2 lowstand triggered aggradation and valley filling across the continental shelf for the Trinity and other Gulf of Mexico fluvial systems (Anderson et al., 2016). Despite the rapid rates of sea-level rise between ~17 ka and ~10 ka the Trinity system maintained a shelf-edge delta until at least ~14 ka before beginning to transgress towards its modern position (Wellner et al., 2004). The record of Holocene sea-level rise in the Gulf of Mexico is relatively well constrained, and captures the transition from relatively rapid rates of 4.2 mm/yr from 12 ka to 1.4 mm/yr at 7.9 ka (Milliken et al., 2008; **Figure 6.2**). From ~10 ka onward the Trinity valley was filled by a series of landward stepping transgressive depositional packages interpreted as successions of fluvial, deltaic, bay, and tidal deposits (Rodriguez et al., 2005; Thomas and Anderson, 1994; **Figure 6.3**). The relatively rapid transition from fluvial deposition to deltaic and estuarine, as well as the back-stepping nature of the deposits towards the modern Trinity delta, has been interpreted as due to the episodic nature of early Holocene sea-level rise, or alternatively due to differential flooding of antecedent topography (Anderson et al., 2008; Rodriguez et al., 2005; Simms and Rodriguez, 2014; Thomas and Anderson, 1994; **Figure 6.2a**). Additionally, the pattern of back-stepping as well as the presence of the modern Galveston Bay throughout the Holocene implies that sediment supply of the Holocene Trinity River was unable to keep up with rates of base-level rise, in contrast to several other Gulf of Mexico rivers (Simms et al., 2006; Anderson et al., 2016).

The stratigraphic architecture of the Trinity valley has been previously interpreted on a broad scale through a combination of cores and geophysical data (**Figure 6.3**; Anderson et al., 2016; Rodriguez et al., 2005; Thomas and Anderson, 1994). The following framework is that built by Thomas (1991). The broad erosional valley base in the study area is located ~30m below the modern seafloor, and is immediately overlain by a 10–15 m thick package of gravels, sands, interbedded silts and clays as well as dense peats and vegetation lenses. This basal unit has been interpreted to represent an amalgamated package of fluvial sands and floodplain sediments deposited during the early Holocene transgression, with some radiocarbon dating indicating the upper portions were deposited as recently as 10.3 kyr bp. Thomas (1991) also noted that the top of this unit is commonly associated with seismic blanking and little acoustic penetration which is a potential signature of coarsegrained material and/or shallow biogenic gas accumulation along

lithologic contacts. Above this unit is a 5–15 m section of interbedded sand, mud, and silt that micropaleontological analyses indicates is comprised of floodplain, deltaic and upper bay sediments, with deposition occurring between 8–10 ka bp. The final unit sees a transition to more open bay or estuarine conditions, and in portions of the study area significant scours associated with flood-tide delta deposits (Anderson et al., 2016; Thomas, 1991). Thomas and Anderson (1994) proposed this succession of units as representative of the overall transgressive sequence, with relatively constant fluvial conditions and backstepping driven by relative sea-level rise rather than aggradation or changes in fluvial dynamics (Figure 6.3).

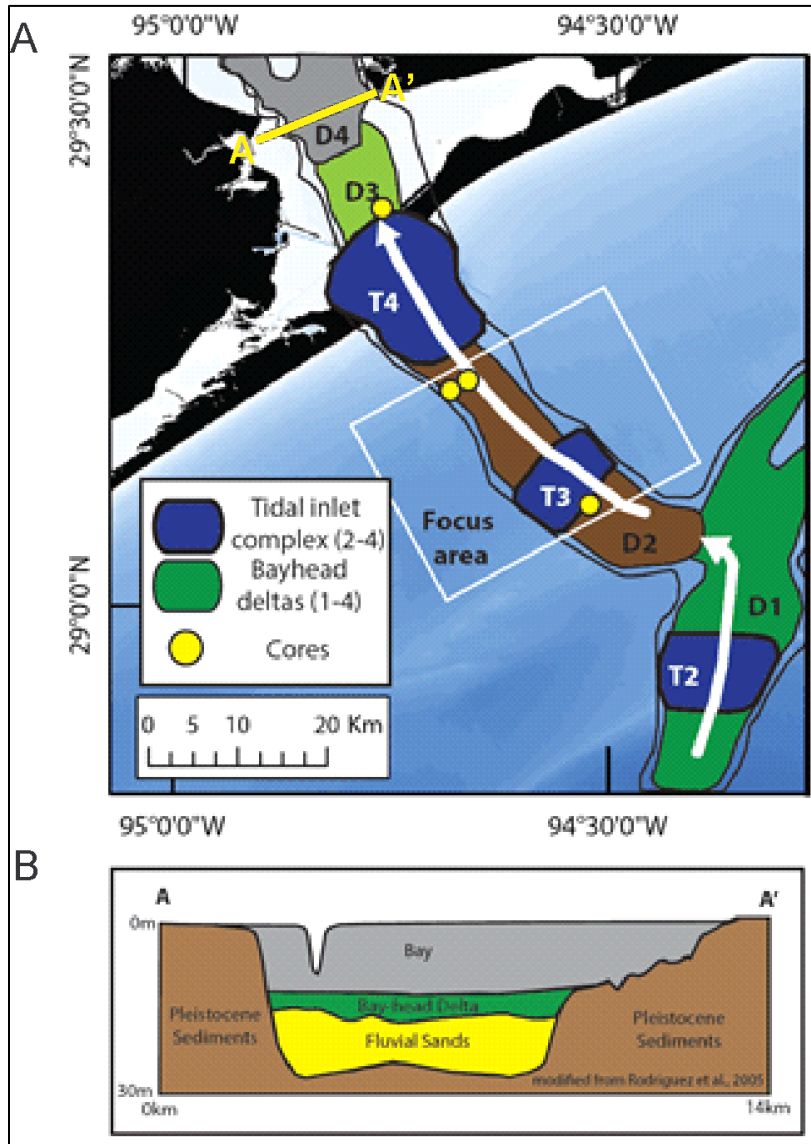


**Figure 6.3. Transgressive depositional sequences of the Trinity valley**

A) Map of backstepping bayhead deltas and associated tidal inlets infilling the Trinity incised valley during the Holocene transgression (modified from Anderson et al., 2016). The study area covers the interpreted delta 2 and tidal inlet complex 3, formed ~7–8 ka. B) Schematized cross section (A–A') showing typical stratigraphy of the incised valley fill.

### 6.3 Methods

We primarily use acoustic chirp subbottom and 3D seismic data in this study. Over ~1000 km of 2D chirp have been collected by the University of Texas Institute for Geophysics (UTIG) over the eastern Gulf of Mexico shelf as part of ongoing sand resource assessment work for the Bureau of Ocean and Energy Management (BOEM) as well as summer field courses (**Figure 6.4**). The main survey consists of 45 15-km long, parallel lines oriented perpendicular to modern seafloor dip and spaced at 200–300 m intervals, forming a survey area of ~175 km<sup>2</sup> (**Figure 6.4**). Chirp data were collected using an Edgetech 512i sub-bottom profiler, configured with a 20 ms, 0.7–12 kHz swept-frequency pulse. The full-waveform output was recorded for each survey, which allows for wavelet-based (seismic) processing and maximum sub-surface resolution (Goff et al., 2015). These full waveform chirp data were processed using Paradigm Echos and the workflow included tide and tow depth corrections, secondary deconvolution, heave removal, and trace equalization (Saustrup et al., 2019). This workflow provides both a high-resolution, full waveform dataset that can be interpreted at nearly decimeter scale resolution, as well as a more conventional envelope dataset which in this case has benefitted from seismic processing steps above and is useful for more regional interpretations (Saustrup et al., 2019; **Figure 6.5**). An additional ~250 km of chirp lines collected by Texas A&M Galveston (TAMUG) and the U.S. Geological Survey (USGS) within the study area were obtained and the chirp datasets partially re-processed, although due to the lack of the original raw output only the re-processed envelope chirp are available. Seismic stratigraphic interpretations were performed using Petrel 2016 and Landmark DecisionSpace Desktop. Chirp interpretation relied on the recognition of distinct seismic horizons that either act as regional unconformities and/or conformable surfaces that separate seismic units: packages of reflectors that represent related stratigraphy (Reijenstein et al., 2011). When appropriate, approximate depths and thicknesses were converted from two-way travel time in milliseconds to meters using an average velocity of 1525 m/s (Abdulah et al., 2004). Interpretation of environment and depositional processes within each unit relies on identification of smaller scale geometries, amplitudes, and reflector continuity (e.g., Liu et al., 2017; Reijenstein et al., 2011).

Seismic surveys collected in the Gulf of Mexico by the energy industry enter the public domain following a 25-year exclusive window. Recently, sets of early 3D surveys on the continental shelf have begun to be publicly released by the BOEM and the USGS. A 3D seismic survey, B-12-93-TX, collected by Shell Offshore in 1993 has a 750 km<sup>2</sup> footprint covering a significant portion of the study area (**Figure 6.4**). This survey was acquired with a 30 m line spacing, 30 m common depth point (CDP) spacing, and a 4 ms sampling interval. The resulting data were processed and time migrated, although details of this processing are not available. The average frequency content of the survey within the upper 100 ms is approximately 25 Hz (**Figures 6.5, 6.6**). The survey was imported into Petrel 2016 and a crossline filter of 90 m (or three lines) applied to the data volume. This smooths, but does not eliminate, striping artifacts present within the upper 500 ms of the data volume that are a result of the acquisition footprint.

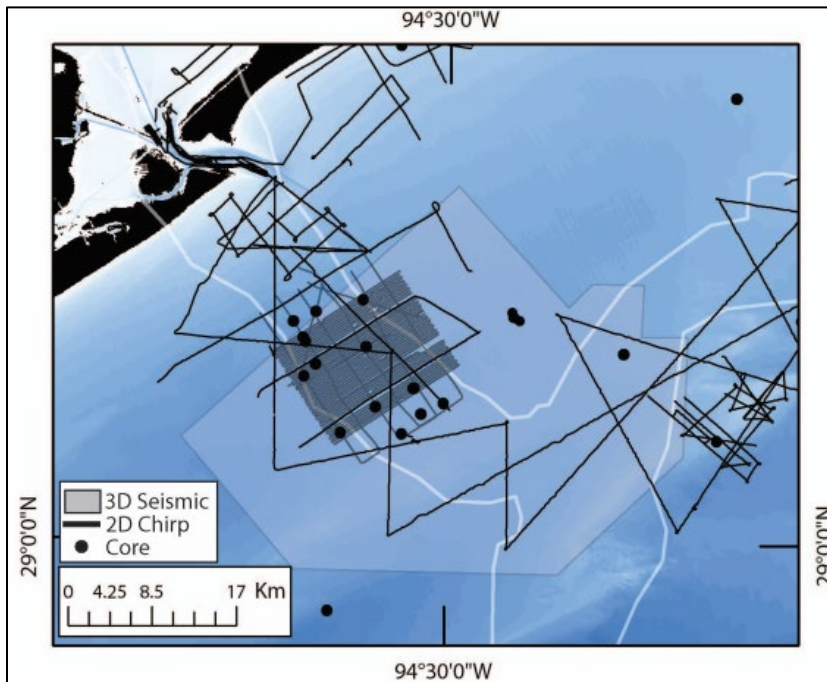


**Figure 6.4. Data coverage of the Trinity incised valley**

Map of available seismic and geologic data for the study area. Black lines represent chirp geophysical data while black dots represent cores acquired as part of this study or digitized from previous reports, literature, or archives. The grey shaded region represents the footprint of an industry 3D seismic survey.

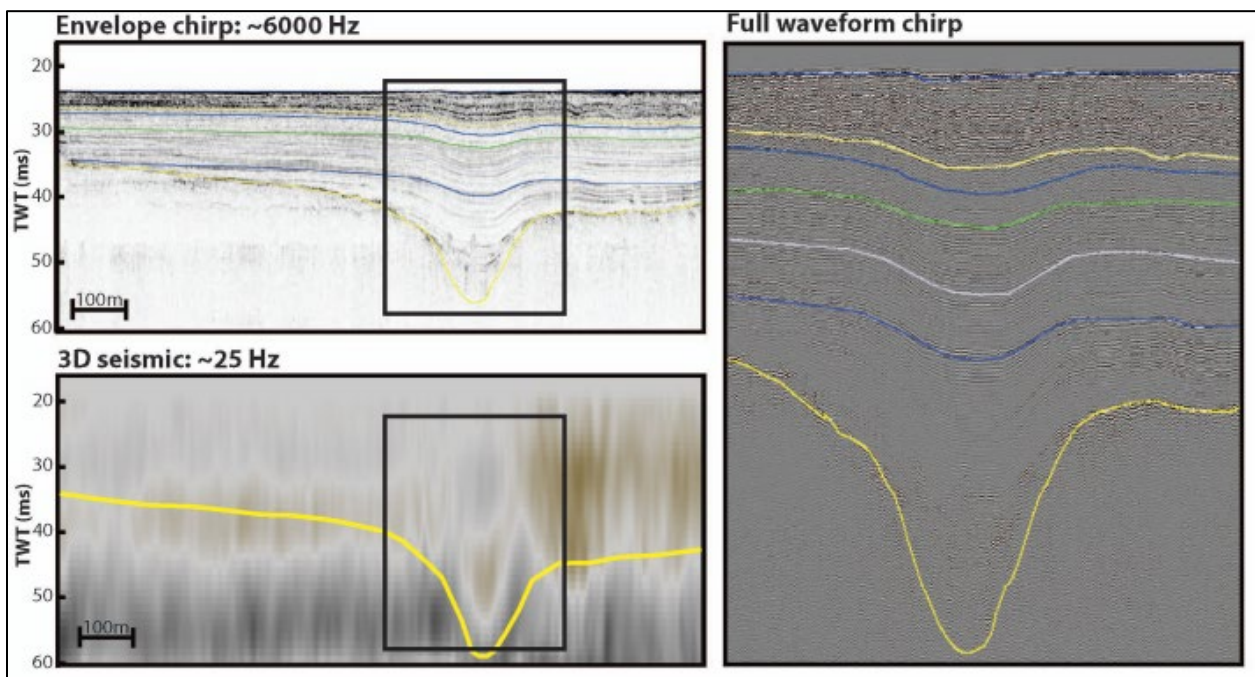


**Figure 6.5. Comparison of seismic data types and resolutions**

Comparison of envelope chirp, full waveform chirp, and 3D seismic crossline resolution for the same location. A set of arbitrary reflections are shown on chirp lines to illustrate high-resolution nature of chirp data. The same yellow horizon is shown on the chirp and 3D seismic to show the difference in vertical resolution and reflector discrimination.

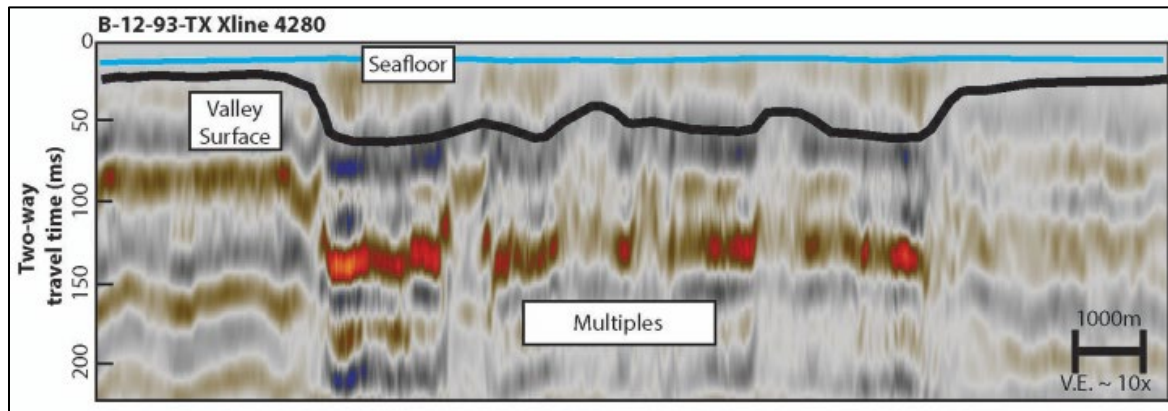


**Figure 6.6. 3D seismic crossline of the Trinity incised valley**

Example crossline from 3D seismic survey showing the appearance of the valley unconformity at ~40–65 ms. The valley surface depth was estimated from published depths as well as appearance in chirp data. Note the significant multiples and acoustic ringing below the valley compared to outside the valley.

Seismic morphology of the Trinity incised valley was analyzed by identification and mapping of a shallow, regionally conformable horizon located between 40–60 ms and the computation of trace attributes (**Figure 6.6**). This value was chosen based on published values of the depth to the valley bottom as well as the approximate depth of the basal layer present within our chirp stratigraphy (**Figure 6.6**; Thomas and Anderson, 1994). The low frequency content of the survey means that any single wavelet, or reflector, is over 20 ms thick (**Figure 6.5 and Figure 6.6**). We map the upper portion of the reflector throughout the entire volume and then calculate a 20 ms envelope median coherency along this horizon. This attribute enhances trace discontinuity present within a given window, and as applied here helps identify anomalous amplitudes that often correspond to channel bodies and other geomorphic elements (e.g., Calves et al., 2008; Reijnenstein et al., 2011). The resulting image allows for qualitative analysis of morphology present within the mapped interval (**Figure 6.7**). Due to the low 3D seismic frequency, combined with the chosen time envelope, the resulting image is likely amalgamating a significant amount of vertical stratigraphy and is not a snapshot of a true geomorphic surface but rather a time-transgressive representation of the unit stratigraphy.

As part of a broader and ongoing BOEM-funded project assessing sand resources throughout the Gulf of Mexico all potential geological records such as cores, geotechnical surveys, shallow boreholes, and other potential datasets have been located, digitized, and archived. These include most of the original cores and geotechnical borings used in initial studies of Trinity incised valley, and notably include several that penetrate tens of meters through the base of the incised valley as well as provide radiocarbon age control for several key intervals (Rodriguez et al., 2005; Thomas and Anderson, 1994). We additionally collected a number of piston cores ranging from 2–6 m in penetration that help constrain the uppermost shelf stratigraphy (**Figure 6.4**). These geologic records are used to help constrain lithology, depositional environment, and potential depositional age.

## 6.4 Results and Interpretation

Three regionally extensive surfaces (H1–H3) were identified and mapped throughout the Trinity incised valley stratigraphy (Figures 6.8–6.13). These surfaces were tied to available piston core and platform borings that provide lithology and paleo-environmental interpretation. These surfaces are found to correlate to previously identified and interpreted contacts between dominantly fluvial, deltaic, and estuarine depositional units (Thomas and Anderson, 1994).

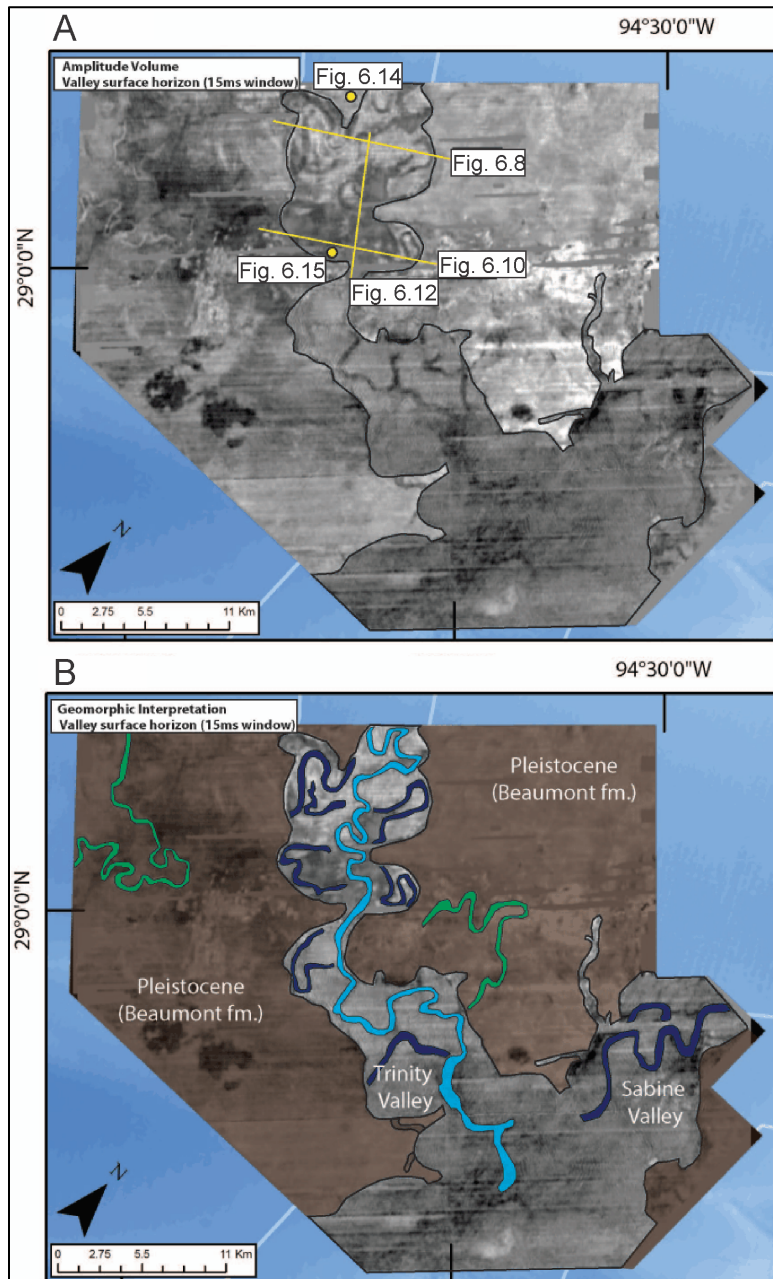


**Figure 6.7. 3D attribute extract of valley surface horizon**

A) Amplitude attribute computed for 3D seismic volume and extracted in a 15 ms window along the mapped valley surface horizon. Note the appearance of multiple potential geomorphic and stratigraphic elements and the chirp lines

in Figures 6.8, 6.10, and 6.12. Figures 6.14 and 6.15 are the locations of core and platform borings used to constrain depositional environment and lithology. B) Interpretation of potential morphological and structural elements present at the valley surface depth. The valley edges are well imaged, as are numerous sinuous channel forms both within and outside of the valley.

Horizon H4 is observed only along the edges of the valley and is a steep unconformity that truncates layers outside the valley, whereas internal valley stratigraphy onlaps onto the horizon (Figures 6.8, 6.10). This horizon corresponds to the erosional unconformity defining the overall extent of the Trinity incised valley, although its base is not observable within the chirp dataset (Thomas, 1991; Rodriguez et al., 2005). The lowermost valley surface, horizon H3, is a varying amplitude reflector that commonly separates low-amplitude laminated seismic facies above from high-amplitude laterally accreting and chaotic reflectors or complete acoustic blanking below (Figures 6.8, 6.10, 6.12). For the majority of the study area, H3 forms a sharp acoustic contact, and the observed masking is characteristic of biogenic gas accumulation along a lithologic contact as observed previously within the Trinity valley and elsewhere (e.g., Rodriguez et al., 2005; Thomas and Anderson, 1994; Garcia-Gil et al., 2002). Where this acoustic blanking is not present lateral accretion surfaces and potential channel forms are observed. Based on its depth and acoustic character, H3 corresponds to the previously interpreted contact between coarse grained amalgamated fluvial sediments deposited during the lowstand and early transgression and initial deltaic deposition (Thomas and Anderson, 1994). H3 is consistently found at depths of 15–20 ms (12–16 m) below the seafloor across most of the study area, and locally shallows to depths of 5–8 ms (3–6 m) (Figure 6.14).

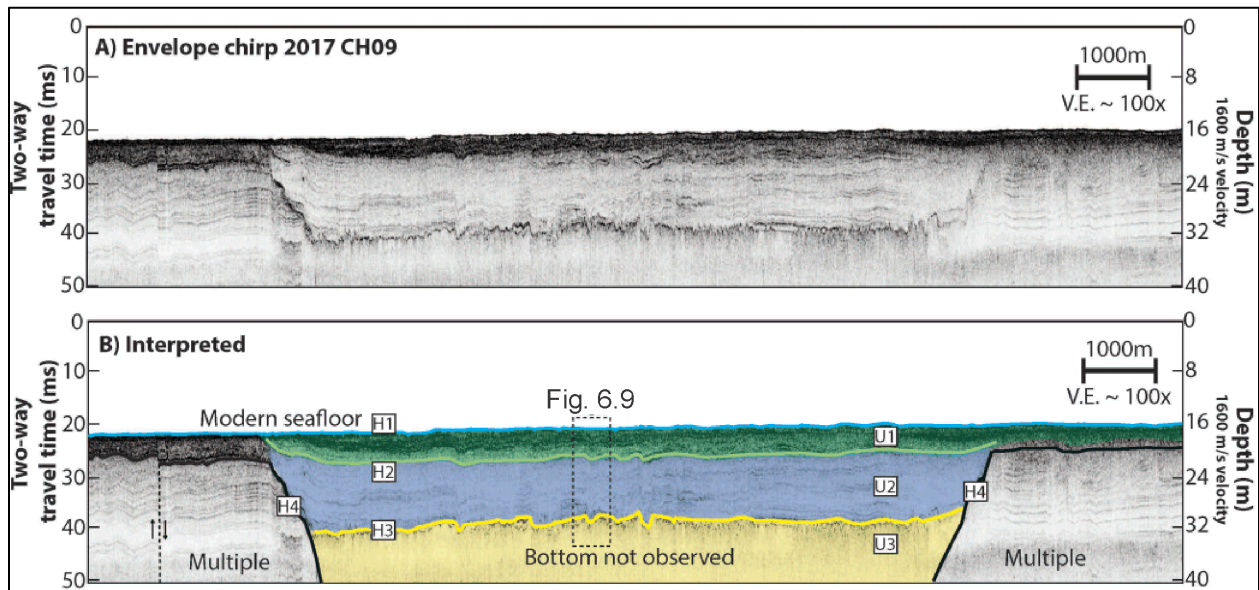


**Figure 6.8. Chirp strike line across the valley close at upper extent of study area**

A) Uninterpreted envelope chirp line across the valley at 100x vertical exaggeration. B) Interpreted envelope chirp with four key horizons (H1–H4) shown. H1 corresponds to the modern seafloor; H4 is the valley unconformity. Note that the base of the valley is not observed due to a combination of energy loss and acoustic blanking along the base of the valley.

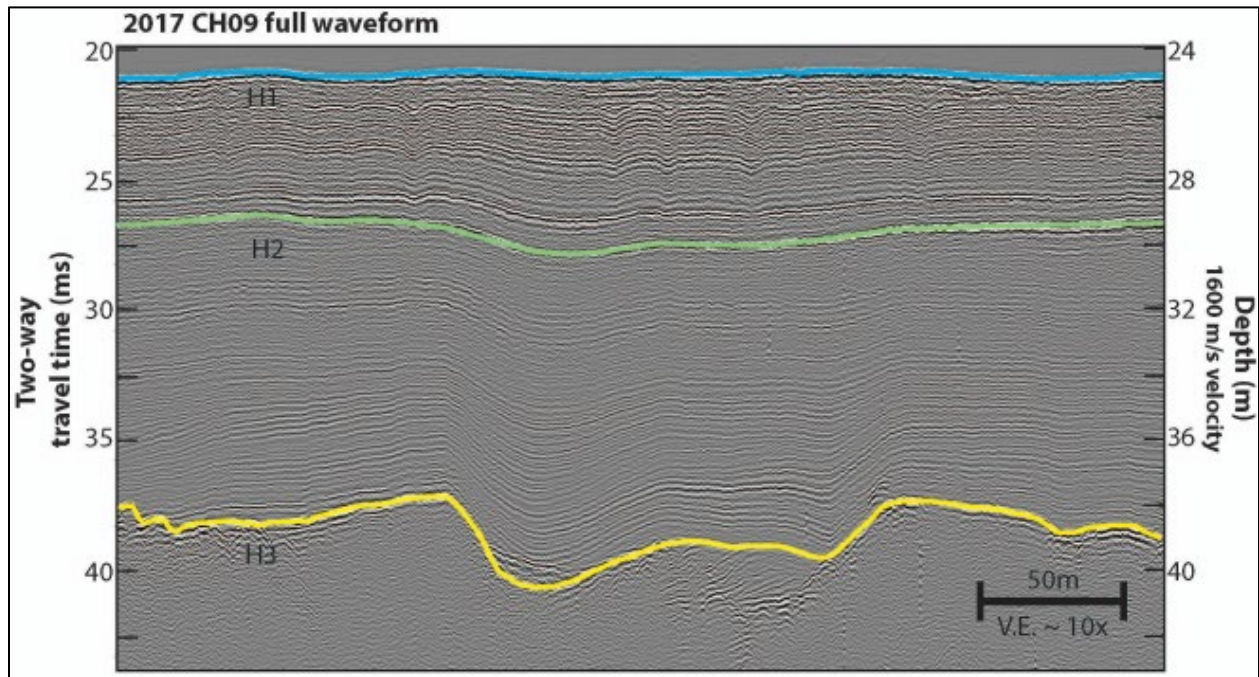


**Figure 6.9. Example of full waveform chirp imaging of valley stratigraphy from Figure 6.8**  
 Note the conformable, layered appearance of all layers above the basal layer H3

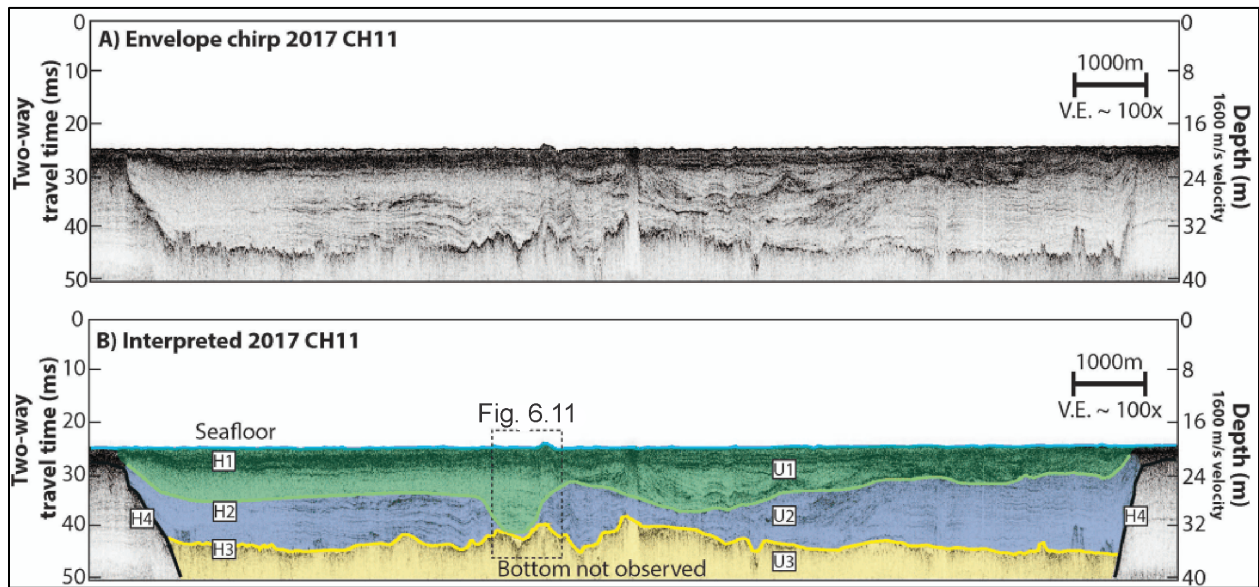


**Figure 6.10. Chirp strike line across the valley close at lower extent of study area**  
 A) Uninterpreted envelope chirp line across the valley at 100x vertical exaggeration. B) Interpreted envelope chirp with four key horizons (H1–H4) shown. Note the apparent relief and unconformable nature of horizon H3 compared to further up-valley.

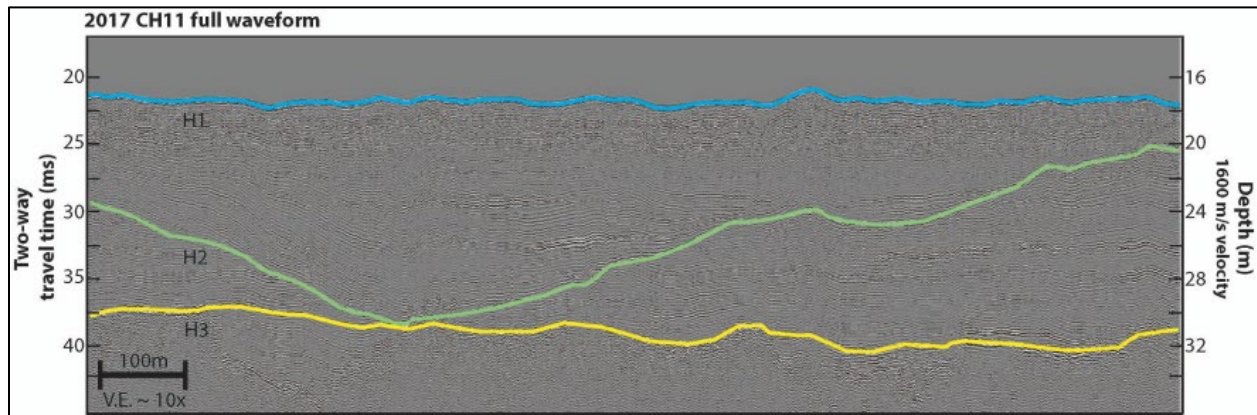


**Figure 6.11. Example of full waveform chirp imaging of valley stratigraphy from Figure 6.10** Significant scours and erosional surfaces are observed, with truncation of H4 and other lower layers.

Coring through these shallow intervals revealed that the acoustic contact is related to a sharp transition between silty, sandy clays, and very fine sands with trace deltaic or upper bay microfossils to barren well-sorted, oxidized sands (**Figure 6.14**). Additionally, in the lower valley H3 correlates with the previously interpreted boundary between floodplain deposits and delta sediments (**Figure 6.15**; Thomas and Anderson, 1994). The base of the valley is located ~10–15 m (~7–12 ms) below H3 and is not observed in the chirp data due to the inability of the acoustic signal of those frequencies to penetrate the fluvial sands (**Figures 6.8, 6.10, 6.12**). The acoustic character and correlation to the lithologic contact between potential fluvial material and delta deposits indicate that surface H3 represents the top of the amalgamated fluvial section. A structure map of H3 shows the presence of numerous deep and sinuous channel forms, lending support to the interpretation of H3 as a fluvial surface (**Figure 6.16**). The shallower intervals of H3 likely correspond to fluvial terraces previously observed within both offshore stratigraphy as well as in the modern Trinity River valley. This interpretation is supported by the lithology encountered in Piston Core 2 (PC-2) (**Figure 6.14**; Morton et al., 1996; Blum and Price, 1998; Rodriguez et al., 2005).

Horizon H2 is a varying amplitude reflector that separates low amplitude laminated seismic facies below from higher amplitude laminated facies above (**Figures 6.8, 6.10, 6.12**). H2 varies between 25 and 50 ms depth and is generally deeper to the south while shallowing along the valley edges and to the north (**Figure 6.16**). In the northern part of the study area, H2 appears sub-parallel and conformable with layers above and below, but towards the south it appears as a sharp unconformity significantly truncating lower stratigraphy while being alternatively draped or overlain by onlapping strata (**Figures 6.8, 6.10, 6.12**). Cores of these sediments consisted of very fine to fine sands, organic rich clays, and fine interbedded sandy clays with significant wood fragments and plant debris, whereas above horizon H2 there is a transition to more silty and sandy clays and less plant matter (**Figures 6.14, 6.15**; Thomas, 1991). The sediments below H2 were deposited in a deltaic or upper-bay environment, whereas above H2 there is a transition to middle bay or open estuarine conditions with less terrestrial input, according to paleo-environmental analysis of foraminiferal abundances (Thomas, 1991). The shallowest horizon, H1, is the modern seafloor (**Figures 6.8, 6.10, 6.12**). H1 varies between 20 and 25 ms depth, with a general dip to the southwest (**Figure 6.16**). Between H1 and H2 layers are typically sub-parallel and laminated in the northern portion of the valley, while to the south more onlapping configurations are observed (**Figures 6.12, 6.13**). The upper stratigraphic interval also includes widespread high-amplitude rugose or corrugated reflectors that appear to be small scale, low relief channel forms (**Figures 6.8, 6.10, 6.12**). The stratigraphy between H1 and H2 corresponds with the middle-bay or estuarine unit defined by Thomas (1991) and Rodriguez et al. (2005).

Together these horizons define the observed seismic units: U3 is the unit of fluvial deposition between H3 and H4, U2 is the deltaic unit between H2 and H3, and U1 is the final estuarine unit between H1 and H2 (Figures 6.16, 6.17). U1 is on average 10 ms, or ~7 meters, thick, but increases substantially to the south to 20 ms, or ~15 meters, corresponding with the deepest apparent erosion associated with H2 of the underlying strata (Figures 6.12, 6.16, 6.17). U2 is also 10 ms thick on average, but the pattern of deposition differs from U1. The thickest regions of U2 appear to correlate with the deepest portions of H3, or the top of the fluvial section (Figures 6.16, 6.17).

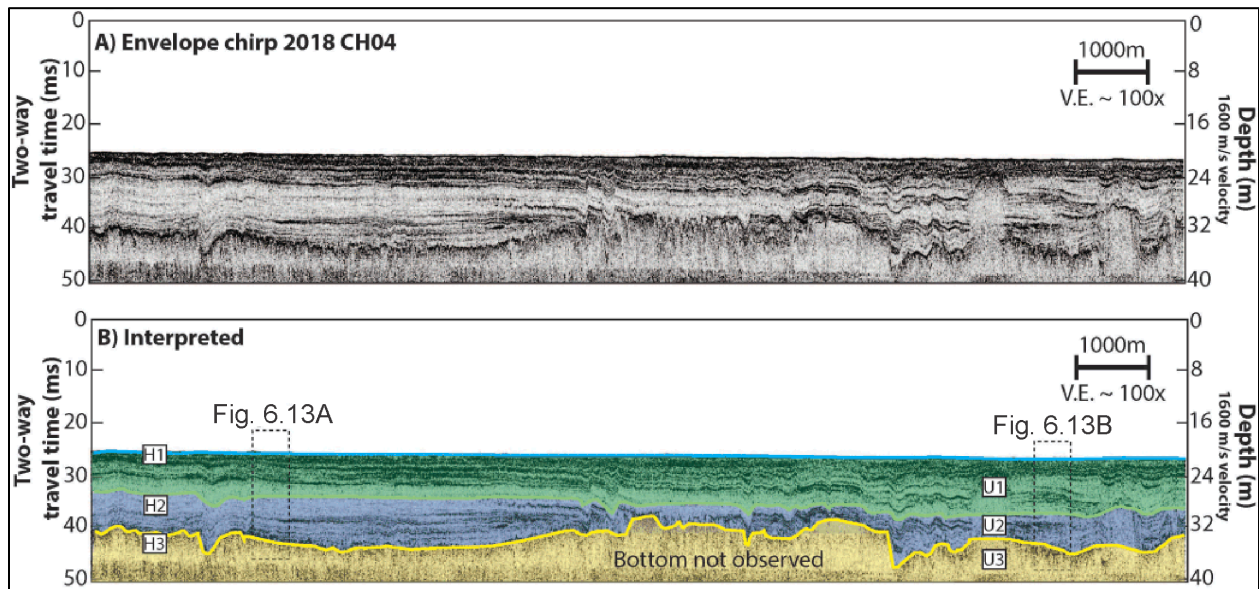


**Figure 6.12. Chirp dip line down center of the valley**

A) Uninterpreted envelope chirp down the valley axis at 100x vertical exaggeration. B) Interpreted envelope chirp with six key horizons (H1–H6) shown. Note the transition from conformable, sub-parallel layered stratigraphy upvalley to significant relief and erosional unconformities downvalley.

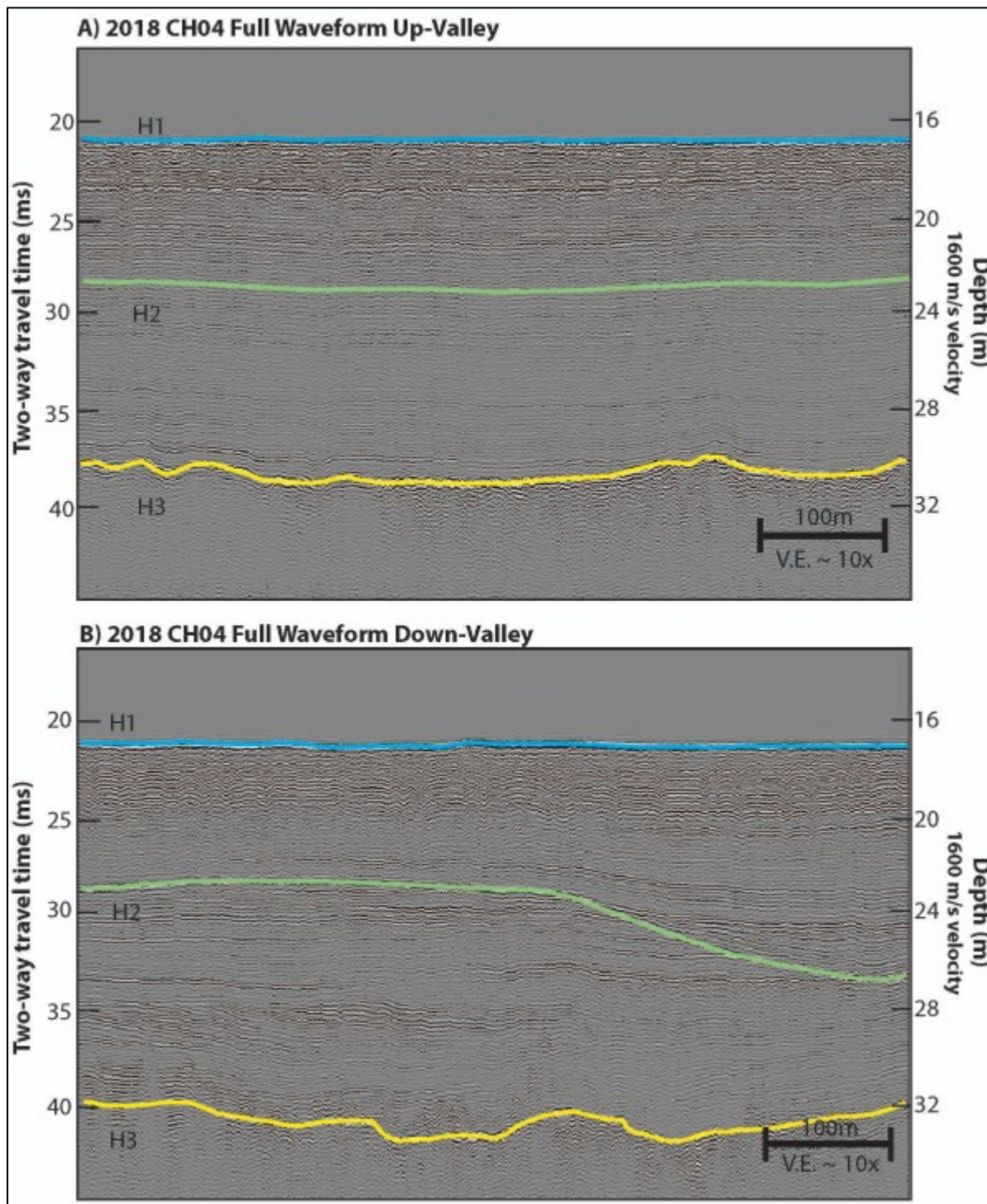


**Figure 6.13. Example of full waveform chirp imaging of valley stratigraphy from Figure 6.12**  
 A) Full waveform example of up valley stratigraphy showing conformable layers. B) Full waveform example down valley showing same horizons transitioning from conformable to unconformable and scouring out lower valley stratigraphy.

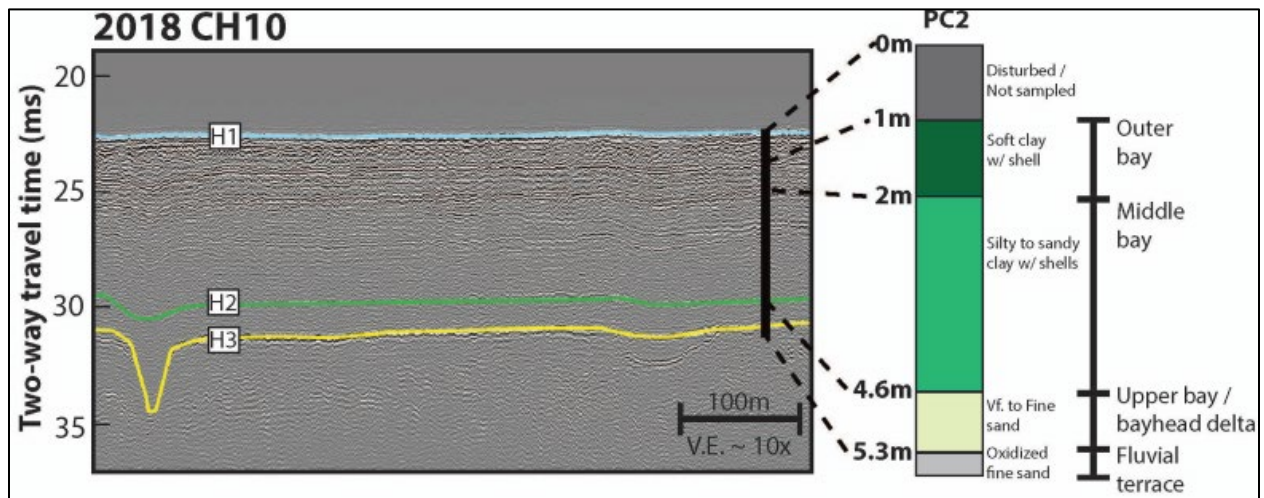


**Figure 6.14. Core penetrating top of fluvial terrace and correlation to full waveform chirp**

Piston core that penetrated the top of a fluvial terrace imaged in chirp. Paleo-environmental interpretation is based on relative abundance of foraminifera species. The majority of the core sampled H1–H2 which correlates to outer and middle bay, and a thin layer of upper bay and/or bay-head delta. The base of the core recovered oxidized sands with no forams, indicating terrestrial conditions.

## 6.5 Discussion

The characteristic backstepping stratigraphic architecture of fluvial, deltaic, and estuarine sediments within the Trinity incised valley have formed the basis of conceptual models of alluvial river response to relative sea-level rise (e.g., Blum and Tornqvist, 2000; Anderson et al., 2016). The specific fluvial sedimentation patterns that occur during an overall period of transgression are not as well constrained as the broader spatial patterns, however. Earlier interpretation of the Trinity valley stratigraphy implicitly included assumptions of relatively invariant fluvial form and morphodynamics along the entirety of the coastal reach, and that fluvial channels with insufficient sediment supply would be “flooded” by transgression and the resulting relict topography covered by more deltaic or estuarine sediments separated by a distinct flooding surface (e.g., Pearson et al., 1986; Thomas and Anderson, 1994; Zaitlin et al., 1994). In-channel aggradation because of base-level rise was held to be geologically instantaneous and would be overwhelmed by sufficient rates of relative sea-level rise (Thomas, 1991). We test these earlier interpretations using more advanced geophysical imaging techniques and place them in the context of recent advances in understanding of fluvial morphodynamic adjustment (e.g., Lentsch et al., 2009; Martin et al., 2009; Moran et al., 2017). We observe a broadly similar set of depositional units as in previous work but with significant differences in the internal architecture and associated formational processes.

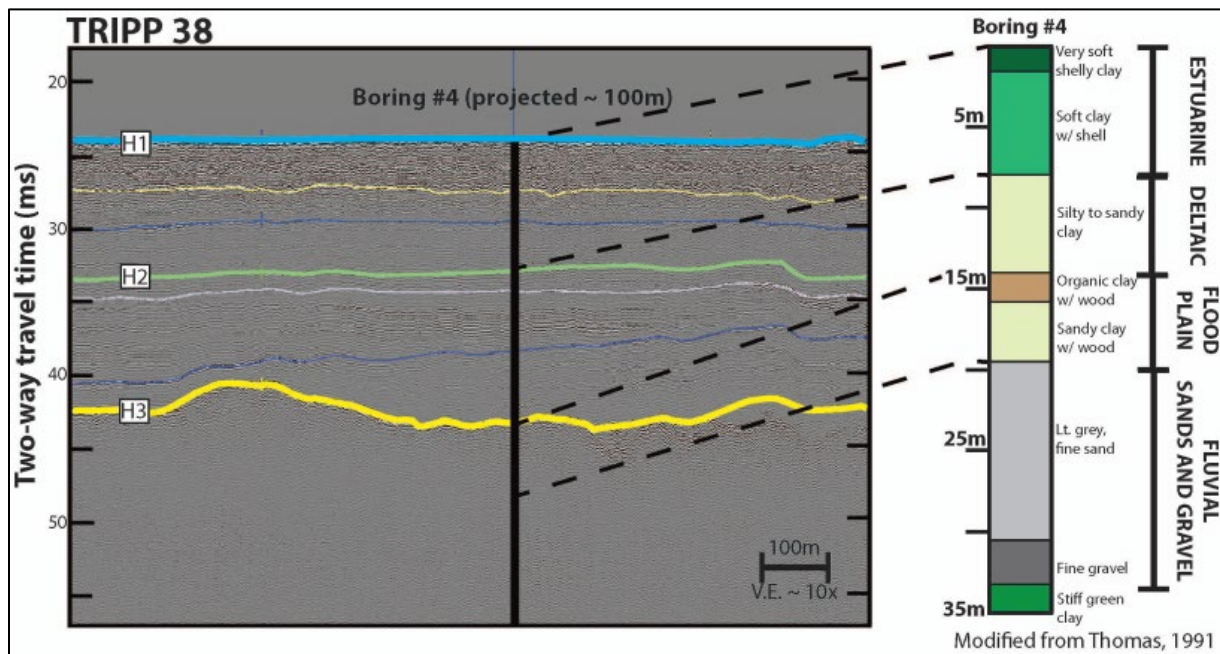


**Figure 6.15. Paleo-environments of valley fill stratigraphy based on core-full waveform chirp correlation**

Platform boring that penetrated entire Trinity valley stratigraphy. Lithology and interpreted environment from Thomas (1991) with correlation to mapped horizons. H2 correlates with the transition to estuarine from deltaic conditions. H3, or the top of the acoustically impenetrable package, correlates with the top of the floodplain/fluvial sediments.

Though the exact basal valley surface is hard to observe within either our 3D seismic dataset or the high-resolution chirp reflection data, the edges and overall valley extent are well-defined (Figures 6.7, 6.8, 6.10). Earlier work proposed that the lowermost unit contained within the valley corresponds to fluvial sediments deposited within the early to middle Holocene but lacked the necessary line density or resolution to observe specific morphological elements corresponding to the paleo-Trinity River (Thomas and Anderson, 1994; Rodriguez et al., 2005). Qualitative geomorphic interpretation of the 3D seismic interval associated with this fluvial unit shows the presence of numerous sinuous channel forms, lateral accretion surfaces forming potential point bar deposits, and shallow terraces (Figure 6.7). These elements are similar to those observed within modern alluvial river valleys including the Trinity as well as other incised valley systems investigated using 3D seismic (e.g., Morton et al., 1996; Reijenstein et al., 2011; Durkin et al., 2017). The overall valley extent appears to coincide with the maximum extent of the basal meander belt (Figures 6.7, 6.8, 6.10). This relationship potentially indicates that a large proportion of the overall valley stratigraphic form was created during the early Holocene transgression, rather than the period of downcutting and erosion during earlier sea-level fall (Anderson et al., 2016). The overall thickness of this unit as observed within cores and platform borings is on average 12 meters (Thomas and Anderson, 1994). This thickness is over twice the formational flow depth of the Trinity River and has been used to interpret the basal fluvial unit as representing a period of significant reworking and amalgamation due to avulsion and reworking by lateral migration (Moran et al., 2017). The variable acoustic facies of the fluvial unit, seismic morphology, and presence of a high percentage of sands and interbedded organic rich material support the interpretation of this unit as an amalgamated channel belt (e.g., Gibling, 2006). The total channel belt width varies between 6–10 km whereas the observed channel width of the paleo-Trinity within the chirp and 3D seismic is on roughly 100–200m leading to channel belt width to channel width ratios of 25–50. These ratios are higher than observed in other preserved and modern systems (e.g., Karssenbergh and Bridge, 2008; Fernandes et al., 2016). The overall thickness

of this basal unit has been interpreted as representing the total amount of Holocene fluvial aggradation within the valley before continued transgression (Thomas and Anderson, 1994; Moran et al., 2017).

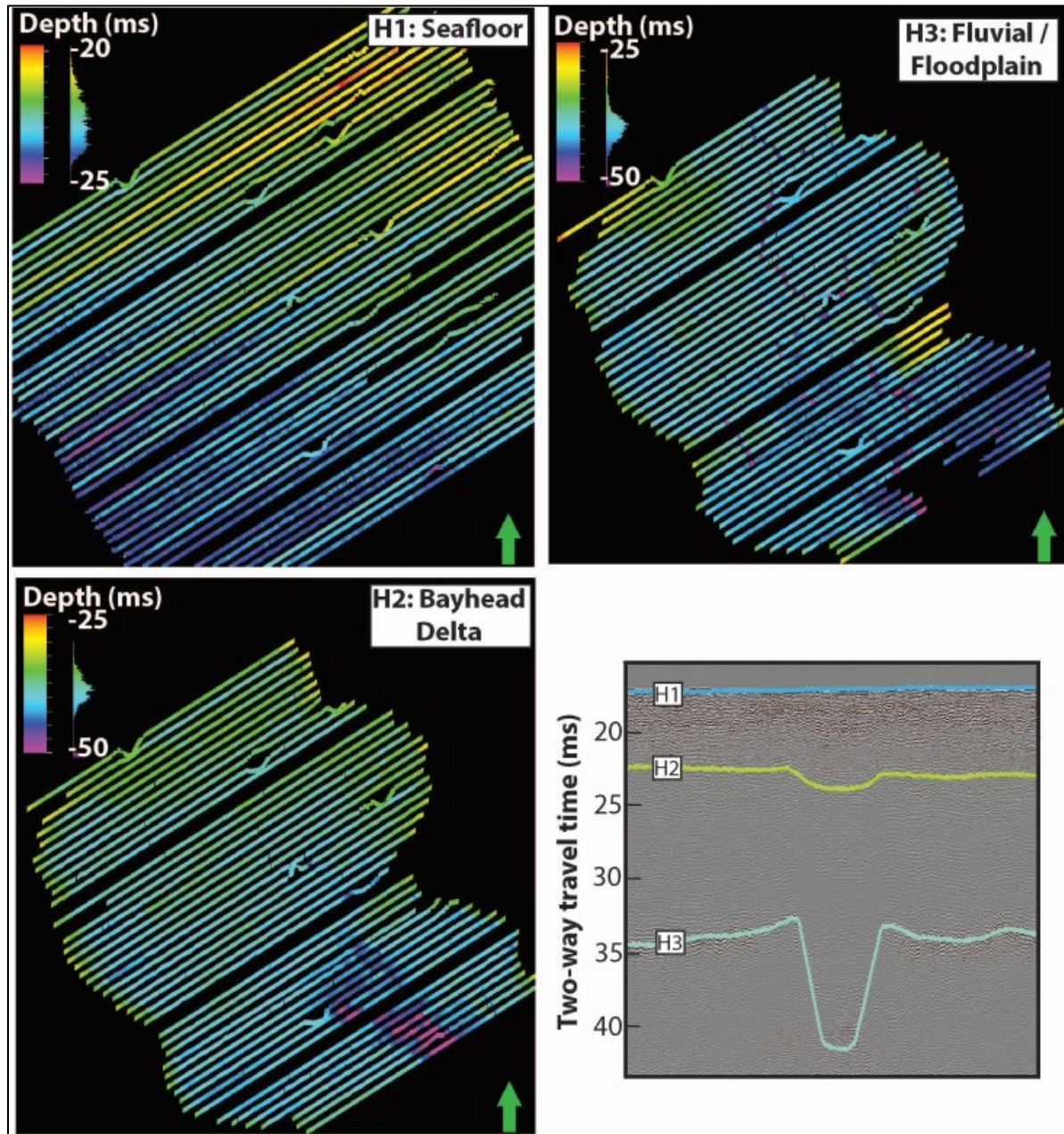


**Figure 6.16. Time structure maps of key horizons and example full waveform chirp line**

Time-structure mapping of H1, 2, and 3. Horizons are not interpolated between lines to preserve fine-scale details. Warm colors correspond to shallow depths, while cool colors are deeper. Paleo-environmental interpretations from Thomas and Anderson (1994) and this study. A) H1, or the modern seafloor. B) H2, or bayhead delta / upper bay. C) H3, or fluvial and/or floodplain. Note the appearance of numerous narrow, deep segments that form sinuous channel courses. D) Example full-waveform chirp line illustrating mapped horizons H1, 2, and 3.

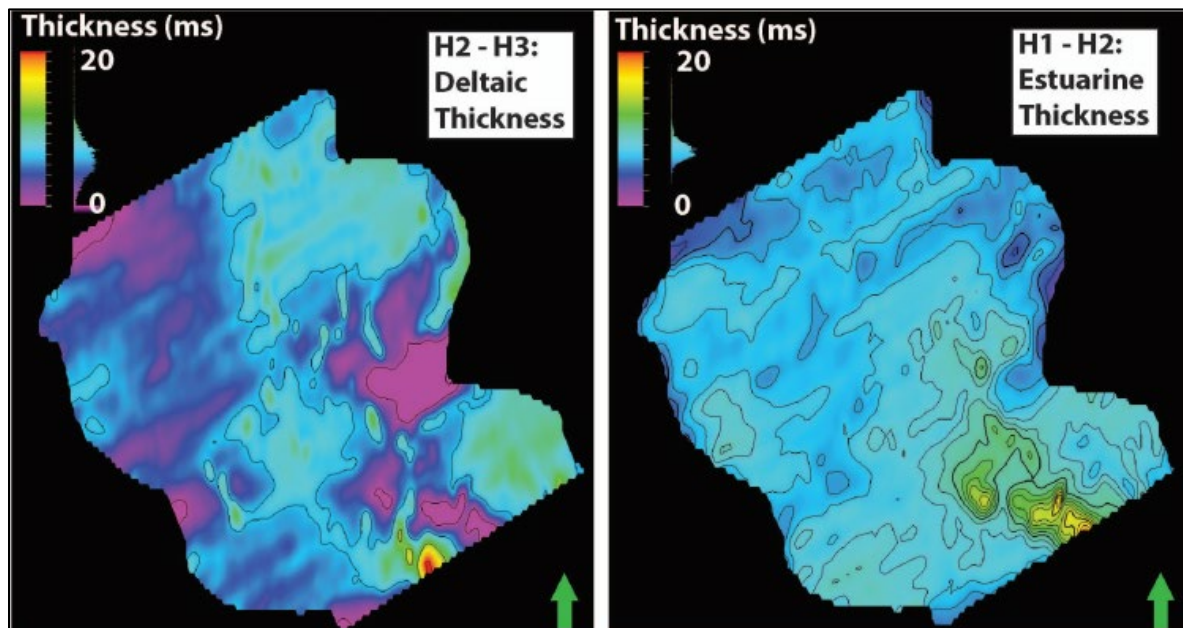


**Figure 6.17 Thickness maps (ms) of Trinity valley stratigraphy**

Time-thickness maps of key stratigraphic intervals: (A) Thickness of the estuarine (H1–H2), or U1, package, and (B) thickness of the deltaic (H2–H3), or U2, package.

Earlier work identified a flooding surface at the top of the basal channel belt marking the transition from fluvial to bay and deltaic conditions (Thomas and Anderson, 1994; Rodriguez et al., 2005). We do not observe such a sharp transition. Rather, the transition from fluvial to deltaic appears to coincide with a significant adjustment in channel behavior of the paleo-Trinity. Though the basal channel belt is time-transgressive and consists of numerous channel avulsions and reworked fluvial deposits, a potential “last” channel can be observed within the chirp structure map of horizon H3 (Figure 6.16). This channel likely corresponds to the position of the Trinity River at the fluvio-deltaic transition. Although the lines are separated by 200–300 m, a sinuous course of this channel is present roughly 5–10 ms deeper than the surrounding surface, which corresponds with one of the observed channel forms identified within the 3D seismic extract (Figures 6.7, 6.17). The channel form appears to have been created during the period of lateral migration and avulsion that deposited the broader channel belt. However, rather than being filled by channel abandonment facies or reworked as observed elsewhere in the system, it instead appears to play a key role in subsequent deltaic deposition. In the shallow portion of the valley, the channel form propagates upward maintaining 2–5 m of relief (Figure 6.18). Reflectors originating from the edges of the channel appear to downlap on the surrounding paleo-floodplain, suggesting continued levee and floodplain growth sourced from the channel during this overall period of aggradation (Figures 6.17, 6.18). This transition in geometry and channel behavior is associated with a shift from coarse grained deposition to fine grained organic rich clays and silts which corresponds with the observed change in seismic facies (Figure 6.15; Thomas, 1991). This change from a system dominated by lateral migration to vertical aggradation in the upper valley differs significantly from previously interpreted models of rapid flooding and transgression. Downstream the channel course becomes difficult to observe, and the stratigraphic complexity above horizon H3 increases (Figures 6.8, 6.10, 6.18). Rather than a single aggradational channel and associated floodplain sediments, numerous erosional unconformities, clinoforms, and dipping strata are observed (Figure 6.18). This transition in seismic facies potentially corresponds to the lateral transition from more fluvial or delta surface deposition to the delta front and estuarine dynamics (e.g., Aschoff et al., 2018). The latest transition from floodplain and/or deltaic

deposition to bay and estuarine conditions is at H2, which appears to erosionally truncate the paleo-Trinity channel in the upper valley and have removed significant portions of delta stratigraphy lower in the study area (**Figures 6.10, 6.11, 6.16, 6.18**). This transition is associated with the appearance of potential tidal inlet complexes and a significant shift in foraminiferal abundances indicating more open or middle bay conditions (**Figures 6.14**; Rodriguez et al., 2005).

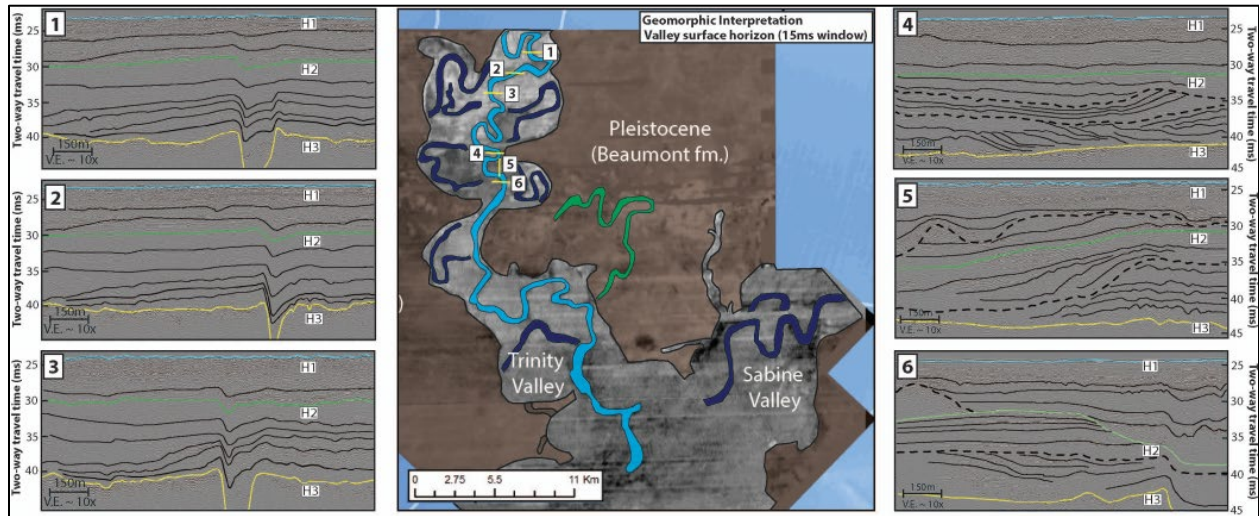


**Figure 6.18. Chirp lines crossing paleo-Trinity channel**

Representative chirp cross sections across the interpreted paleo-Trinity channel. Cross sections 1–3 illustrate vertical channel aggradation and associated horizon downlap on H3 (floodplain). Cross sections 4–6 show lower valley stratigraphy previously interpreted as deltaic made up of numerous progradational clinoforms, scour surfaces, and sigmoidal depositional packages. Paleo-channel forms in association with H3 not commonly observed.

## 6.6 Conclusions

The succession of incised valley fill deposits located within the Trinity paleovalley broadly represents a transgressive backstepping of depositional environments. However, we find that the many of the internal changes in architecture and lithology are more likely due to changes in fluvial morphology and associated patterns of sedimentation during relative sea-level rise. In contrast to earlier work that focused on discrete flooding events driving transgression followed by periods of progradation, the paleo-fluvio to deltaic transition highlighted here appears to be more gradual and associated with a shift from lateral migration and reworking of coarse-grained sediments to a period of vertical channel aggradation and enhanced fine grained floodplain and levee deposition. It is only towards the upper portion of the valley stratigraphy that evidence of significant transgression of the fluvial system is observed, and a marked transition to more bay or estuarine conditions. We find that the patterns of floodplain and delta sedimentation are closely correlated with position and geometry of the channel set during the period of channel belt growth and amalgamation, showing that rather than being a relict surface that is rapidly flooded and then deposited over it remains an active sediment routing pathway through much of the period recorded within the valley stratigraphy.

## 7 Estuarine and Tidal Stratigraphy

This chapter is excerpted from Burstein et al. (2021).

### 7.1 Introduction

Estuaries are uniquely dynamic depositional systems controlled by the interplay of river, wave, and tidal forces. They develop within incised valleys, which are formed through fluvial incision during periods of lower relative sea level (Anderson et al., 2004; Nordfjord et al., 2006). Incised valleys act as topographic hollows, providing accommodation for subsequent lowstand and transgressive deposits (Vail et al., 1977; Van Wagoner et al., 1988, 1990; Allen and Posamentier, 1993; Nordfjord et al., 2006). This accommodation provides protection from transgressive erosion, which cannibalizes older underlying sediment (Swift and Thorn, 1991; Cattaneo and Steel, 2003). Acting as sediment sinks for terrestrial, estuarine, and marine deposits, incised valleys provide a natural laboratory to investigate the rich depositional and erosional history of past sea-level cycles (Belknap and Kraft, 1981, 1985; Dalrymple et al., 1992; Allen and Posamentier, 1993; Zaitlin et al., 1994; Thomas, 1991; Thomas and Anderson, 1994; Cattaneo and Steel, 2003; Anderson et al., 1996, 2004, 2008, 2014, 2016; Rodriguez et al., 2004, 2005; Reijenstein et al., 2011).

Preserved estuarine sediments within incised valley fills enable comprehensive studies investigating estuarine response to relative sea-level rise (Thomas and Anderson, 1994; Storms et al., 2008; Simms et al., 2008; Rodriguez et al., 2004, 2005; Anderson et al., 2004, 2014, 2016; Reijenstein et al., 2011; Ronchi et al., 2018, 2019; Shawler et al., 2020). In particular, the Holocene estuarine record within the Gulf of Mexico incised valley fills have been extensively studied due to excellent preservation and well-constrained rates of sea-level rise during this time period (Milliken et al., 2008; Anderson et al., 2016). These studies have led to the commonly applied stratigraphic model of estuarine and barrier island response to episodic changes in relative sea-level rise (RSLR; Thomas and Anderson, 1994; Anderson et al., 2008; Anderson et al., 2010), changes in climate, which regulates sediment supply (Anderson et al., 2008), and flooding of antecedent fluvial topography (Rodriguez et al., 2004, 2005; Anderson et al., 2008) in the form of flooding surfaces. In response to increased RSLR, decreased sediment supply, or increased surface area of fluvial terraces, estuarine systems will experience rapid landward back-stepping, wherein fluvial and bayhead delta sequences are overlain by bay, tidal, barrier, and marine deposits. This results in an incised valley fill characterized by discontinuous, landward-stepping, deepening-upward successions (Thomas and Anderson, 1994; Anderson et al., 2016).

Antecedent topography is another factor that is increasingly understood to play a pivotal role in controlling the evolution of estuarine and barrier island systems in a multitude of ways. Previous authors found that flooding of antecedent fluvial terraces within the incised valley results in increased surface area for rapid bay expansion (Rodriguez et al., 2005; Anderson et al., 2008; Simms et al., 2008). This increased surface area within the incised valley also allows for the development of a deposition center, or sediment sink, which can then serve as local sand sources to supply the transgressing barrier (Rodriguez et al., 2004). Through a comprehensive field and morphodynamic modelling study, Shawler et al. (2020) found that antecedent topographic highs play a central role in how barrier islands respond to sea-level rise. They found that steep antecedent slopes and decreased back-barrier accommodation provides both increased elevation and erodible sediment supply to essentially anchor the island despite high rates of sea-level rise, and thus promotes barrier resilience. Conversely, increased back-barrier accommodation may lead to rapid landward migration.

To investigate the role of antecedent topography in the evolution of an ancient barrier island system, we focus on the Trinity incised valley offshore modern Galveston Bay in the central Gulf of Mexico (**Figure 7.1**; Anderson et al., 2016). The regional estuarine stratigraphic framework has been previously studied, identifying fluvial and deltaic units overlain by estuarine units including lower bay and tidal-inlet sands (Thomas and Anderson, 1994; Anderson et al., 2004; Rodriguez et al., 2004, 2005; Swartz et al., 2022; Chapter 6). Rates of RSLR in the northern Gulf of Mexico over the last 10 kyr are well-constrained, displaying a decrease from 5 mm/yr to 3 mm/yr (Milliken et al., 2008). However, previous authors have focused on identifying the adjustment and evolution of the fluvial-deltaic system during RSLR (Swartz et al., 2022; Chapter 6), or have lacked the geophysical resolution to accurately identify fine-scale stratigraphic architecture necessary to capture the complex nature of the estuarine section (Thomas and Anderson, 1994; Anderson et al., 2004; Rodriguez et al., 2004, 2005).

In this study, we use a dense (~250 m line spacing) grid of high-resolution chirp data, in combination with micropaleontological, sedimentological, and radiocarbon dating methods to investigate the role of the antecedent geology on the initiation and evolution of a paleo-barrier island system. This study provides a methodology to study the evolution of a paleo-barrier system where little of the barrier itself is preserved in the stratigraphy. Using this methodology, we revise the established Holocene paleoshoreline model for the Trinity incised valley.

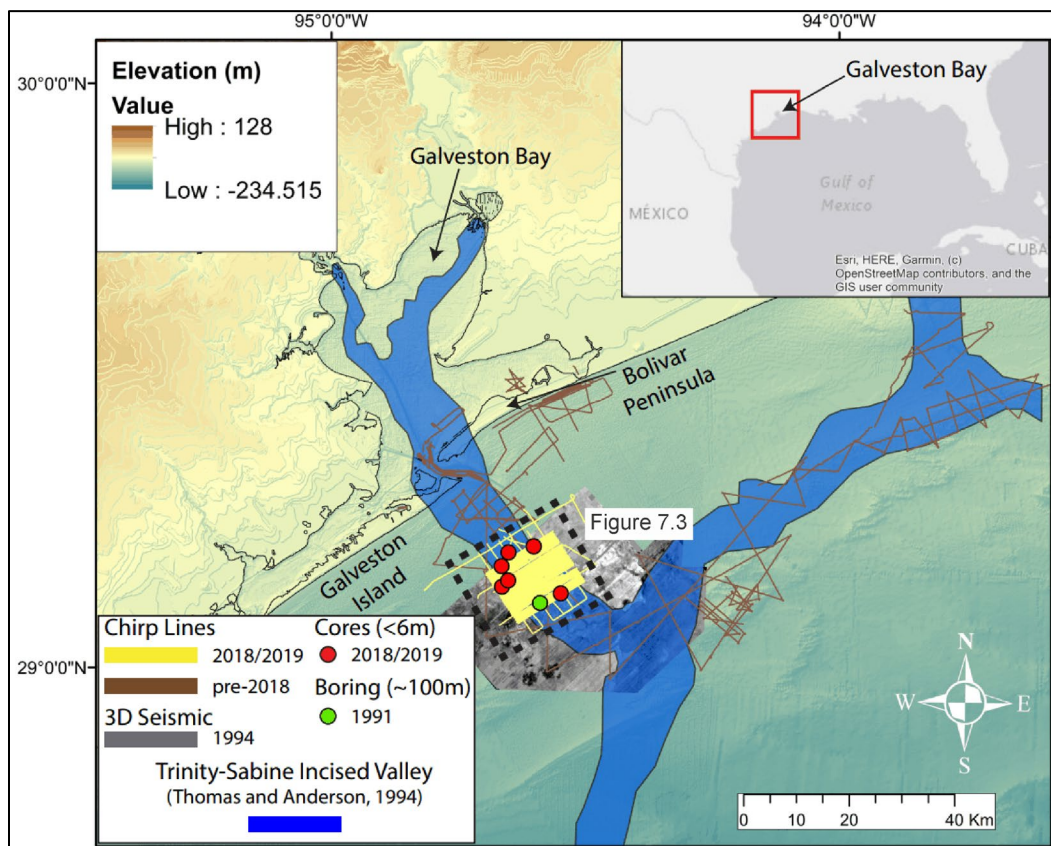


**Figure 7.1. Map of the east Texas inner shelf**

Blue polygon represents the extent of the Trinity-Sabine incised valley (modified from Thomas and Anderson, 1994). Brown tracklines represent available geophysical data. Yellow lines represent chirp geophysical data used in Swartz et al., 2022 and this study. Grey coherency extraction represents spatial extent of archived 3D seismic data used in

Swartz et al., 2022 and this study. Red circles represent gravity and piston cores used in Standing et al. (2021) and this study. The green circle represents Boring 4 from Thomas (1991).

## 7.2 Study Area

The northern Gulf of Mexico experiences highly variable regional basin subsidence, exhibiting relatively low rates in coastal regions (0.03 mm/yr), yet high rates along the shelf edge ( $> 1.0$  mm/yr) (Anderson et al., 2016). The central Texas region is currently classified as a dry subhumid region (Thornthwaite, 1948). However, multiple studies focused on the post-glacial climatic history of central Texas observe marked changes from cool and wet  $\sim 18$ – $7.5$  ka, to warm and dry  $\sim 7.5$ – $3.5$  ka, and finally variable, millennial scale shifts between cool-wet and warm-dry conditions since 3.5 ka (Humphrey and Ferring, 1994; Nordt et al., 1994, 2002; Toomey et al., 1993). The oceanographic circulation along the inner shelf is dominated by a strong westward current called the Louisiana Coastal Current (Cochane and Kelly, 1986; Oey 1995; Jarosz and Murray, 2005).

The Trinity incised valley formed during Marine Isotope Stages (MIS) 5–3, approximately 119 to 22 ka. During this time, the region experienced  $\sim 120$  m in episodic sea-level fall, prompting a stepped downcutting of the fluvial system into the continental shelf. This resulted in an incised valley with a terraced morphology extending from the modern Galveston Bay to the shelf margin (**Figure 7.1**; Thomas and Anderson, 1994; Anderson et al., 2016). The incised valley reached its most basinward location during MIS 2 approximately 22 to 17 ka, depositing a large shelf edge delta and basin floor fan complex (Pirmez et al., 2012; Anderson et al., 2016). Thomas and Anderson (1994) measured the valley surface to have 30–40 m of total relief; however, upper portions of the valley have since been infilled or removed by the transgressive erosion during subsequent sea-level rise, and only lower portions of the valley exist offshore overlain by the seafloor.

Following the MIS2 lowstand, rapid sea-level rise ( $\sim 4.2$  mm/yr) between  $\sim 17$  and 10 ka prompted a shift from progradation to aggradation, retrogradation, and valley filling for much of the fluvial systems across the Gulf of Mexico (Milliken et al., 2008; Anderson et al., 2016). By 10 ka, the rate of sea-level rise slowed progressively from 4.2 mm/yr to 1.4 mm/yr, leading to slower rates of transgression, better preservation of thick transgressive deposits, and, as a result, a more complete sedimentological record (Milliken et al., 2008; Anderson et al., 2014; 2016). After 10 ka, the Trinity valley was infilled by a series of discontinuous, landward stepping depositional packages consisting of fluvial, deltaic, bay and tidal packages (Thomas and Anderson, 1994; Rodriguez et al., 2004; Anderson et al., 2016).

Previous authors have interpreted large shelf sand bodies on the inner shelf as remnants of coastal barriers formed during sea-level stillstands, and subsequently overstepped and reworked during transgression (Rodriguez et al., 1999; Rodriguez et al., 2004; Anderson et al., 2016). Rodriguez et al. (2004) identified estuarine muds overlain by shoreface and/or tidally influenced sands within cores beneath Heald Bank and Sabine Bank (**Figure 7.2**). Ages acquired from the estuarine units at both locations suggest that estuaries existed at Heald Bank and Sabine Bank from 8.4 to 7.7 ka and 7.4 to 4.7 ka, respectively. Dates taken from estuarine packages in West and East Bay (**Figure 7.2**) suggest that a lagoon existed in those areas since at least 7.5 and 7.7 ka, respectively. Thus, the shoreface and/or tidally influenced unit below Heald Bank was interpreted as the 7.7 ka barrier island location, fronting a 50-km long estuary extending from Heald Bank to West and East Bays (Rodriguez et al., 2004). These authors suggested that the western portion of the barrier shoreline rapidly retreated during RSLR until Galveston Island began prograding approximately 5.3 ka.

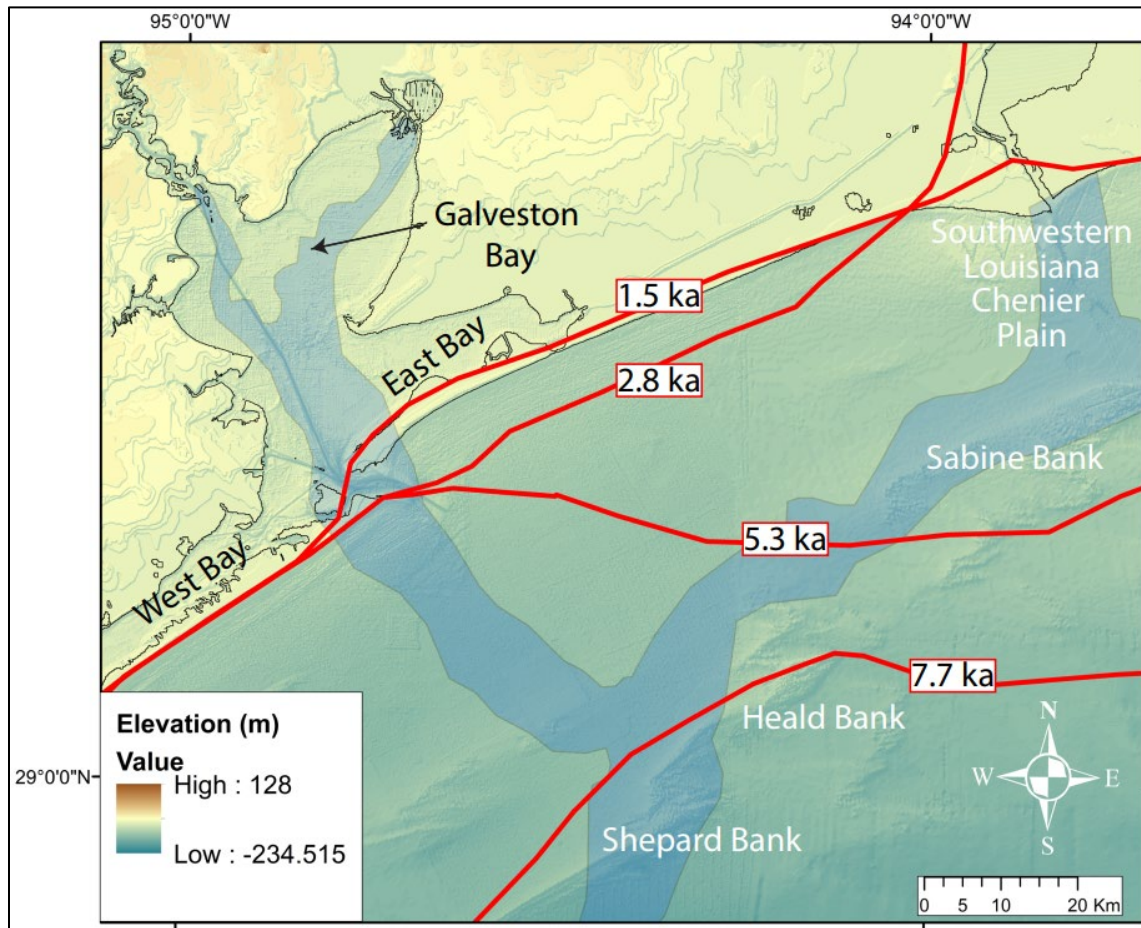


**Figure 7.2. Proposed shoreline history of the Texas inner shelf**

Blue polygon representing the Trinity-Sabine incised valley extent, modified from Thomas and Anderson (1994). Red lines represent paleoshorelines modified from Rodriguez et al. (2004).

Conversely, according to Rodriguez et al. (2004), the eastern portion of the barrier shoreline remained relatively stable reaching Sabine Bank around 5.3 ka, leading to an irregular, perpendicular shoreline extending from Sabine Bank to East Bay (**Figure 7.2**). The shoreline gradually retreated to the southwestern Louisiana chenier plain by 2.8 ka, and again to Bolivar Peninsula by 1.5 ka as it began to form by spit creation, washover, and ephemeral flood-tidal delta deposition (**Figure 7.2**; Gould and McFarlan 1959). The stabilization and subsequent rapid retreat of the paleoshoreline has been attributed to the presence of fluvial deposits directly beneath Heald and Sabine Banks within the Trinity-Sabine incised valley (Rodriguez et al., 2004). As the shoreline retreated, the fluvial deposits provided both an anchor point and a local sediment supply to remain relatively stable; however, once these sources were depleted and/or a ratio of sediment supply to sea-level threshold was surpassed, rapid shoreline retreat ensued.

Alternatively, Thomas and Anderson (1994) earlier proposed that these sand banks do not have origins as submerged, overstepped barriers, but rather as modern marine sand bodies. They observe Sabine and Heald Banks to overlie a ravinement eroding underlying estuarine and tidal deposits from relict barrier island systems. Therefore, it is possible that these sand bodies are marine sand bodies reworking relict barrier island material, and established at shoreline positions that pre-date the formation of the bank.

## 7.3 Methods

### 7.3.1 Chirp and 3D Seismic Data

This study uses high-resolution chirp sub-bottom reflection data and archived 3D seismic datasets. Over 1000 km of 2D chirp data have been collected by the University of Texas Institute for Geophysics (UTIG) as part of the continuing effort of characterizing offshore sand resources. These data were collected aboard the R/V *Manta* in 2017, the R/V *Brooks McCall* in 2018, and R/V *Trident* in 2018, and consist of 45 profiles parallel to the modern shoreline ~15 km in length, along with 6 perpendicular profiles ~18 km in length, providing a survey area of ~175 km<sup>2</sup>(**Figure 7.3**). Chirp data were acquired using an Edgetech 512i sub-bottom profiler towfish configured with a 20 ms, 0.7 to 12 kHz pulse, a 0.0046 ms sample interval, and ~135 ms record length. Full waveform and envelope records were processed in Paradigm Echos software. This workflow includes heave compensation, tide and towfish depth corrections, secondary deconvolution, trace equalization, and a layback correction for navigation (Saustrup et al., 2019). The result of this processing workflow is high-resolution, full waveform data with near decimeter vertical resolution, along with conventional envelope data.

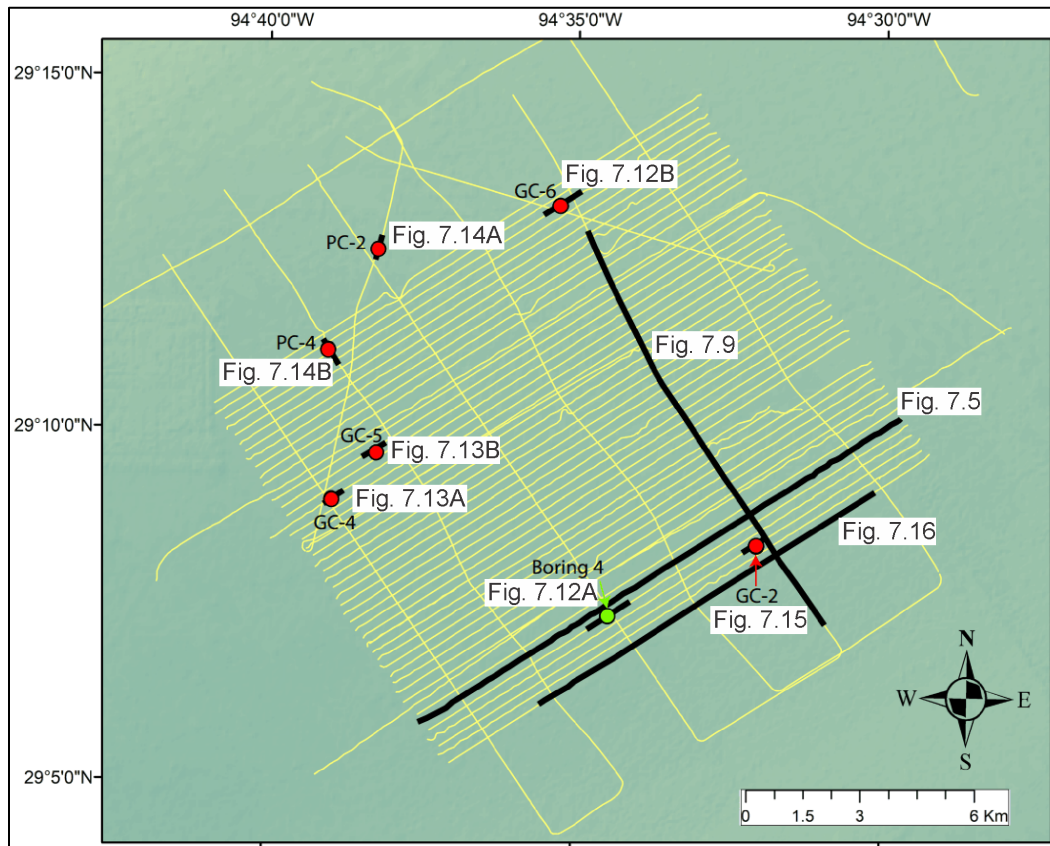


**Figure 7.3. Chirp geophysical tracklines**

Chirp track represented as yellow lines. Bolded black lines indicate succeeding figure locations used in this study. Red circles represent cores used in Standing et al. (2021) and this study. The green circle represents Boring 4 from Thomas (1991).

Seismic stratigraphic interpretations were conducted in Landmark DecisionSpace® Desktop software. Seismic horizons and units were identified by analyzing a combination of reflection amplitude, configuration, continuity, geometry, and stratigraphic superposition. Approximate depths and thicknesses of seismic horizons and units, respectively, were calculated by converting two-way travel time in milliseconds (ms) to depth in meters below sea level (m) using an average velocity of 1525 m/s (Abdulah et al., 2004).

An archived 3D seismic dataset (B-12-94-TX) was originally acquired commercially in 1994 for geophysical and geological exploration of oil and gas prospects on the U.S. Outer Continental Shelf. Following a 25-year exclusion window, these data were publicly archived BOEM and made available by USGS on the National Archive of Marine Seismic Surveys<sup>2</sup>). This survey was acquired with a 30 m line spacing, 30 m common depth point spacing, and a 4 ms sampling interval. The processing workflow of these data is not available.

Swartz et al. (2022) retrieved this dataset and conducted further processing steps in Petrel 2016. A crossline filter of 90 m was applied to the data volume in order to smooth striping artifacts resulting from the survey's acquisition footprint. A shallow, regionally conformable horizon located between 40–60 ms interpreted as the base of the Trinity incised valley was mapped and agrees with previous interpretations (Thomas and Anderson, 1994). A 20 ms envelope median coherency attribute was calculated and extracted from this horizon. The result of this median coherency extraction is an amalgamated, time-transgressive representation of the Trinity incised valley fill, highlighting the most anomalous amplitudes within the stratigraphic section.

### 7.3.2 Core Data

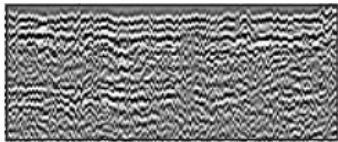
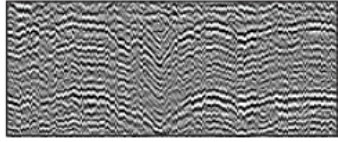
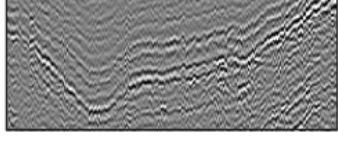
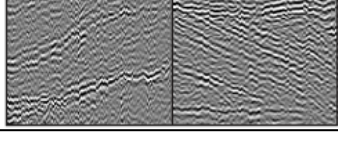
This study uses two piston cores, four gravity cores, and one platform boring to ground-truth seismic datasets. The platform boring was originally collected for foundation studies for drilling rigs and production platforms by Fugro-McClelland Engineers in Houston, which was subsequently reexamined by for lithological and environmental interpretation by Thomas (1991). Gravity cores were collected aboard the R/V *Manta* in 2019, and piston cores were collected aboard the R/V *Brooks McCall* during UTIG's 2018 Marine Geology and Geophysics Field Course. Core sites were selected based on shallow seismic stratigraphic structures observed within seismic data to characterize key transitions within the incised valley fill, evaluate paleoenvironmental settings, date the transitions from key paleoenvironments, and interpret depositional processes. Thorough detail on the acquisition, processing, and analysis of core data is provided by Standring et al. (2021) (Chapter 5).

## 7.4 Results and Interpretation

Interpretation of chirp data is divided into five seismic facies analyzed from full-waveform data (**Figure 7.4**), and eight seismic horizons that bound seven seismic units (**Figures 7.5–17**) analyzed on both envelope and full-waveform data. Seismic horizons and units are correlated to stratigraphic (**Figure 7.12A**), foraminiferal, and radiocarbon data within cores (**Figures 7.12B–15**) in order to interpret the depositional environment and age of each unit.

---

<sup>2</sup> See <https://walrus.wr.usgs.gov/namss/>

Facies	Example	Description	Units Found In
SF1		Medium- to high-amplitude, chaotic to discontinuous internal parallel reflections, with some truncations within the facies.	U1, U3, U3b
SF2		Medium- to high-amplitude, U-shaped to wavy, parallel, aggrading reflections, with some internal truncations.	U2, U3, U3b
SF3		Low-amplitude, sub-parallel, laminated to transparent reflections.	U3, U3a, U4, U5
SF4		Medium- to low-amplitude, draping reflections with internal truncations that depict a cut-and-fill evolution.	U3, U3a
SF5		High-amplitude, unidirectional dipping reflectors that display progradation.	U3, U3b

**Figure 7.4. Seismic facies diagram**

Examples of SF1–5 observed in this study, along with descriptions and the seismic units in which they are found.

### 7.4.1 Seismic Facies

We recognize and map five seismic facies throughout the Trinity incised valley fill (**Figure 7.4**), based on reflection amplitude, configuration, continuity, and geometry.

#### 7.4.1.1 Seismic Facies 1 (SF1)

SF1 (**Figure 7.4**) is composed of medium- to high-amplitude, chaotic to discontinuous internal parallel reflections, with some internal truncations within the facies. This facies is most commonly observed composing seismic unit U1 (**Figures 7.6–7.8, 7.10–7.15, 7.17**), but is also observed within seismic units U3 and U3b (**Figures 7.10, 7.11, 7.15**).

#### 7.4.1.2 Seismic Facies 2 (SF2)

SF2 (**Figure 7.4**) consists of medium- to high-amplitude, U-shaped to wavy, parallel, aggrading reflections with some internal truncations. This facies is most commonly associated with seismic unit U2 (**Figures 7.6–7.8, 7.10–7.15, 7.17**), as well as seismic units U3 and U3b (**Figures 7.8, 7.10, 7.12B, 7.15**).

#### 7.4.1.3 Seismic Facies 3 (SF3)

SF3 (**Figure 7.4**) is characterized by low-amplitude, sub-parallel, laminated to transparent reflections. SF3 is frequently found composing seismic unit U4 (**Figures 7.6–7.8, 7.10, 7.12–7.15, 7.17**); however, it

is also observed within seismic units U3, U3a (**Figures 7.12A, 7.14A**), and U5 (**Figures 7.6, 7.8, 7.14A, 7.17**).

#### 7.4.1.4 Seismic Facies 4 (SF4)

SF4 (**Figure 7.4**) is composed of medium- to low- amplitude, draping reflections with internal truncations that depict a cut and fill evolution (e.g., Ronchi et al., 2019). SF4 is found in seismic units U3 and U3a (**Figures 7.7, 7.17**).

#### 7.4.1.5 Seismic Facies 5 (SF5)

SF5 (**Figure 7.4**) consists of high-amplitude, unidirectional dipping reflectors that display progradation. SF5 is observed to compose seismic units U3 and U3b (**Figures 7.8, 7.11, 7.15, 7.17**).

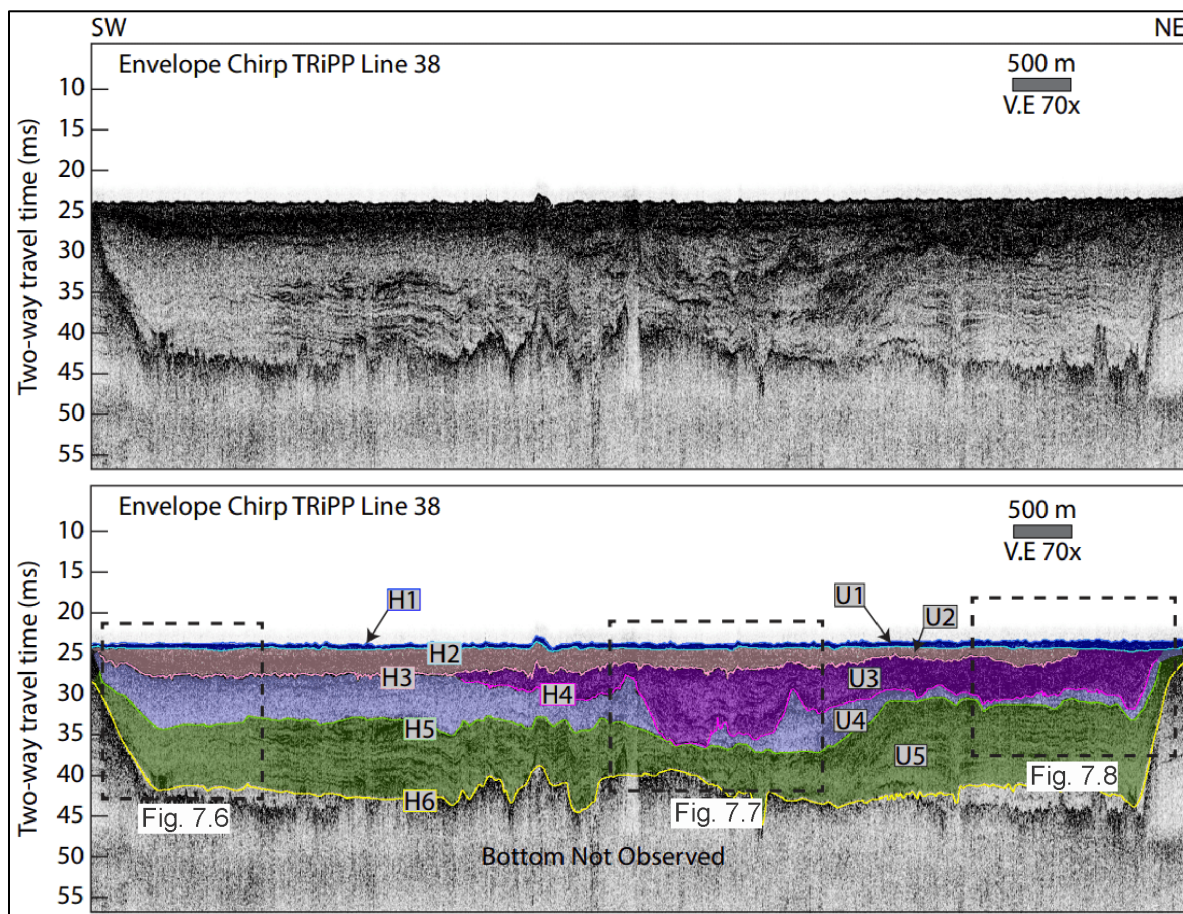


**Figure 7.5. TRiPP Line 38 envelope record.**

Uninterpreted (top) and interpreted (bottom) envelope chirp data of strike-oriented TRiPP Line 38 displaying the seismic horizons (H1–H6) that bound seismic units (U1–U5). Insets indicate the locations for **Figures 7.6–7.8**. The location for this chirp line can be found in **Figure 7.3**.

## 7.4.2 Seismic Horizons

Eight seismic horizons have been mapped bounding characteristic components of the Trinity incised valley fill (Figures 7.5–7.17). These surfaces have been defined based on stratigraphic superposition, termination style, and when necessary, associated seismic facies both above and below a given horizon. Time-structure maps were created using a combination of Python and GMT 6 programming scripts, in which horizons were gridded and interpolated onto 50-meter cells (Figure 7.18). When appropriate, horizons were converted from TWT in ms to depth in meters below sea level (mbsl) using an average velocity of 1525 m/s (Abdulah et al., 2004).

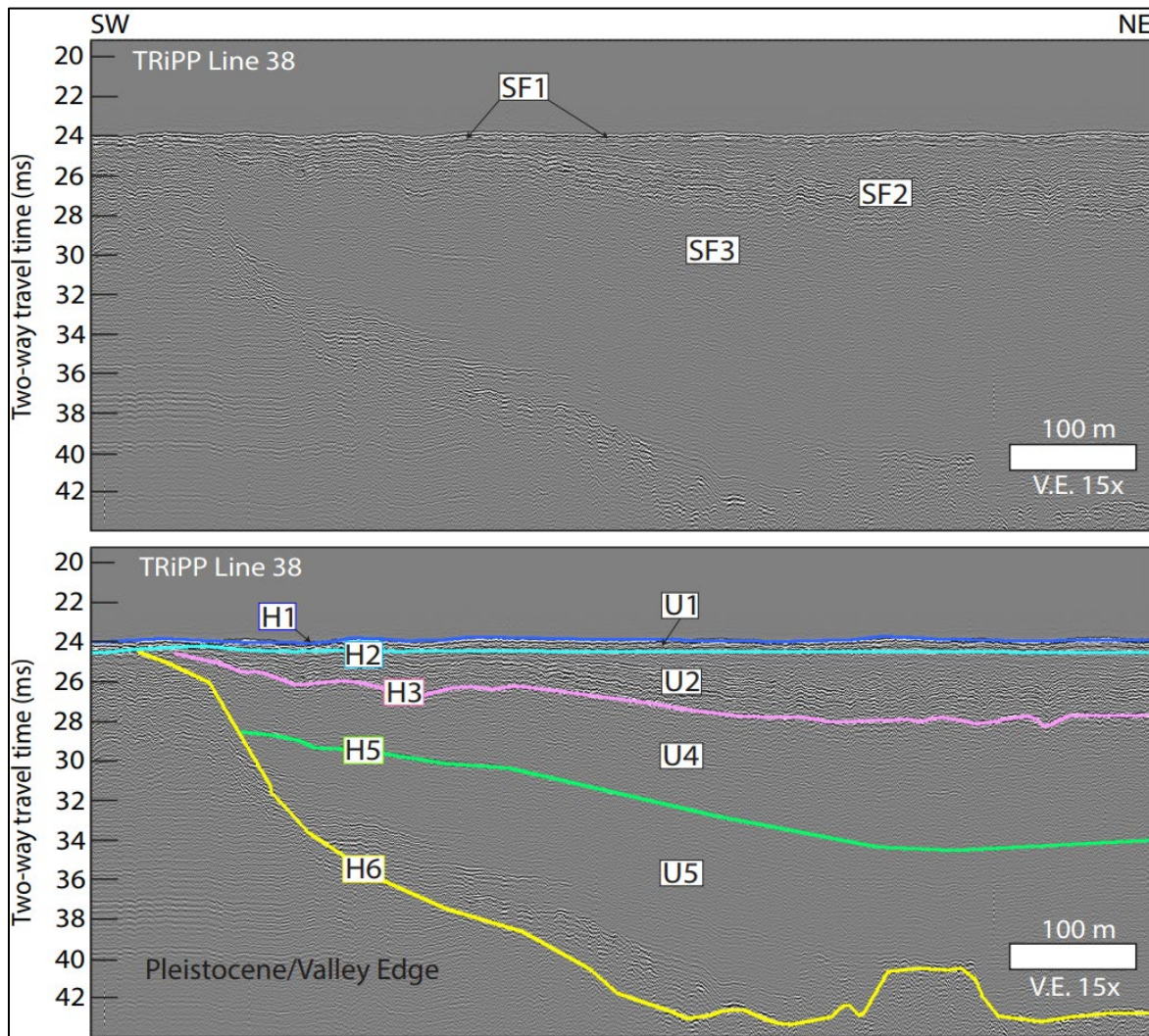


**Figure 7.6. TRiPP Line 38 full waveform record west**

Top: Seismic facies analysis of full-waveform data on TRiPP Line 38. Bottom: Interpretation of full-waveform data on TRiPP Line 38. Displayed here is the western edge of the Trinity incised valley, defined by H6. Seismic units U5, U4, and U2, bound by seismic horizons H6, H5, H3, and H2, are seen either onlapping the valley wall, or truncated by H2. H1 represents the seafloor. The location for this chirp line can be found in Figures 7.3 and 7.5.

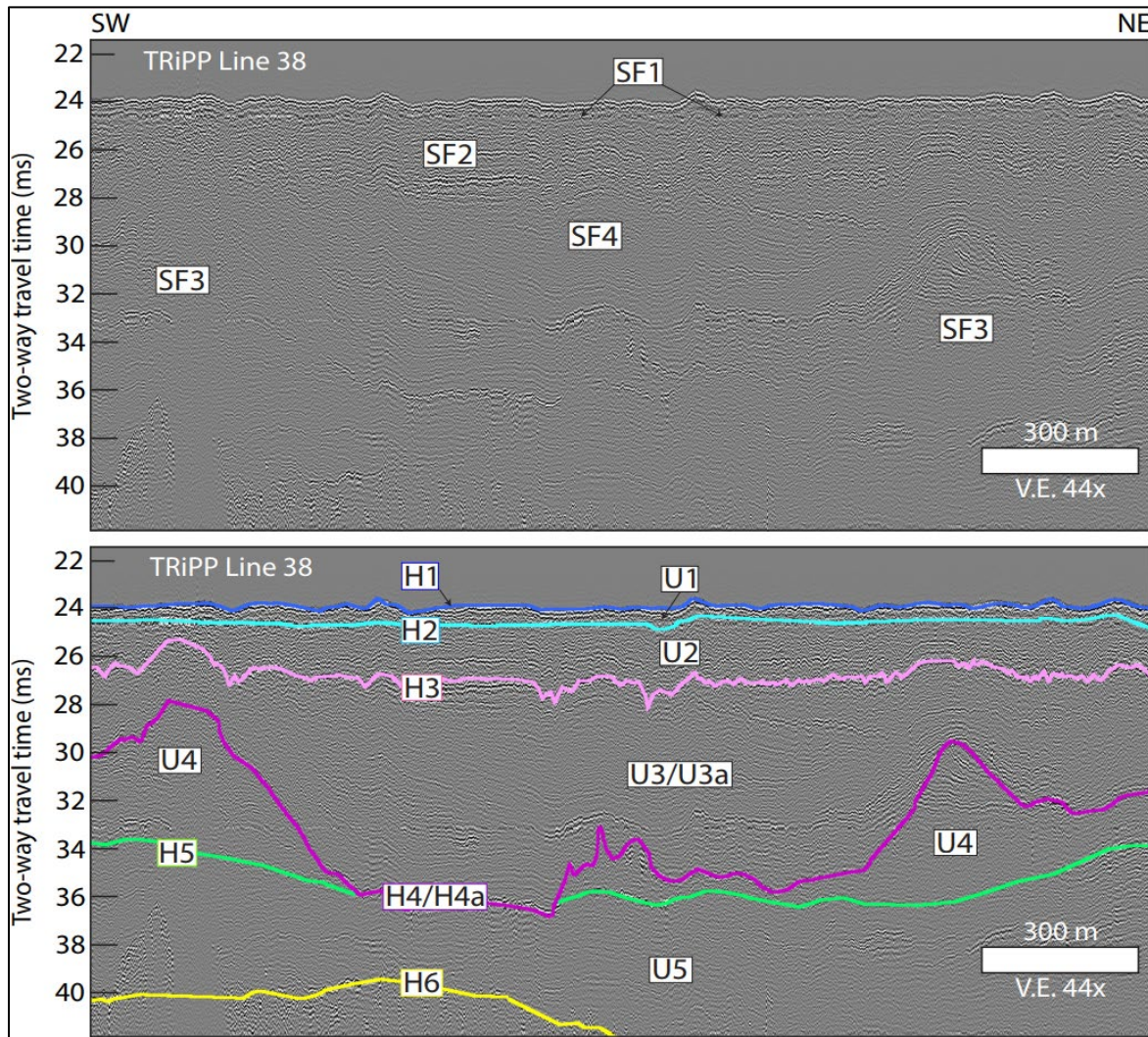


**Figure 7.7. TRiPP Line 38 full waveform record central**

Top: Seismic facies analysis of full-waveform data on TRiPP Line 38. Bottom: Interpretation of full-waveform data on TRiPP Line 38. Displayed here is the central portion of the Trinity incised valley. H6 is shown in the bottom of the figure as a channelized, continuous reflector. H5, defining the top of U5, is truncated by overlying horizons. H4/H4a, which forms the lower boundary of U3/U3a, is composed of SF4. Horizons H3 and H2 bound unit U2. H1 is the seafloor. The location for this chirp line can be found in **Figures 7.3** and **7.5**.

#### 7.4.2.1 Horizon H1

H1 is the modern seafloor, which displays a general southwestward dip (**Figure 7.18–H1**). H1 is shallowest within the northeastern portion of the study area at 19 ms depth (~14.5 mbsl) and deepest within the southwestward portion at 25 ms depth (~19 mbsl). This horizon is often erosional in nature, and frequently amalgamates with the underlying H2 horizon (**Figures 7.5–7.7, 7.12A, 7.13, 7.14A**).

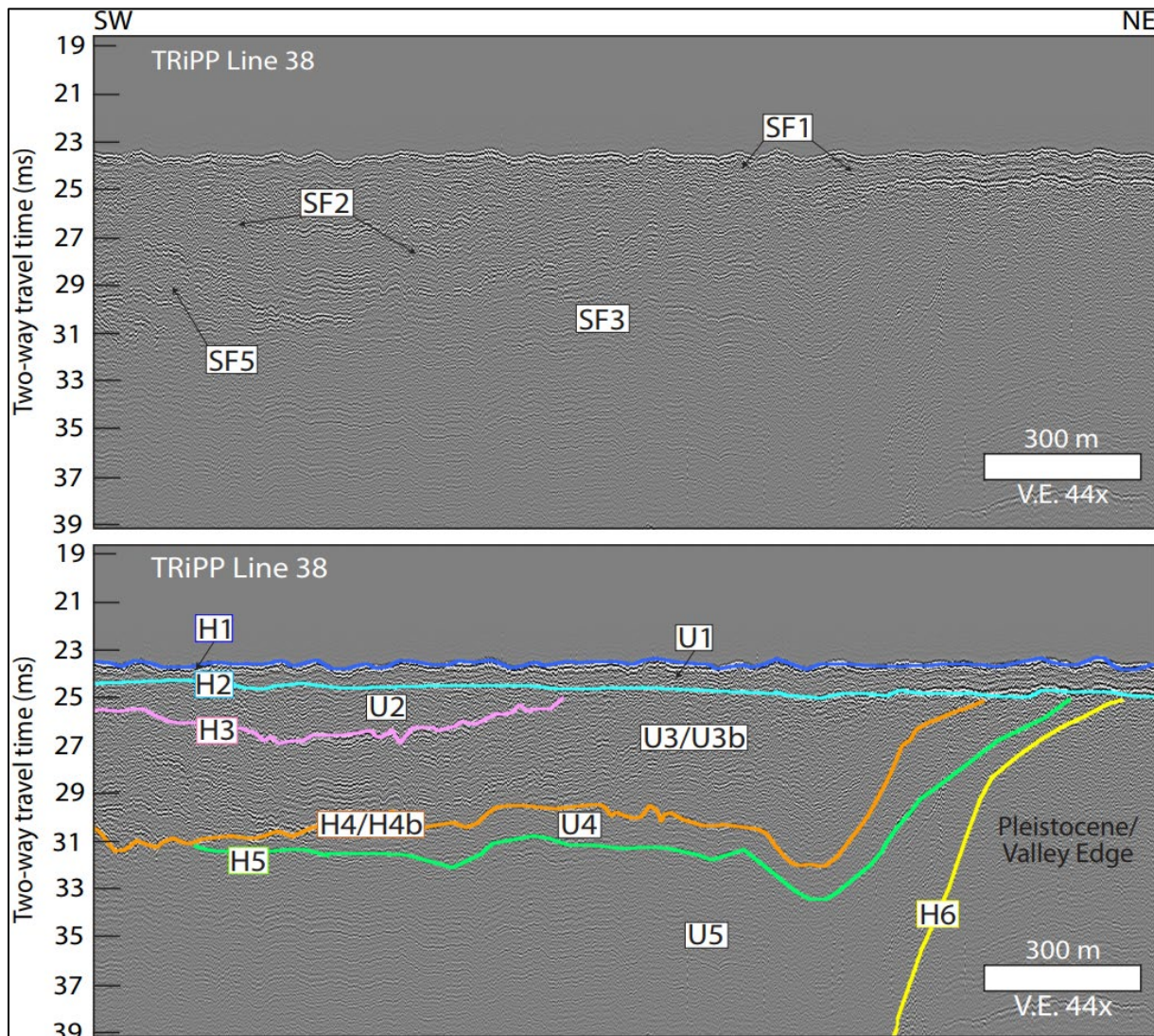


**Figure 7.8. TRiPP Line 38 full waveform record east**

Top: Seismic facies analysis of full-waveform data on TRiPP Line 38. Bottom: Interpretation of full-waveform data on TRiPP Line 38. Displayed here is the eastern portion of the Trinity incised valley. H6 is shown on the right to define the incised valley edge. H5, defining the top of U5, is truncated H4/H4b. H4/H4b, which forms the lower boundary of U3/U3b, is composed of SF2 and SF5. Horizons H3 and H2 bound unit U2. H1 is the seafloor. The location for this chirp line can be found in **Figures 7.3 and 7.5**.

#### 7.4.2.2 Horizon H2

H2 is a varying amplitude erosional surface that truncates underlying reflectors (**Figure 18-H2**) and varies between 20 and 26 ms depth (~15 and 20 mbsl). Frequently, this horizon amalgamates with the overlying H1 horizon and mimics underlying topography (**Figures 7.5–7.7, 7.12A, 7.13, 7.14A**). This horizon is erosional in nature, where it is observed to truncate underlying strata in the form of multiple 2–4.5 km long, 1.3–1.5 km wide, 0.75–2.8 ms (~1 to 2 m) deep channel-like features (**Figures 7.8, 7.12B, 7.18**). Due to its truncation of underlying reflectors (**Figures 7.6, 7.8, 7.9, 7.12B, 7.13A, 7.16**), and its correlation beneath a transgressive lag in core GC-6 (**Figure 7.12B**), this horizon is interpreted to be the

transgressive ravinement, which is a diachronous surface cut during the process of erosional shoreface retreat (e.g., Nummedal and Swift, 1987) that has been subsequently reworked by the modern seafloor.

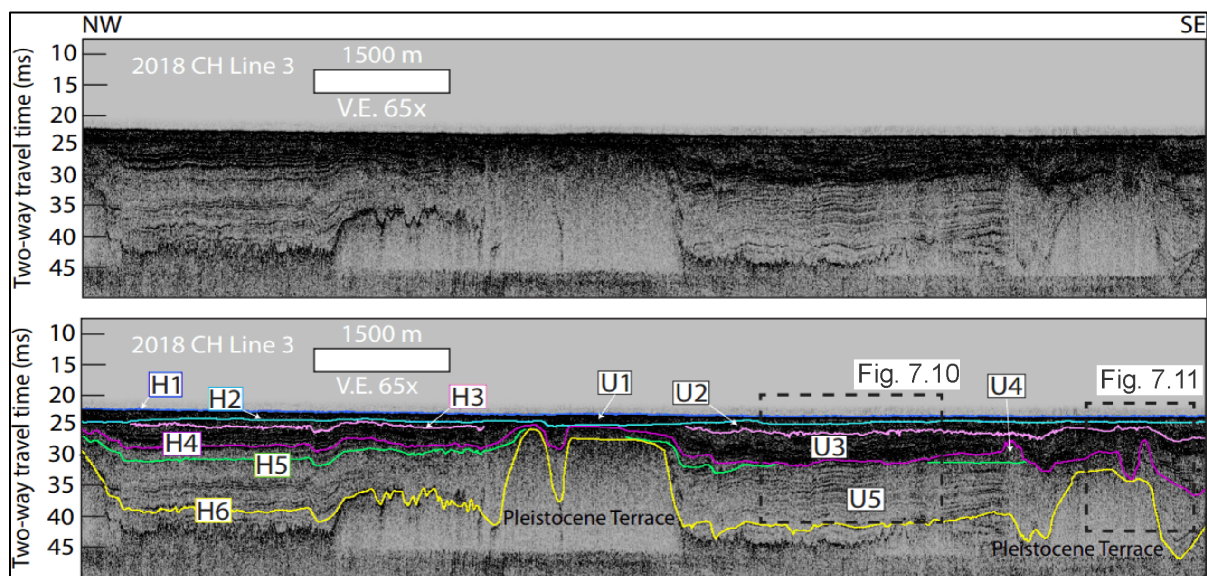


**Figure 7.9. 2018 CH Line 3 envelope record**

Uninterpreted (top) and interpreted (bottom) envelope chirp data of the dip-oriented 2018 CH Line 3 displaying seismic horizons (H1–H6) that bound seismic units (U1–U5). Channels initiated by H6 are propagated throughout the overlying stratigraphic section. Insets indicate the locations for **Figures 7.10** and **7.11**. The location for this chirp line can be found in **Figure 7.3**.

#### 7.4.2.3 Horizon H3

H3 is a high-amplitude, channelized erosional surface that truncates underlying strata, and varies between 23 and 30 ms depth (~17.5 and 23 mbsl) (**Figure 7.18-H3**). This horizon is truncated by the overlying H2 (**Figures 7.5–7.9, 7.12B, 7.13A, 7.16**). H3 is deepest and appears most continuous along the western and seaward portions of the study area (**Figures 7.5–7.7, 7.9–7.11, 7.12A, 7.13A–7.13B, 7.14A, 7.15, 7.16–7.18**). Conversely, this horizon is shallowest and least continuous along the eastern and landward portions of the study area (**Figures 7.5, 7.8, 7.9, 7.12B, 7.18**), or above fluvial terraces (**Figure 7.14B**). Based on foraminiferal analyses (Standring et al., 2021; Chapter 5), H3 is interpreted to be the base of (**Figures 7.13–7.15**) or lie within (**Figure 7.12B**) outer bay sediments, a high-energy environment just landward of ancient barriers formed by tidal, storm, and wave processes (Dalrymple et al., 1992; Zaitlin et al., 1994).

#### 7.4.2.4 Horizon H4

H4 is a varying amplitude, highly erosional surface that truncates the underlying H5 horizon (**Figures 7.5, 7.7–7.10, 7.15, 7.16, 7.17**) and varies between 22 and 44 ms depth (~16.5 to 33.5 mbsl) (**Figure 7.18-H4**). This horizon is subsequently truncated either by H3 along the western portion of study area (**Figures 7.5, 7.16**) or H2 along the eastern portion (**Figures 7.5, 7.8, 7.9, 7.16**). H4 is deepest within the seaward portion of the study area, defining an approximately 3.5 to 5 km wide channel that rapidly shallows landward (**Figure 7.18-H4**). Due to its erosional nature and channelized geometry (**Figures 7.5, 7.7–7.11, 7.12B, 7.15, 7.16–7.18**), the horizon is interpreted as a tidal ravinement (e.g. Cattaneo and Steel, 2003) formed in a high tidal energy environment adjacent to or just landward of the barrier (Dalrymple et al., 1992; Zaitlin et al., 1994). H4 is divided into two sub-horizons H4a and H4b based on seismic facies characterizations of SF4 and SF5 overlying them, respectively (**Figures 7.7, 7.8, 7.10, 7.11, 7.15, 7.17**).

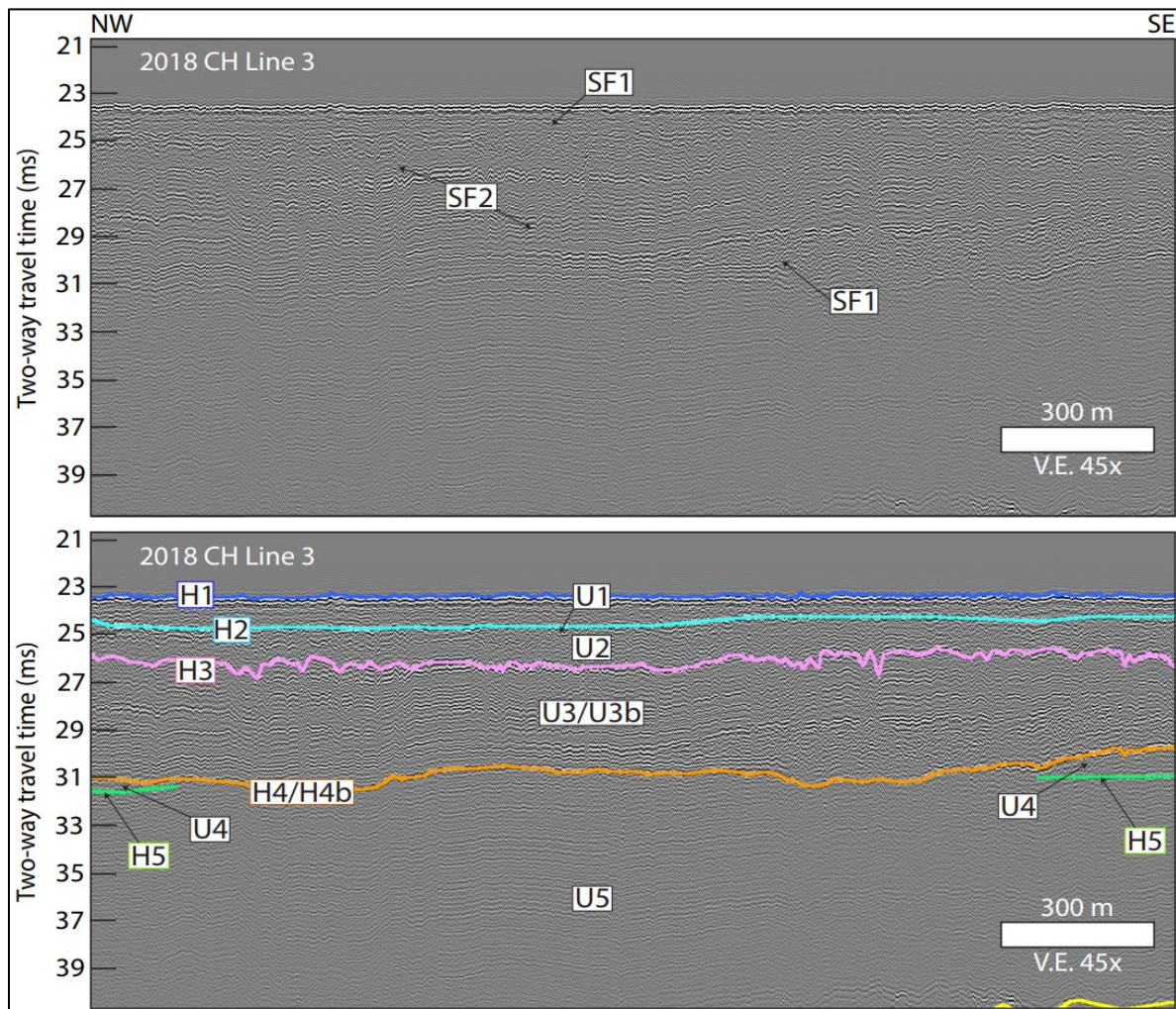


**Figure 7.10. 2018 CH Line 3 full waveform record central**

Top: Seismic facies analysis of full-waveform data on 2018 CH Line 3. Bottom: Interpretation of full-waveform data on 2018 CH Line 3. Displayed here is a dip-oriented line, highlighting the truncation of H5 by H4/H4b. U3/U3b, in which H4/H4b represents its lower boundary, is composed of SF1 and SF2. Horizons H3 and H2 bound unit U2. H1 is the seafloor. The location for this chirp line can be found in **Figure 7.3** and **7.9**.

#### 7.4.2.5 Horizon H4a

H4a is varying amplitude, deeply channelized, highly erosional surface that truncates the underlying H5 horizon (**Figures 7.7, 7.17**) and is truncated by the overlying H3 horizon (**Figures 7.5, 7.16**). H4a varies between 22 and 44 ms (~16.5 to 33.5 mbsl) (**Figure 7.18-H4a**). This horizon is distinct from H4b due to the presence of seismic facies SF4 overlying it (**Figures 7.7, 7.17**). H4a displays a highly erosional channel approximately 2 km wide at its maximum extent (**Figure 7.18-H4a**). Deep erosional cuts made by this horizon are focused within the seaward extent of the study area (**Figures 7.7, 7.17**), which quickly shallows landward and along the channel margins (**Figures 7.5, 7.9, 7.14A, 7.16, 7.18**). Based on its highly erosional nature, stratigraphic superposition, and overlying seismic facies, H4a is interpreted to be the base of a paleo-tidal inlet (e.g., Storms et al., 2008; Ronchi et al., 2018; Ronchi et al., 2019).

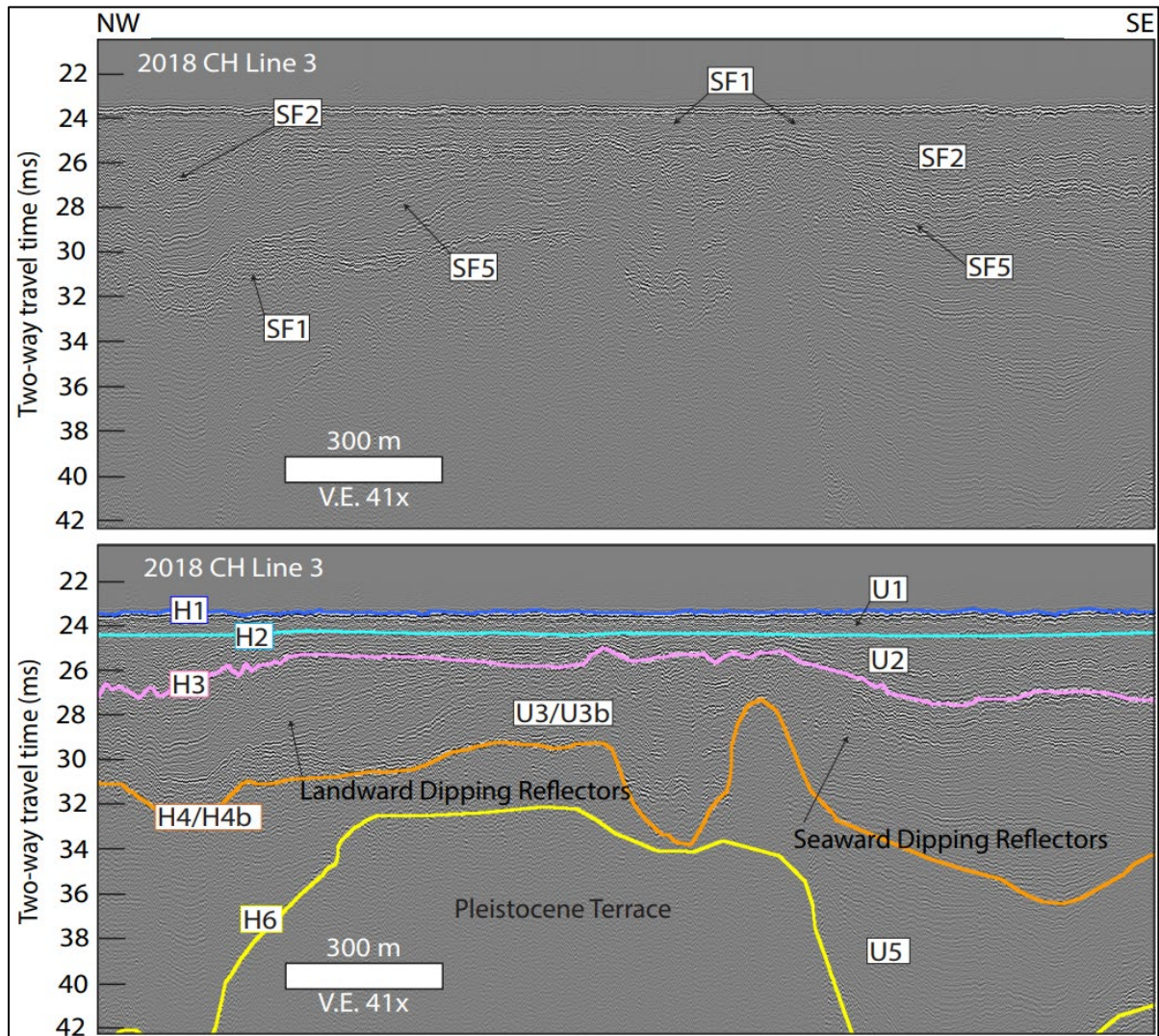


**Figure 7.11. 2018 CH Line 3 full waveform record central**

Top: Seismic facies analysis of full-waveform data on 2018 CH Line 3. Bottom: Interpretation of full-waveform data on 2018 CH Line 3. Displayed here is the seaward most extent of a dip-oriented line. H6 is shown as a mound-like feature interpreted as a Pleistocene fluvial terrace, overlain by U5. U3/U3b, which lies above H4/H4b, is composed of SF1 and SF5, and displays a transition from landward dipping reflectors to seaward dipping reflectors, indicating proximal paleo-barrier position over the Pleistocene fluvial terrace. H3 bounds U2, which is composed of SF2, and is truncated by the overlying H2 horizon. H1 is the seafloor. The location for this chirp line can be found in **Figure 7.3** and **7.9**.

#### 7.4.2.6 Horizon H4b

H4b is a varying amplitude, shallowly channelized, highly erosional surface that truncates the H5 horizon (**Figures 7.8, 7.10, 7.15, 7.17**), and is truncated by the overlying H2 horizon (**Figure 7.8**). H4b varies between 22 and 37 ms depth (~16.5 and 28 mbsl) (**Figure 7.18-H4b**). This horizon is differentiated from H4a by having seismic facies SF5 overlying it (**Figures 7.8, 7.11, 7.15, 7.17**). Additionally, H4b reaches shallower depths than H4a (~5.5 m difference) and is focused along the eastern portion of the study area (**Figures 7.8, 7.10, 7.11, 7.12B, 7.15–7.17**). Given this horizon's highly erosional nature, stratigraphic

superposition, and overlying seismic facies, H4b is interpreted as the base of a paleo-tidal delta (e.g., Rodriguez et al., 1998).

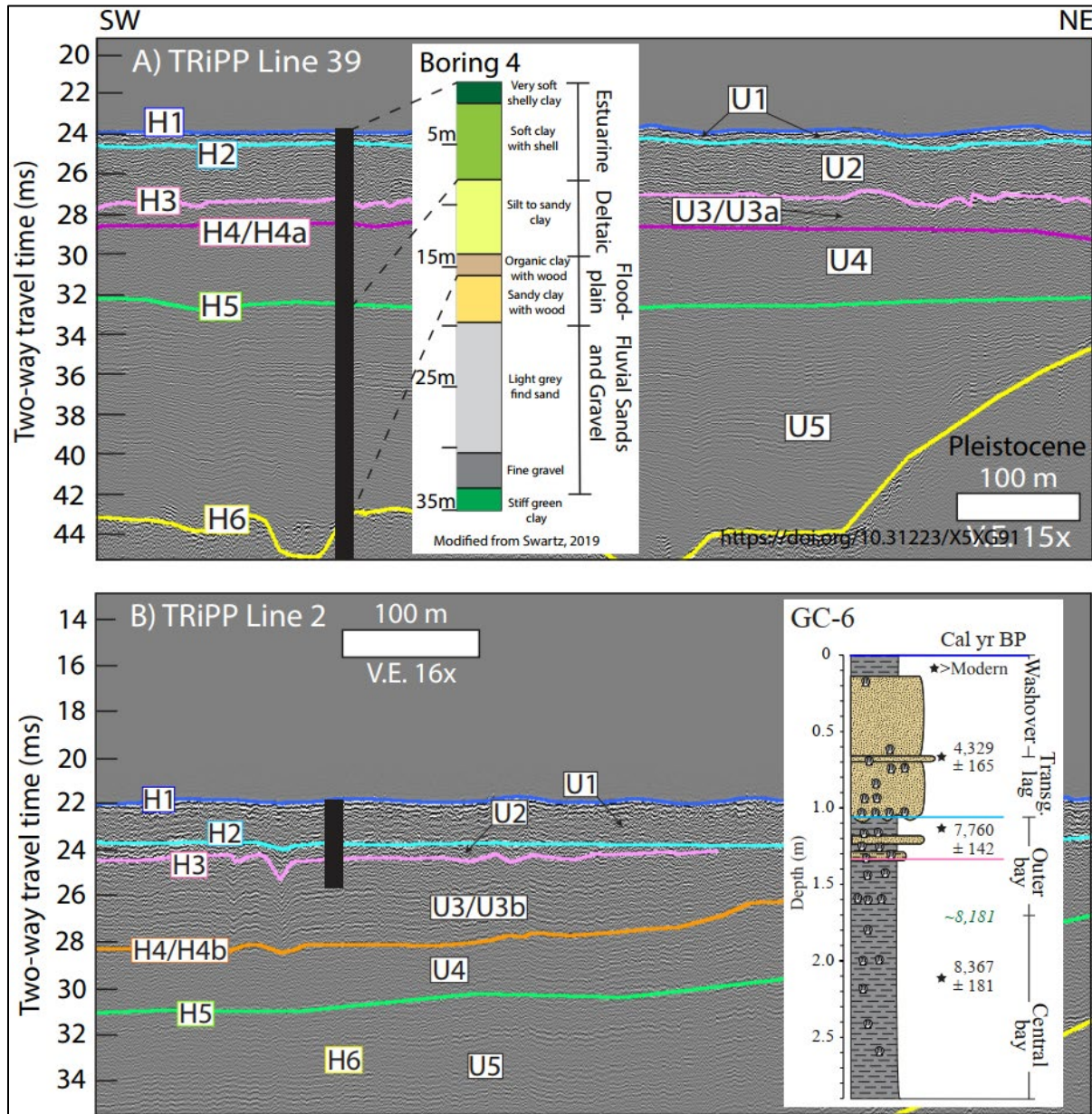


**Figure 7.12. Boring 4 and Gravity Core 6**

A) Interpretation of full-waveform data on TRiPP Line 39. Displayed here is a strike-oriented line, which is tied to Boring 4 from Thomas (1991), and modified from Swartz et al. (2022). Paleoenvironmental shifts interpreted by Thomas (1991) are correlated to seismic stratigraphy. U5, U4, U3/U3a, U2, and U1 are bound by horizons H6, H5, H4/H4a, H3, H2, and H1. The location for this chirp line and boring can be found in **Figure 7.3**. B) Interpretation of full-waveform data on TRiPP Line 2. Displayed here is a strike-oriented line, which is tied to gravity core GC-6 modified by Standring et al. (2021). The core description provides lithologic information, foraminifera sample locations (black stars), radiocarbon dates (small black text), interpolated ages from age models (small green text), and paleoenvironmental interpretations. Horizons that are penetrated by the core are displayed as colored lines. The location for this chirp line can be found in **Figure 7.3**.

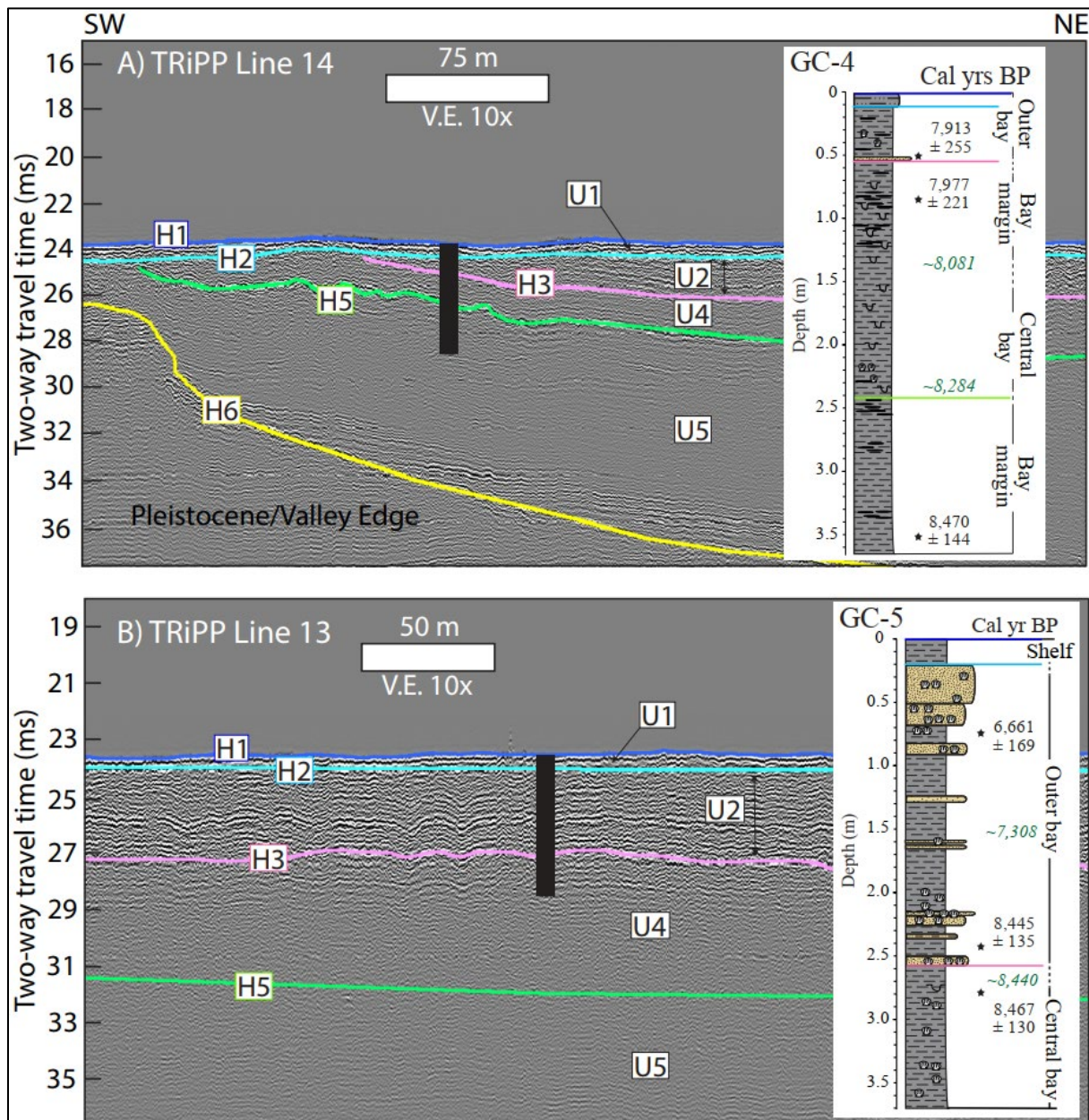


**Figure 7.13. Gravity Cores 4 and 5**

A) Interpretation of full-waveform data on TRiPP Line 14. Displayed here is a strike-oriented line, which is tied to gravity core GC-4 modified by Standing et al. (2021). The core description provides lithologic information, foraminifera sample locations (black stars), radiocarbon dates (small black text), interpolated ages from age models (small green text), and paleoenvironmental interpretations. Horizons that are penetrated by the core are displayed as colored lines. The location for this chirp line can be found in **Figure 7.3**. B) Interpretation of full-waveform data on TRiPP Line 13. Displayed here is a strike-oriented line, which is tied to gravity core GC-5 modified by Standing et al. (2021). The core description provides lithologic information, foraminifera sample locations (black stars), radiocarbon dates (small black text), interpolated ages from age models (small green text), and paleoenvironmental interpretations. Horizons that are penetrated by the core are displayed as colored lines. The location for this chirp line can be found in **Figure 7.3**.

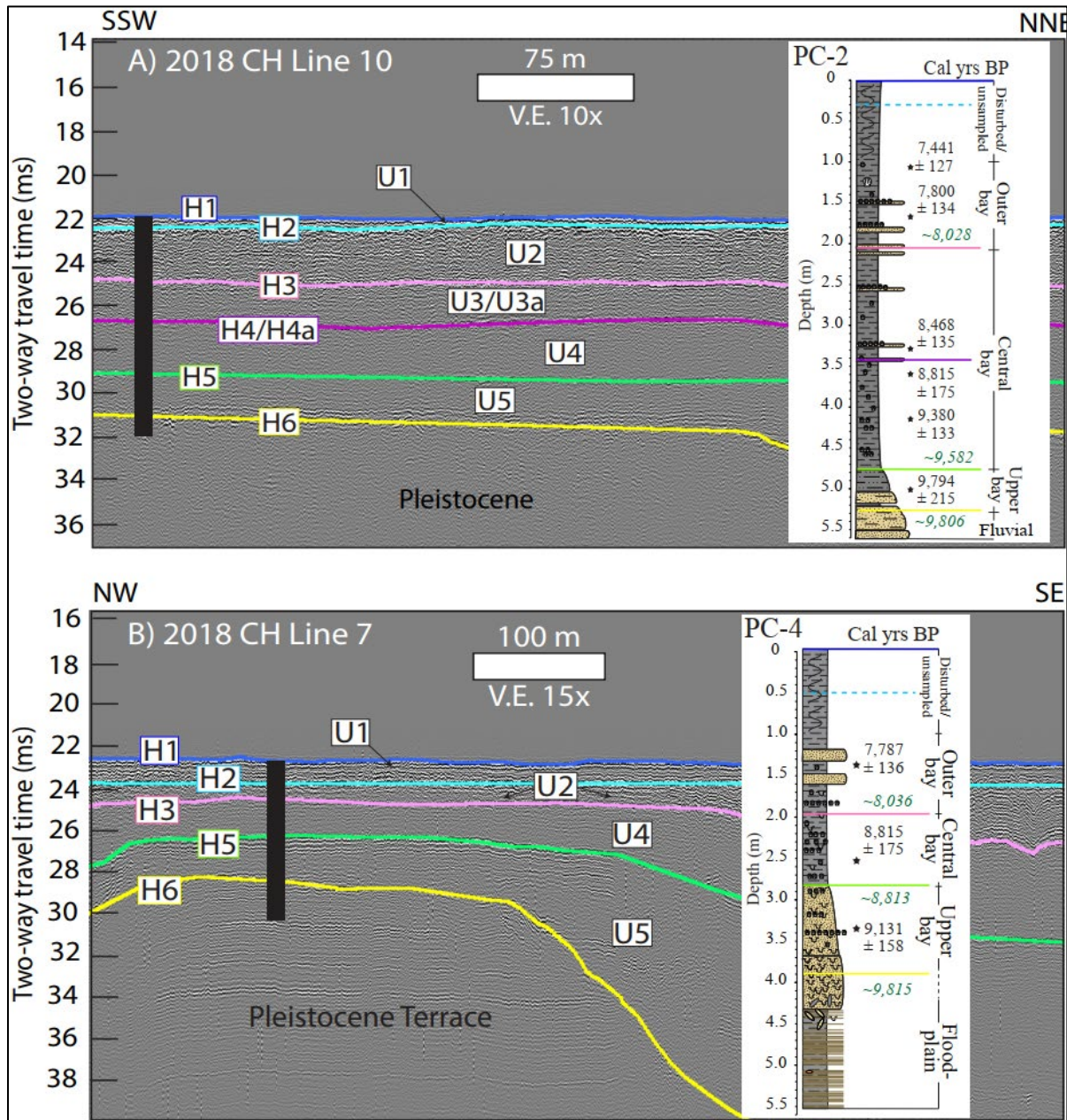


**Figure 7.14. Piston Cores 2 and 4**

A) Interpretation of full-waveform data on 2018 CH Line 10. Displayed here is a dip-oriented line, which is tied to piston core PC-2 modified by Standring et al. (2021). The core description provides lithologic information, foraminifera sample locations (black stars), radiocarbon dates (small black text), interpolated ages from age models (small green text), and paleoenvironmental interpretations. Horizons that are penetrated by the core are displayed as colored lines. The location for this chirp line can be found in **Figure 7.3**. B) Interpretation of full-waveform data on 2018 CH Line 7. Displayed here is a dip-oriented line, which is tied to piston core PC-4 modified by Standring et al. (2021). The core description provides lithologic information, foraminifera sample locations (black stars), radiocarbon dates (small black text), interpolated ages from age models (small green text), and paleoenvironmental interpretations. Horizons that are penetrated by the core are displayed as colored lines. The location for this chirp line can be found on **Figure 7.3**.

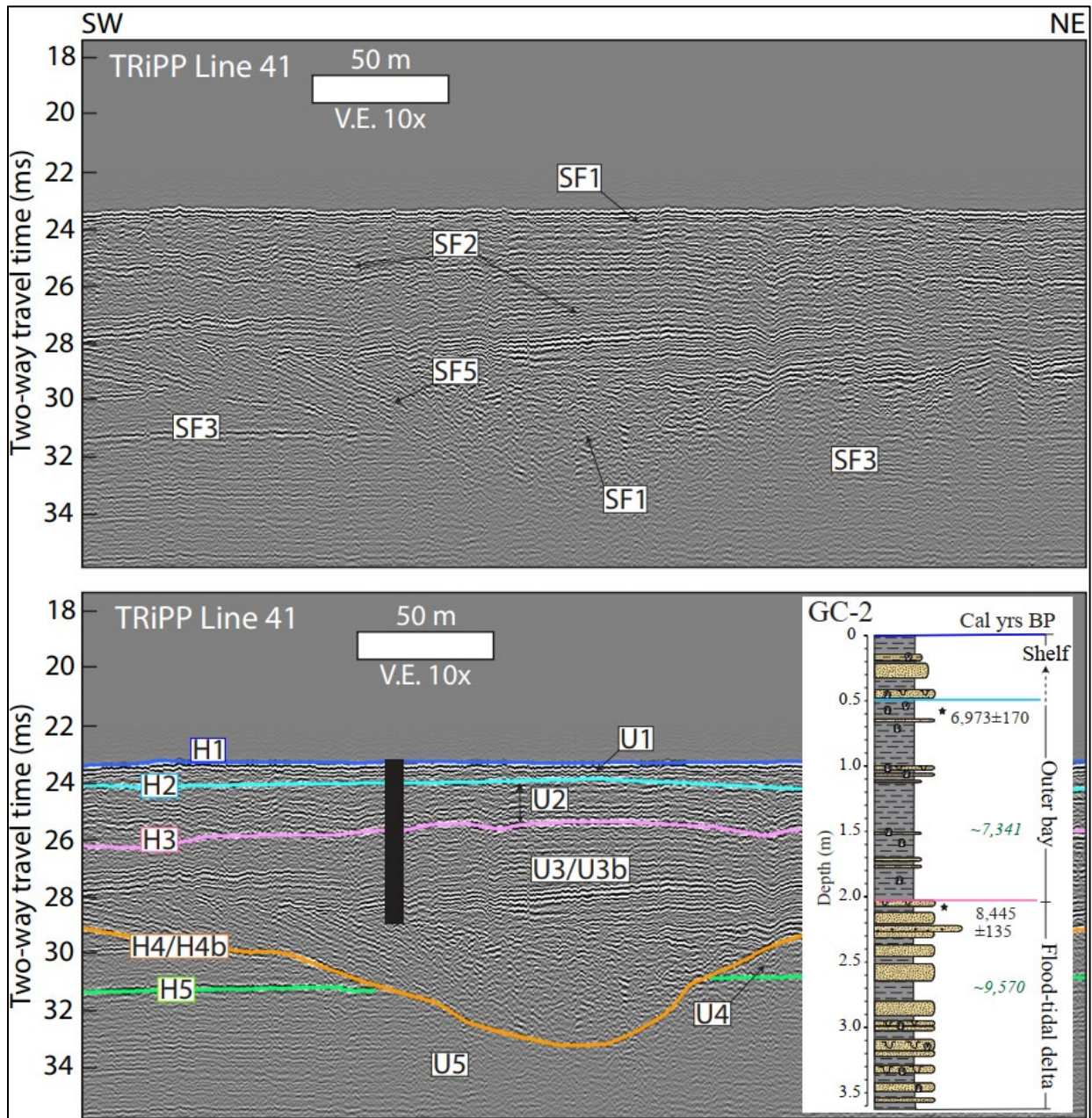


**Figure 7.15. Gravity Core 2**

Top: Seismic facies analysis of full-waveform data on TRiPP Line 41. Bottom: Interpretation of full-waveform data on TRiPP Line 41. Displayed here is a strike-oriented line, which is tied to gravity core GC-2 modified by Standing et al. (2021). The core description provides lithologic information, foraminifera sample locations (black stars), radiocarbon dates (small black text), interpolated ages from age models (small green text), and paleoenvironmental interpretations. Horizons that are penetrated by the core are displayed as colored lines. The location for this chirp line can be found in **Figure 7.3**.

#### 7.4.2.7 Horizon H5

H5 is a varying amplitude reflection that onlaps the incised valley walls (**Figures 7.5, 7.6, 7.16**) or is truncated by H2 along the valley margins (**Figures 7.5, 7.8, 7.13A**). This horizon varies between 23 and 37 ms depth (~17.5 and 28 mbsl). (**Figure 7.18-H5**). H5 is extensive throughout most of the study area, but frequently truncated by H4, H4a, and H4b within the seaward portion of the study area (**Figures 7.7–7.10, 7.15–7.17**), resulting in holes within the H5 horizon time-structure map (**Figure 7.18-H5**). This horizon is deepest within the seaward portion of the study area, reaching its maximum depth of 37 ms (~28 mbsl) within a 2 km wide channelized feature (**Figure 7.18-H5**). H5 then rapidly shallows toward the valley margins and the landward portion of the study area (**Figure 7.18-H5**). H5 has been previously interpreted as the boundary between underlying deltaic or upper-bay sediments and overlying bay sediments (Thomas, 1991; Swartz et al, 2022; Chapter 6).

#### 7.4.2.8 Horizon H6

H6 is a low-to-high-amplitude planar to rugose reflection (**Figures 7.–7.9, 7.11, 7.12A, 7.13A, 7.14A–7.14B, 7.16**). This horizon varies between 19 ms depth (~14.5 mbsl) and 50 ms depth (~38 mbsl) (**Figure 7.18-H6**). Along the edges of the valley, H6 truncates strata lying outside the valley, while strata within the valley onlap this surface (**Figures 7.6, 7.8, 7.13A**). This horizon has been previously interpreted as a sharp acoustic and sedimentological boundary between underlying fluvial sediments and overlying deltaic sediments (**Figure 7.12A**; Thomas 1991; Thomas et al., 1994; Swartz et al., 2022; Chapter 6).

### 7.4.3 Seismic Units

Seven seismic units are bound by these eight upper and lower seismic horizons (**Figures 7.5–7.17**). The units have been characterized by bounding surface stratigraphic position and seismic facies association, and ground-truthed by stratigraphic and foraminiferal core data (**Figures 7.12–7.15**). Time-thickness maps, or isopachs, were created using a combination of Python and GMT 6 programming scripts by differencing the two-way travel time for bottom and top boundaries of the identified seismic unit, and then gridding and interpolating these values onto 50-meter cells (**Figure 7.19**). Seismic units were converted from two-way travel time in milliseconds to thickness in meters using an average velocity through unconsolidated sand/mud of 1525 m/s (Abdulah et al., 2004).

#### 7.4.3.1 Unit 1–Transgressive Deposits (U1)

U1 has an upper boundary of H1, a lower boundary of H2, and is composed of SF1 (**Figures 7.5–7.17**). This unit ranges in thickness from 0 to 2.8 ms (~0 to 2 m) (**Figure 7.19-U1**) and is unique in that it is the only unit in this study to have been deposited beyond the valley walls. Sediments cored from this unit vary from uncompacted, “soupy” sediments (**Figures 7.13–7.14**) to coarser-grained sediments (**Figures 7.12B, 7.15**). U1 is generally thinnest along the western portion of the study area, where its lower bounding horizon U2 amalgamates near or directly with the seafloor and corresponds to disturbed core samples due to uncompacted sediment (**Figure 7.14**). Where U1 is better preserved in flat-lying regions, foraminiferal data, which display an overall increase in diversity (Standring et al., 2021), reveal U1 is likely derived from an inner shelf environment (**Figures 7.13B, 7.15**).

This unit reaches its greatest thickness along the eastern portion of the study area where it infills deep channel-like features formed by the horizon H2 (**Figures 7.12B, 7.18, 7.19**). Sediment cored from the margin of the largest of such channel-like features shows U1 to be composed of an ~0.8 m package of sandy sediments (**Figure 7.12B**). This coarse-grained package overlies horizon H2, which is observed to truncate the underlying H3 horizon (**Figure 7.12B**). Foraminiferal analysis of this isolated package shown

in GC-6 reveal U1 is likely composed of one or multiple washover deposits overlying an erosive transgressive lag deposit (**Figure 7.12B**; Standring et al., 2021).

Dating this unit is difficult due to the removal of material above the transgressive ravinement, apart from a single radiocarbon date taken from a mollusk shell dated to ~4.3 ka (**Figure 7.12B**; Standring et al., 2021). However, age models performed on environmental transitions indicate that the paleo-estuary likely transitioned to an inner shelf environment by ~6.9 ka (Standring et al., 2021). Therefore, U1 is interpreted as a time-transgressive, patchy veneer of sediment composed of either uncompacted fine-grained material derived from an inner shelf environment, or ~2 m thick coarse-grained package composed of washover deposits and transgressive lags derived from a relict barrier, forming at least by ~6.9 ka, and persisting through ~4.3 ka. These unconsolidated muds, sands, and shells are interpreted to be associated with the transgressive ravinement, reworking underlying material over a span of ~2.6 kyr (Nummendal and Swift, 1987; Swift and Thorn, 1991; Cattaneo and Steel, 2003).

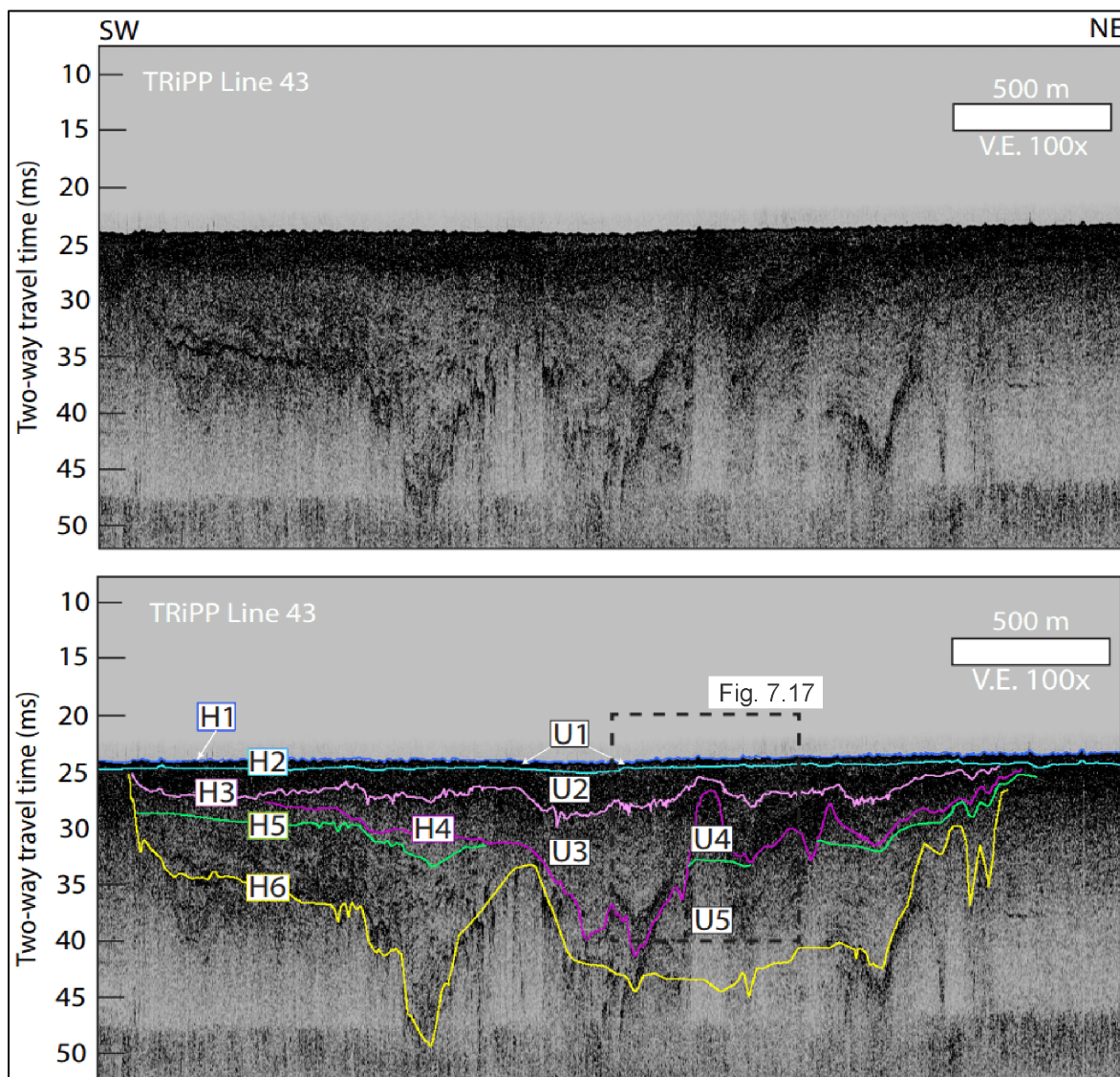


**Figure 7.16.** TRiPP Line 43 envelope record

Uninterpreted (top) and interpreted (bottom) envelope chirp data of strike-oriented TRiPP Line 43 displaying the seismic horizons (H1–H6) that bound seismic units (U1–U5). This is the seaward-most strike-oriented line in this study, displaying a very narrow incised valley extent (~2.5 km in width) funneling the tidal inlet and delta units (U3) toward the eastern (right) side of the valley. Inset indicates the location for **Figure 7.17**. The location for this chirp line can be found in **Figure 7.3**.

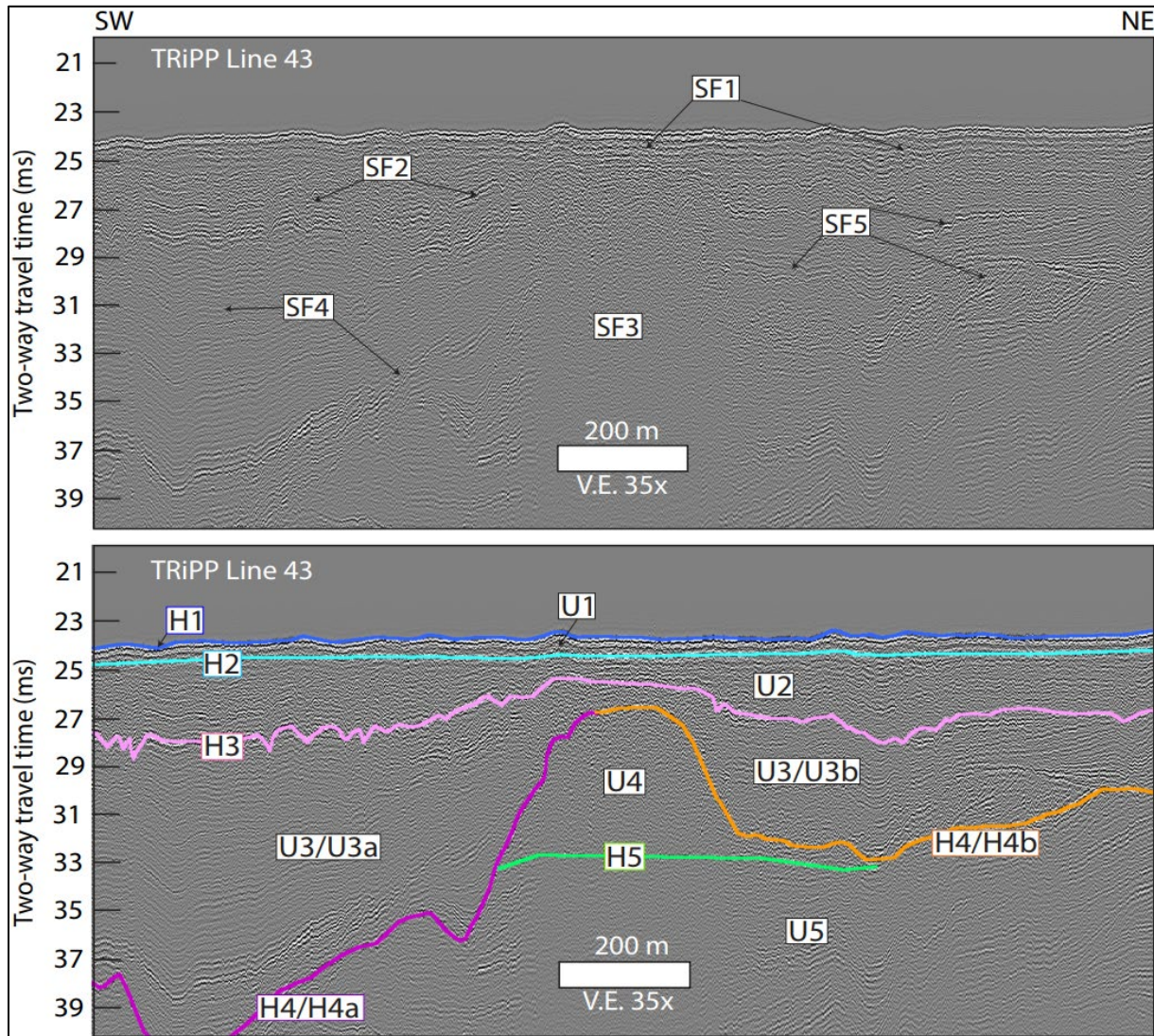


**Figure 7.17. TRiPP Line 43 full waveform record**

Top: Seismic facies analysis of full-waveform data on TRiPP Line 43. Bottom: Interpretation of full-waveform data on TRiPP Line 43. Displayed here is a strike-oriented line, highlighting the differences in seismic facies composing U3/U3a (SF4 = tidal inlet) and U3/U3b (SF5 = tidal delta). Both of these units' lower-bounding horizons (H4/H4a and H4/H4b) truncate H5. H3, which forms the lower boundary of U2, is observed to truncate reflections composing U3/U3a-b. U2 is composed of SF2, characterized as U-shaped, aggrading reflections, which are subsequently truncated by H2. H1 is the seafloor. The location for this chirp line can be found in **Figures 7.16** and **7.3**.

#### **7.4.3.2 Unit 2–Outer Bay (U2)**

U2 has an upper boundary of H2, a lower boundary of H3, and is composed of SF2 (**Figures 7.5–7.17**). This unit ranges in thickness from ~0 to 5.5 ms (~0 to 4.2 m) (**Figure 7.19-U2**). Unit 2 is generally thickest within the western portion of the study area where it fills available accommodation created by underlying stratigraphy (**Figures 7.5–7.7, 7.12A, 7.13A–7.13B, 7.14A, 7.16, 7.17**). This unit shallows toward the east and the valley margins (**Figures 7.8, 7.12B, 7.16, 7.17**), as well as over fluvial terraces (**Figures 7.9, 7.14B, 7.16**), where there is less accommodation is present. Erosion at the base of this unit along H3 is observed to truncate reflections within underlying seismic units U3 (**Figures 7.7, 7.8, 7.10, 7.11, 7.15, 7.16, 7.17**) and U4 (**Figures 7.5, 7.13B**). The U-shaped channels, which describe seismic facies SF2 and compose U2, are generally ~15 m wide and 0.75 ms (~0.5 m) deep (**Figures 7.6–7.8, 7.10–7.15**). These are propagated upwards throughout the section, effectively preserving this channel-form throughout its cut-and-fill history. Cores through this unit indicate its composition varies from mostly muddy sediments (**Figure 7.13A**) to mud interbedded with numerous sand layers (**Figures 7.12B, 7.13B, 7.14A–7.14B, 7.15**).

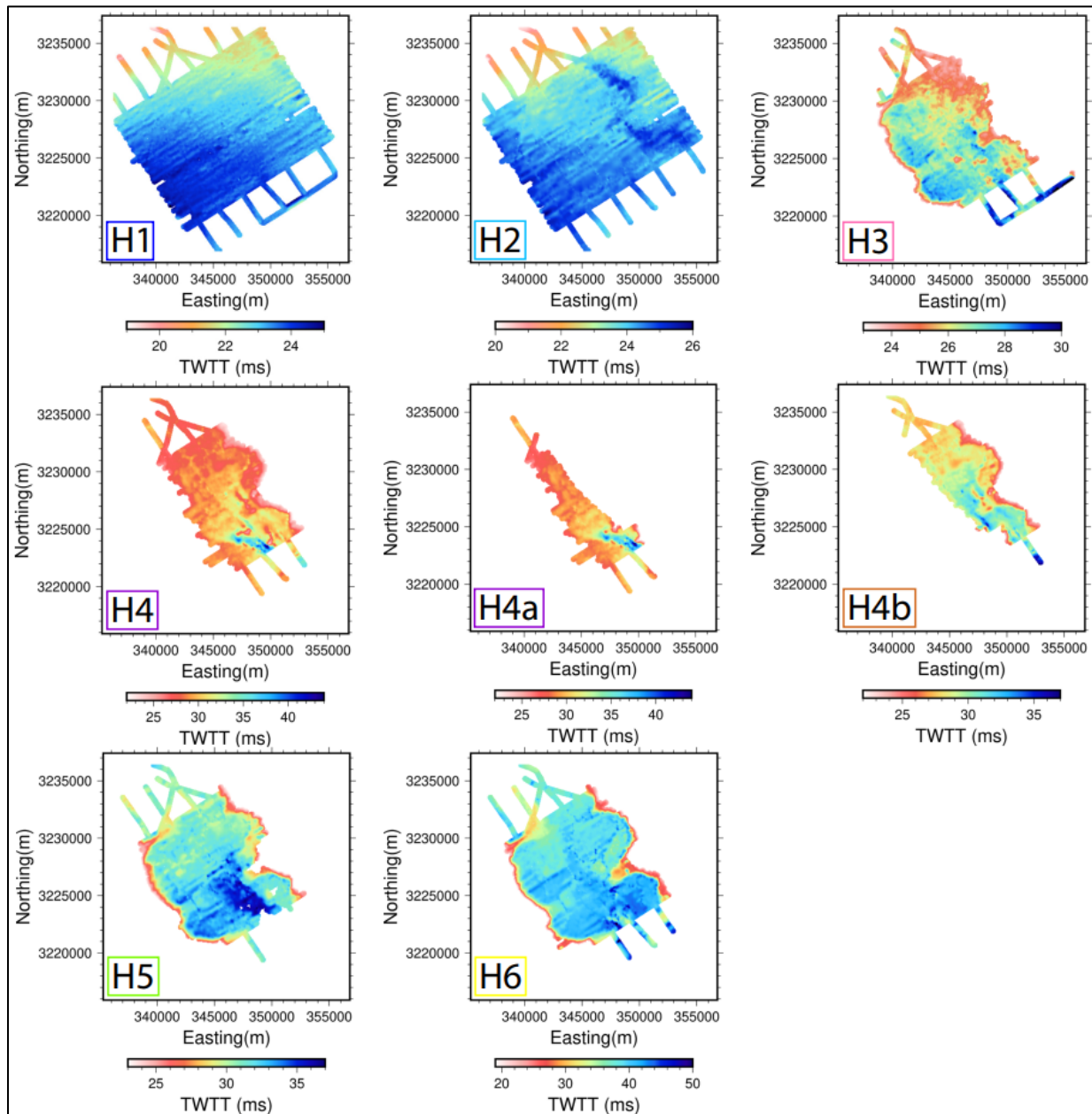


**Figure 7.18 Time-structure maps**

Time structure maps, measured in milliseconds two-way travel-time, of seismic horizons mapped in this study. When relevant, these values are converted to depth (mbsl) using an average velocity of 1525 m/s (Abdulah et al., 2004).

These observations, along with high percentages of the benthic foraminiferal assemblage *Elphidium* (Standring et al., 2021), suggest Unit 2 formed in an outer bay environment—a high-energy environment just landward of the paleo-barriers subject to frequent variations in energy source, ranging from tidal, storm, and wave processes (Dalrymple et al., 1992; Zaitlin et al., 1994). Radiocarbon dates within this unit suggest it began forming no later than ~8.5 ka, lasted until ~6.9 ka (Standring et al., 2021).

### 7.4.3.3 Unit 3–Tidal Fill (U3)

U3 has an upper boundary of H2 and H3, and a lower boundary of H4/H4a/H4b (**Figures 7.5, 7.7–7.12, 7.14A, 7.15–7.17**). This unit is generally composed of SF4 and SF5 (**Figures 7.7, 7.8, 7.11, 7.15, 7.20**), but occasionally displays SF1 near the bottom of the unit (**Figures 7.10, 7.11, 7.15**), and SF2 and SF3 within the unit (**Figures 7.8, 7.10, 7.12, 7.13, 7.15, 7.17**).

This unit ranges in thickness from ~0 to 16 ms (~0 to 12 m) (**Figure 7.19-U3**) and is thickest within the seaward portion of the study area where it infills an ~11 km long, 3.5 to 5 km wide channel-like feature along horizon H4/H4a that rapidly shallows landward and to the west (**Figures 7.5, 7.9, 7.17**). The fill of this large channel-like feature is composed of SF4, but rapidly changes to SF3 in the landward portion of the study area (**Figures 7.12A, 7.14A**).

Additionally, U3 is observed within the eastern portion of the study area overlying the erosive, channelized horizon H4/H4b, and composed of SF1 and SF5 (**Figures 7.8, 7.10, 7.11, 7.15, 7.17**), but rapidly transitions to SF2 within the unit (**Figures 7.8, 7.10, 7.12B, 7.15**).

Based on this unit's stratigraphic position, the highly erosional and channelized nature of its basal horizons H4, H4a, and H4b, this unit is interpreted as tidal fill encompassing both tidal inlet and tidal delta sediments. This is a high tidal energy environment proximal to the barriers (Dalrymple et al., 1992; Zaitlin et al., 1994). Unit 3 is divided into two sub-units–U3a and U3b–based on their association with SF4 and SF5, respectively.

### 7.4.3.4 Unit 3a–Tidal Inlet Fill (U3a)

U3a has an upper boundary of H3, and a lower boundary of H4a (**Figures 7.7, 7.12A, 7.14A, 7.17**). This unit is composed of SF4 within the seaward portion of the study area (**Figures 7.7, 7.17**), and SF3 within the landward portions of the study area (**Figures 7.12A, 7.14A**). This unit varies in thickness from ~0 to 16 ms (~0 to 12 m) (**Figure 7.19-U3a**). U3a is thickest toward the seaward portion of the study area within an 11 km long, 1 to 2 km wide, 16 ms (~12 m) deep channel along horizon H4a that curves toward the northwest, interpreted as the tidal inlet (**Figure 7.19-U3a**). Although this unit is present within an 11 km long channelized feature, the highly erosive nature of its basal horizon H4a is most evident within the first 5 km of the seaward portion of the study area (**Figure 7.18-H4a**). Within this erosive channel form, U3a is composed of SF4, characterized by internal reflections that onlap adjacent erosional surfaces within the unit, and are generally arranged in a draping pattern that reflects its deeply incised, channelized lower boundary. This cut-and-fill reflector configuration is indicative of multiple aggradational packages separated by periods of erosive channel formation, which is commonly observed within paleo-tidal inlets (Siringan and Anderson, 1993; Anderson et al., 2008; Storms et al., 2008; Ronchi et al., 2018, 2019).

U3a transitions to SF3 toward the landward portion of the study area, consisting of low-amplitude, parallel, laminated to transparent reflections (**Figures 7.12A, 7.14A**). Coring through the landward portion of this unit by PC-2 reveals it is mostly composed of mud with some sandy intervals containing foraminiferal assemblages indicative of a central bay environment (**Figure 7.14A**). A radiocarbon date found within PC-2 returns a date of ~8.5 ka for this unit (**Figure 7.14A**; Standring et al., 2021). The landward transition in seismic facies from draping, onlapping reflections (SF4) to parallel, laminated reflections (SF3) filling the tidal inlet has been interpreted as the stratigraphic response to filling an empty tidal inlet, resulting in SF4, versus filling an almost-completely filled one (e.g., Storms et al., 2008; Zecchin et al., 2008; Ronchi et al., 2018, 2019).

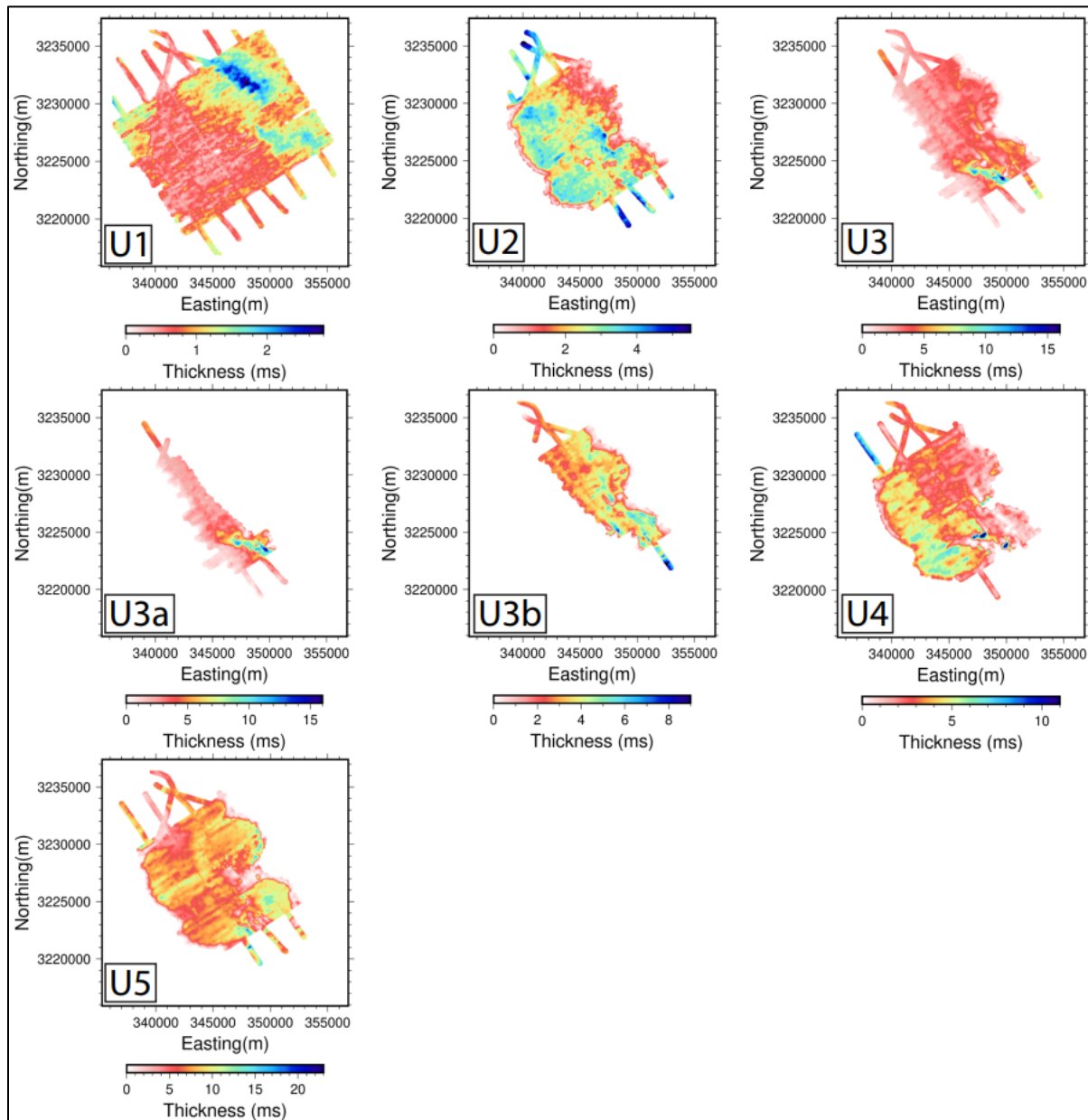


**Figure 7.19. Time-thickness maps**

Time thickness maps measured in milliseconds two-way travel-time, of seismic units mapped in this study. When relevant, these values are converted to depth (mbsl) using an average velocity of 1525 m/s (Abdulah et al., 2004).

#### 7.4.3.5 Unit 3b–Tidal Delta Fill (U3b)

U3b has an upper boundary of H2 and a lower boundary of H4b (Figures 7.8, 7.10, 7.11, 7.12B, 7.15, 7.17). This unit is generally composed of SF1 and SF5 near its base (Figures 7.8, 7.10, 7.11, 7.15, 7.17), and SF2 within the unit (Figures 7.8, 7.10, 7.12B, 7.15). U3b ranges in thickness from ~0 to 9 ms (~0 to 7 m) (Figure 7.19-U3b), where it is thickest within 11 km long, 50 to 75 m wide, 5.5 to 9 ms (~4 to 7 m) deep channels that meander along the eastern portion of the study area, and thinnest along the valley margins (Figure 7.19-U3b). SF5 is common within the base of these channels: unidirectional dipping

internal reflections that display progradation and lateral accretion (**Figures 7.8, 7.11, 7.15, 7.17**). Seismic characteristics of this nature have been commonly associated with tidal deltas (Siringan and Anderson, 1993; Rodriguez et al., 1998, 2005; Anderson et al., 2008). SF1 is also common within the base of these channels, observed as chaotic to discontinuous reflections with internal truncations (**Figures 7.10, 7.11, 7.15**). Commonly, SF5 lies adjacent to SF1 (**Figures 7.11, 7.15**), where unidirectional dipping reflections (SF5) transition into chaotic to discontinuous reflections (SF1) within a short distance. It is possible that stratigraphically these facies both represent dipping, laterally accreting strata composing the tidal delta unit, but is at times not well-imaged either due to large grain sizes or unfavorable dip directions, resulting in SF1.

Coring of this unit by GC-2 further lends support for the interpretation that U3b is a tidal delta (**Figure 7.15**), in which its unidirectional dipping, laterally accreting reflections are observed to be composed of muds with numerous layers of silty sand. Carbon dates taken from the transition from tidal delta to outer bay sediments in GC-2 (**Figure 7.15**) provided ages of ~8.5 ka, confirming this tidal delta was active during this time (Strandring et al., 2021).

SF2 is also common within this unit: a facies composed of high-amplitude, U-shaped, aggrading reflections commonly associated with an outer bay environment proximal to the barriers (**Figures 7.8, 7.10, 7.12B, 7.15**). This marked change from laterally accreting to aggrading reflections is likely due to a change in tidal regime associated with the infilling of the tidal inlet by ~8.5 ka, as observed in PC-2 (**Figure 7.14A**). Thus, as the tidal inlet unit U3a infilled by ~8.5 ka, the adjacent tidal delta unit U3b reflected this change in tidal regime by switching from a laterally accreting (SF1/SF5) to an aggrading (SF2) seismic facies.

#### **7.4.3.6 Unit 4—Central Bay (U4)**

U4 has an upper boundary of H2, H3, and H4, and a lower boundary of H5 (**Figures 7.5–7.10, 7.12–7.17**). This unit is primarily composed of SF3 (**Figures 7.6–7.8, 7.12–7.15, 7.17**). U4 varies in thickness from ~0 to 11 ms (~0 to 8.5 m) (**Figure 7.19-U4**). This unit is generally thickest within the western portion of the study area, passively filling accommodation left by underlying stratigraphy, and thinnest along the eastern margin where tidal-related horizons H4, H4a and H4b have heavily reworked it (**Figures 7.5, 7.7–7.10, 7.15–7.17**).

Coring of this unit indicates U4 is composed of mostly fine-grained mud, with some interbedded muddy sand intervals (**Figures 7.13, 7.14**). This fine-grained composition, along with foraminiferal evidence of a spike in *Ammonia* (Strandring et al., 2021), support the interpretation that these sediments were deposited in a low-energy, quiescent central bay environment landward of the barriers (e.g., Dalrymple et al., 1992; Zaitlin et al., 1994; Rodriguez et al., 2005; Anderson et al., 2008). Carbon dates from this unit found in PC-2 and PC-4 indicate that this environment initiated as early as ~9.6 ka (**Figure 7.14A**) and lasted until ~8.0 ka, when it transitioned to an outer bay environment (**Figure 7.14**; Strandring et al., 2021).

Although U4 is generally thickest in the western portion of the study area, U4 reaches its maximum thickness in the form of three mound-like features measuring ~500 m in width, ~8 m in height (**Figures 7.5, 7.7, 7.9, 7.16, 7.17, 7.19**). Goff et al. (2016) have interpreted similar mound-like features in Corpus Christi Bay, Texas as fossil oyster reefs, described as having a high-amplitude, draping reflection as its upper boundary, a chaotic to acoustically blank interior, a varying amplitude, planar reflection at its base, and adjacent onlapping reflections. A similar configuration is observed within the mound-like features in this study, having a high-amplitude upper boundary defined by H4, H4a, and H4b, a chaotic to acoustically blank interior associated with SF3, a varying amplitude lower boundary defined by H5, and adjacent onlapping reflections by U3a and U3b (**Figures 7.7, 7.17**). These mound-like features have not

been sampled, so their depositional environment cannot be confirmed without further investigation into its stratigraphic and palaeontologic composition.

#### **7.4.3.7 Unit 5–Bayhead Delta (U5)**

U5 has an upper boundary of H2, H4, and H5 and a lower boundary of H6 (**Figures 7.5–7.17**), and varies in thickness between ~0 to 23 ms (~0 to 17.5 m) (**Figure 7.19-U5**). This is the thickest unit observed in this study, composing over half of the total incised valley fill. This unit is thinnest along the flanks of the valley (**Figures 7.5, 7.6, 7.8, 7.13A, 7.17**), above or adjacent to underlying Pleistocene fluvial terraces (**Figures 7.9, 7.14, 7.16**), or when it is heavily reworked by tidal-related horizons units H4, H4a, and H4b within the seaward portion of the study area (**Figures 7.7, 7.8, 7.11, 7.15–7.17**). U5 is thickest when it is filling in accommodation provided by the underlying fluvial geology (**Figures 7.5, 7.9, 7.12A, 7.16**), as evidenced by the correlation between its lower bounding horizon H6 (**Figure 7.18-H6**) and lateral variations in thickness of U5 (**Figure 7.19-U5**).

This unit is primarily composed of high-amplitude, laterally accreting to aggrading reflections (**Figures 7.5–7.15**; Swartz, 2019; Thomas, 1991). Coring of this unit reveals it is composed of very fine to fine sands, organic rich muds and clays, and clays interbedded with fine sandy layers with organic wood fragments and plant debris (**Figures 7.12A, 7.14**; Thomas, 1991). Lack of foraminifera in these sediments suggest a terrestrial depositional environment. Therefore, sediments in U5 are interpreted as deriving from an upper bay or bayhead delta environment (Swartz et al., 2022; Chapter 6).

Age models from cores PC-2 (**Figure 7.14A**) and PC-4 (**Figure 7.14B**) indicate that the environment transitioned from fluvial to upper bay ~9.8 ka (Standring et al., 2021). This upper bay environment lasted until at least ~8.8 ka as the system was inundated and transitioned into a central bay environment (**Figure 7.14B**).

## **7.5 Discussion**

### **7.5.1 Preservation of Estuarine Deposits**

As rising sea levels act upon a barrier island system, features of the coastal lithosome are generally eroded by wave, storms, and tidal forces associated with the transgressive ravinement (e.g., Swift and Thorn, 1991; Cattaneo and Steel, 2003). Commonly referred to as a “wave ravinement surface” (e.g., Allen and Posamentier, 1993; Cattaneo and Steel, 2003) to highlight the assumed erosive mechanism, the creation of this surface has also been attributed to downwelling coastal storm currents (Swift and Thorn, 1991) and major storms (Goff et al., 2015). Generally, this strong erosive action removes estuarine sediments, and transfers eroded sediment seaward from the barrier island system to the marine sediment sheet overlying the ravinement. Due to the erosive nature of the transgressive ravinement, subaerial and shallow features of the barrier island system, including the barriers themselves, are often removed, preserving only deep back-barrier sediments, such as bay and tidal facies, within the stratigraphic record (Ronchi et al., 2018; Ronchi et al., 2019).

There have been documented studies within the Adriatic Sea (Storms et al., 2008) and Tijucas Bay, Brazil (Cooper et al., 2016), investigating the preservation of the barriers throughout transgression through a process called “overstepping”, in which the barrier is stranded on the continental shelf as a marine sand body (Carter, 1988). The overstepping and preservation of the barrier during transgression has been attributed to rapid sea-level rise, rapid increase in back-barrier accommodation, little wave action, or rapid burial by shoreface sediments (Storms et al., 2008; Cooper et al., 2016).

This is one interpretation of paleoshoreline evolution across the northern Gulf of Mexico, wherein Sabine and Heald Banks are interpreted as relict, overstepped barriers preserved on the inner shelf as sand bodies (**Figure 7.2**; Rodriguez et al., 1999; Rodriguez et al., 2004). Sabine bank is located approximately 30 km offshore in water depths of 5 to 12 m, while Heald banks is approximately 45 km offshore in 9 to 15 m water depth. Rodriguez et al. (2004) claim that these shorelines retreated over terraced fluvial deposits within the Trinity-Sabine incised valley, which served as local sand sources for barrier island stabilization and persistence throughout sea-level rise. These barriers were then overstepped and stranded on the inner shelf as isolated sand bodies once these fluvial sand sources were depleted, sea-level rise reached a critical threshold, or both (Rodriguez et al., 2004).

Conversely, it has been proposed that the origin of modern sand banks is not as drowned, overstepped, detached barriers (i.e., Snedden et al., 1999), but rather as modern marine deposits that have reworked underlying remnant estuarine and tidal deposits (Thomas and Anderson, 1994; Dyer and Huntley, 1999). Thomas and Anderson (1994) observe that Sabine and Heald Banks overlie a ravinement reworking underlying estuarine and tidal delta facies. Thus, it is possible that these sand banks have a marine origin forming from the reworking of remnant estuarine and tidal facies, rather than as drowned, overstepped barriers.

In this study, erosion associated with the transgressive ravinement, interpreted as the H2 horizon, has significantly reworked underlying estuarine sediments (**Figures 7.5–7.17**), and completely eroded and removed the barrier within our study area. Observations of interpreted overstepped barriers include elongated, shore-parallel sand bodies with reflectors that prograde both seaward and landward, with a coarsening-upward stratigraphic composition (Storms et al., 2008; Cooper et al., 2016). These seismic stratigraphic and lithologic indicators are not observed within this study, supporting the interpretation that the paleo-barrier within this study area was not overstepped, but instead completely removed by transgressive erosion.

Despite significant transgressive erosion, considerable preservation of deltaic (U5) and back-barrier (U2–U4) strata is observed in this study (**Figures 7.5–7.17**). The transgressive ravinement (H2) is observed to rework shallow back-barrier units (U2, U3, U3a, U3b), while only reworking the distal flanks of the deeper central bay and bayhead delta units along the valley edges (U4, U5). Although preservation of the barrier can give excellent insights into the mode in which the estuarine system transgressed (i.e., erosional, rollover, overstepping Carter, 1988), preserved deltaic, bay, and tidal facies can provide convincing spatial and temporal evidence for understanding the morphological evolution of the estuarine system throughout transgression (i.e., Ronchi et al., 2018; 2019).

### **7.5.2 Estuarine Interaction with Underlying Geology**

Heterogeneity in the underlying, antecedent geology in which the barrier island system transgresses has long been recognized as a major control on its evolution (e.g., Belknap and Kraft, 1985; Riggs et al., 1995; Mallinson et al., 2018; Shawler et al., 2020). These are often paleodrainage systems that cut into the landscape by fluvial incision during subaerial exposure, and now filled with fluvial, coastal, and shelf facies as the system was flooded (e.g., Allen and Posamentier, 1993; Dalrymple et al., 1992; Zaitlin et al., 1994). Deep topographic lows cut by the paleodrainage system form the incised valley and are important in defining the estuaries which transgress them, including controlling the location of the tidal inlet (Morton and Donaldson, 1973). Additionally, topographic highs in the form of fluvial interfluves and terraces provide both increased elevation in which barrier islands are pinned upon (e.g., Raff et al., 2018; Shawler et al., 2020), as well as sediment supply to the barrier via wave and tidal forces (e.g., Riggs et al., 1995; Anderson et al., 2016; Hollis et al., 2019). This study supports this growing body of literature and finds that the estuarine system is intimately controlled by its antecedent geology.

The underlying fluvial topography, interpreted as horizon H6 (**Figures 7.18-H6, 7.20B–7.20C**), is observed to control the morphology of all overlying units by providing accommodation in which subsequent stratigraphic units fill. H6 is observed as a channelized, erosional surface within the seaward portion of the study area, reaching depths of ~50 ms (~38 mbsl), and that gradually shallows landward within the valley to ~22 ms depth (~29 mbsl) (**Figures 7.18-H6, 7.20B–7.20C**). Where H6 is relatively deep, accommodation is created in which overlying units preferentially fill. This is clearly observed as the deep topography of H6 along the eastern and western flanks of the seaward portion of the study area correlate well with the lateral variations in thickness of seismic units U5, U4, U3, U3a, U3b and U2 (**Figures 7.18-H6, 7.19**). This is compounded by the observation that channels created by the underlying fluvial surface are propagated upward throughout the stratigraphic section, owing to the influence in which this surface has on the spatial variations in channelization of strata above (**Figures 7.5, 7.9, 7.11, 7.16**).

Beyond creating accommodation for estuarine sediments to fill, the morphology of the incised valley itself appears to promote barrier island initiation. **Figure 7.20A** displays a 20 ms envelope median coherency extracted for the approximate base of the Trinity incised valley (Swartz et al., 2022; Chapter 6). This coherency extraction, although likely incorporating anomalous amplitudes throughout the entire incised valley fill, shows the presence of sinuous channel forms, shallow fluvial terraces, lateral accretion surfaces, and a well-defined overall valley extent (Swartz et al., 2022; Chapter 6). In the seaward-most portion of the study area, the valley extent narrows to ~2.5 km in width (**Figures 7.18, 7.20A**), which rapidly widens landward to ~10 km in width (**Figures 7.5, 7.20A**) over a distance of ~1 km (**Figure 7.20A**). This framework effectively “bottlenecks” the estuarine system, promoting tidal units (U3, U3a, U3b) to preferentially deposit along the seaward and eastern portions of the study area (**Figures 7.16, 7.19, 7.20D**). The influence of the valley extent on determining the location of tidal deposits, and by proxy paleo-barrier island position (e.g., Thomas and Anderson, 1994; Rodriguez et al., 2004; Anderson et al., 2016), is best seen in **Figure 7.11**, where reflectors associated with the tidal delta unit (U3b) switch dip direction from landward-dipping to seaward dipping. Dip direction is a key indicator of flow direction, interpreted as landward-dipping, flood-tidal delta deposits, and seaward-dipping, ebb-tidal delta deposits (e.g., Rodriguez et al., 1998; Anderson et al., 2008). The presence of a fluvial terrace underlying this switch in tidal flow direction is thus interpreted as the underlying fluvial topography providing a direct “pinning point” for the barrier (e.g., Raff et al., 2018; Shawler et al., 2020). However, the underlying fluvial geology does not act as a sediment source for the paleo-barrier island system, which may be expected from previous studies (e.g., Riggs et al., 1995; Anderson et al., 2016; Hollis et al., 2019; Shawler et al., 2020). This is demonstrated by the top of fluvial sediments (H6) very rarely being truncated and reworked by overlying tidal (H4, H4a, H4b) or wave erosional surfaces (H2) (**Figures 7.5, 7.7–7.9, 7.11, 7.16**). Instead, sediment sources reworked by tidal units U3, U3a, and U3b, and supplied to the barrier island system, are preferentially from the bayhead delta (U5) and central bay (U4) units (**Figures 7.5, 7.7–7.10, 7.15–7.17**).

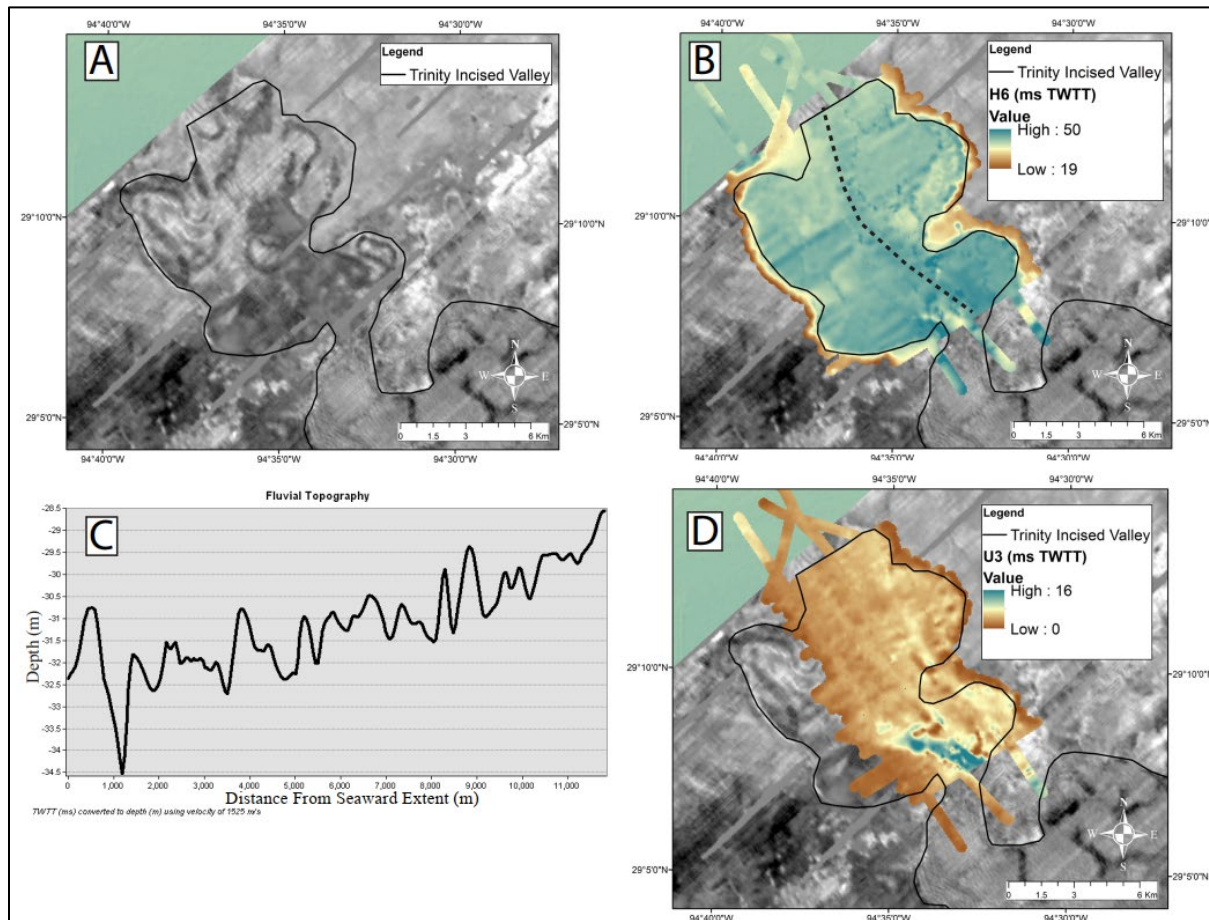


**Figure 7.20. Paleovalley morphology**

A) Coherency attribute extracted from 3D seismic data (modified from Swartz et al. (2022). Extraction displays sinuous channel forms, shallow fluvial terraces, lateral accretion surfaces, and a well-defined overall valley extent (bold black polygon). Valley observed to “bottleneck” toward the seaward extent, increasing from ~2.5 km in width, to ~10 km in width over a distance of ~1 km. B) A time-structure map of horizon H6, which is interpreted to be the top of fluvial strata, overlays the 3D coherency extraction. A topographic profile track is shown as a dotted line traveling up-dip. C) A topographic profile graph from panel B. Profile is taken over a depth-converted structure map of H6 to reflect the landward increase in elevation of the underlying, antecedent fluvial geology. D) A time-thickness map of U3, interpreted as the thickness of tidal deposits in the study area. Maximum thickness is seen within the paleo-inlet, displayed as an ~5 km long, 1 to 2 km wide, 16 ms (~12 m) deep channel. The extremely narrow extent of the incised valley is interpreted to control the preferential deposition of tidal inlet and tidal delta deposits along the seaward and eastern portions of the valley.

In addition, the relatively shallow fluvial topography within the landward portion of the study area provides decreased accommodation within the back-barrier, promoting the aggradation of barrier-proximal outer bay unit (U2) for ~2.5 ka (Figures 7.5–7.17; Standing et al., 2021). The transition from an active tidal inlet and tidal delta (PC-2, Figure 7.14A) or central bay environment (PC-4, Figure 7.14B) to an outer bay environment occurred ~8.5 ka (Standing et al., 2021), indicating the deactivation and infilling of the tidal inlet at this point in time. This evolution is manifested by the lower bounding surface of the outer bay unit (H3) truncating strata within tidal units, and depositing channelized, aggradational outer bay strata above (Figures 7.7, 7.8, 7.10, 7.11, 7.15–7.17) until the onset of inner shelf sediments (U1) ~6.9 ka (Standing et al., 2021). The deactivation of a tidal inlet has been proposed to be followed by the complete overstepping and in-place drowning of the barrier island system, wherein an

abrupt increase in back-barrier accommodation would increase tidal prism, drown low-lying marshes and tidal flats, and lead to the complete drowning of the estuary (FitzGerald et al., 2006; Fitzgerald et al., 2008; Storms et al., 2008; Ronchi et al., 2019). However, following the deactivation and closure of the tidal inlet, the landward increasing fluvial elevation helped to promote the vertical aggradation of outer bay strata, and possibly stability for the barrier island system, as opposed to retrogradation and barrier disintegration or overstepping associated with an increase in back-barrier accommodation. This finding therefore agrees with previous studies suggesting the reduced back-barrier accommodation provided by antecedent topographic highs can stabilize a barrier island system (e.g., Shawler et al., 2020).

### 7.5.3 Paleo-barrier Island Evolution

The initiation of the estuarine system within this study area is proposed to occur ~9.8–9.6 ka (**Figures 7.21A–7.21B**), indicated by the transition from a fluvial to upper bay/bayhead delta environment in cores PC-2 (**Figure 7.14A**) and PC-4 (**Figure 7.14B**; Standring et al., 2021). During this time, it has been proposed that a large, 75 km long estuary extended from approximately 20 km offshore modern Galveston Bay, to seaward of Thomas Bank (**Figure 7.21A**; Thomas and Anderson, 1994; Anderson et al., 2008, 2016). Thomas and Anderson (1994) identified a paired tidal inlet and upper bay/bayhead delta facies bound by upper and lower flooding surfaces, in which the tidal inlet facies was located just seaward of Thomas Bank (**Figure 7.21A**). A flood tidal delta facies was identified extending landward ~20 km from this tidal inlet location. The upper bay/bayhead delta sequence was located depositing within and landward of the confluence of the Trinity-Sabine river valleys, and of which its most landward extent reached into this study's area of focus (**Figure 7.21A**). Dating of this parasequence shows it initiated by ~10 ka (Thomas and Anderson, 1994), agreeing well with dates within cores PC-2 (**Figure 7.14A**) and PC-4 (**Figure 7.14B**) that an upper bay/bayhead delta environment existed within this study's area of focus during this time. Thus, we suggest that the upper bay/bayhead delta deposits observed in this study, identified as seismic unit U5, initiated ~9.8–9.6 ka, and represents the landward-most component of an estuary extending almost 75 km seaward (**Figures 7.21A–7.21B**; Thomas and Anderson, 1994).

At approximately 8.8 ka, the area transitioned from an upper bay/bayhead delta environment to a central bay environment (**Figures 7.21C–7.21D**), although PC-2 provides a date within this unit of ~9.6 ka (**Figure 7.14**; Standring et al., 2021). The deposition of central bay sediments (U4) draped on top of bayhead delta strata, passively filling accommodation, but was largely confined within the valley walls (**Figures 7.5, 7.6, 7.8, 7.13A, 7.16, 7.21C–7.21D**). Although the true extent of the bay may have extended beyond the valley extent, severe subsequent reworking by the tidal (H4, H4a, H4b) (**Figures 7.5, 7.7–7.10, 7.15–7.17**) and transgressive (H2) ravinements (**Figures 7.8, 7.13A**) limits this interpretation. It is also likely that the initiation of the tidal inlet and delta (U3a, U3b) occurred during this time (**Figures 7.21C–7.21D**), as carbon dates provided in GC-2 (**Figure 7.15**) and PC-2 (**Figure 7.14A**) provide an age of at least 8.5 ka (Standring et al., 2021). The extreme narrowing of the incised valley within the seaward and eastern portion study area effectively controlled the spatial extent of the tidal inlet and delta, and thus the location of barrier island (**Figures 7.20D, 7.21C–7.21D**).

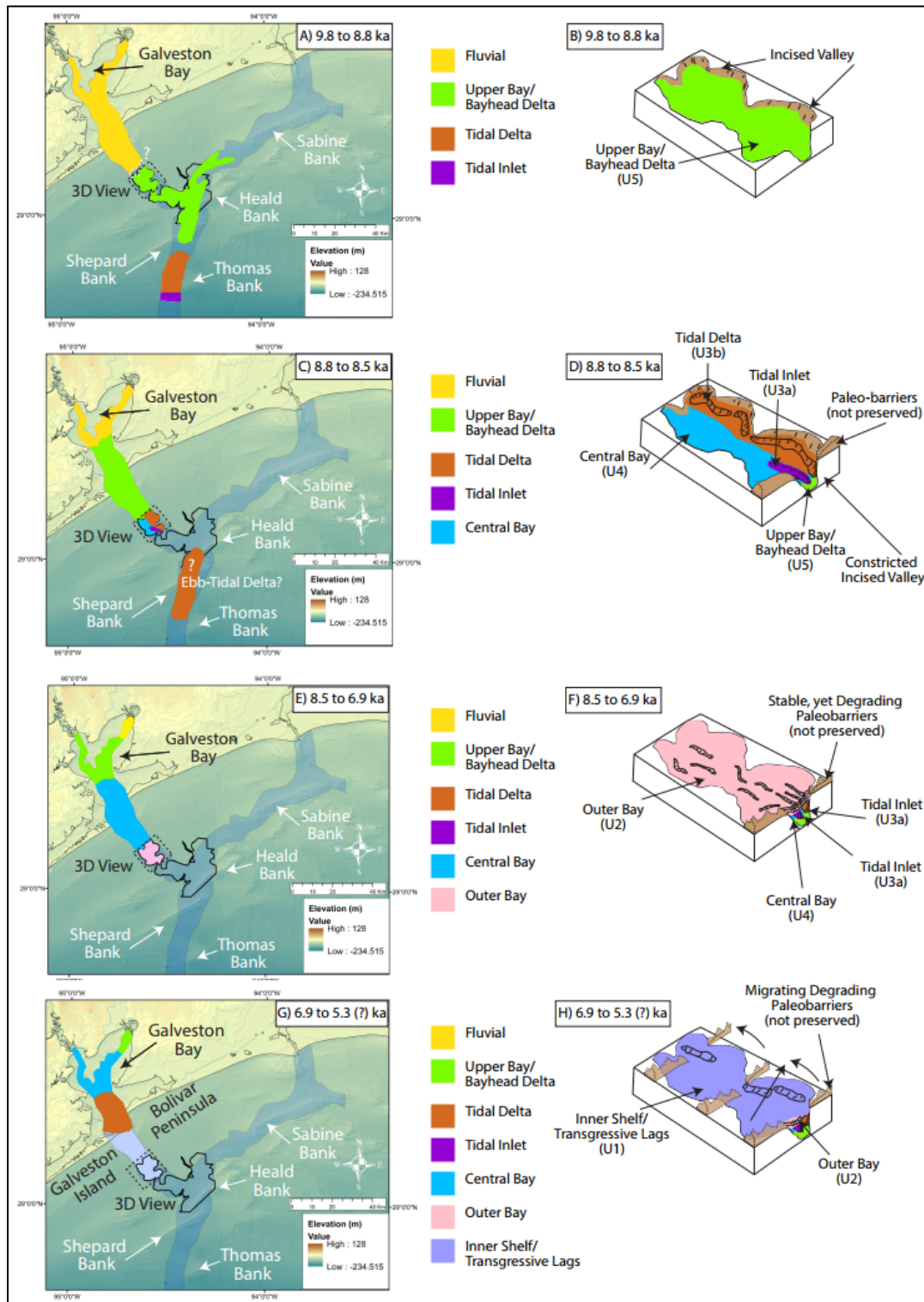


**Figure 7.21. Model for paleovalley evolution**

A) Paleoshoreline evolution map from 9.6 to 8.8 ka for the northern Gulf of Mexico inner shelf. The Trinity-Sabine incised valley is drawn as an opaque blue polygon (Thomas and Anderson, 1994). A revised interpretation of the Trinity incised valley from Swartz et al. (2022) is displayed as a bold dark polygon. Locations and extent for tidal inlet,

tidal delta, and upper bay/bayhead delta are modified from Thomas and Anderson (1994). Fluvial extent is modified from Anderson et al. (2008), although the boundary between fluvial and upper bay/bayhead delta facies is not available, as denoted by a white question mark and dotted boundary. Black dotted box represents outline of three-dimensional schematic. B) Three-dimensional schematic of the Trinity incised valley within this study. An upper bay/bayhead delta facies, identified in this study as U5, deposits within the valley overlaying fluvial sediments. C). Paleoshoreline evolution map from 8.8 to 8.5 ka. The tidal delta facies lying ~30 km seaward, and adjacent to Heald and Sabine Banks, has been modified from Thomas and Anderson (1994). This has been re-interpreted as a possible ebb-tidal delta. D) Three-dimensional schematic of the Trinity incised valley within this study. The estuarine system is initiated and controlled by the incised valley's constricted geometry. This results in the development of stable barriers, the deposition of central bay sediments (U4), and the preferential deposition of tidal inlet (U3a) and tidal delta (U3b) deposits along the eastern portion of the valley. E) Paleoshoreline evolution map from 8.5 to 6.9 ka. F) Three-dimensional schematic of the Trinity incised valley within this study. Stable, yet degrading barriers led to the burial of tidal inlet (U3a) and tidal delta (U3b) units, and the widespread deposition of outer bay (U2) sediments. Decreased back-barrier accommodation resulting from increased fluvial topography promoted aggradation and resilience of outer bay sediments as opposed to retrogradation and marine incursion. G) Paleoshoreline evolution map from 6.9 to 5.3 ka. H) Three-dimensional schematic of the Trinity incised valley within this study. Degrading barriers migrated landward across the study area, leading to the deposition of inner shelf/transgressive lag deposits (U1). Large channels composed of washover deposits and transgressive lags are remnants of the now-eroded barriers. The paleoshoreline at this time likely transgressed to Galveston Island by 5.3 ka (Rodriguez et al., 2004).

These data are inconsistent with previous interpretations that assert a barrier island existed adjacent to Shepard and Heald Banks from 8.7 to 7.7 ka (Thomas and Anderson, 1994; Rodriguez et al., 2004). Thomas and Anderson (1994) observe a large tidal delta deposit within the Trinity-Sabine valley extending seaward from Heald Bank to just landward of Thomas Bank (**Figure 7.21C**). However, this tidally influenced facies lacks evidence of a tidal inlet deposit, which can be more precise in locating paleo-barrier position than solely tidal deltas due their smaller and more discrete geographic extent (e.g., Thomas and Anderson, 1994). Additionally, Rodriguez et al. (2004) interpret estuarine strata beneath Heald Bank with dates ranging from 8.4 to 7.7 ka. They describe this facies as consisting of landward-dipping seismic reflectors characteristic of a flood-tidal delta's landward transport direction, and indicates the paleoshoreline lies seaward of this location. However, the seismic data in which these cores were tied to were of low quality (Rodriguez et al., 1999), and the direction of dipping reflectors may be untrustworthy without reprocessed and/or new geophysical data. Therefore, this large tidal delta deposit, given its age constraints of 8.7 to 7.7 ka, possibly represents the ebb-tidal delta component of the barrier island system initiating ~8.8 ka within this study's area of focus (**Figure 7.21C**). However, sparse geophysical data between these two areas hinder conclusive evidence for how this tidal facies relates to this study.

By ~8.5 ka, the estuarine system experienced a major shift from central bay (**Figure 7.14B**), tidal inlet and delta environments (**Figures 7.12B, 7.14A**), to that of an outer bay environment (**Figures 7.21E–7.21F**; Standring et al., 2021). This is a high-energy environment just landward of the barrier inclined to a mixture of tidal, storm, and wave processes (Dalrymple et al., 1992; Zaitlin et al., 1994). This led to the closure and infilling of the tidal inlet and tidal delta units, providing a total lifespan of the tidal system of ~300 years (**Figures 7.21E–7.21F**). Rather than a complete overstepping and in place drowning of the estuary, which is expected following the deactivation of the tidal inlet (e.g., FitzGerald et al., 2006, FitzGerald et al., 2008), reduced back-barrier accommodation provided by increased landward antecedent topography (**Figures 7.20B–7.20C, 7.21E–7.21F**) helped to promote the aggradation of outer bay sediments, and barrier island stability for the next ~1.6 kyr.

By ~6.9 ka, cores GC-2 and GC-5 indicate a shift to an inner shelf environment, leading to the deposition of U1 (**Figures 7.13B, 7.15, 7.21G–7.21H**; Standring et al., 2021; Chapter 5). During this time, the paleo-barrier retreated and degraded, as evidenced by multiple washover deposits overlying an erosive transgressive lag in GC-6 (**Figure 7.12B**). This barrier-related material filled multiple 2 to 4.5 km long, 1.3 to 1.5 km wide, 0.75 to 2.8 m (~1 to 2 m) deep channel-like features focused on the eastern side of

the valley (**Figures 7.19-U1, 7.21G–7.21H**). It is possible that the preservation of this unit is focused on the eastern side of the valley (**Figures 7.21G–7.21H**) due to its heavy reworking of underlying mud-rich outer bay and sand-rich tidal delta units (**Figures 7.5, 7.8, 7.12B**), as opposed to the western side of the valley where it predominantly reworks solely mud-rich outer bay and central bay units (**Figures 7.5, 7.6, 7.8, 7.13A**). Barrier retreat and degradation along the eastern side of the valley persisted until at least ~4.3 ka, as observed by a dated transgressive lag shell in GC-6 (**Figure 7.12B**), while the western side of the valley rapidly transitioned into an inner shelf environment. During this ~1.7 kyr span, the estuarine system was likely inundated by marine sediments, the barrier was degrading, and the shoreline was landward of the study area, possibly forming the Galveston Island by 5.3 ka and Bolivar Peninsula by 2.8 ka (**Figure 7.21G**; Rodriguez et al., 2004; Standring et al., 2021); however, the lack of data between this study's focus area and the modern shorelines hinder the ability to analyze the paleoshoreline evolution past ~6.9 ka as observed in cores GC-2 (**Figure 7.15**) and GC-5 (**Figure 7.13B**).

## 7.6 Conclusions

To investigate the role of antecedent topography in the evolution of an ancient barrier island system, we focus on the Trinity incised valley offshore modern Galveston Bay in the central Gulf of Mexico. We show that the underlying fluvial topography in which the barrier island system is transgressing plays a significant role in barrier island initiation and stability. Although there is little to no tidal reworking and redistribution of the underlying fluvial sediments, this section provides higher elevation and reduced accommodation for back-barrier sediments. This increased fluvial elevation promotes vertical aggradation of back-barrier sediments and barrier island stability as opposed to transgression and barrier island disintegration. This study also provides a methodology to study the evolution of a paleo-barrier island system with sparse preservation of the barrier itself; instead, we investigate preserved back-barrier (deltaic, bay, and washover) and tidal (inlets and deltas) sediments to construct the depositional and erosional evolution of this paleo-barrier island system. Last, we revise the established Holocene paleoshoreline model proposed by Rodriguez et al., 2004, to suggest that the model includes a paleoshoreline position within our study area landward of Heald Bank, in agreement with previous authors (Thomas and Anderson 1994; Anderson et al., 2016).

## 8 Reconnaissance Surveys of Trinity-Sabine Paleovalley System

In the final year of the Texas Coop, UTIG was tasked with collecting additional chirp data and cores extending seaward of the TRiPP survey area, completing a reconnaissance of the Trinity River Paleovalley to the confluence with the Sabine River Paleovalley, and continuing as far as possible shoreward along the Sabine (**Figure 8.1**). This fifth survey of the Texas Coop was delayed a year due to the Covid-19 pandemic and took place in April 2021 aboard the R/V *Tommy Munro*. Subsequently, BOEM also provided funds to the Texas General Land Office (GLO) to extend their state-waters regional reconnaissance, performed by APTIM, into federal waters, covering primarily the Sabine, Heald and Shepard sand banks (**Figure 8.2**) and portions of the Sabine River paleovalley up to the state-federal boundary (**Figure 8.1**). The Texas GLO also contracted with UTIG to process those chirp data and to provide a regional geologic interpretation. Because the UTIG and APTIM surveys overlap (**Figure 8.1**), it was decided, in consultation with BOEM personnel, to generate a joint interpretation of the two data sets and report those combined results in this final report. Because of the Covid-19 delay, we eventually combined field efforts with a GLO-funded effort in state waters. That work included a sparker and/or streamer system owned and operated by Texas A&M University, and they permitted collecting additional sparker data during our BOEM-funded effort at no cost to the project. A separate description of those data is included in Section 8.3.

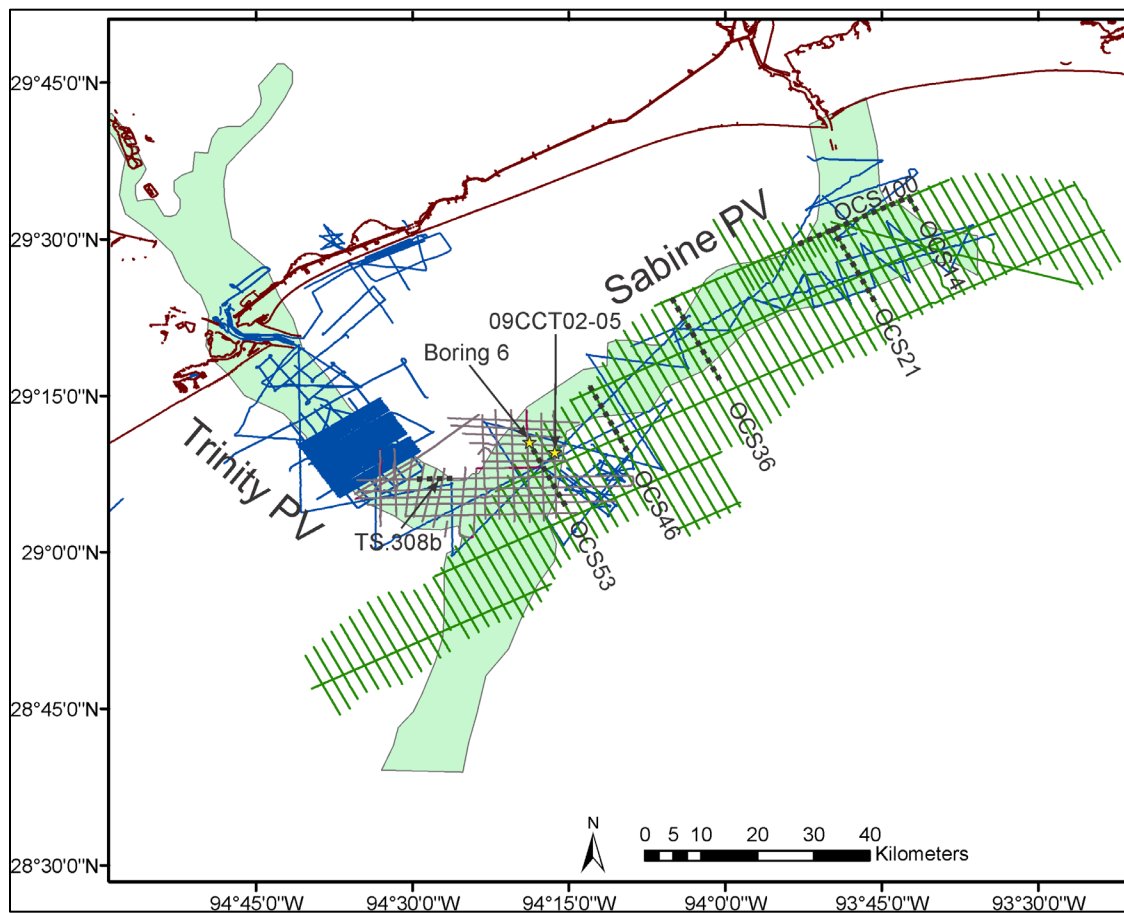


**Figure 8.1. Chirp track locations**

APTIM (green) and UTIG (grey) chirp track lines in the OCS area. Blue lines indicate previous chirp data. The green shaded area is the location of Trinity and Sabine paleovalleys (PVs) as mapped by Thomas and Anderson (1994).

Unfortunately, our survey was hampered by a number of significant setbacks. The first and most severe occurred early during the GLO phase of the survey when a ship operator error brought the ship too close to a moored freighter, causing our 512i chirp towfish (0.5 to 12 kHz) to be dragged over the freighter's anchor chain. This completely disabled our 512i towfish and forced us to rely on our smaller, 216 towfish (2 to 16 kHz) for the remainder of the survey. The 216 performed well, although at higher frequency and thus unable to penetrate as deeply into the subsurface. Second, the weather was quite poor, forcing us to suspend operations periodically and affording us very little sufficiently calm weather to attempt cores on *Munro*, which did not have good station-keeping abilities. Nevertheless, we ended up collecting ~260 nm of chirp data, ~180 nm of sparker data, and four gravity cores. Our third significant setback was discovered after the cruise was over. In an attempt to maximize penetration, we selected the lowest frequency pulse available on the Edgetech system (2–10 kHz, 20 ms). This had proved effective with the 512i towfish in certain circumstances. However, post-cruise we discovered that this pulse has a lower sampling interval than usual, which rendered the full-waveform record undersampled, and was inadequate for applying our standard chirp processing workflow. The envelope records are high quality but required custom processing techniques to address the issues we encountered. Also, poor weather throughout the cruise precluded the deployment of the vibracorer, and gravity core deployments were limited to brief windows of favorable sea state.

## 8.1 Chirp Analysis: Heald and Sabine Banks

The origins of Heald, Shepard, and Sabine banks have been the topic of debate in the literature as the nature of the banks is of great significance to ascertaining the suitability of using these sediments for beach renourishment projects. Earlier research by Thomas and Anderson (1991) attributed both banks to a post-transgressive marine deposition, based on identification of the transgressive ravinement underlying the banks. Subsequently, Rodriguez et al. (1999) interpreted both banks as remnant barrier islands, based on identification of landward-dipping reflectors and core evidence of barrier sedimentary facies. Such reflections are strong indicators of accumulation of sediments on the landward side of a barrier island. The new, high-quality chirp data provide us with an opportunity to reexamine these conflicting interpretations.

### 8.1.1 Heald Bank Unit

The topographic high of Heald Bank is underlain by a largely transparent acoustic unit (**Figure 8.3**). The base of this Heald Bank Unit is marked by a horizon H1, which separates the transparent unit from the strongly laminated seismic facies of the Sabine estuarine sequence that is deposited within the paleovalley, with uppermost portions of the estuary extending seaward outside of the paleovalley (**Figure 8.3**) as is true for modern examples, such as Galveston Bay. Portions of H1 are seen to clearly truncate the underlying strata of the Sabine estuarine sequence (**Figures 8.3, 8.4**), supporting the interpretation of Thomas and Anderson (1991) that Heald Bank is underlain by the transgressive ravinement. No landward-dipping reflectors were observed in Heald Bank, which is contrary to the observations of Rodriguez et al. (1999), based on seismic imaging of much older and less well-resolved technology. However, we do frequently observe a single horizontal reflector within the Heald Bank Unit below Heald Bank itself (**Figure 8.4**). This solitary reflector could be evidence of a basal lag associated with modern bedforms, up to 2 meters (m) high, that are observed atop Heald Bank (Rodriguez et al., 1999).

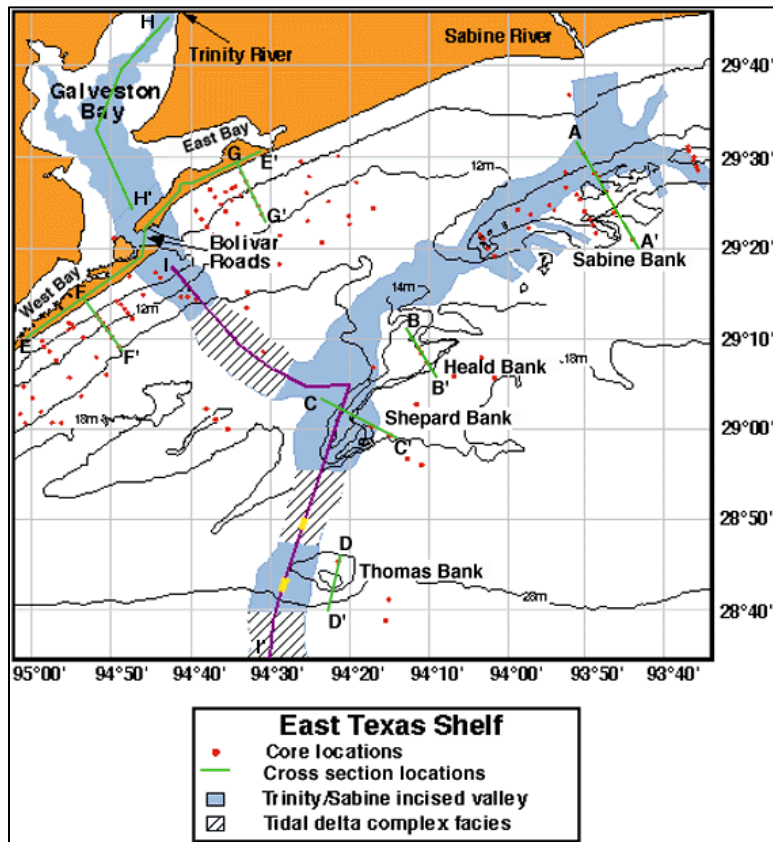


**Figure 8.2. East Texas shelf**

Location of offshore sandbanks in relationship to the Sabine and Trinity paleovalleys. Adapted from Rodriguez et al. (1999) by [https://gulf.rice.edu/ETexas/gulfeTexasS\\_T\\_SJ\\_tst.html](https://gulf.rice.edu/ETexas/gulfeTexasS_T_SJ_tst.html).

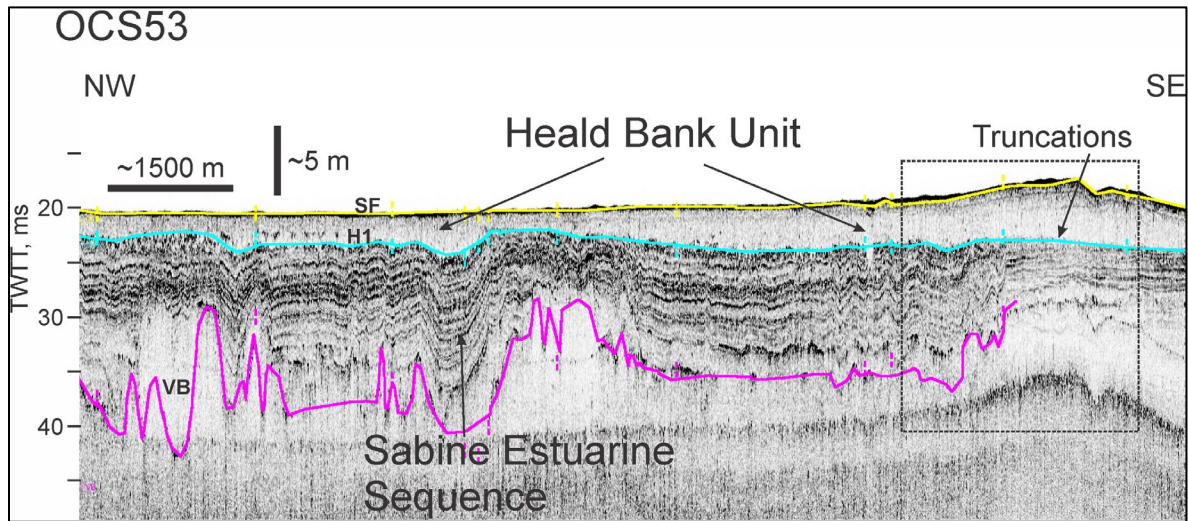


**Figure 8.3. Chirp line OCS53**

Interpreted envelope chirp record crossing Heald Bank and extending shoreward across part of the Sabine River Paleovalley. Location shown on **Figure 8.1**. Picked horizons include seafloor (SF; yellow), the base of the Heald Bank Unit (H1; cyan), and the acoustic base of the Sabine River Paleovalley (VB; magenta). The dotted-line box is location of **Figure 8.4**.

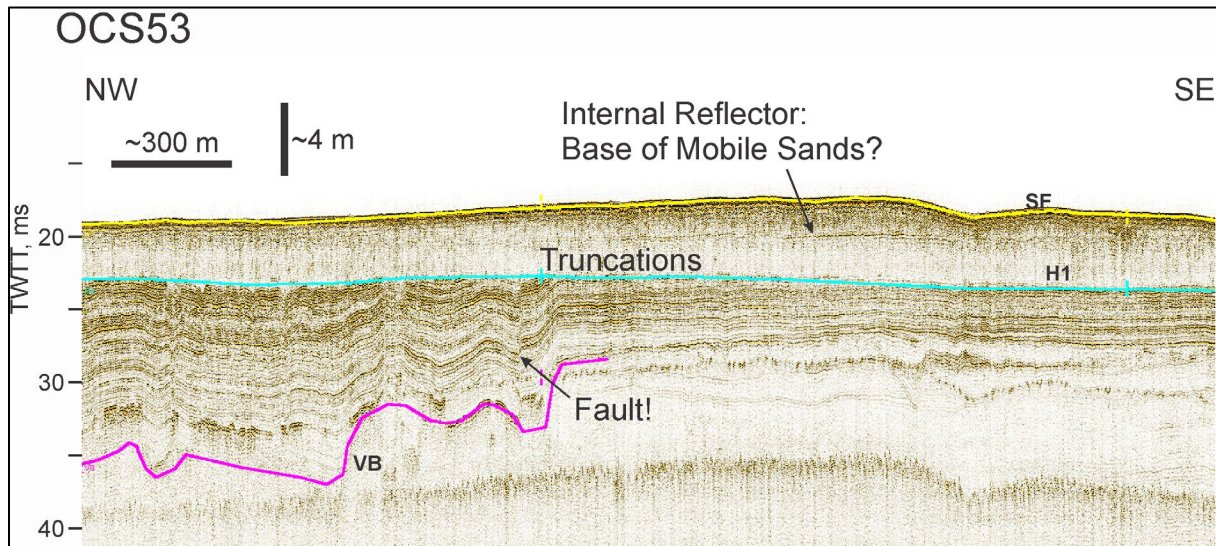


**Figure 8.4. Chirp Line OCS53 enlargement**

Full waveform record image of a portion of Heald Bank, illustrating truncations of the laminated strata of the Sabine estuarine sequence by horizon H1, as well as a horizontal reflector within the bank that may mark the base of modern bedform movement. Location shown in **Figure 8.3**. Picked horizons include seafloor (SF; yellow), base of Heald Bank unit (H1; cyan), and acoustic base of the Sabine River Paleovalley (VB; magenta).

The Heald Bank Unit is not confined to the topographic high of Heald Bank. Rather, this unit extends broadly landward across the Sabine River paleovalley (**Figure 8.3**). Archival core logs (**Figure 8.5**) confirm that the Heald Bank unit is composed of a silty sand body well distanced from the bank itself, indicating that it could represent a potentially vast, easily accessible (due to no overburden) source of sand that is not tied to the topographic high of the bank (**Figure 8.6**). The Heald Bank Unit extends

landward into the Trinity River paleovalley and southwest to connect with Shepard Bank farther offshore (**Figure 8.6**). To the NE, the Heald Bank Unit is overlain by the Sabine Bank Unit, which is described in the next section. To the southwest, the Heald Bank Unit is contiguous with Shepard Bank sands, and we identify these bodies as a single unit (**Figure 8.6**).

### 8.1.2 Sabine Bank Unit

As with line OCS53 (**Figure 8.3**), the Heald Bank Unit extends landward from the bank (**Figure 8.7**). However, another reflector was observed at this location, which is identified as H2, atop the Heald Bank Unit. Progressing farther east, to chirp line OCS36 (**Figure 8.8**), which crosses the western end of Sabine Bank, the strata above H2 has thickened to form a series of landward-dipping reflectors that form the basis for the topographic high forming Sabine Bank. These strata overlie the remnants of the Heald Bank Unit. These sediments above H2 are identified as the Sabine Bank Unit. The seismic facies of this unit also change from being highly reflective at the left of the image to being weakly reflective at the right, indicating a gradation in the physical properties between highly contrasting to the left (e.g., mud and sand layering) and more homogeneous (presumably more sandy) to the right.

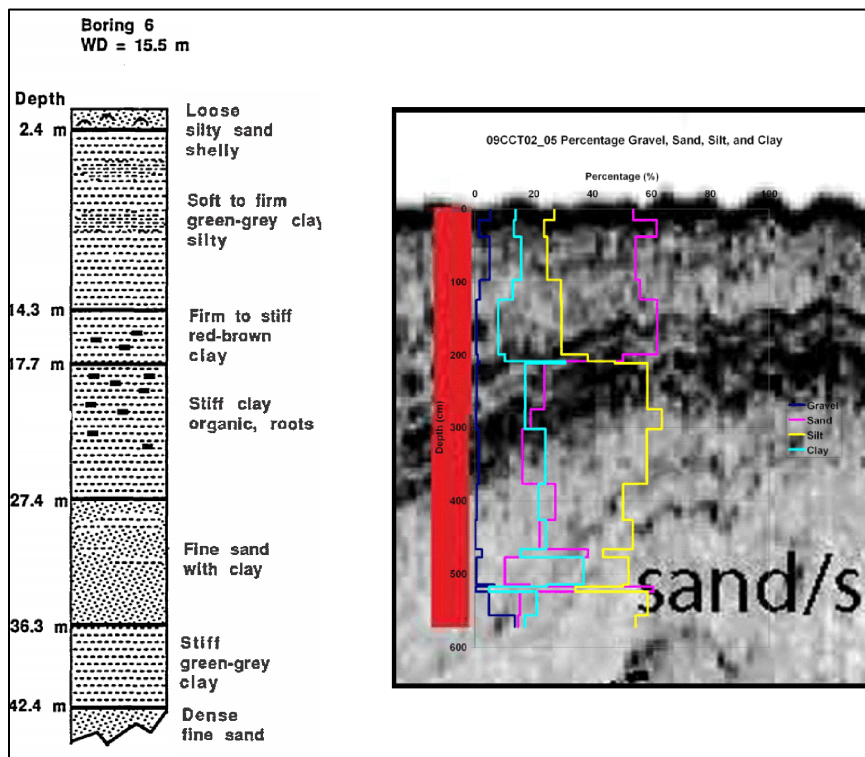


**Figure 8.5. Archival core logs of Heald Bank Unit**

Lithologs from Boring 6 in Thomas (1991) (left) and vibracore 09CCT02\_05 in Dellapenna (2009) (right), indicating that the Heald Bank Unit landward of Heald Bank is composed of silty sand 2–2.4 m thick. Locations are shown in **Figure 8.1**. Boring 6 is located at the NW end of OCS53 shown in **Figure 8.3**.

This complex seismic facies of the Sabine Bank Unit continues farther to the east, as shown on chirp line OCS21, which crosses Sabine Bank where it has the highest relief (**Figure 8.9**). Here the gradation in dip angle is more pronounced across the section. In addition, in the upper portion of the bank, a prograding section of landward-, steeply-dipping reflectors was observed suggesting a late-stage modification to the Sabine Bank Unit (**Figures 8.9** and **8.10**). An isopach map of the Sabine Bank Unit is shown in **Figure**

**8.11.** Based on defining H2 as the first reflector to exhibit above the Heald Bank Unit, we tentatively identify a limited branch of the Sabine Bank Unit to the west, overlying the Trinity River paleovalley (Figures 8.11 and 8.12).

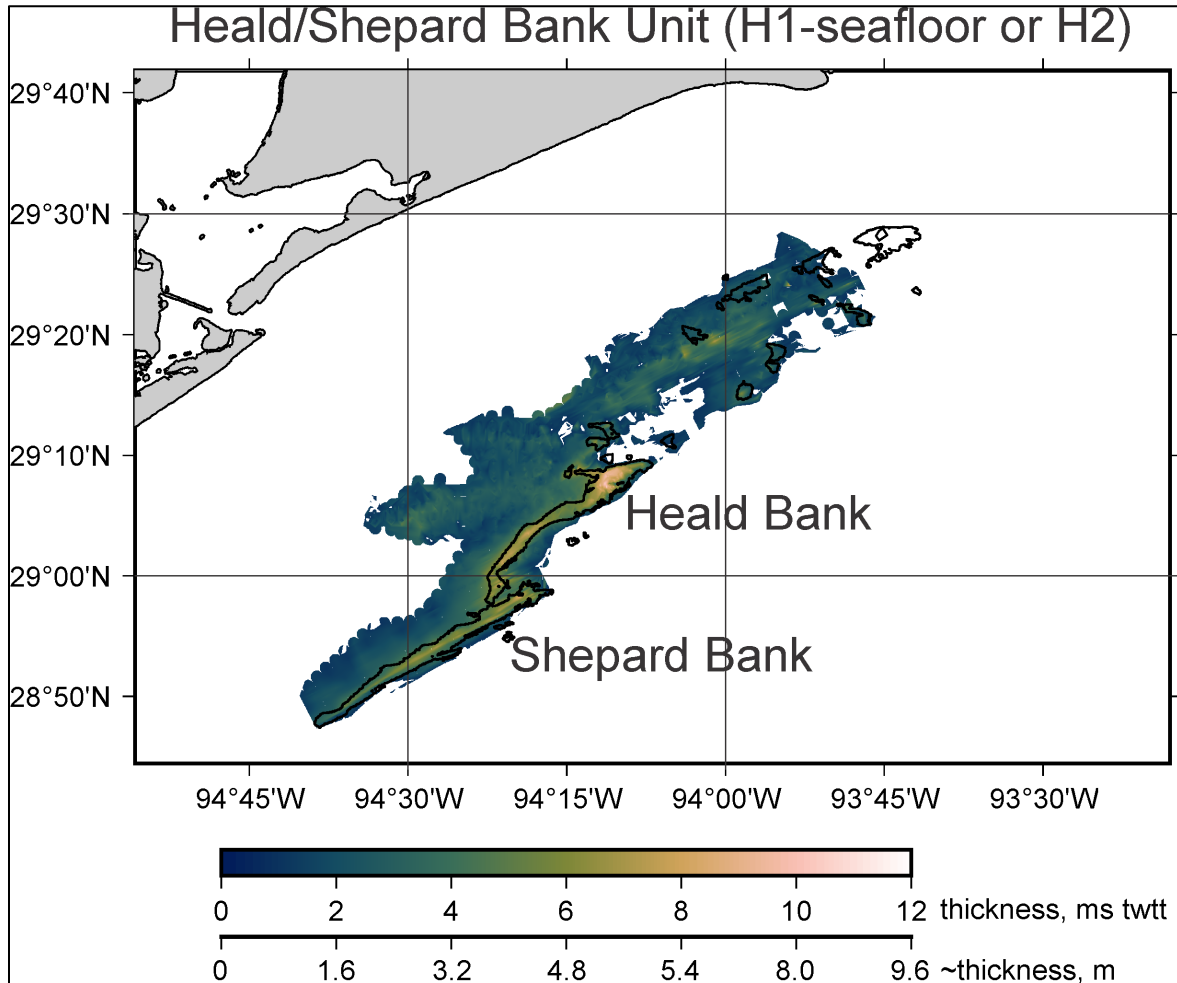


**Figure 8.6. Isopach map of the Heald/Shepard Bank Unit**

Heald Bank Unit (which is contiguous with Shepard Bank) over the APTIM-UTIG survey areas. Black outlines indicate extent of modeled shoals by Pickens et al. (2021) based on topographic considerations.

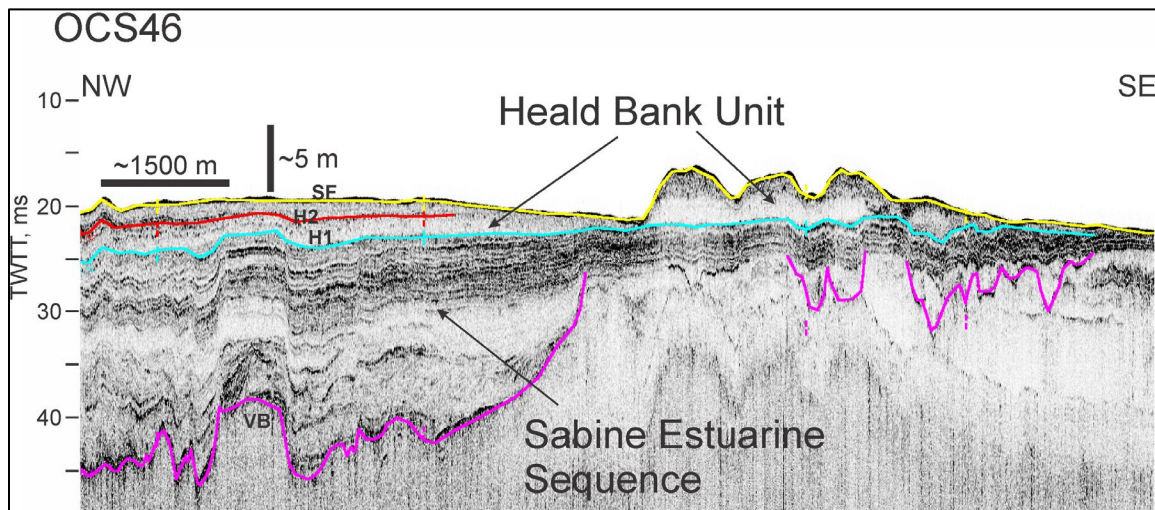


**Figure 8.7. Chirp line OCS46**

Interpreted envelope chirp record crossing Heald Bank and extending shoreward across part of the Sabine River paleovalley. Location shown on **Figure 8.1**. Picked horizons include seafloor (SF; yellow), base of the Heald Bank Unit (H1; cyan), base of Sabine Bank Unit (H2; red), and acoustic base of the Sabine River paleovalley (VB; magenta).

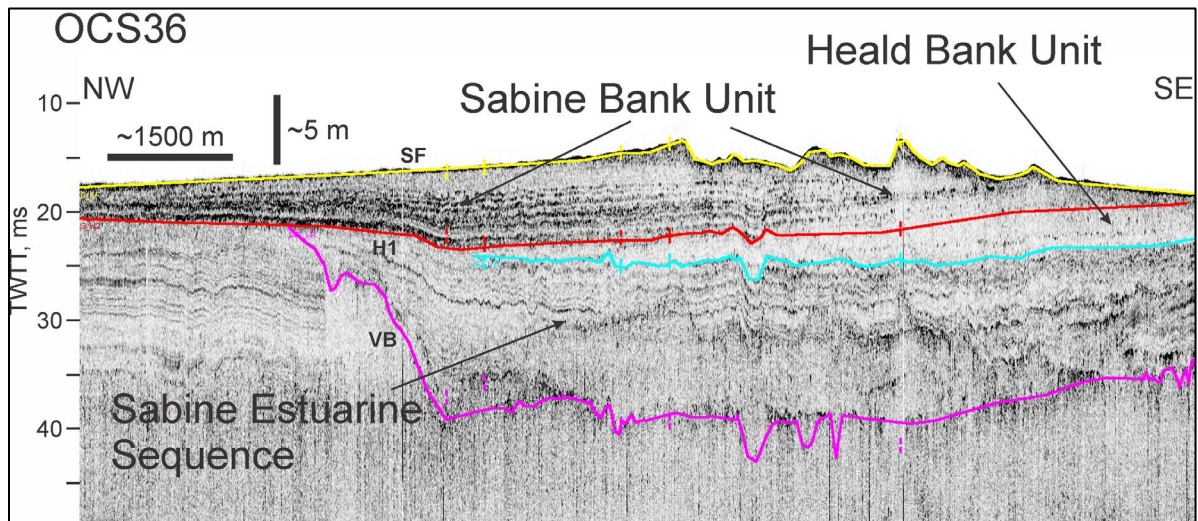


**Figure 8.8. Chirp line OCS36**

Interpreted envelope chirp record crossing Sabine Bank and portions of the Sabine River paleovalley. Location shown on **Figure 8.1**. See **Figure 8.7** for horizon identifications. Picked horizons include seafloor (SF; yellow), base of the Heald Bank Unit (H1; cyan), base of Sabine Bank Unit (H2; red), and acoustic base of the Sabine River paleovalley (VB; magenta).

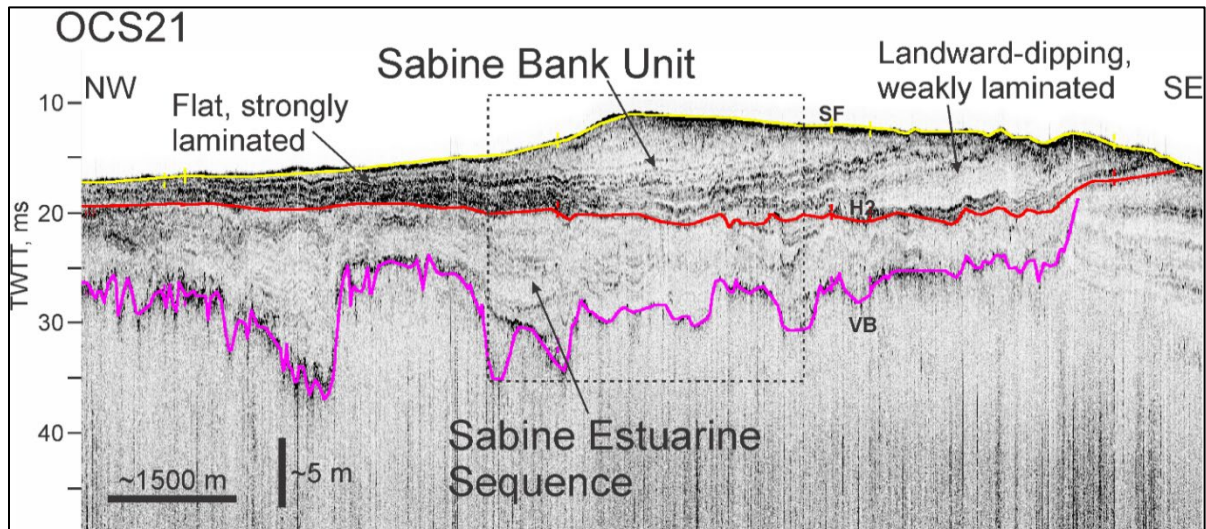


**Figure 8.9. Chirp line OCS216**

Interpreted envelope chirp record crossing Sabine Bank and portions of the Sabine River paleovalley. Location shown on **Figure 8.1**. Picked horizons include seafloor (SF; yellow), base of Sabine Bank Unit (H2; red), and acoustic base of the Sabine River paleovalley (VB; magenta). The dotted-line box is the location of **Figure 8.10**.

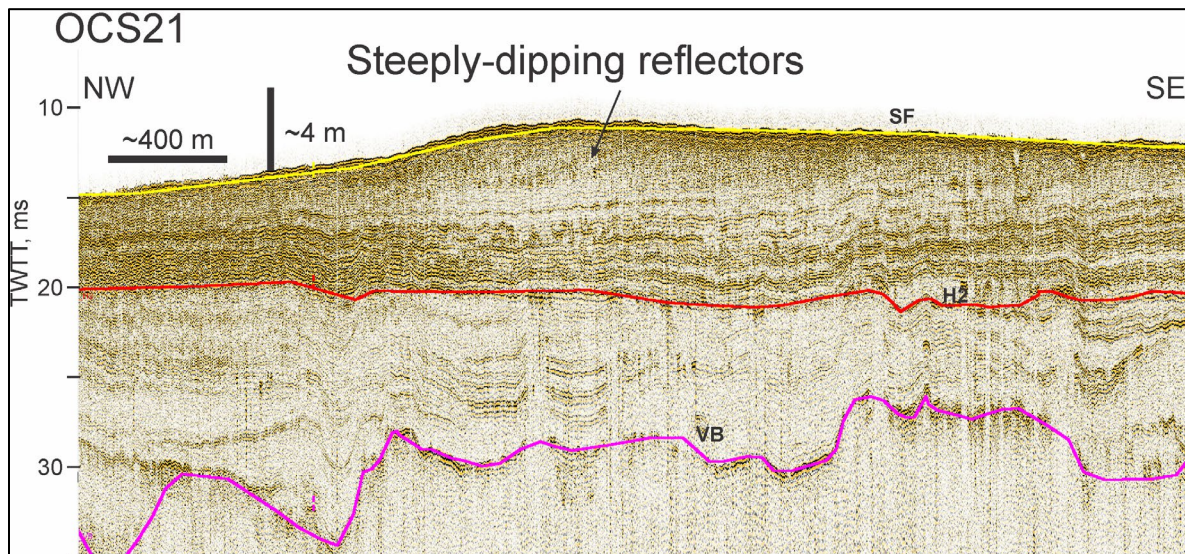


**Figure 8.10. Chirp Line OCS53 enlargement**

Full waveform record image of a portion of Heald Bank, illustrating truncations of the steeply-dipping, late-stage reflectors in the upper portion of Sabine Bank. Picked horizons include seafloor (SF; yellow), base of Sabine Bank unit (H2; red), and acoustic base of the Sabine River paleovalley (VB; magenta). The location is shown in **Figure 8.9**.

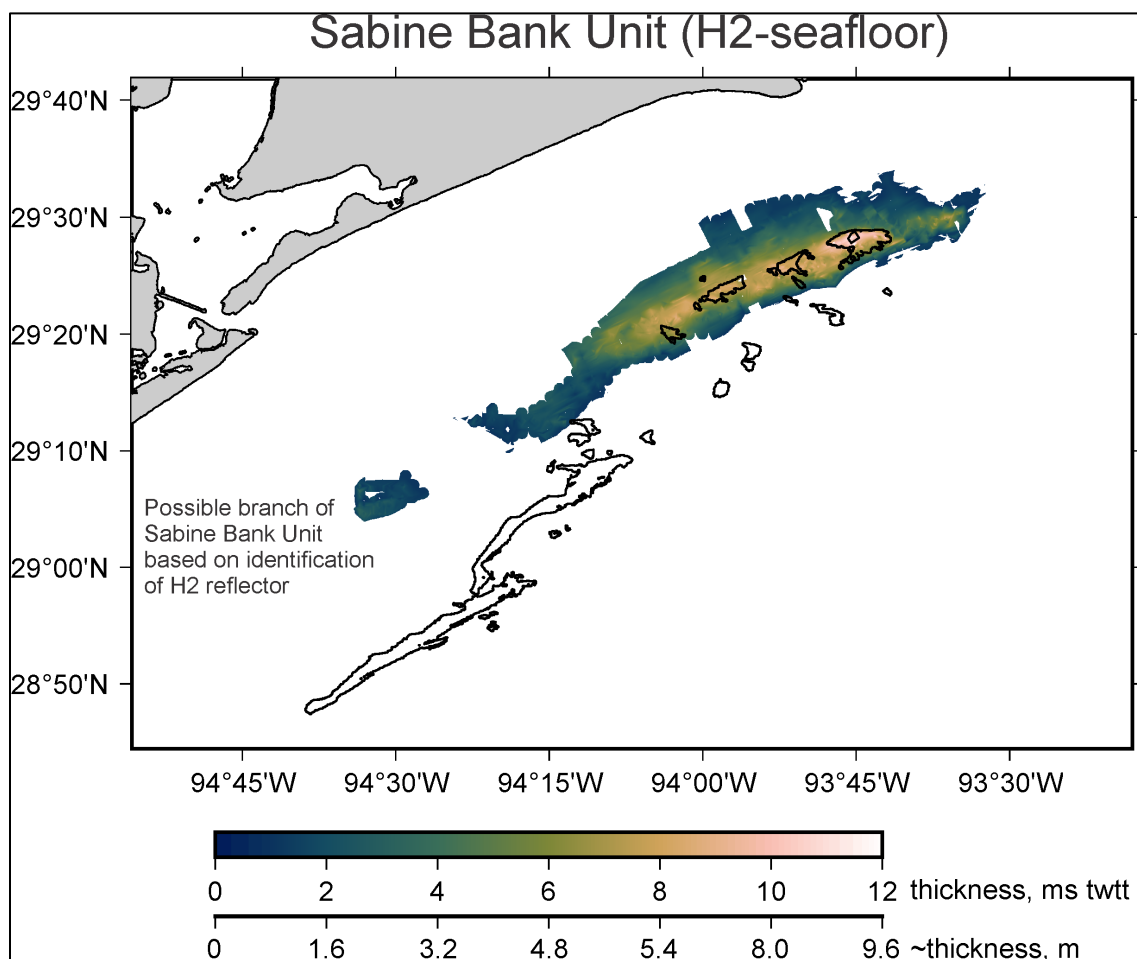


**Figure 8.11. Isopach map of the Sabine Bank Unit**

Isopach map depicting the full extent of the Sabine Bank Unit over the APTIM/UTIG survey areas. Black outlines indicate extent of modeled shoals by Pickens et al. (2021) based on topographic considerations.

### 8.1.3 Discussion

Stratigraphic observations of Heald-Shepard and Sabine Banks from this study indicate that the banks were formed by fundamentally different processes. Heald Bank, as Thomas and Anderson (1991) noted, sits atop an erosional unconformity that is likely associated with the transgressive ravinement, i.e., the surface formed by the landward migration of the shoreline. There is no evidence of any landward-dipping reflectors that would indicate in situ barrier strata. Therefore, we concur with Thomas and Anderson (1991) that the Heald Bank Unit (including Shepard Bank) formed in a marine environment offshore, rather than as a remnant of the barrier island. It is possible that the sands composing the unit may have derived in whole or in part from deconstructed barrier deposits, but any such structure has been lost and the sediments largely homogenized in the depositional process. The origin of the Heald Bank Unit remains an open question and should be a topic of future investigation.

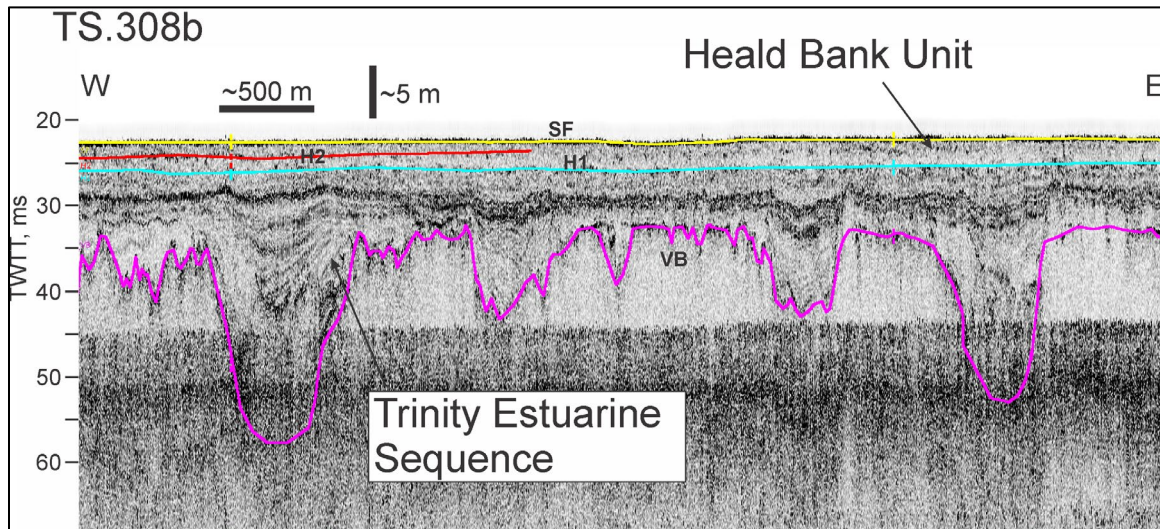


**Figure 8.12. Chirp line TS308b**

Interpreted envelope chirp record crossing a portion of the Trinity River paleovalley where the estuarine sequence thins in places to < 10 m. Location shown on **Figure 8.1**. Picked horizons include seafloor (SF; yellow), base of Sabine Bank Unit (H2; red), and acoustic base of the Sabine River Paleovalley (VB; magenta).

The stratigraphy of Sabine Bank, in contrast, is fully consistent with conclusions of Rodriguez et al. (1999) that it represents the remnants of a barrier island. In particular, the landward dipping reflectors, combined with the gradation in seismic facies, is consistent with a proximal washover sequence where, closer to the barrier, the sediments are nearly homogenous sand whereas, more distally, a greater degree of interbedding of mud and sand is expected (**Figure 8.13**). The later addition of more landward-, steeply-dipping reflectors (**Figure 8.10**) suggests that, like Heald Bank, Sabine Bank is subject to continued modern reworking in the marine environment.

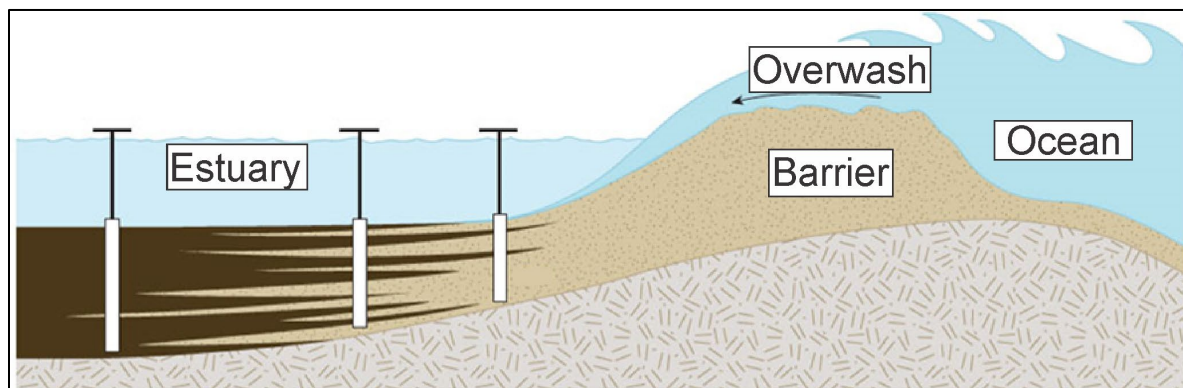


**Figure 8.13. Illustration of proximal washover stratigraphy**

Barrier sands are indicated in stippled tan, and estuarine muds are indicated in dark brown. With distance from the barrier, the stratigraphy changes from homogenous sands to interbedded sands and muds with landward dip, and ultimately to flat-lying muds. Adapted from <https://www.americanscientist.org/article/uncovering-prehistoric-hurricane-activity>.

Our interpretation that Heald and Shepard Banks are marine in origin, whereas Sabine Bank is terrestrial, raises a number of important research questions worthy of study. Perhaps foremost among these: what is the source of sands that formed the Heald Bank Unit? Also: what is the relative timing of the Heald and

Sabine Bank units, and what is their stratigraphic relationship to each other? Why was the barrier island associated with Sabine Bank partially preserved, whereas barriers formed elsewhere along the shelf were completely removed by the transgression? We can also consider what influence the Sabine and Trinity river systems—their particular geography and paleo-fluvial history—might have played in influencing the differences in the Sabine and Heald banks. The close association of Sabine Bank, in particular, with the southeast bank of the Sabine River paleovalley, at the point where the paleovalley reorients to a nearly shore-parallel direction (**Figure 8.2**), is highly suggestive of a causal link. However, considerable additional work will be required to discern such relationships.

## **8.2 Chirp Analysis: Trinity and Sabine River Paleovalley System**

The Trinity and Sabine river paleovalleys both hold potentially significant quantities of possible sand resources within the fluvial sections at the base of the valleys. Fluvial sands are deposited in the subaerial environment primarily as point bar deposits by the meandering river and confined within the larger river valley. The chirp data were unable to penetrate through this fluvial section but did image the top of the fluvial section as represented by the “VB” (valley bottom) horizon in **Figures 8.3, 8.4, 8.7–8.10**. A few core boring logs (Thomas, 1991; **Figure 8.5**) do penetrate the full fluvial sand layer, finding a thickness of ~10 m. However, the overburden for these sands, represented primarily by the Trinity and Sabine estuarine sequences, is typically quite thick, on the order of 15 m or more. Nevertheless, in a number of locations the estuarine sequence is considerably thinner (~5–7 m), most notably within the outer Trinity River paleovalley (**Figure 8.12**), the inner Sabine River paleovalley (**Figure 8.14**), and within several tributaries of the Sabine River paleovalley to the east (**Figure 8.15**). **Figure 8.16** displays an isopach of the valley fill units of both the Trinity and Sabine River paleovalleys, along with several important tributaries, based on new and archival data in both State and Federal waters. This map illustrates where overburden to the fluvial section is thicker or thinner.

The estuarine sequences in the outer Trinity and Sabine River paleovalleys are complex, with additional potential for sand resources in tidal and overwash deposits as was found for the TRiPP survey area. Our regional interpretation did not identify any clear candidates for such deposits. However, we plan to investigate the Sabine River paleovalley estuarine sequence in much greater detail with student-led research over the coming years.

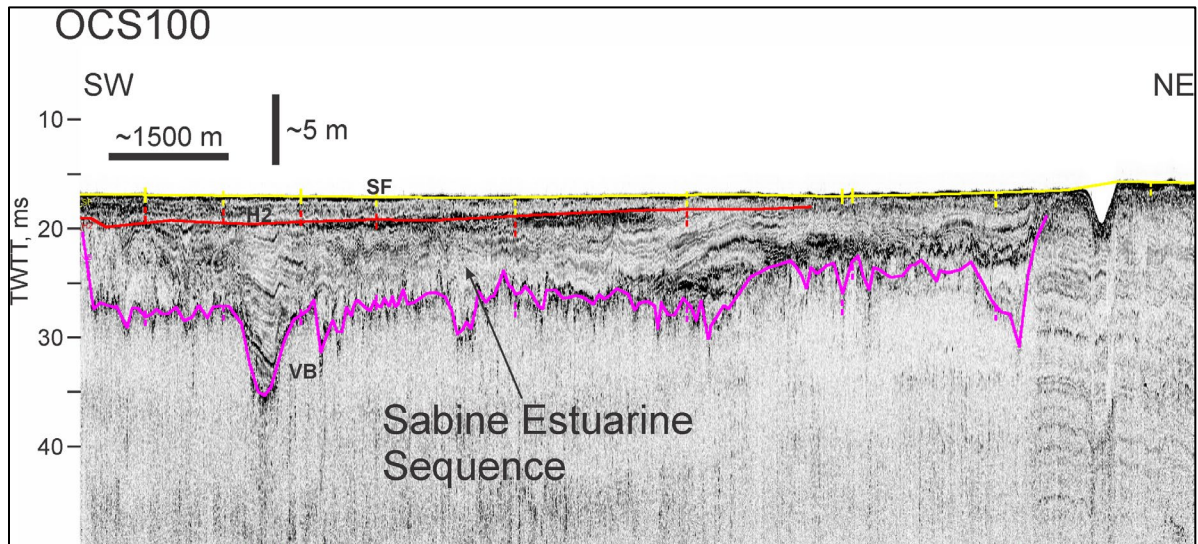


**Figure 8.14. Chirp line OCS100**

Interpreted envelope chirp record crossing a portion of the Sabine River paleovalley where the estuarine sequence thins in places to < 5 m. Location is shown on **Figure 8.1**. Picked horizons include seafloor (SF; yellow), base of Sabine Bank unit (H2; red), and acoustic base of the Sabine River Paleovalley (VB; magenta).

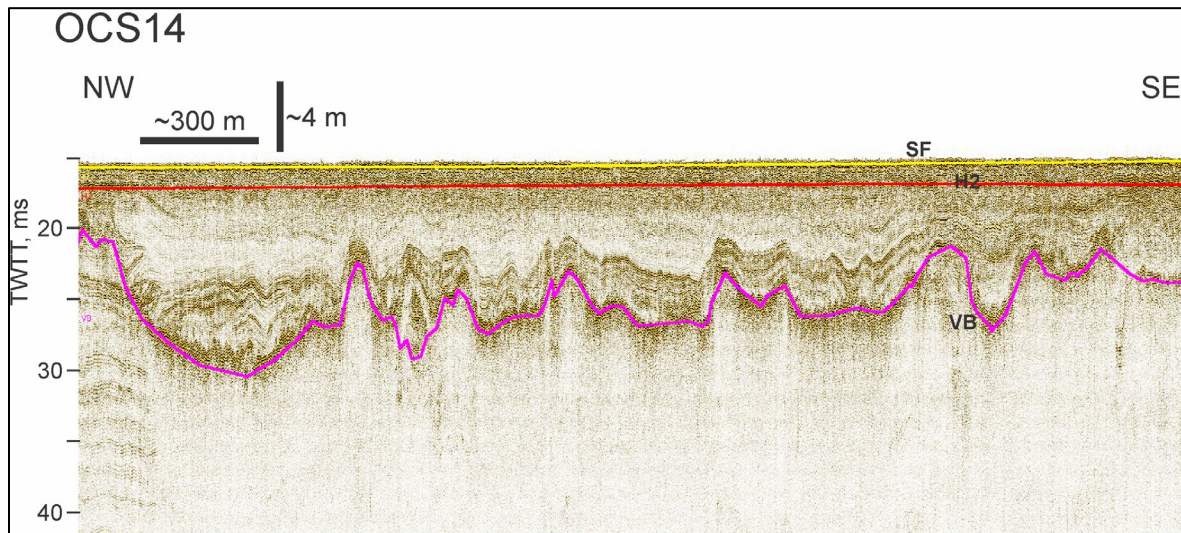


**Figure 8.15. Chirp line OCS14**

Interpreted full waveform chirp record crossing a portion of a tributary of the Sabine River paleovalley where the estuarine sequence thins in places to < 5 m. Location is shown on **Figure 8.1**. Picked horizons include seafloor (SF; yellow), base of Sabine Bank unit (H2; red), and acoustic base of the Sabine River Paleovalley (VB; magenta).

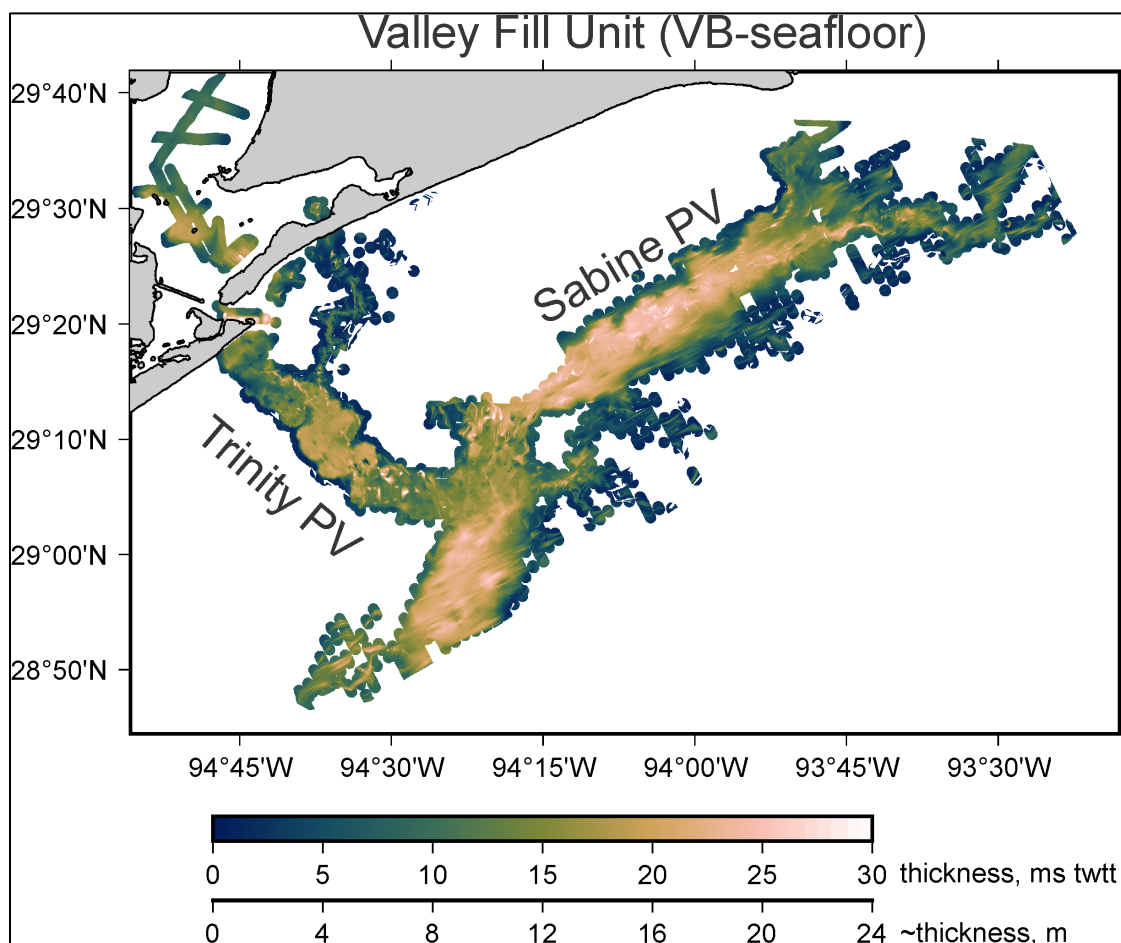
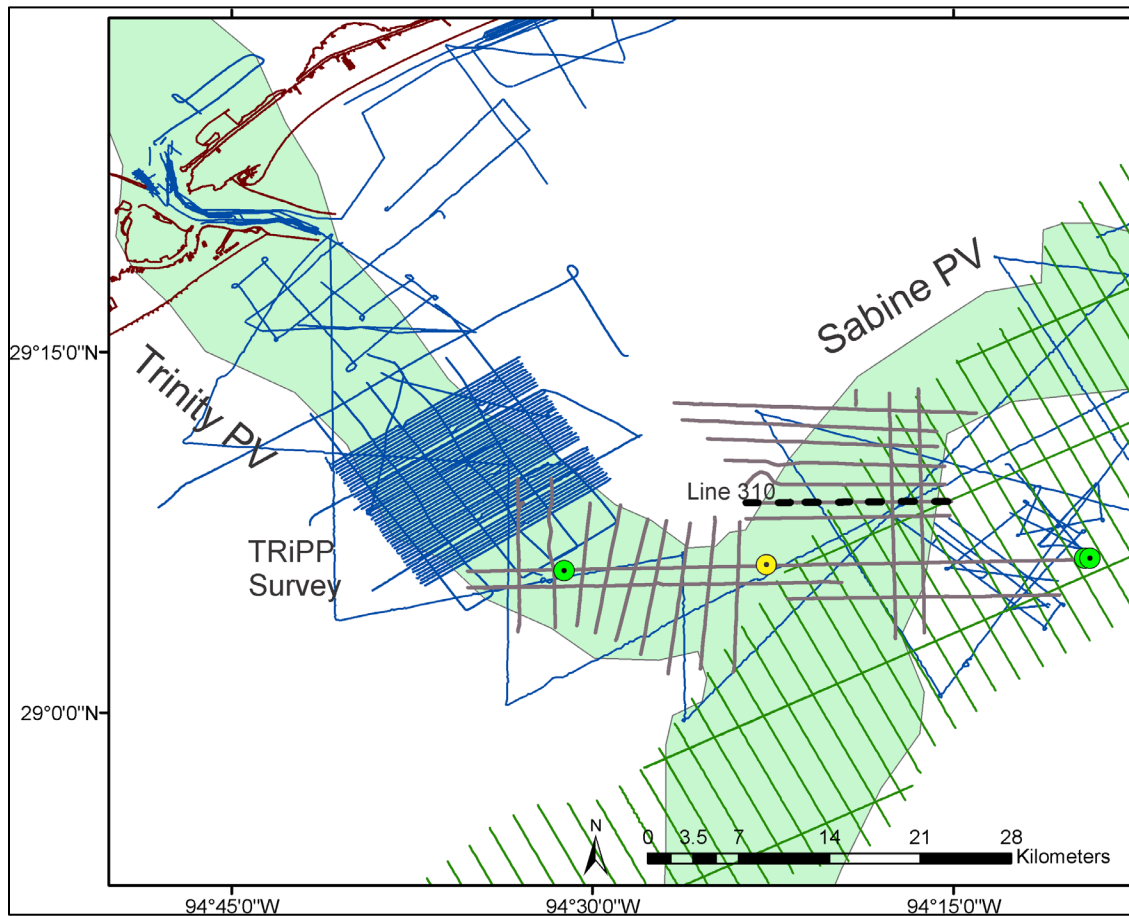


**Figure 8.16. Isopach map of the valley fill unit**

Isopach map of the valley fill unit (seafloor to the top of the fluvial section) of both the Trinity and Sabine River paleovalleys, along with several important tributaries, based on new and archival data in both state and federal waters.

### 8.3 Sparker Data

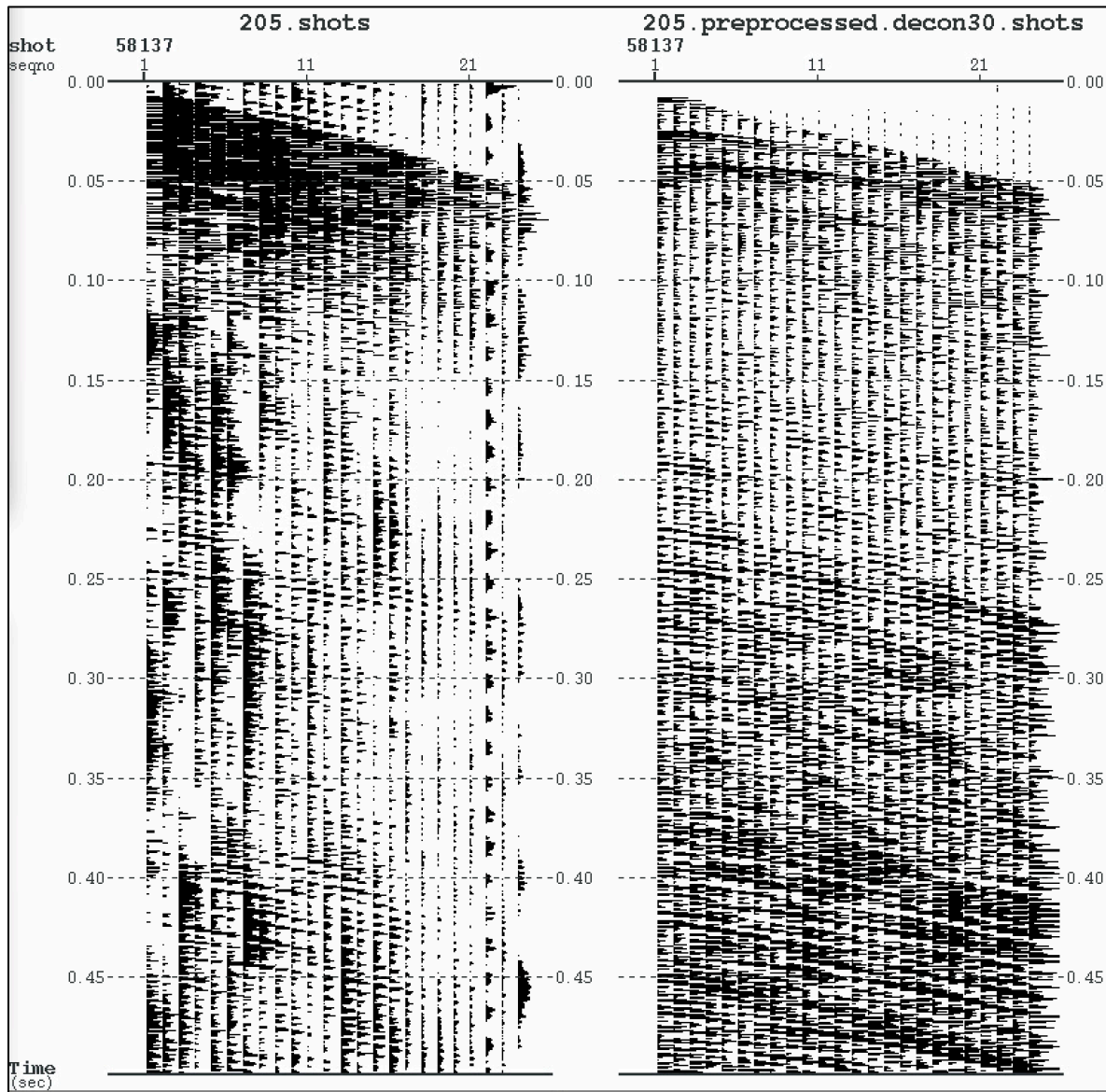
The 2021 cruise on the R/V *Tommy Munro* included simultaneous acquisition of chirp subbottom profiler and sparker seismic data. This is possible because the low frequency of the chirp data (either 0.7 kHz or 2 kHz) are higher than the dominant usable high frequency energy of the sparker data. Specifically, the Dura-Spark used for this cruise produced a source that spanned from 150 Hz–2 kHz; however, some energy above ~1.3 kHz is largely noise and the majority of the higher amplitude signal lies within the 160–640 Hz range. The only concern regarding these two instruments operating simultaneously would be the chirp recording some of the sparker source energy. However, we did not observe any significant “cross-talk” during acquisition. The sparker used for this acquisition was supplied by Texas A&M University and is an Applied Acoustics Dura-Spark 240 consisting of 80 electrodes (“tips”) in each of rows (240 total). These create a consistent pulse source that was recorded to the UTIG 24 channel analog seismic streamer with channels spaced 3.25 m apart. Approximately 180 nm of sparker data were acquired (Figure 8.17).



**Figure 8.17. Sparker track locations**

Sparker track lines (grey) on map including APTIM (green) and other previous (blue) chirp track lines in the OCS area. Green dots indicate successful gravity cores attempts; the red dot indicates an unsuccessful attempt. Two cores were attempted at the eastern end, near Heald bank, because initial penetration in the sandy sediment was low. The green shaded area is the location of Trinity and Sabine paleovalleys (PVs) as mapped by Thomas and Anderson (1994). Sparker line 310 is shown in **Figure 8.19**.

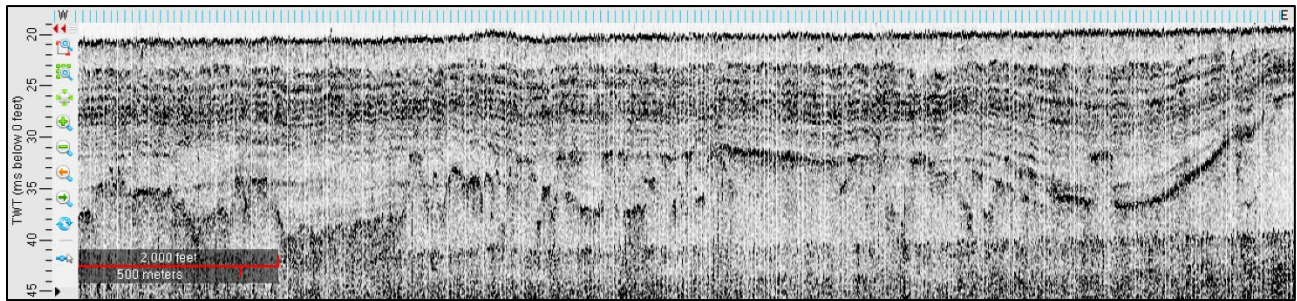
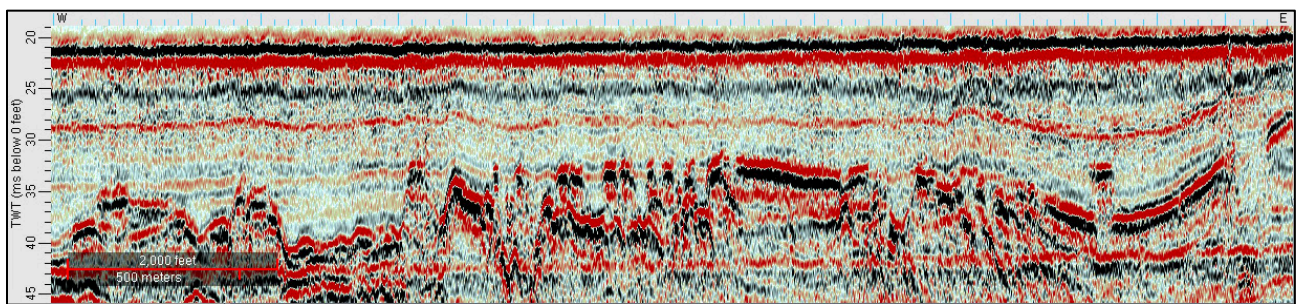
The resultant common midpoint gathers were 1.625 m apart, but the precise number of traces in each bin was dependent on ship speed; most bins have nine traces (thus nine-fold data), but some have 10. Processing steps included converting data from SEG-Y, defining geometries, bandpass filtering to ramp down below 120 and above 1800 Hz, spherical divergence correction, deconvolution, sorting to common midpoint gathers, velocity analysis and muting, stacking, and fk-migration. **Figure 8.18** shows before and after processing of the shot gathers. Note beyond the low frequency noise caused by ocean swells, there is spiky electrical noise on channel 22, which only appeared after the seismic streamer was dragged over the anchor chain.



**Figure 8.18. Example before and after processing shot gathers for sparker data**

Raw shot data on the left from the Dura-Spark recorded on the UTIG streamer and digitized with a marine geode. The loss of energy with time, low frequency swell noise, inconsistent amplitudes, and short period source related multiples are all removed in the processed version to the right.

Analysis of these sparker data compared to the chirp data proved extremely useful. In particular, the sparker data imaged throughout the entire paleovalley fills show previous generations of paleovalleys. Of particular importance for sand resource analysis, the sparker data were able to image the fluvial facies at the base of paleovalleys where the chirp data generally do not penetrate these sand-rich facies. These sparker data will allow quantification of the formative processes and thickness of these fluvial deposits and make an excellent partner data to the chirp. An example is shown in **Figure 8.19** and a table of acquired sparker lines are shown in **Table 8.1**.

**A****B**

**Figure 8.19. Example of imaging using the Edgetech 216 and the Dura-Spark**

Line 310 with the chirp envelope data shown in A and sparker data of the same location shown in B. Note the top of the fluvial section appears as a single reflector in the chirp, but the sparker illuminates internal structure and the base of this sand-rich unit can be determined. Conversely, the definition of layers and units about the fluvial section is much clearer in the chirp data. Thus, simultaneous acquisition is beneficial for sand resource assessment. The location is shown in **Figure 8.17**.

## 8.4 Core Analyses

Three gravity cores were collected along a transect over Heald Bank (**Figure 8.17**). Penetration in the sandy substrate was poor (cores were 0.76 m, 0.55 m, and 0.21 m long, restricted to the uppermost Heald Bank unit), but rough sea state precluded the deployment of the vibrocorer, which is better suited to sandy sediments. Analysis of microfossils within these cores revealed a relatively diverse assemblage of inner shelf taxa (including *Ammonia*, *Elphidium*, *Uvigerina*, *Hanzawaia*, and numerous miliolids) along with ostracodes, echinoid spines, and other bioclasts which indicate deposition on the modern shelf. This assemblage stands in marked contrast to the estuary assemblage described above in the TRIPP study area. The absence of common marsh foraminifera species in these cores argues against the hypothesis that Heald Bank is a reworked barrier island; if it is indeed a relict barrier island then it has been extensively colonized by modern shelf species, and back barrier species have been somehow removed or destroyed.

Grain size analysis in each of the three cores varies between sand-rich and sand-poor sediments, although the shallow penetration of these cores means that these data are merely a surficial look at a much thicker body. GC-9 contains 60–80% sand (i.e., >63  $\mu\text{m}$  grain size). GC-11 is muddier, mostly silty-sandy clay (sand varying from 13–40%, with a single layer of muddy sand a few inches thick reaching 60% sand). Finally, GC-12, contains between 40–50% sand over its 7-inch thickness. A fourth core, GC-10, impacted firm substrate and fell over on the seafloor; no sediments were recovered.

Overall, these results reflect the limitations caused by the weather and available equipment during the reconnaissance cruise, and any future coring cruise targeting sand sediments of Heald or Sabine banks will need to be scheduled in the summer, when a favorable sea state is most likely.

**Table 8.1 List of acquired sparker lines during 2021 R/V *Tommy Munro* acquisition**

Line name	Starting shot	Ending shot	SEGY output file name	PROCSEGY file name
305	46870	57311	46824.sgy	305.stk.segy
306	31868	36925	31868.sgy	306.stk.segy
306b	36926	41983	36926.sgy	306b.stk.segy
307	21433	31867	21384.sgy	307.stk.segy
309	20344	24048	20344.sgy	309.stk.segy
310	24049	27462	24049.sgy	310.stk.segy
311	27463	31224	27463.sgy	311.stk.segy
312	31225	34873	31225.sgy	312.stk.segy
313	34875	39211	34874.sgy	313.stk.segy
314	39213	43235	39212.sgy	314.stk.segy
315	43237	48858	43236.sgy	315.stk.segy
401	57312	60725	57312.sgy	401.stk.segy
402	60726	63961	60726.sgy	402.stk.segy
403	3	2653	3a.sgy	403.stk.segy
404	2654	5125	2654.sgy	404.stk.segy
405	5126	7771	5126.sgy	405.stk.segy
406	7772	10780	7772.sgy	406.stk.segy
407	10788	14023	10788.sgy	407.stk.segy
408	14024	17334	14024.sgy	408.stk.segy
409	17335	20343	17335.sgy	409.stk.segy
413	4892	5238	4889.sgy	413.stk.segy
414	4	4888	4.sgy	414.stk.segy
415	48859	53642	48859.sgy	415.stk.segy

## References

- Abdulah KC. 1995. The evolution of the Brazos and Colorado fluvial/deltaic systems during the Late Quaternary: an integrated study, offshore Texas [dissertation]. Houston (TX): Rice University.
- Abdulah KC, Anderson JB, Snow JN, Holdford-Jack L. 2004. The Late Quaternary Brazos and Colorado deltas, offshore Texas, U.S.A.: their evolution and the factors that controlled their deposition. In: Anderson JB, Fillon RH, editors. Late Quaternary stratigraphic evolution of the Northern Gulf of Mexico region. SEPM Special Publication 79. Tulsa (OK): Society for Sedimentary Geology. p. 237–269.
- Al Mukaimi ME, Dellapenna TM, Williams JR. 2018. Enhanced land subsidence in Galveston Bay, Texas: interaction between sediment accumulation rates and relative sea-level rise. *Estuar Coast Shelf Sci.* 207: 183–193.
- Allen GP, Posamentier HW. 1993. Sequence stratigraphy and facies model of an incised valley fill: the Gironde estuary, France. *J Sediment Petrol.* 63: 378–391.
- Anderson JB, Abdulah K, Sarzalejo S, Siringan F, Thomas MA. 1996. Late Quaternary sedimentation and high-resolution sequence stratigraphy of the east Texas shelf. In: De Batist M, Jacobs P, editors. Geology of siliciclastic shelf seas. Geological Society Special Publication 117. London (GB): J Geol Soc London. p. 95–124.
- Anderson JB, Rodriguez AB, Abdula KC, Fillon RH, Banfield LA, McKeown HA, Wellner JS. 2004. Late Quaternary stratigraphic evolution of the northern Gulf of Mexico margin: a synthesis. In: Anderson JB, Fillon RH, editors. Late Quaternary stratigraphic evolution of the Northern Gulf of Mexico region. SEPM Special Publication 79. Tulsa (OK): Society for Sedimentary Geology. p. 1–23.
- Anderson JB, Rodriguez AB, Milliken K, Taviani M. 2008. The Holocene evolution of the Galveston estuary complex, Texas: Evidence for rapid change in estuarine environments. In: Anderson B, Rodriguez AB, editors. Response of Upper Gulf Coast estuaries to Holocene climate change and sea-level rise. Special Paper 443. Boulder (CO): Geological Society of America. p. 89–104.
- Anderson JB, Wallace DJ, Simms AR, Rodriguez AB, Milliken KT. 2014. Variable response of coastal environments of the northwestern Gulf of Mexico to sea-level rise and climate change: implications for future change. *Mar Geol.* 352: 348–366.
- Anderson JB, Wallace DJ, Simms AR, Rodriguez AB, Weight RWR, Taha ZP. 2016. Recycling sediments between source and sink during a eustatic cycle: systems of late Quaternary northwestern Gulf of Mexico basin. *Earth Sci Rev.* 153: 111–138.
- Aschoff JL, Olariu C, Steel, RJ. 2018. Recognition and significance of bayhead delta deposits in the rock record: A comparison of modern and ancient systems. *Sedimentol.* 65, 62–95.
- Bamber JL, Oppenheimer M, Kopp RE, Aspinall WP, Cooke, R.M. 2019. Ice sheet contributions to future sea-level rise from structured expert judgment. *Proc Natl Acad Sci.* 116: 11195–11200
- Banfield LA. 1998. The Late Quaternary evolution of the Rio Grande system, offshore south Texas [dissertation]. Houston (TX): Rice University.

- Banfield LA, Anderson JB. 2004. Late Quaternary evolution of the Rio Grande delta: complex response to eustasy and climate change. In: Anderson JB, Fillon RH, editors. Late Quaternary stratigraphic evolution of the Northern Gulf of Mexico region. SEPM Special Publication 79. Tulsa (OK): Society for Sedimentary Geology. p. 289–306.
- Bardello L. 2014. An improved processing sequence for uncorrelated Chirp sonar data. *Mar Geophys. Res.* 35: 337–344.
- Belknap DF, Kraft JC. 1981. Preservation potential of transgressive coastal lithosomes on the US Atlantic shelf. *Mar Geol.* 42: 429–442.
- Bernstein A, Gustafson MT, Lewis R. 2019. Disaster on the horizon: the price effect of sea-level rise. *J Financ Econ.* 134: 253–272.
- Blaauw M, Christen JA. 2011. Flexible paleoclimate age-depth models using an autoregressive gamma process. *Bayesian Anal.* 6: 457–474.
- Blum MD, Price DM. 1998. Quaternary alluvial plain construction in response to interacting glacio-eustatic and climatic controls, Texas Gulf Coastal Plain. In: Shanley KW, McCabe PJ, editors. Relative role of eustasy, climate, and tectonism in continental rocks. SEPM Special Publication 59. Tulsa (OK): Society for Sedimentary Geology. p. 31– 48.
- Blum MD, Tornqvist T. 2000. Fluvial response to climate and sea-level change: a review and look forward. *Sedimentol.* 47: 2–48.
- Blum MD, Martin JM, Milliken KT, Garvin M. 2013. Paleovalley systems: Insights from Quaternary analogs and experimental studies. *Earth-Sci Rev.* 116(January): 128–169
- Brenner OT, Moore LJ, Murray AB. 2015. The complex influences of back-barrier deposition, substrate slope and underlying stratigraphy in barrier island response to sea-level rise: insights from the Virginia Barrier Islands, Mid-Atlantic Bight, U.S.A. *Geomorphol.* 246:334–350.
- Burstein J, Goff JA, Gulick SPS, Lowery CL, Standing P, Swartz JM. 2021. Tracking barrier island response to early holocene sea-level rise: high resolution study of estuarine sediments in the Trinity River paleovalley. *Geology.* (1 October). doi: 10.31223/X5VP7Q
- Buzas MA. 1990. Another look at confidence limits for species proportions. *J Paleontol.* 2(2):842–843.
- Calves G, Huuse M, Schwab A, Clift P. 2008. Three-dimensional seismic analysis of high-amplitude anomalies in the shallow subsurface of the Northern Indus Fan: sedimentary and/or fluid origin. *J Geophys Res.* 113 (B11):103. [accessed 12 May 2022]; <https://doi.org/10.1029/2008JB005666>
- Carter RWG. 1988. Coastal environments: an introduction to the physical, ecological and cultural systems of coastlines. London (GB): Academic Press. 617 p.
- Cattaneo A, Steel RJ. 2003. Transgressive deposits: a review of their variability. *Earth Sci Rev.* 62: 187–228.
- Chatanantavet P, Lamb MP, Nittrouer JA. 2012. Backwater controls of avulsion location on deltas. *Geophys Res Lett.* 39(1): L01402–L01408.

- Cochrane JD, Kelly FJ. 1986. Low-frequency circulation on the Texas–Louisiana continental shelf. *J Geophys Res.* 91(C9):10645–10659.
- Cooper JA, Green A, Loureiro C. 2018 Geological constraints on mesoscale coastal barrier behaviour. *Global Planet Change.* 168(Sept):15–34.
- Cronin TM, Vogt PR, Willard DA, Thunell R, Halka J, Berke M, Pohlman J. 2007. Rapid sea-level rise and ice sheet response to 8,200-year climate event. *Geophys Res Lett.* 34(20): L20603–L20609.
- Culver SJ. 1988. New foraminiferal depth zonation of the northwestern Gulf of Mexico. *PALAIOS.* 3(1): 69–85.
- Dalrymple RW. 1992. Tidal depositional systems. In: Walker RG, James NP, editors. *Facies models—response to sea level change.* Newfoundland (CA): Geological Association of Canada. p. 195–218.
- Davis RA, Hayes MO. 1984. What is a wave-dominated coast? *Mar Geol.* 60(1–4): 313–329.
- Dellapenna Tm, Cardenas A, Johnson K, Flocks J. 2009. Report of the sand source investigation of the Paleo-Sabine-Trinity marine features (PSTMF). Final report for Texas General Land Office. Cooperative Agreement Number MO7AC12518. 384. p.
- Devine PE. 1991. Transgressive origin of channeled estuarine deposits in the Point Lookout Sandstone, Northwestern New Mexico: a model for Upper Cretaceous, cyclic regressive parasequences of the U.S. Western Interior. *AAPG Bull.* 75(6):1039–1063.
- Dutton A, Carlson AE, Long AJ, Milne GA, Clark PU, DeConto R, Horton BP, Rahmstorf S, Raymo ME. 2015. Sea-level rise due to polar ice-sheet mass loss during past warm periods. *Science* 349(6244):aaa4019.
- Dyer KR, Huntley DA. 1999. The origin, classification and modelling of sand banks and ridges. *Cont Shelf Res.* 19(10):1285–1330.
- Evans AM. 2012. Out of site but not out of mind: submerged prehistoric landscapes on the northwestern Gulf of Mexico outer continental shelf [dissertation]. Baton Rouge (LA): Louisiana State University.
- Fernandes AM, Tornquist TE, Straub KM, Mohrig D. 2016 Connecting the backwater hydraulics of coastal rivers to fluvio-deltaic sedimentology and stratigraphy. *Geology.* 44(12): 979–982.
- FitzGerald, DM, Buynevich IV, Argow BA. 2006. Model of tidal inlet and barrier island dynamics in a regime of accelerated sea-level rise. *J Coast Res. Special Issue No. 39.* 2(Winter):789–795.
- FitzGerald DM, Fenster MS, Argow BA, Nuynevich IV. 2008. Coastal impacts due to sea-level rise. *Annu Rev Earth Planet Sci.* 36(May): 601–647.
- Phleger, FB. 1960. Sedimentary patterns of microfaunas in northern Gulf of Mexico. In: Shepard FB, Phleger FB, van Andel TH, editors *Recent sediments, Northwestern Gulf of Mexico.* Tulsa(OK):: American Association of Petroleum Geologists. p. 267–301.

- Fruergaard M, Møller I, Johannessen PN, Nielsen LH, Andersen TJ, Nielsen L, Sander L, Pejrup M. 2015. Stratigraphy, evolution, and controls of a Holocene transgressive–regressive barrier island under changing sea level: Danish North Sea coast. *J Sediment Res.* 85(7): 820–844.
- Garcia-Gil S, Vilas F, Garcia-Garcia A. 2002. Shallow gas features in incised-valley fills (Ría de Vigo, NW Spain): a case study. *Cont Shelf Res.* 22(16):2303–2315.
- Gehrels WR. 2013. Microfossil-based reconstruction of Holocene relative sea-level change. In: Elias SA, Mock CJ, editors. *Encyclopedia of quaternary science* (second ed.). Amsterdam (NL): Elsevier. p. 419–428.
- Gibling MR. 2006. Width and thickness of fluvial channel bodies and valley fills in the geological record: A literature compilation and classification. *J Sediment Res.* 76(5):731–770.
- Goff JA, Allison MA, Gulick SPS. 2010. Offshore transport of sediment during cyclonic storms: Hurricane Ike (2008), Texas Gulf Coast, USA. *Geology.* 38(4): 351–354.
- Goff JA, Allison MA, Gulick SPS, Reece R, Davis M, Duncan D, Sastrup S. 2015. Shoreface ravinement evolution tracked by repeat geophysical surveys following Hurricane Ike, Bolivar Peninsula, Texas, 2008-2013. *Geophysics.* 80(3):WB1–WB10.
- Goff JA, Flood RD, Austin Jr JA, Schwab WC, Christensen B, Browne CM, Denny JF, Baldwin WE. 2015. The impact of Hurricane Sandy on the shoreface and inner shelf of Fire Island, New York: Large bedform migration and limited erosion. *Cont. Shelf Res.* 98 (15 April): 13–25.
- Goff JA, Lugrin L, Gulick SPS, Thirumalai K, Okumura Y. 2016. Oyster reef die-offs in stratigraphic record of Corpus Christi Bay, Texas, possibly caused by drought-driven extreme salinity changes. *Holocene.* 26(4): 511–519.
- Gould HR, McFarlan E. 1959. Geologic history of the chenier plain, southeastern Louisiana. *Gulf Coast Assoc Geol Soc Trans.* 9:261–270.
- Greene DL. 2006. *Seismic stratigraphy and Late Quaternary evolution of Mobile Bay and Mississippi Sound, Alabama: a record of large- and small-scale fluvial systems through multiple sea-level cycles* [dissertation]. Tuscaloosa (AL): University of Alabama.
- Greene DL, Rodriguez AB, Anderson JB. 2007. Seaward-branching coastal-plain and piedmont incised-valley systems through multiple sea-level cycles: Late Quaternary examples from Mobile Bay and Mississippi Sound, U.S.A. *J Sed Res.* 77(2):139–158.
- Haslett J, Parnell A. 2008. A simple monotone process with application to radiocarbon-dated depth chronologies. *J R Stat Soc C.* 57(4):399–418.
- Hawkes AD, Horton BP. 2012. Sedimentary record of storm deposits from Hurricane Ike, Galveston and San Luis Islands, Texas. *Geomorphol.* (171–172): 180–189.
- Heaton TJ, Köhler P, Butzin M, Bard E, Reimer RW, Austin WEN, et al. 2020. Marine20—The Marine Radiocarbon Age Calibration Curve (0–55,000 cal BP). *Radiocarbon.* 62(4): 1–42.

- Hollis RJ, Wallace DJ, Miner MD, Gal NS, Dike C, Flocks JG. 2019. Late Quaternary evolution and stratigraphic framework influence on coastal systems along the north-central Gulf of Mexico, USA. *Quat Sci Rev.* 23 (1 Nov): 105910.
- Horton NP, Kopp RE, Dutton A, Shaw TA. 2019. Geological records of past sea-level changes as constraints for future projections. *Past Global Change Mag.* 27(1): 28–29.
- Hoyal D, Sheets BA. 2009. Morphodynamic evolution of experimental cohesive deltas. *J Geophys Res.* 114: F02009.
- Hudson PF, Kesel RH. 2000. Channel migration and meander-bend curvature in the lower Mississippi River prior to major human modification. *Geology.* 28(6):531–534.
- Humphrey JD, Ferring CR. 1994. Stable isotopic evidence for latest Pleistocene and Holocene climatic change in North-Central Texas. *Quat Res.* 41(2): 200–213.
- IPCC [Intergovernmental Panel on Climate Change]. 2022. Summary for policymakers. In: *Climate change 2021: the physical science basis. Contribution of Working Group I to the Sixth Assessment Report of the Intergovernmental Panel on Climate Change.* Cambridge (GB): Cambridge University Press. 32 p. [accessed 16 May 2022]; [https://www.ipcc.ch/report/ar6/wg1/downloads/report/IPCC\\_AR6\\_WGI\\_SPM.pdf](https://www.ipcc.ch/report/ar6/wg1/downloads/report/IPCC_AR6_WGI_SPM.pdf)
- Jarosz E, Murray SP. 2005. Velocity and transport characteristics of the Louisiana–Texas Coastal Current. In: Sturges W, Lugo-Fernandez A, editors. *Circulation in the Gulf of Mexico: observations and models.* Washington (DC): American Geophysical Union. p. 143–156.
- Jennings A, Andrews J, Pearce C, Wilson L, Ólafsdóttir S. 2015. Detrital carbonate peaks on the Labrador shelf, a 13–7ka template for freshwater forcing from the Hudson Strait outlet of the Laurentide Ice Sheet into the subpolar gyre. *Quat Sci Rev.* 107(1 Jan): 62–80.
- Jerolmack DJ. 2009. Conceptual framework for assessing the response of delta channel networks to Holocene sea-level rise. *Quat Sci Rev.* 28(17): 1786–1800.
- Jerolmack DJ, Swenson JB. 2007. Scaling relationships and evolution of distributary networks on wave-influenced deltas. *Geophys Res Lett.* 34(23): L23402.
- Karssenberg D, Bridge JS. 2008. A three-dimensional model of sediment transport, erosion, and deposition within a network of channel belts, floodplain and hill slope: extrinsic and intrinsic controls on floodplain dynamics and alluvial architecture. *Sedimentol.* 55(6): 1717–1745.
- Kirwan ML, Megonigal JP. 2013. Tidal wetland stability in the face of human impacts and sea-level rise. *Nature.* 504: 53–60.
- Lamb MP, Nittrouer JA, Mohrig D, Shaw J. 2012. Backwater and river plume controls on scour upstream of river mouths: implications for fluviodeltaic morphodynamics. *J Geophys Res.* 117(F1):FO1002.
- Lambeck K, Rouby H, Purcell A, Sun Y, Sambridge M. 2014. Sea level and global ice volumes from the Last Glacial Maximum to the Holocene. *Proc Natl Acad Sci.* 111(43):15296–15303.

- Lambert WJ, Aharon P, Rodriguez AB. 2003. An assessment of the late Holocene record of severe storm impacts from Lake Shelby, Alabama. *Gulf Coast Assn Geol Soc Trans.* 53(2003): 443–452.
- Lambert WJ, Aharon P, Rodriguez AB. 2008. Catastrophic hurricane history revealed by organic geochemical proxies in coastal lake sediments: A case study of Lake Shelby, Alabama (USA). *J Paleolimn.* 39: 117–131.
- Lentsch N, Finotello A, Paola C. 2018. Reduction of deltaic channel mobility by tidal action under rising relative sea level. *Geology.* 46(7): 599.
- Lentz EE, Hapke CJ, Stockdon HF, Hehre RE. 2013. Improving understanding of near-term barrier island evolution through multi-decadal assessment of morphologic change. *Mar Geol.* 337:125–139.
- Leopold LB, Bull WB. 1979. Base level, aggradation, and grade. *Proc Am Phil Soc.* 123(3):168–202.
- Liu S, Goff JA, Austin Jr JA. 2017. Seismic morphology and infilling structure of the buried channel system beneath the inner shelf off western Long Island, New York: accessing clues to palaeo-estuarine and coastal processes. *Mar Geol.* 387(1 May):12–30.
- Lorenzo-Trueba J, Ashton AD. 2014. Rollover, drowning, and discontinuous retreat: Distinct modes of barrier response to sea-level rise arising from a simple morphodynamic model. *J Geophys Res Earth Surf.* 119(4):779–801.
- Mackin JH. 1948. Concept of the graded river, *GSA Bull.* 59(5):463–512.
- Mallinson D, Culver S, Leorri E, Mitra S, Mulligan R, Riggs S. 2018. Barrier island and estuary co-evolution in response to Holocene climate and sea-level change: Pamlico Sound and the Outer Banks Barrier Islands, North Carolina, USA. In: Moore LJ, Murray AB, editors. *Barrier dynamics and response to changing climate.* Copenhagen (DK): Springer Cham. p. 91–120.
- Martin J, Sheets B, Paola C, Hoyal D. 2009. Influence of steady base-level rise on channel mobility, shoreline migration, and scaling properties of a cohesive experimental delta. *J Geophys Res.* 114(F3).
- Mason J, Mohrig D. 2018. Using time-lapse lidar to quantify river bend evolution on the meandering coastal Trinity River, Texas, USA. *J Geophys Res.* 123(5): 1133–1144.
- Miall A. 2014. *Fluvial depositional systems.* New York (NY): Springer. 316 p.
- Miller MM, Shirzaei M. 2021. Assessment of future flood hazards for southeastern Texas: synthesizing subsidence, sea-level rise, and storm surge scenarios. *Geophys Res Lett.* 48(8): e2021GL092544.
- Milliken KT, Anderson JB, Rodriguez AB. 2008. A new composite Holocene sea-level curve for the northern Gulf of Mexico. In: Anderson B, Rodriguez AB, editors. *Response of Upper Gulf Coast estuaries to Holocene climate change and sea-level rise.* *Geol Soc Am.* 443: 1–11.
- Moodie AJ, Nittrouer JA, Ma H, Carlson BN, Chadwick AJ, Lamb MP, Parker G. 2019. Modeling deltaic lobe-building cycles and channel avulsions for the Yellow River Delta, China. *J Geophys Res Earth Surface.* 124(11):2438–2462.
- Moore LJ, List JH, Williams SJ, Stolper D. 2010. Complexities in barrier island response to sea-level rise: insights from numerical model experiments, North Carolina Outer Banks. *J Geophys Res Earth Surface.* 115(F3):F03004.

- Moran KE, Nittrouer JA, Perillo MM, Lorenzo-Trueba J, Anderson JB. 2017. Morphodynamic modeling of fluvial channel fill and avulsion time scales during early Holocene transgression, as substantiated by the incised valley stratigraphy of the Trinity River, Texas. *J Geophys Res Earth Surface*. 122(1): 215–234.
- Morton RA, Blum MD, White WA. 1996. Valley fills of incised coastal plain rivers. *Gulf Coast Assoc Geol Soc Trans*. 46: 321–331.
- Morton RA, Donaldson AC. 1973. Sediment distribution and evolution of tidal deltas along a tide-dominated shoreline, Wachapreague, Virginia. *Sediment Geol*. 10(4): 285–299.
- Nittrouer JA, Shaw J, Lamb MP, Mohrig D. 2012. Spatial and temporal trends for water-flow velocity and bed-material sediment transport in the lower Mississippi River. *Geol Soc Am*. 124(3–4): 400–414.
- NOAA [National Oceanic and Atmospheric Administration]. 2021. Sea level trends. Tides and currents. Washington (DC): National Ocean and Atmospheric Administration. [accessed 16 May 2022]; <https://tidesandcurrents.noaa.gov/sltrends/>
- Nordfjord, S, Goff JA, Austin Jr J, Sommerfield CK. 2005. Seismic geomorphology of buried channel systems on the New Jersey outer shelf: assessing past environmental conditions. *Mar Geol*. 214(4): 339–364.
- Nordfjord S, Goff JA, Austin Jr JA, Gulick SPS. 2006. Seismic facies of incised valley fills, New Jersey continental shelf: implications for erosion and preservation processes acting during latest Pleistocene–Holocene transgression. *J Sediment Res*. 76(12):1284–1303.
- Nordt LC, Boutton TW, Hallmark CT, Waters MR. 1994. late quaternary vegetation and climate changes in central Texas based on the isotopic composition of organic carbon. *Quat Res*. 41(1): 109–120.
- Nordt LC, Boutton TW, Jacob JS, Mandel RD. 2002. C4 plant productivity and climate-CO<sup>2</sup> variations in south-central Texas during the Late Quaternary. *Quat Res*. 58(2):182–188.
- Oey L-Y. 1995. Eddy- and wind-forced shelf circulation. *J Geophys Res Oceans*. 100(C5):8621–8637.
- Olsen TR. 1998. High-resolution sequence stratigraphy of prograding shoreface systems—a comparison between the Rannoch/Etive Formations, Tampen Spur area, northern North sea and the Point Lookout Formation, Mancos Canyon, southwest Colorado. In: Gradstein FM, Sandvik KO, Milton NJ, editors. *Sequence stratigraphy—concepts and application*. Amsterdam (NL): Elsevier. p. 355– 372.
- Olson HC, Leckie RM, editors. 2003. *Micropaleontologic proxies for sea-level change and stratigraphic discontinuities*. Tulsa (OK): Society for Sedimentary Geology.
- Paine JG. 1993. Subsidence of the Texas coast: inferences from historical and late Pleistocene sea levels. *Tectonophysics*. 222(3–4):445–458.
- Palermo RV, Piliouras A, Swanson TE, Ashton AD, Mohrig D. 2021. The effects of storms and a transient sandy veneer on the interannual planform evolution a low-relief coastal cliff and wave-cut platform at Sargent Beach, Texas, USA. *Earth Surf Dyn*. 9(5): 1111–1123.

- Penland S, Boyd R, Suter JR. 1988. Transgressive depositional systems of the Mississippi Delta plain; a model for barrier shoreline and shelf sand development. *J. Sediment. Res.* 58(6): 932–949.
- Phillips JD, Slattery MC, Musselman ZA. 2004. Dam-to-delta sediment inputs and storage in the lower trinity river, Texas. *Geomorphol.* 62(1–2):17–34.
- Phleger FB, Parker FL. 1951. Ecology of foraminifera, northwest Gulf of Mexico. *Geological Society of America Memoir* 46. New York (NY): Geological Society of America.
- Phleger FB. 1965. Patterns of marsh foraminifera, Galveston Bay, Texas. *Limnol Oceanogr.* 10(Supplement): R169–R184.
- Pirmez C, Prather BE, Mallarino G, O’Hayer WW, Droxler AW, Winker CD. 2012. Chronostratigraphy of the Brazos–Trinity depositional system, western Gulf of Mexico: implications for deepwater depositional models. In: Prather BE, Deptuck ME, Mohrig D, Van Hoorn B, Wynn RB, editors. *Application of the principles of seismic geomorphology to continental-slope and base-of-slope systems: case studies from seafloor and near-seafloor analogues.* SEPM Special Publication 99. Tulsa (OK): Society for Sedimentary Geology. p. 111–143.
- Poag CW. 1981. *Ecological atlas of benthic foraminifera of the Gulf of Mexico.* Woods Hole (MA): Marine Science International.
- Port of Houston. 2020. Statistics. Port of Houston. [accessed 17 May 2022]; <https://porthouston.com/about-us/statistics/>
- Raff JL, Shawler JL, Ciarletta DJ, Hein EA, Lorenzo-Trueba J, Hein CJ. 2018. Insights into barrier-island stability derived from transgressive/regressive state changes of Parramore Island, Virginia. *Mar Geol.* 403 (1 Sept):1–19.
- Ramsey CB. 2009. Bayesian analysis of radiocarbon dates. *Radiocarbon.* 51(1):337–360.
- Rehkemper LJ. 1969. *Sedimentology of Holocene Estuarine Deposits, Galveston Bay, Texas [dissertation].* Houston (TX): Rice University.
- Reimer PJ, Austin WEN, Bard E, Bayliss A, Blackwell PG, et al. 2020. The IntCal20 Northern Hemisphere Radiocarbon Age Calibration Curve (0–55 cal kbp). *Radiocarbon.* 62(4): 725–757.
- Reijnenstein HM, Posamentier HW, Bhattacharya JP. 2011. Seismic geomorphology and high-resolution seismic stratigraphy of inner shelf fluvial, estuarine, deltaic and marine sequences, Gulf of Thailand. *AAPG Bull.* 95(11):1959–1990.
- Riggs SR, Cleary WJ, Snyder SW. 1995. Influence of inherited geologic framework on barrier shoreface morphology and dynamics. *Mar Geol.* 126(1–4): 213–234.
- Rodriguez A, Anderson JB, Bradford J. 1998. Abstract: Holocene Tidal Deltas of the Trinity Incised Valley: Analogs for Exploration and Production. *Gulf Coast Assoc Geol Soc Trans.* 48:373–380., 82 (1998).
- Rodriguez AB. 1999. *Sedimentary facies and evolution of Late Pleistocene to recent coastal lithosomes on the East Texas Shelf [dissertation].* Houston (TX): Rice University.

- Rodriguez AB, Anderson JB, Siringan FP, Taviani M. 1999. Sedimentary facies and genesis of Holocene sand banks on the East Texas inner continental shelf. In: Bergman KM, Snedden JW, editors. *Isolated shallow marine sand bodies: Sequence stratigraphic analysis and sedimentologic interpretation*. SEPM Special Publication 64. Tulsa (OK): Society for Sedimentary Geology. p. 165–178.
- Rodriguez AB, Anderson JB, Banfield LA, Taviani M, Abdulah K, Snow JN. 2000. Identification of a –15 m Wisconsin shoreline on the Texas inner continental shelf. *Palaeogeogr Palaeoclimatol Palaeoecol.* 158(1–2): 25–43.
- Rodriguez AB, Anderson JB, Siringan FP, Taviani M. 2004. Holocene evolution of the east Texas coast and inner Continental Shelf: along-strike variability in coastal retreat rates. *J Sediment Res.* 74(3):405–421.
- Rodriguez AB, Anderson JB, Simms AR. 2005. Terrace inundation as an autocyclic mechanism for parasequence formation: Galveston Estuary, Texas, U.S.A. *J Sediment Res.* 75(4): 608–620.
- Rodriguez AB, Greene DL, Anderson JB, Simms AR. 2008. Response of Mobile Bay and eastern Mississippi Sound, Alabama, to changes in sediment accommodation and accumulation. In: Anderson JB, Rodriguez AB, editors. *Response of Upper Gulf Coast estuaries to Holocene climate change and sea-level rise*. *Geol Soc Am.* 443: p. 13–29.
- Ronchi L, Fontant A, Correggiari A, Asioli A., L., Fontana, A., Correggiari, A., and Asioli, A., 2018. Late Quaternary incised and infilled landforms in the shelf of the northern Adriatic Sea (Italy). *Mar Geol.* 405: 47–67.
- Ronchi L, Fontant A, Correggiari A, Remia A. 2019. Anatomy of a transgressive tidal inlet reconstructed through high-resolution seismic profiling. *Geomorphol.* 343: 65–80.
- Ryan WBF, Carbotte SM, Coplan J, O’Hara S, Melkonian A, et al. 2009. Global Multi-Resolution Topography (GMRT) synthesis data set. *Geochem Geophys Geosyst.* 10(3): Q03014
- Saustrup S, Goff JA, Gulick SPS (University of Texas Institute for Geophysics). 2019. Recommended “best practices” for chirp acquisition and processing. New Orleans (LA): US Department of the Interior, Bureau of Ocean Energy Management. 15 p. Agreement No.: M16AC00020. Report No.: OCS Report BOEM 2019-039. <https://doi.org/10.31223/osf.io/7csjh>
- Shackleton N., 2000. The 100,000-year ice-age cycle identified and found to lag temperature, carbon dioxide, and orbital eccentricity. *Science.* 289(5486): 1897–1902.
- Shawle JL, Connel JE, Boggs BQ, Hein CJ. 2020. Relative influence of antecedent topography and sea-level rise on barrier-island migration: sediment core data. *William & Mary Virginia Institute of Marine Science*. [accessed 17 May 2022]; <https://doi.org/10.25773/8wx5-zq69>
- Shawler JL, Ciarletta DJ, Connell JE, Boggs BQ, Lorenzo-Trueba J, Hein CJ. 2021. Relative influence of antecedent topography and sea-level rise on barrier-island migration. *Sedimentol.* 68(2):639–669.
- Simms AR, Rodriguez AB. 2014. Where do coastlines stabilize following rapid retreat? *Geophys Res Lett.* 41(5): 1698–1703.
- Simms AR, Anderson JB, Taha ZP, Rodriguez AB. 2006. Overfilled versus underfilled incised valleys: examples from the Quaternary Gulf of Mexico. In: Dalrymple RW, Lecki DA, Tillman RW, editors.

Incised valleys in time and space. SEPM Special Publication 85. Tulsa (OK): Society for Sedimentary Geology. p. 117–139.

- Simms AR, Anderson JB, Milliken KT, Taha ZP, Wellner JS. 2007. Geomorphology and age of the oxygen isotope stage 2 (last lowstand) sequence boundary on the northwestern Gulf of Mexico continental shelf. In: Davies RJ, Posamentier HW, Wood LJ, Cartwright JA., editors. Seismic geomorphology: applications to hydrocarbon exploration and production. Special Publication 277. London(GB): Geological Society of London. p. 29–46.
- Simms AR, Anderson JB, DeWitt R, Lambeck K, Purcell A. 2013. Quantifying rates of coastal subsidence since the last interglacial and the role of sediment loading. *Global Planet Change*. 111(December): 296–308.
- Siringan FP, Anderson JB. 1993. Seismic facies, architecture, and evolution of the Bolivar Roads tidal inlet/delta complex, East Texas Gulf Coast. *J Sediment Res*. 63(5): 794–808.
- Siringan FP, Anderson JB. 1994. Modern shoreface and inner-shelf storm deposits off the east Texas coast, Gulf of Mexico. *J Sediment Res* 64(2b): 99–110.
- Smith VB, Mohrig D. 2017. Geomorphic signature of a dammed Sandy River: The lower Trinity River downstream of Livingston Dam in Texas, USA. *Geomorphol*. 297(15 November):122–136.
- Snedden JW, Dalrymple RW. 1999. Modern shelf sand ridges: from historical perspective to a unified hydrodynamic and evolutionary model. In: Bergman KM, Snedden JW, editors. Isolated shallow marine sand bodies: sequence stratigraphic analysis and sedimentological interpretation. SEPM Special Publication 64. Tulsa (OK): Society for Sedimentary Geology. p. 13– 28.
- Standing P, Lowery CL, Burstein J, Swartz JM, Goff JA, Gulick SPS. 2021. Foraminiferal analysis of Holocene sea-level rise within Trinity River incised paleo-valley, offshore Galveston Bay, Texas. *EarthArXiv*. Preprint, version 2. [accessed 17 May 2022]; <https://doi.org/10.31223/X5XG91>.
- Storms J, Weltje G, Terra G, Cattaneo A, Trincardi F. 2008. Coastal dynamics under conditions of rapid sea-level rise: Late Pleistocene to Early Holocene evolution of barrier–lagoon systems on the northern Adriatic shelf (Italy). *Quat Sci Rev*. 27(11):1107–1123.
- Sutherland MD, Dafforn KA, Scanes P, Potts J, Simpson SL, Sim VXY, Johnston EL. 2017. Links between contaminant hotspots in low flow estuarine systems and altered sediment biogeochemical processes. *Estuar Coast Shelf Sci*. 198(Part B):497–507.
- Swartz JM. 2019. Channel processes and products in subaerial and submarine environments across the Gulf of Mexico [dissertation]. Austin (TX): University of Texas at Austin. 139 p.
- Swartz JM, Standing P, Goff JA, Gulick S, Lowery C. 2022. Coastal river response to transgression: A new look at the Trinity Incised Valley using multi-resolution seismic imaging. Preprint version 1. *EarthArXiv*. [accessed 17 May 2022]; <https://doi.org/10.31223/X5P044>
- Swift DJP, Thorne JA. 1991. Sedimentation on continental margins; I, a general model for shelf sedimentation. In: Swift DJP, editors Shelf sand and sandstone bodies: geometry, facies and sequence stratigraphy. Special publication 14. New York (NY): Wiley, International Association of Sedimentologists. p. 3–31.

- Thomas MA. 1991. The impact of long-term and short-term sea-level changes on the evolution of the Wisconsin–Holocene Trinity/Sabine incised-valley system, Texas continental shelf [dissertation]. Houston (TX): Rice University.
- Thomas MA, Anderson JB. 1994. Sea-level controls on the facies architecture of the Trinity/Sabine incised-valley system, Texas continental shelf. In: Dalrymple RW, Boyd R, Zaitlin BA, editors. Incised-valley systems: origin and sedimentary sequences. SEPM Special Publication 51. Tulsa (OK): Society for Sedimentary Geology. p. 63–82.
- Toomey RS, Blum MD, Valastro S. 1993. Late Quaternary climates and environments of the Edwards Plateau, Texas. *Global Planet Change*. 7(4): 299–320.
- Törnqvist TE, Bick SJ, González JL, van der Borg K, de Jong AFM, J.L., Borg, K. van der, Jong, A.F.M. de, 2004. Tracking the sea-level signature of the 8.2 ka cooling event: new constraints from the Mississippi Delta. *Geophys Res Lett*. 31:L23309.
- Torres MA, Limaye AB, Ganti V, Lambd MP, West AJ, Fischer WW. 2017. Model predictions of long-lived storage of organic carbon in river deposits. *Earth Surf Dyn*. 5(4):711–730.
- Trower EJ, Ganti V, Fischer WW, Lamb MP. 2018. Erosional surfaces in the Upper Cretaceous Castlegate Sandstone (Utah, USA): sequence boundaries or autogenic scour from backwater hydrodynamics? *Geology*. 46(8):707–710.
- Ullman DJ, Carlson AE, Hostetler SW, Clark PU, et al. 2016. Final Laurentide ice-sheet deglaciation and Holocene climate-sea level change. *Quat Sci Rev*. 152(\$): 49–59.
- Vail PR, Mitchum Jr RM, Todd RG, Widmier JM, Thompson III S, et al. 1977. Seismic stratigraphy and global changes of sea-level. In: Payton, CE, editor. Seismic stratigraphy—applications to hydrocarbon exploration. Vol. 26. Tulsa (OK): American Association of Petroleum Geologists. p. 49–212.
- Van Wagoner JC, Posamentier HW, Mitchum RM, Vail PR, Sarg, et al. 1988. An overview of the fundamentals of sequence stratigraphy and key definitions. In: Wilgus CK, Hastings, Posamentier H, Van Wagoner J, Ross CA, Kendall CGSt-C, editors. Sea-level changes—an integrated approach. SEPM Special Publication, no.. 42. Tulsa (OK): Society for Sedimentary Geology. p. 39–45.
- Van Wagoner JC, Mitchum RM, Campion KM, Rahmanian VD, editors. 1990. Siliciclastic sequence stratigraphy in well logs, cores, and outcrops: concepts for high-resolution correlation of time and facies. AAPG Methods in Exploration Series, no. 7. Tulsa (OK): American Association of Petroleum Geologists.
- Vitousek S Barnard PL. Fletcher CH, Frazer N, Erikson L, Storlazzi CD. 2017. Doubling of coastal flooding frequency within decades due to sea-level rise. *Sci Rep*. 7(1):no. 1399.
- Wagner AJ, Guilderson TP, Slowey NC, Cole JE. 2009. Pre-bomb surface water radiocarbon of the Gulf of Mexico and Caribbean as recorded in hermatypic corals. *Radiocarbon*. 51(3): 947–954.
- Wallace DJ, Anderson JB, Fernandez RA. 2010. Transgressive ravinement versus depth of closure: a geological perspective from the Upper Texas coast. *J Coast Res*. 26(6): 1057–1067.

- Wantland KF. 1969. Distribution of modern brackish-water foraminifera in Trinity Bay. In: Lankford RR, Rogers JJW, editors. *Holocene geology of the Galveston Bay area*. Houston (TX): Houston Geological Society. p. 93–117.
- Weight RWR, Anderson JB, Fernandez R. Rapid mud accumulation on the Central Texas Shelf linked to climate change and sea-level rise. *J Sediment Res.* 81(10):743–764.
- Wellner JS, Sarzalejo S, Lago M, Anderson JB. 2004. Late Quaternary stratigraphic evolution of the West Louisiana/East Texas continental shelf. In: Anderson JB, Fillon RH, editors. *Late Quaternary stratigraphic evolution of the Northern Gulf of Mexico region*. SEPM Special Publication 54. Tulsa (OK): Society for Sedimentary Geology. p. 217–235.
- White WA, Morton RA, Holmes CW. 2002. A comparison of factors controlling sedimentation rates and wetland loss in fluvial–deltaic systems, Texas Gulf coast. *Geomorphol.* 44(1–2): 47–66.
- Zaitlin BA, Dalrymple RW, Boyd R. 1994. The stratigraphic organization of incised-valley systems associated with relative sea-level change. In: Dalrymple RW, Zaitlin BA, Scholle PA, editors. *Incised-valley systems: origin and sedimentary sequences*. SEPM Special Publication, no. 51. Tulsa (OK): Society for Sedimentary Geology. p. 45–60.
- Zecchin M, Brancolini G, Tosi L, Rizzetto F, Caffau M, Baradello L. 2009. Anatomy of the Holocene succession of the southern Venice lagoon revealed by very high-resolution seismic data. *Cont Shelf Res.* 29(10):1343–1359.
- Zheng S, Edmonds DA, Wu B, Han S. 2019. Backwater controls on the evolution and avulsion of the Qingshuigou channel on the Yellow River delta. *Geomorphol.* 333(15 May):137–151.



### **Department of the Interior (DOI)**

The Department of the Interior protects and manages the Nation's natural resources and cultural heritage; provides scientific and other information about those resources; and honors the Nation's trust responsibilities or special commitments to American Indians, Alaska Natives, and affiliated island communities.



### **Bureau of Ocean Energy Management (BOEM)**

The mission of the Bureau of Ocean Energy Management is to manage development of U.S. Outer Continental Shelf energy and mineral resources in an environmentally and economically responsible way.